Colección de Estudios de Física 90

μSQUID susceptometry of molecular qubits

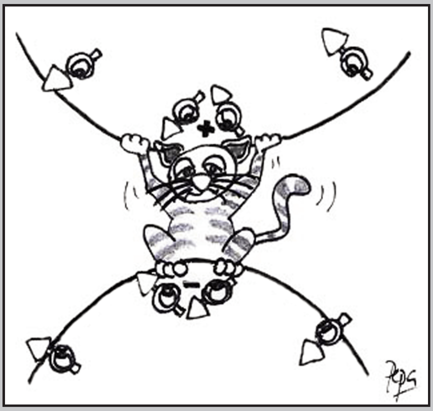

María José Martínez Pérez

μSQUID susceptometry of molecular qubits

Colección de Estudios de Física
Vol. 90

Esta colección recoge las tesis presentadas en el Departamento de Física de la Materia Condensada de la Universidad de Zaragoza desde su constitución en 1987.

Colección de Estudios de Física Vol. 90

μSQUID susceptometry of molecular qubits

María José Martínez Pérez

1542

Prensas Universitarias
Universidad Zaragoza

MARTÍNEZ PÉREZ, María José
µSQUID susceptometry of molecular qubits / María José Martínez Pérez. — Zaragoza : Prensas Universitarias de Zaragoza, 2011
XVII, 254 p. : il. ; 25 cm. — (Colección de Estudios de Física ; 90)
Bibliografía: p. 225-249. — ISBN 978-84-15274-82-7
Materiales magnéticos–Tesis doctorales
537.622(043.2)

1.ª edición, 2011

Prensas Universitarias de Zaragoza. Edificio de Ciencias Geológicas, c/ Pedro Cerbuna, 12,
50009 Zaragoza, España. Tel.: 976 761 330. Fax: 976 761 063
puz@unizar.es http://puz.unizar.es

Impreso en España
Imprime: Servicio de Publicaciones. Universidad de Zaragoza
D.L.: Z-3584/2011

Contents

Introduction

Molecular nanomagnets offer innumerable possibilities for the study of quantum spin dynamics. Magnetic Nanoparticles (NPs) and Single Molecule Magnets (SMMs) are characterized by a permanent magnetic moment and behave as tiny magnets or, rather, giant spins. At low enough temperatures ($T \sim 1 - 10$ K typically), their magnetic moments become blocked along a certain direction defined by the cluster's easy anisotropy axis leading to an Ising-like behavior.

Let us distinguish between two groups of nanomagnets. Magnetic NPs, on the one hand, are relatively complex systems consisting of, tipically, $\sim 10^3 - 10^4$ magnetic atoms. On the other hand, SMMs are simpler clusters consisting of ”only” $1 - 10$ magnetic atoms [1]. Just as electronic spins do, magnetic nanoparticles and SMMs should in principle exhibit the effects of Quantum Mechanics. These include spin inversion due to quantum tunneling of the magnetization or the possibility to observe states that are superpositions of the classical ones [2,3]. However, the difference in their complexity, together with other facts, leads to dramatic differences in the quantum behavior of both systems. Roughly speaking, one could say that magnetic nanoparticles lie closer to the ”macroscopic” or classical world whereas SMMs belong to the so-called ”microscopic” or quantum world.

One of the most complex entities able of showing quantum behavior is an ubiquitous protein called ferritin. In its natural form, ferritin contains 4500 Fe atoms approximately, forming an amorphous antiferromagnetic material similar to ferrhydrite. This molecule gained much popularity in the 90's after D. Awschalom and co-workers [4] claimed the observation of quantum coherence in ferritin below ~ 200 mK. Although controversial, this finding prompted many scientists to look for quantum effects in ferritin and other ”highly complex” magnetic NPs [5,6].

SMMs, on the other hand, are much simpler in the sense that their size and number of components is much smaller. This fact, together with their homogeneous size and structural symmetry (as they are usually ordered in

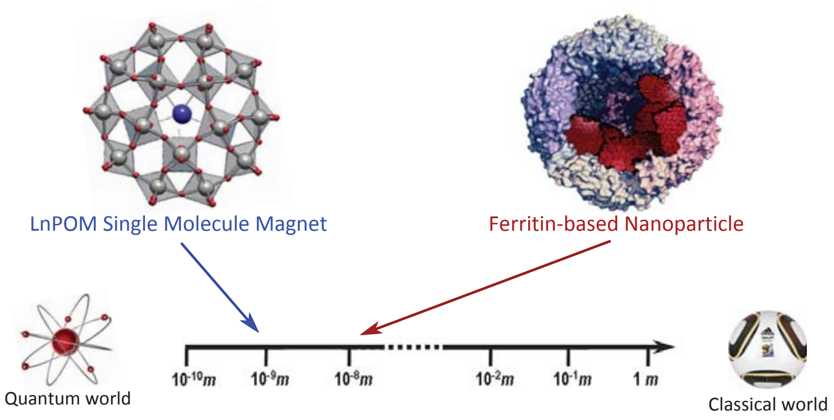

Figure 1: This thesis work deals with the study of two types of molecular nanomagnets. Ferritin-based NPs, on the one hand, exhibit a behavior closer to that expected in a classical object. POM-based SMMs, on the other hand, are much simpler, lying closer to the atomic or quantum limit.

regular lattices) provides SMM with their extraordinary quantum character. Appealing quantum phenomena, like resonant quantum tunneling of the magnetic moment as well as quantum coherence, were indeed observed in Mn_{12} in the late 90's [7–11]. SMMs appear, in this way, as almost ideal systems for the test of fundamental theories of quantum mechanics as well as for the study of the fuzzy transition from classic to quantum physics [12, 13]. Based on these properties SMMs have been proposed as physical realizations of quantum bits or qubits [14]. A qubit is nothing but a two-level system (e.g. a particle with effective $S = 1/2$) that is able of preserving its quantum coherence during a sufficiently long time. Qubits are the building blocks of quantum computers, which would enable to perform certain operations unimaginably fast [15].

The goal of the thesis work has been to perform a detailed study of the classical or quantum behavior of samples belonging to both worlds, quantum and classical. For this, we have concentrated on magnetic NPs synthesized artificially inside ferritin as an example of a ”macroscopic” entity. The ”microscopic” world has been investigated by means of a novel family of SMM consisting of individual lanthanide atoms encapsulated between polyoxometalate (POM) clusters [16]. Both ferritin-based NPs and POM-based SMM can be classified as molecular nanomagnets and exhibit certain similarities. Both consist of a central magnetic core encapsulated within a cage. The latter is a biological clothing in the case of ferritin, and an architecture of polyatomic anions in the case of POM-based molecules (see Fig. 1).

The study of quantum spin dynamics faces however some technical difficulties. To begin with, experiments need to be performed at extremely low temperatures. This is very important in order to decrease the influence of thermal fluctuations that destroy any possibility of observing quantum phenomena. Secondly, the dynamical response of a quantum system can vary several decades depending on its temperature. Quantum phenomena, like tunneling of the magnetization, occur at timescales that can vary over many orders of magnitude, depending on the parameters of the system ($\leq 1\ \mu$s), whereas classical relaxation process become extremely slow as temperature decreases ($\geq 10^3$ s). For this reason, sensors should work in as large as possible frequency bandwidths. Finally, interactions between the spins and their surroundings (which include nuclear spins, neighboring molecules...) play also a determinant role in the quantum behavior, usually tending to destroy it. For this reason, experiments performed on small spin populations or magnetically diluted samples are preferred. A very attractive alternative, which is also very interesting for applications, is the study of molecular nanomagnets deposited directly over the sensor's surface. These studies demand the use of extremely sensitive devices and require an optimized coupling between samples and sensors. This coupling strongly depends on the sample position with respect to the sensing areas [17] and, therefore, on the deposition technique. Much effort has been recently dedicated to both approaches, improving the sensor's sensitivity on the one hand [18, 19] and developing new particle patterning techniques on the other [20].

For these reasons, much of the time devoted to this thesis work was dedicated to the development of an user-friendly instrument able of fulfilling, to some extent at least, the conditions mentioned above. This instrument consists of a microsusceptometer coupled to an ultra-sensitive Superconducting Quantum Interference Device (SQUID) [21]. Our sensors are installed inside the mixing chamber of a dilution refrigerator which enables us to decrease the temperature down to the neighborhood of absolute zero (~ 13 mK). The signal readout is performed using extremely-fast commercial SQUID electronics fabricated by the Physikalisch-Technische Bundesanstalt (PTB-Berlin) and Magnicon GmbH [22]. This fact provides our devices with one of the world's broadest frequency bandwidths operating in flux locked loop mode (1 mHz $\leq f \leq 1$ MHz). Finally, our μSQUID susceptometers inherit the exceptional flux sensitivity provided by the μSQUID sensors fabricated by the PTB/Magnicon (the flux noise at mK temperatures is $\sim 0.2\ \mu\Phi_0/\mathrm{Hz}^{1/2}$ typically). The first two chapters of this manuscript provide a detailed description of the design, fabrication and installation of these sensors inside the mixing chamber of a dilution refrigerator as well as a brief description of other experimental techniques used during this work.

Once we have done that, we will move onto the physical studies of nanomagnets. This is divided into two parts, dealing with ferritin-based NPs and

SMMs, respectively. In any case, the chapters are self-contained and include detailed introductions that will help the reader to follow each of them separately.

Chapters 3 and 4 are devoted to the study of the ”macroscopic” or classic world. For this purpose we will analyze the magnetic characteristics of two types of magnetic NPs synthesized at the Instituto de Nanociencia de Aragón (INA). On the one hand, we will study limit size effects on different samples of ferrimagnetic nanoparticles grown inside ferritin (magnetoferritin). On the other, we will perform a detailed study of the magnetic response of antiferromagnetic nanoparticles, also grown inside ferritin. A brief theoretical introduction to these questions will be provided in chapter 3 while chapter 4 is left for the experimental results.

It turns out that ferritin is a well suited carrier to achieve a controlled deposition of NPs onto different substrates. A group from the Centre d'investigació en Nanociència i Nanotecnologia (CIN2) in Barcelona found recently that monolayers of ferritin-based nanomagnets can be easily fabricated through Dip Pen Nanolithography (DPN) [23]. The latter is a direct-write technique [24], called in this way for its analogy with a traditional dip or fountain pen, which enables the nanostructuration of molecules on different substrates, e.g. the surface of our sensor. In chapter 5 we will show how the combination of DPN and the high sensitivity of our sensors has enabled the direct characterization of a submonolayer arrangement of 10^7 particles grown inside ferritin.

Chapters 6 and 7 deal with the ”microscopic” or quantum world. For this purpose, we will concentrate on a novel family of SMMs [16] synthesized at the Instituto de Ciencia Molecular (ICMoL) from Valencia. These molecules offer numerous opportunities for the study of quantum spin dynamics. In chapter 6 we will show, for instance, how the magnetic characteristics of these clusters can be effectively tailored by means of chemistry. The molecular symmetry strongly affects the molecule's hamiltonian and, as we will show, clusters optimized for their application as qubits could be chemically engineered.

Chapter 7 is devoted to the study of the transference of energy between a spin system and the crystal lattice where it belongs to. That is, to the phenomenon of spin-lattice relaxation in the region of very low temperatures. Although very old, quite surprisingly this problem is not fully understood yet. This question is linked to some basic aspects of quantum mechanics and magnetism. In addition, these studies could be successfully applied to the recent effort in studying and manipulating individual spins in solids [25–27]. In fact, quantum computing relies on the ability of maintaining spins under off-equilibrium conditions, e.g. in coherent states, for as long as possible.

To summarize, the work that we present here is aimed to ameliorate our understanding of the intriguing classical-to-quantum transition. Our experiments could preface future investigations in which both worlds could be combined together. We envisage, for instance, to study the influence of classical macroscopic entities on quantum microscopic systems. For this purpose we plan to study the magnetic behavior of ferritin dimers in which two of our ”macroscopic” ferritin molecules containing different nanoparticles are brought together. Even further, we plan to combine single ”macroscopic” ferritin molecule with single ”microscopic” magnetic ions like those forming part of the single molecule magnets described previously. These experiments are beyond the scope of this thesis and remain for future works.

Chapter 1

Experimental Techniques

1.1 Introduction

In this thesis we present an experimental study of the magnetic properties of molecular nanomagnets. For this purpose, we have combined commercial magnetic characterization techniques with more sophisticated tools designed and fabricated by us on purpose.

Commercial setups are well suited and calibrated to enable a quick and user-friendly operation. Magnetometers and spectrometers allow the study of spin dynamics and quantum phenomena in magnetic materials by analyzing the magnetic response of the sample under different ambient conditions, e.g. applied magnetic field, temperature, frequency, radiation etc. In this chapter, we will first present a detailed description of the experimental commercial techniques used during this thesis. These include the use of SQUID magnetometers and calorimeters from the company Quantum Design [28].

Most of the measurements that we present here have been performed at extremely low temperatures. For this purpose, a dilution refrigerator from Leiden Cryogenics was properly adapted. Low temperature techniques have been in fact fundamental for the success of our experiments. For this reason, the second part of this chapter is dedicated to provide some basic ideas about low temperature physics and setups.

In chapter 6 we will present a set of measurements performed in a non-commercial setup. This is an Electron Paramagnetic Resonance (EPR) spectrometer that enables to measure within a broad bandwidth of frequencies. These experiments were possible thanks to the collaboration of J. Van Slageren and C. Schlegel from the University of Stuttgart. The instrument was developed by C. Schlegel during his thesis and a brief description will be provided here.

These measurements appear however to be insufficient in many cases. The study of quantum properties often demands the use of more sophisticated characterization techniques. During the course of this work, most of our experimental time has been dedicated to the development of a non-commercial, highly-versatile and user-friendly setup for the characterization of magnetic materials under extreme conditions of low temperature and frequency. It is a μSQUID susceptometer integrated on a 3 mm × 3 mm chip. The development of this tool has been possible thanks to the combination of: (1) SQUID sensor manipulation and performance testing. (2) Sensor modification by Focused Ion Beam (FIB) and nanodeposition of superconducting material to obtain a magnetic SQUID microsusceptometer. (3) Sensor implementation inside the mixing chamber of a especially designed dilution refrigerator.

The successful fabrication and operation of our μSQUID susceptometers demanded the use of different equipments. To begin with, the μSQUID sensor modifications performed to fabricate the microsusceptometers, have been possible thanks to the use of a ”Nanolab” device. This is a dual-beam setup from FEI that enables the visualization and manipulation of materials with nanoscale precision. A brief introduction to the working principles and main characteristics of this device will be provided at the end of this chapter. The complete description of the design, fabrication and operation of our μSQUID susceptometers is left for the next chapter.

1.2 Sample characterization: MPMS and PPMS from Quantum Design

Magnetization and magnetic susceptibility measurements provide much information about basic parameters such as the spin and the anisotropy of magnetic samples. Ac susceptibility provides additional information about the dynamic behavior of spins and the relaxation processes to thermal equilibrium, the interaction between spins, and the ensuing magnetic phase transitions. Specific heat measurements provide us complementary information about the lattice vibrations, the hyperfine couplings to nuclear spins and the magnetic anisotropy. In this section, we describe the operation of the two commercial setups used in this thesis work for the routine characterization of our samples in the temperature range comprised between 1.8 K$\leq T \leq$ 300 K (for the MPMS) and 0.3 K $\leq T \leq$ 300 K (for the PPMS). These instruments are part of the Research Support Services of the University of Zaragoza [29].

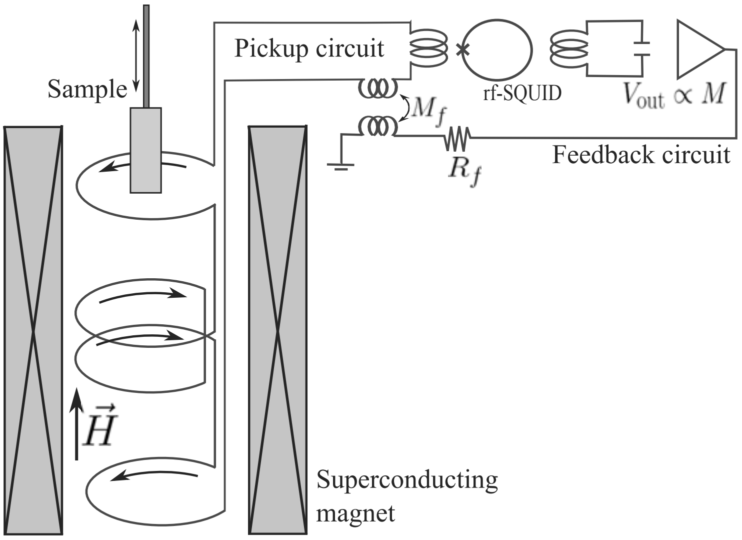

Figure 1.1: Scheme of the measurement circuit. The sample's signal is coupled to the pickup circuit and, from it, to a rf-SQUID loop. The resulting signal is amplified and feedback to the pickup circuit. The output is proportional to the sample's magnetization.

1.2.1 MPMS system: SQUID magnetometer

The MPMS (Magnetic Property Measurement System) is a commercial set up from Quantum Design that we used to perform most of the "high" temperature ($1.8 - 300$ K) magnetization and susceptibility measurements reported in this thesis. The MPMS works inside an ^{4}He refrigerator which provides a minimum temperature of 1.8 K.

The main component of the MPMS is a SQUID magnetometer. Superconducting Quantum Interference Devices (SQUIDs) are very sensitive flux-to-voltage transducers that behave also as low-noise current amplifiers. SQUIDs can therefore be used for the detection of very small magnetic signals. A more detailed description of the performance of a SQUID magnetometer can be found in the next chapter (see section 2.2).

Figure 1.1 shows schematically the components of the MPMS. The magnetometer consists of a second order gradiometer made of NbTi inductively coupled to a rf-SQUID. The excitation magnetic field is created by a NbTi superconducting magnet able to attain dc magnetic fields up to 5 T and a maximum ac-excitation field of $h_{\text{ac}} = 4$ Oe. The sample is moved through the gradiometric pickup coils in a number of passes. This induces an electrical current in the superconducting pickup coil circuit which is inductively transferred to the rf-SQUID. From the rf-SQUID, the signal is transferred to a feedback circuit that keeps the current in the pickup coil circuit equal to zero. In this way, the system behaves as a current-null detector, as seen in Fig. 1.1. This circuit provides a voltage that is proportional to the magnetization of the sample ($V_{\text{out}} \propto M$). The maximum sensitivity reached with this method is 2×10^{-8} emu when operating in ac mode. The ac bandwidth is limited from 0.1 Hz up to 1 kHz. The measurement in the MPMS is completely automated and controlled by an user-friendly interface.

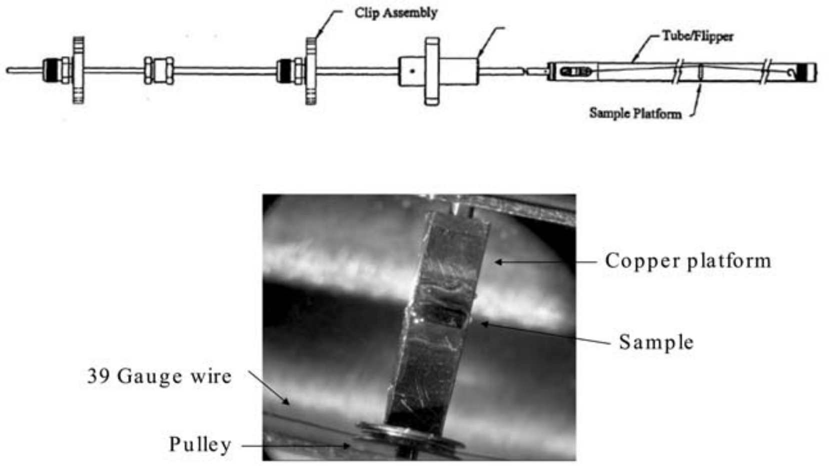

Figure 1.2: Schematic view of the rotating holder components (top panel). Magnification of the sample platform (bottom panel).

1.2.2 Rotating holder

The MPMS enable us to measure the magnetization and susceptibility of single crystals along different directions. This can be done by measuring the magnetic response at different relative angles between the sample and the magnetic field using a special holder than can rotate the sample in situ (Fig. 1.2). This holder is an oxygen-free copper 1.6 mm × 5.8 mm plate that can rotate 360° with a relative accuracy of 0.05°.

The relative angle formed by the applied magnetic field and the crystal axes can be determined in the following way. The copper holder exhibits a quite strong dependence with the ac magnetic field due to the production of eddy currents. This contribution becomes maximum when the holder plane is perpendicular to the applied field (see Fig. 1.3). Under these circumstances, the imaginary component of the magnetization is maximum whereas the real part remains approximately zero. In addition, this contribution increases with frequency. In this way, measurements can be performed by varying the holder

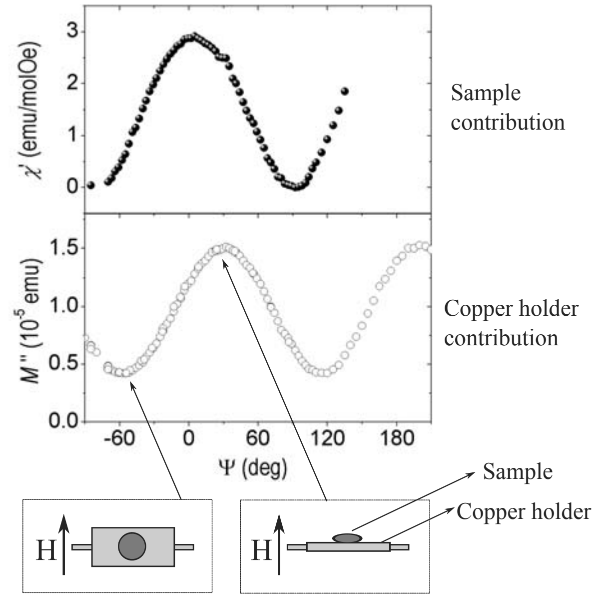

Figure 1.3: Measurements performed using the rotating option of the MPMS on a crystal of ErW_{10} (more details of this sample can be found in chapter 7). At high enough temperatures, when the paramagnetic crystal exhibits no imaginary response, the imaginary part of the susceptibility will only depend on the copper holder position with respect to the applied magnetic field (bottom panel). On the other hand, the real part of the susceptibility reflects only the sample's response since the contribution from the copper holder is approximately zero (top panel).

angle with respect to the applied magnetic field and measuring, at each point, the imaginary component of the high frequency susceptibility ($f \sim 1$ kHz), and the low frequency susceptibility. The former will provide us the information regarding the holder position and the latter will provide us information about the sample's response. An example of these kind of measurements can be seen in Fig. 1.3. This method proves to be very useful in the study of the magnetic anisotropy in single crystals.

1.2.3 PPMS system: heat capacity measurements

Specific heat measurements have been performed using a commercial calorimeter installed in a PPMS (Physical Property Measurement System) form Quantum Design. This setup is inserted in an ^{3}He refrigerator that provides a minimum temperature of 350 mK.

The calorimeter consists of a flat platform that contains a sample holder made of sapphire, a thermometer and a heater (see Fig. 1.4). The thermometer is a Cernox^{TM} (ceramic oxynitride) resistance and the heater is a metallic

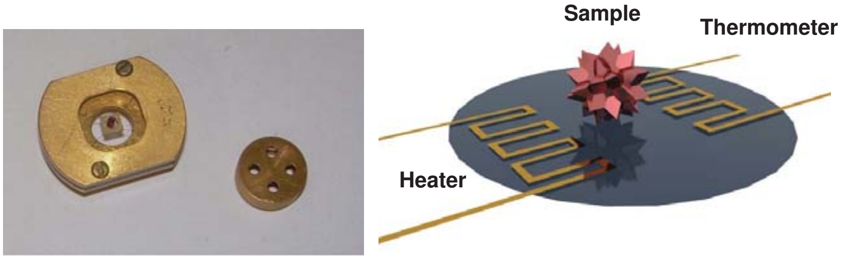

Figure 1.4: Photograph of the 721-model calorimeter from Quantum Design (left-hand panel). Schematic representation of the calorimeter (right-hand panel).

film resistor. The heat capacity resolution of the system is 10 nJ/K at 2 K [28]. This platform is connected to a metallic cage through four superconducting NbTi wires. Two of these wires are used to supply electric current to the heater and the other two are used to measure the electrical resistance of the thermometer. The whole system is shielded from external radiation by a metallic cover. We will usually measure powdered samples ($\sim$ 1 mg typically) prepared as flat platelets using a portable press. This platelet is conveniently located over the holder using a small quantity (1 mm^3) of Apiezon N grease that provides a good thermal contact with the plate.

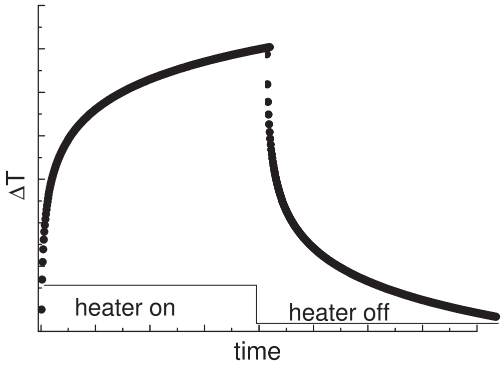

Figure 1.5: The figure shows an example of a typical specific heat measurement. The temperature increases exponentially while the heat pulse is on whereas the sample relaxes exponentially to equilibrium after the heat pulse is switched off.

We will use the semiadiabatic relaxation method [30] to measure heat capacity. The latter consists of the application of a square heat power pulse P during a period of time Δt. This energy either heats the sample, leading to an increase of the temperature, or flows towards the metallic cage through the NbTi wires. The variation of temperature is monitored as a function of time. The evolution of the sample's temperature $T(t)$ with respect to T_0, i.e. the temperature of the metallic cage considered as the thermal bath, satisfies the following relation

$$T(t) - T_0 = \frac{P}{K}\left[1 - e^{-\frac{\Delta t}{\tau}}\right] \tag{1.1}$$

where K is the thermal conductivity of the NbTi wires and $\tau = C/K$ is a characteristic relaxation time, C being the heat capacity of the calorimeter plus the sample. The duration of the pulse and the heat power are usually set to attain a 5% change in the temperature of the sample. The experiment is usually performed by first applying an excitation pulse and monitoring the exponential increase of T and the subsequent exponential relaxation when the pulse is switched off as seen in Fig. 1.5. The obtained curves can be simultaneously fitted with Eq. (1.1) which provides the values of K and $\tau = C/K$.

1.3 Low temperature physics

The conquest of cold started already in prehistoric times as man realized that meat could be kept for longer periods when it is stored in cold places like caves. This principle was used by the ancient Egyptians, Romans, Greeks or Chinese for storing food. But it was not until the 17^{th} Century when the nature of 'cold' and 'hot' was first studied from a scientific point of view by R. Boyle. The true history of cryogenics began later in the 19^{th} century when scientists managed to liquefy nitrogen (Z. Wróblewski and K. Olszewski) and oxygen (L. Cailletet and R. Pictet), the gases that were thought to be "permanent" by Faraday. Hydrogen was liquefied soon after by J. Dewar, the inventor of the cryogenic storage flasks that we still use today.

The last gas to be liquefied was helium. This element was first discovered in the spectroscopic investigations of the Sun and later also on Earth, forming large natural gas reserves. The striking properties of helium that make it so scarce on Earth, also make it the most difficult in being liquefied. This elusive goal was achieved by the Dutch physicist H. Kamerlingh Onnes in 1908 at the University of Leiden. H. Kamerlingh Onnes reached in this way a temperature of just 4.2 degrees over the absolute zero. This achievement enabled him to discover superconductivity in mercury for which he was awarded with the Nobel prize in 1913.

Even colder temperatures were later achieved by pumping the "hot" vapor atoms produced by a liquid bath of helium. Pumping ^{4}He enables for instance to reach temperatures of ~ 1.8 K. Using an even more scarce isotope of helium, ^{3}He, the minimum temperature could be eventually lowered down to ~ 300 mK. Finally, using a ^{3}He-^{4}He mixture in a so-called dilution refrigerator, the

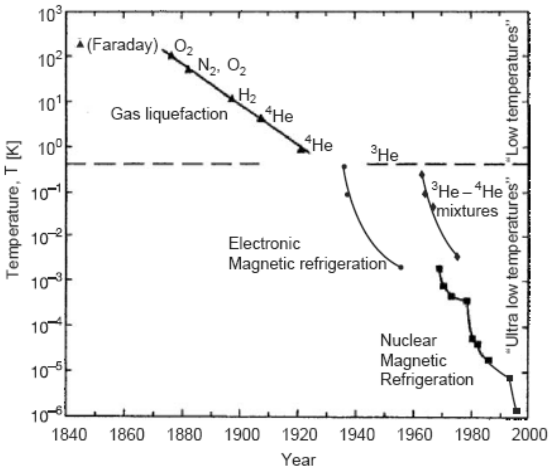

Figure 1.6: Historical evolution of cryogenics, from the liquefaction of air in the 19^{th} to the nuclear magnetic refrigeration in our days. From [31]

milikelvin temperature range was first open for the humankind. This technique will be the subject of this section.

Dilution refrigerator-based technologies provide the lowest temperatures attainable using cryogenic liquids. To go down even further other techniques are required. Nuclear magnetic refrigeration, for instance, is able to provide temperatures of a few microkelvin. Laser cooling methods enable to go down to the nanokelvin range. The minimum temperature reached to date was 100 picokelvin, obtained in the Low Temperature Laboratory of Helsinki in 1999.

1.3.1 Helium, a quantum cryogenic liquid

There are two stable isotopes of helium. The most common one is ^{4}He, consisting of two neutrons and two protons. The other stable isotope is ^{3}He, which is made of two protons and one neutron. The different nature of the isotopes gives rise to some properties that are essential for cryogenics, as we will see below.

The alpha decay of heavy elements is the source of most natural ^{4}He that can be found in gas reserves. On the other hand, ^{3}He is extremely scarce in Earth and can be commercially obtained as a sub-product of nuclear reactors. ^{3}He is in addition the best-known isotope used for neutron detection, that can be used for the detection of radioactive materials in shipping containers. This fact, together with its scarcity, makes ^{3}He an extremely expensive strategic resource (2000\$/liter of gas at atmospheric pressure [32]).

	^{3}He	^{4}He
Boiling point,T_b(K)	3.19	4.21
Critical temperature, T_c(K)	3.32	5.20
Maximum superfluid transition temperature,T_c(K)	0.0025	2.1768
Density[a], ρ (g cm^{-3})	0.082	0.1451
Molar volume[a], V_m(cm^3 mol^{-1})	36.84	27.58
Melting pressure[b], P_m(bar)	34.39	25.36
Minimum melting pressure, P_m(bar)	29.31	25.32
Gas-to-liquid volume ratio[c]	662	866

[a] At saturated vapor pressure and $T = 0$ K

[b] At $T = 0$ K

[c] Liquid at 1 K, NTO gas (300 K, 1 bar)

Table 1.1: Summary of ^{3}He and ^{4}He main properties. From [31].

The main properties of ^{4}He and ^{3}He isotopes are summarized in table 1.1. Both isotopes have extremely low densities due to the weakness of their intermolecular interactions. This fact, together with the low mass of helium, leads to strong zero point fluctuations. As a result, ^{4}He and ^{3}He are characterized by their extremely low boiling points, 4.2 K and 3.19 K respectively, and the fact that helium can not be solidified at atmospheric pressure.

The main properties that make a liquid suitable or not for cryogenics are the latent heat of evaporation L and the vapor pressure P_{vap}. The latent heat of evaporation is the heat absorbed by the liquid during its evaporation, which occurs without a change in temperature. The vapor pressure is the pressure of vapor in thermodynamic equilibrium with the liquid. Liquid helium evaporates easily with any thermal excitation leading to a very small latent heat of evaporation and large vapor pressure. It can be demonstrated [31] that P_{vap} is given by

$$P_{\text{vap}} \propto e^{-\frac{L}{RT}} \tag{1.2}$$

where R is the gas constant. Liquid helium can be cooled below its boiling point by pumping the ”hot” gas that evaporate from it. The cooling power of this method is given by

$$\dot{Q} = \dot{n}L \propto e^{-\frac{L}{RT}} L \tag{1.3}$$

where $\dot{n}$ is the mass flow through the liquid-vapor boundary. Assuming that the pumping speed is constant, $\dot{n}$ is proportional to the vapor pressure $P_{\text{vap}}(T)$ leading to an exponential dependence of $\dot{Q}$ on T. In this way, the minimum temperature attainable with ^{4}He and ^{3}He refrigerators is limited to $T \sim 1$ K and $T \sim 350$ mK, respectively. At these temperatures the vapor pressure floating over the helium bath nearly disappears and the cooling power eventually becomes smaller than the external heat flowing to the bath. Nevertheless, even lower temperatures can be achieved by using the especial properties of both isotopes combined together in a dilution refrigerator. These instruments are detailed on the next section.

1.3.2 ^{3}He-^{4}He dilution refrigerators

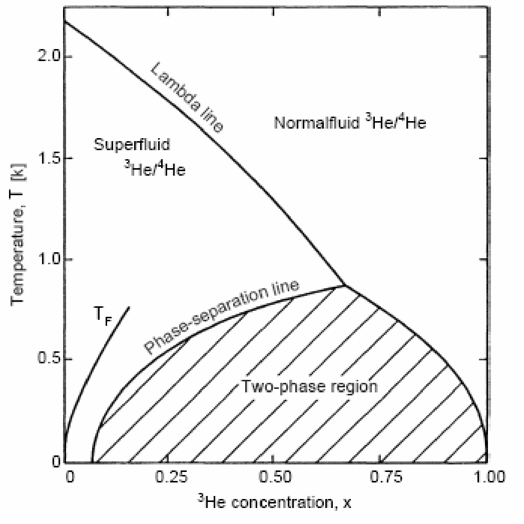

Figure 1.7: Phase diagram of liquid ^{3}He-^{4}He mixture as a function of x, i.e. the concentration of ^{3}He. The shaded region is a non-accessible region. From [31]

The ^{3}He-^{4}He dilution refrigerator was first proposed by Heinz London in 1962 as a method to cool down below 300 mK based on the especial properties of a liquid solution of both helium isotopes. The minimum temperature obtained with a ^{3}He-^{4}He dilution refrigerator is 2 mK, achieved by Giorgio Frossati in Grenoble [31].

The phase diagram of a ^{3}He-^{4}He mixture as a function of the concentration x of ^{3}He is shown in Fig. 1.7. The lambda line marks the onset of the superfluid ^{4}He phase that depends on x. Let us remind the reader that ^{3}He does not undergo any transition to a superfluid phase down to milikelvin temperatures. The shaded area in the phase diagram corresponds to a non-accessible region of temperatures and concentrations for helium mixtures. Two different phases appear below $T = 0.87$ K , one rich in ^{3}He, usually referred to as the concentrated phase, and the other one rich in ^{4}He, referred to as the diluted phase. The concentrated phase becomes nearly pure at sufficiently low temperatures having $\sim$ 100% of ^{3}He atoms. In contrast, the diluted phase has a constant concentration of 6.6% ^{3}He down to the absolute zero.

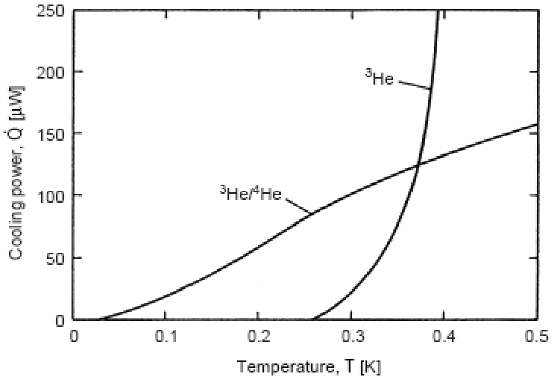

Figure 1.8: Cooling power of ^{3}He and ^{3}He-^{4}He. From [31]

The concentrated phase is less dense and floats over the diluted phase. The latter is superfluid and behaves as an "inert background" with negligible heat capacity. The ^{3}He atoms belonging to the diluted phase can be extracted or "pumped" playing therefore the role of the "vapor pressure" in a conventional ^{4}He- or ^{3}He-refrigerator. By doing so, there will be a continuous flow of ^{3}He forced to go from the pure to the diluted phase in order to keep the 6.6% ^{3}He constant. The "vapor pressure" of a dilution refrigerator does not decrease with temperature providing sufficient cooling power even at mK temperatures as it can be seen in Fig. 1.8.

Figure 1.9 shows schematically how a dilution refrigerator works. It is introduced in a liquid ^{4}He bath and is completely isolated from the environment by vacuum shields. The ^{3}He-^{4}He mixture is pre-cooled through thermal contact with the so-called 1 K pot. This is a chamber that collects helium from the helium bath that surrounds the device. Temperatures of about 1.3 K can be reached by pumping the 1 K pot, enough to liquefy the ^{3}He-^{4}He mixture. The liquid enters then into the mixing chamber filling part of the still as well. Pumping the still forces ^{3}He atoms going from the concentrated to the diluted phases with the ensuing temperature lowering. The pumped helium is then taken back to circulation in a closed circuit. At room temperature, ^{3}He gas is passed through liquid nitrogen and liquid helium "traps". In these traps, impurities such as oxygen, nitrogen or water are cryopumped so that they remain attached to the walls of the trap, while helium continues circulating.

The heat exchangers are one of the most critical parts of a dilution refrigerator determining the minimum temperature attainable. In the heat exchangers, the warm incoming ^{3}He is cooled down to milikelvin temperatures by transferring heat to the cold outgoing helium. These are designed to maximize the contact area between the helium flow and the heat exchanger itself

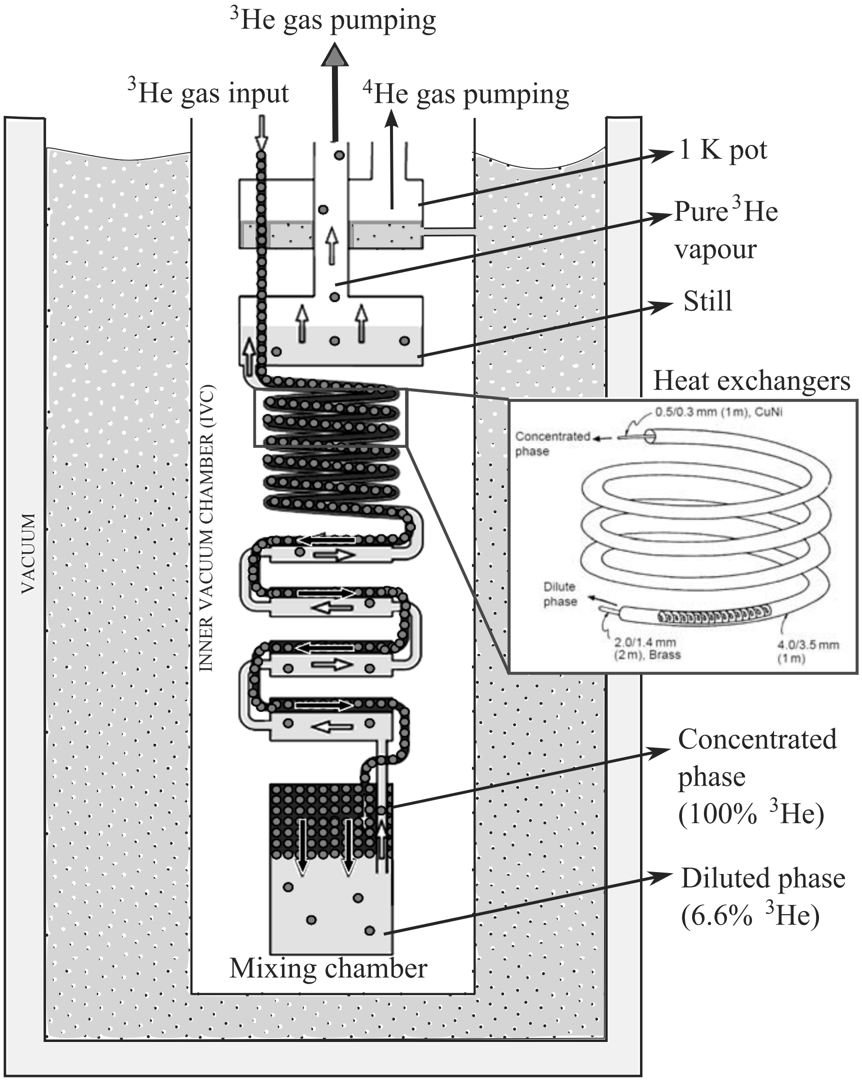

Figure 1.9: Schematic view of a ^{3}He-^{4}He dilution refrigerator. The inset shows an amplified view of the heat exchangers taken from Ref. [31].

providing values as large as ~ 100 m^2. This can be achieved by using spiral coils as shown in Fig. 1.9. These tubes are additionally filled with sintered metal powder to increase the contact surface area. The use of sintered metal powder provides an additional advantage as amorphous solids contain an enhanced density of low energy phonons that favor the heat transfer with the helium bath at low temperatures.

After the ^{3}He leaves the heat exchangers it has eventually reached the temperature of the helium leaving the mixing chamber. It is then introduced again in the chamber through a capillary or impedance to make sure that it is liquid. The optimum working temperature at the still is ~ 0.7 K which can be controlled by a heater. At this temperature, almost all the vapor pressure is due to ^{3}He.

1.3.3 Minikelvin 126-TOF model from Leiden Cryogenics

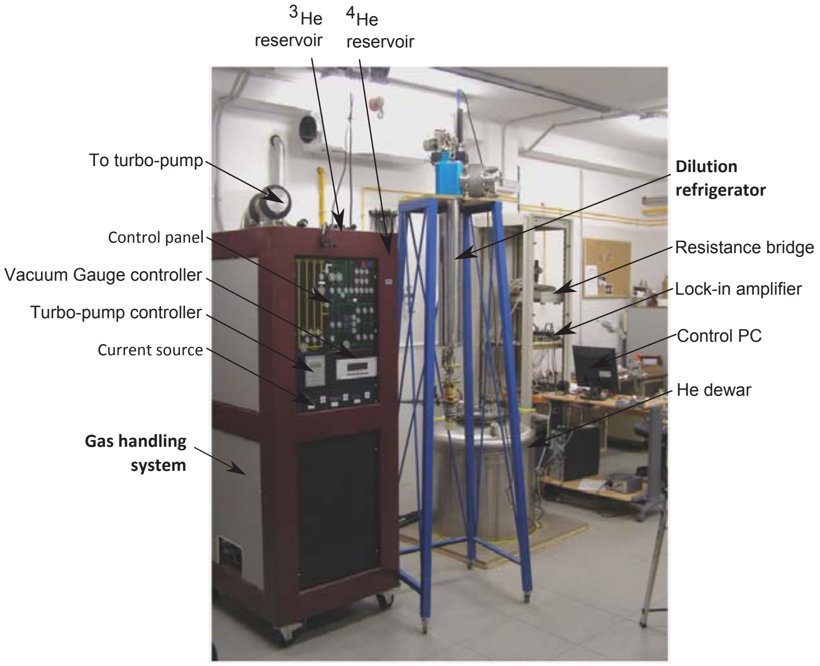

Figure 1.10: Minikelvin 126-TOF dilution refrigerator by Leiden Cryogenics located in the Low Temperature Laboratory of the ICMA (Instituto de Ciencia de Materiales de Aragón). The operational base temperature is 13 mK. The system is optimized to work with a μSQUID susceptometer under no external dc magnetic field.

The dilution refrigerator unit used during this thesis work is a Minikelvin 126-TOF model by Leiden Cryogenics. Our model incorporates two special features. On the one hand, the mixing chamber is removable and made of

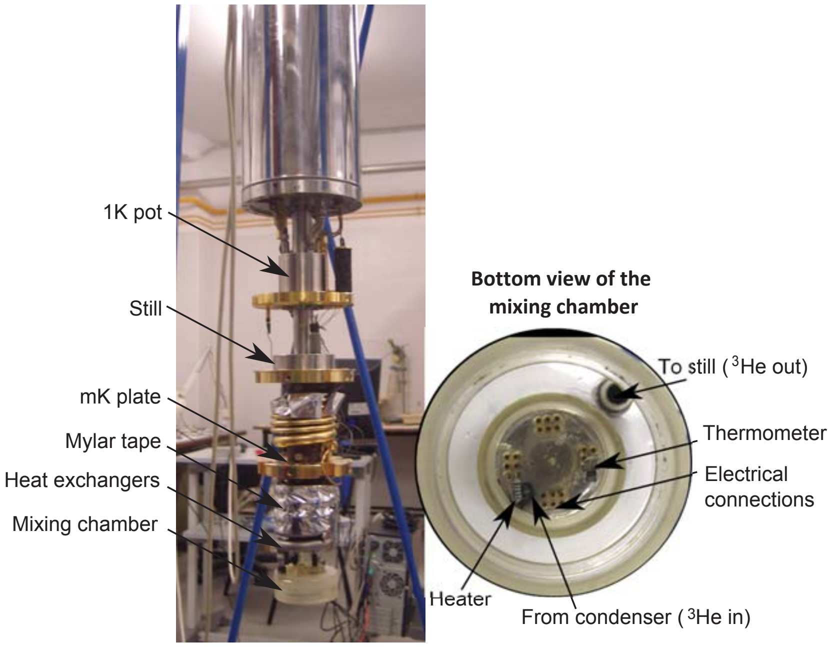

Figure 1.11: Minikelvin 126-TOF dilution refrigerator. The inset shows an amplified bottom view of the plastic mixing chamber.

plastic. Probes, samples and other instruments can be plugged directly inside, immersed therefore in the ^{3}He-^{4}He mixture. The mixing chamber can be closed using a simple screw top or one including a plastic tail. The latter is designed in such a way that the ^{3}He atoms are forced to cover all the way from the top to the bottom of the tail, providing, in this way, a very good thermalization of the whole mixing chamber. This option has been designed for allowing measurements under high magnetic fields. The tail of the mixing chamber can be introduced inside the cylindric cavity of a superconducting magnet while probes and samples remain immersed in the ^{3}He-^{4}He mixture. In this this thesis we will concentrate however in measurements at zero dc applied magnetic field, this option has therefore not been used. The second special feature is related to the fact that the effective volume of the mixing chamber can vary depending on the configuration that is used. For this reason, the relative quantity of ^{3}He and ^{4}He must be variable as well. Both gases are stored in separate tanks enabling the user to choose the amount of ^{3}He and ^{4}He used in every run. ^{3}He is condensed and circulated first followed by ^{4}He. When the temperature decreases below ~ 0.87 K the separation of phases occurs and the system works as a normal dilution refrigerator.

Our setup consists of a gas handling system that is connected to the dilution refrigerator, or inset, through flexible stainless-steel gas lines as it can be seen in Fig. 1.10. The gas handling system contains three pumps used in the refrigerator operation (one turbo-pump and two rotary-pumps) a nitrogen dewar used for cold trapping, the triple current source controller and the vacuum gauge controller. Hidden inside the stainless steel cabinet of the gas handling system there are two leak-tight reservoirs. The upper one, having a volume of 36 liter, is used for storing ^{3}He. The lower one, with capacity for 142 liters, is used for the ^{4}He-rich mixture.

The insert is introduced in a conventional He dewar. Liquid helium flows from the He bath to the 1 K pot through two lines. One is direct, with a high impedance and the other goes through a bypass needle valve that can be controlled manually from the top of the inset. Attached to the 1 K pot there are a still, a cold-plate and the mixing chamber plus a series of heat exchangers. The whole inset is covered with two radiation shields screwed to the cold-plate and the still, respectively. Finally, a stainless steel shield is used to close the Inner Vacuum Chamber (IVC).

The IVC is pumped at the beginning of the process assisted by a turbo-molecular pump. For reaching an even higher vacuum, a sorption pump is used for the final evacuation. The mixture is then condensed and circulated by means of the turbo-molecular drag-pump backed by a dry rotary pump. The ^{3}He is first condensed, which enables decreasing the temperature down to $\sim$ 800 mK rather quickly. The ^{4}He begins then to circulate. In this way, the total time consumed until the lowest temperature is reached is typically $\sim$ 5 hours. The temperatures in the 1 K pot, still and sorb pump are measured by 10 kΩ RuO$_2$ thermometers. The temperature in the mixing chamber is measured by a Dale 1582 Ohm thermometer. The resistances of the thermometers are measured with an Oxford AVS-47 resistance bridge. The minimum temperature we have reached using this dilution refrigerator unit has been 11 mK.

This equipment is optimized to measure ac susceptibility by using an ultra-sensitive μSQUID susceptometer developed thanks to a collaboration between our laboratories and the Physikalisch-Technische Bundesanstalt of Berlin. The development of this instrument has taken up much of the time dedicated to this thesis work. For this reason, its design, fabrication and performance will be detailed in the next chapter.

1.4 Electron Paramagnetic Resonance (EPR) spectroscopy

Electron Paramagnetic Resonance (EPR) or Electron Spin Resonance (ESR) is a spectroscopic technique that enables the study of paramagnetic substances. The electronic energy levels of a given ion or molecule split under the action of a magnetic field (Zeeman effect). The magnitude of such split depends on the magnitude of the applied field, the electronic state and the electron Landé g-factor. Transitions between the different electronic levels separated by an energy difference ΔE, can be induced by electromagnetic radiation at the resonant frequency $\omega = \Delta E/\hbar$. The latter leads to a certain number of resonances that provide information about the hyperfine couplings, the zero field splitting parameters etc. Figure 1.12a shows two examples of how the electronic levels of two ions with different anisotropy parameters split when a magnetic field is applied. High field transitions disappear when decreasing temperature for the case of axial-preferred symmetry ($D < 0$) whereas the contrary occurs for planar-preferred symmetry ($D > 0$).

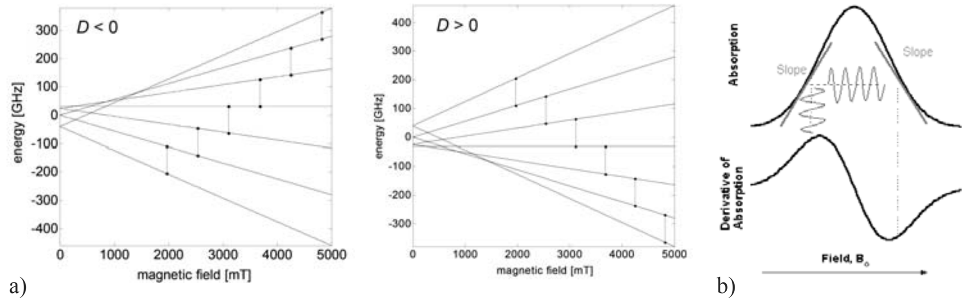

a) b)

Figure 1.12: a) Energy corresponding to the different electronic levels of an ion with $S = 3$ as a function of the applied magnetic field. Two examples are shown, one with $D < 0$ which corresponds to easy-axis symmetry and one with $D > 0$, which corresponds to easy-plane symmetry. b) Absorption and first derivative EPR spectra.

Spectra can be directly recorded (absorption spectra) or through modulation with an external magnetic field at a frequency of typically $\sim$ 100 kHz. The latter provides a better sensitivity since the output signal can be then distinguished from the electronic noise by using conventional lock-in detection. When using field modulation, spectra are recorded as the first derivative of the absorption spectra (see Fig. 1.12b).

Most EPR setups operate at fixed frequency and varying the external magnetic field. Table 1.2 summarizes the conventional frequency bands used in EPR and the corresponding typical values of the magnetic field employed. Measurements at different frequencies and varying the external magnetic field

	Frequency (GHz)	Magnetic Field (T)
L-Band	1.0	0.036
S-Band	3.5	0.12
X-Band	9.8	0.35
K-Band	24	0.86
Q-Band	34	1.2
W-Band	95	3.4

Table 1.2: Frequency bands and their corresponding typical values for the magnetic field.

are possible thanks to a tunable-cavity setup developed in the University of Stuttgart by J. van Slageren and C. Schlegel [33, 34]. A brief description of this device is provided in the next section.

1.4.1 Broad Band EPR with tunable cavity setup (University of Stuttgart)

EPR will be used in chapter 6 to study the anisotropy parameters describing the spin hamiltonian of GdW_{10} and GdW_{30}. As we will show, EPR spectroscopy will be very useful to determine the magnetic anisotropy of both molecules. The setup we used was developed during the thesis of C. Schlegel [33, 34] and it is briefly described next. A copper cylindrical cavity was built for this purpose. It consist of a static upper plunger and a bottom cap that can be moved for adjusting the cavity length and therefore the resonant frequency. The resulting cavity has a diameter of 27 mm and a length of 0–40 mm that can be varied in-situ. A resonance at approximately 14 GHz corresponds to the maximum length of 40 mm in vacuum. On the other hand, cavity heights < 4 mm are not used since they lead on an inhomogeneous magnetic field in the sample volume. The resonant frequency corresponding to 4 mm is 40 GHz.

This system operates inside a superconducting magnet that is able to apply a magnetic field as high as 10 T. The stationary top part of the cavity is used for coupling the microwave magnetic field that is driven from a network analyzer through a coaxial cable. This piece can also be used for attaching the sample in such a way that the external stationary magnetic field is perpendicular to the oscillating magnetic field in the cavity. The external applied magnetic field is not modulated and the data will be therefore recorded as absorption spectra.

Once the sample has been properly mounted in the cavity, the set up is cooled down using a variable temperature insert from Oxford Instruments.

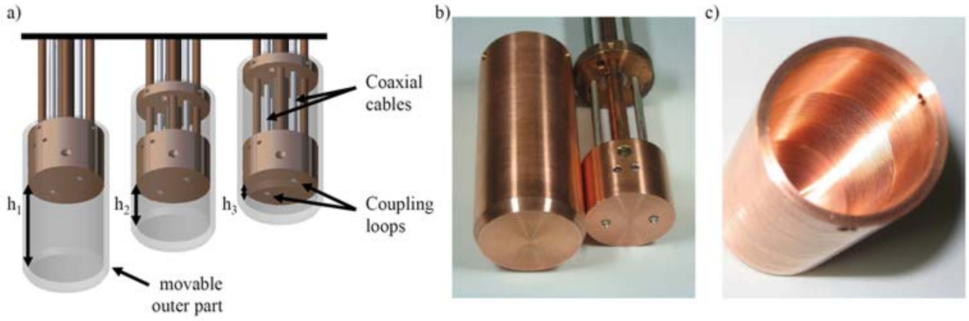

Figure 1.13: Tunable cavity setup developed by C. Schlegel and co-workers [34]. a) Drawing of the cavity at three different positions of the movable outer part. The top plunger of the cavity stays fixed in the laboratory frame. (b) and (c) show photographs of the actual setup.

The temperature of the cavity can be controlled in this way from 1.5–300 K by pumping helium from the reservoir that is connected to the insert through a needle valve. The temperature is stabilized during a long period (typically overnight) to avoid frequency fluctuations due to the thermal expansion of the cavity.

The measurement starts by setting the first value of the stationary magnetic field. Then the transmission is measured as a function of the frequency and averaged over several cycles. These data are fitted to a Lorentzian curve that provides an accurate value of the frequency and width of the resonance for the corresponding magnetic field. In this way, the measurement process is repeated for every point as the magnetic field is swept.

1.5 Circuit edit

The last setup we have used during this thesis work is not related with the study of magnetic properties. As we have already advanced in section 1.3.3, many of the measurements that we will present have been performed using an ultra-sensitive μSQUID susceptometer developed by us. The fabrication of this instrument has been possible thanks to the combination of several elements. On the one hand, we have used highly sensitive commercial μSQUID sensors fabricated at the Physikalisch-Technische Bundesanstalt (PTB-Berlin). On the other, we have exploited our ability of modifying and creating superconducting microcircuits, a concept referred to as 'circuit-edit'. The setup we are about to describe here has been used to 'circuit-edit' the commercial μSQUID sensors from the PTB. For this, we have used both the visualization and manipulation capabilities offered by a Nanolab, a DualBeam SEM/FIB system from FEI.

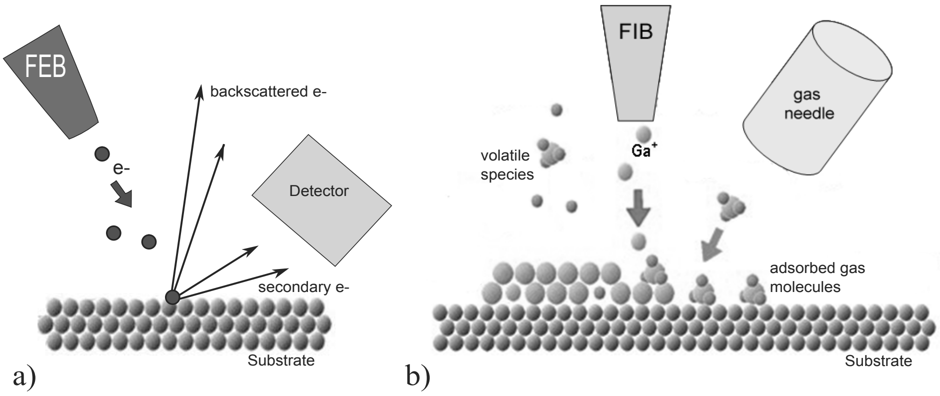

Figure 1.14: a) SEM operation. Secondary electrons are produced as a result of the ionization of a surface when a Focused Electron Beam (FEB) is targeted towards it. These electrons provide information about the topography and composition of the surface b) Focused Ion Beam Induced Deposition (FIBID) operation. Accelerated Ga^+ ions are targeted towards a substrate that contains adsorbed molecules proceeding from a precursor gas. As a consequence, a material gets eventually deposited. The later consist of a mixture of Ga^+ ions and the precursor gas.

1.5.1 Scanning Electron Microscopy (SEM) and Focus Ion Beam (FIB)

A high-energy beam ($\sim$ keV) of electrons directed towards a sample leads to a number of effects. Amongst others, one can find the production of secondary electrons ($\sim$ eV), as a result of the ionization of the sample, back-scattered electrons ($\sim$ keV), that are beam electrons scattered by the sample, or transmitted electrons, that are transmitted through the sample. In a Scanning Electron Microscopy (SEM), secondary electrons (also backscattered electrons) are detected to provide information about the sample's surface topography and composition (see Fig. 1.14a).

Focused ion beam (FIB) is a widely used technology that enables a direct and local patterning of structures at the nanometer scale. It is based on the effects that a beam of accelerated ions (e.g. Ga^+ at 30 keV) produces when it is focused on the surface of a sample. On the one hand, the surface is locally etched by the collision of highly energetic ions. On the other, when a precursor gas is injected close to the sample, the Ga^+ ions can decompose the molecules adsorbed on the surface, and eventually a local deposit is obtained [35] (see Fig. 1.14b). FIB Induced Deposition (FIBID)is commonly used in the semiconductor industry, e.g. for repairing or modifying valuable masks for optical lithography, making cross sections for the analysis of fabrication process, or the preparation of samples (lamellae) for transmission electron microscopy.

1.5.2 The Nanolab: a DualBeam SEM/FIB system from FEI

We used a commercial Nova 200 Nanolab dual-beam system from FEI. This setup enables us to perform imaging, characterization, etching and deposition of different materials at the nanoscale. It is a dual beam system, which means that it incorporates a Scanning Electron Microscopy (SEM) column and a Focused Ion Beam (FIB) column at 52° (see Fig. 1.15a and b).

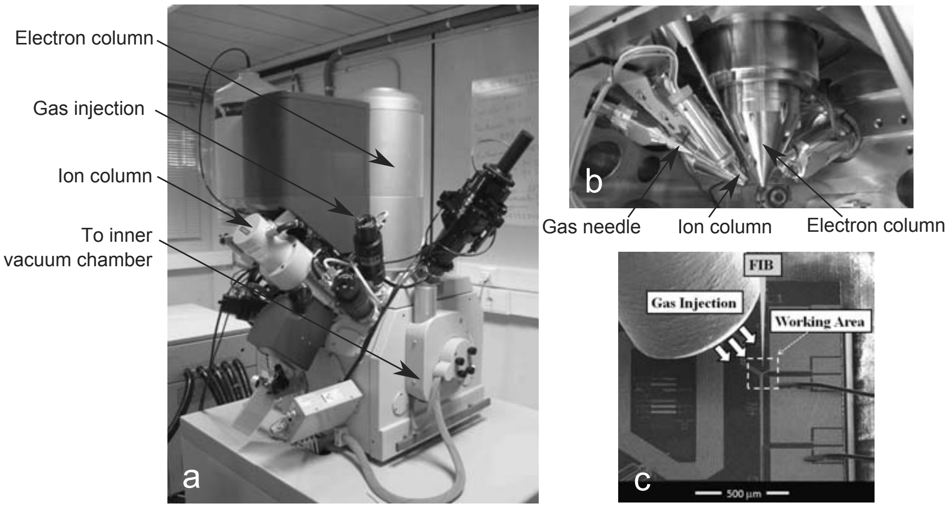

Figure 1.15: a) Image of the Nova 200 Nanolab dual-beam system and the sample chamber (b). The instrument is located in the laboratories of the INA (Instituto de Nanociencia de Aragón) c) SEM image (52° tilted) of superconducting chip wire-bonded to a PCB with the Gas Injection needle inserted.

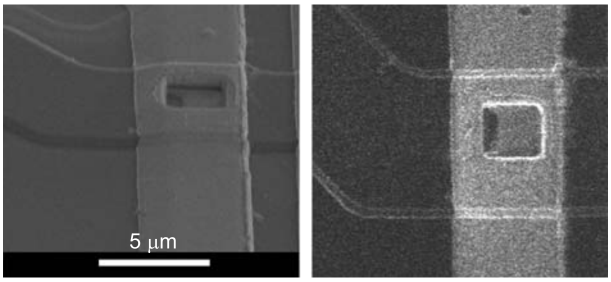

Figure 1.16: These images show the dual-beam system visualization capabilities. The image on the left is obtained by scanning the focused electron beam (SEM picture with sample tilted 52°); the image on the right is obtained by scanning the focused ion beam over the same area.

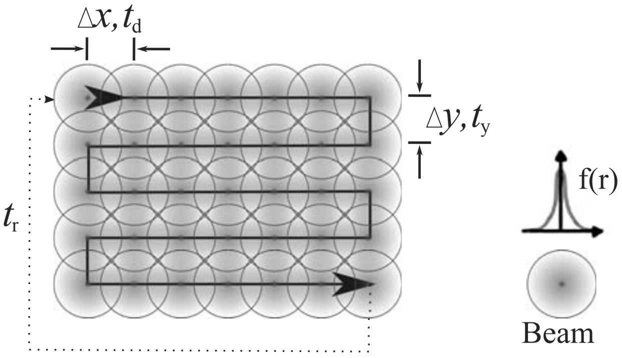

Figure 1.17: The focused ion beam is scanned over the surface in a winding fashion as indicated by the arrow. The spot diameter of the FIB depends on the current. The distance between every pass can be varied and receives the name of pitch scan (Δx, Δy). The time that the ion beam spends at each pass receives the name of dwell time (t_d).

Samples are usually mounted on a SEM specimen holder using carbon or copper conducting tape to ensure a good electrical contact. This is important in order to avoid charging effects due to the production of secondary electrons. Imaging is possible by using both the electron column and the ion column. These provide however different visualization capabilities although the images are obtained with the same secondary electrons detector. The interaction volume of ions is much lower than that of electrons. As a result, the secondary electron emission produced by the ions is very ”surface-sensitive”. Images obtained with the ion beam provide therefore a good contrast between different materials (see Fig. 1.16).

Figure 1.15c shows a SEM image of a superconducting microcircuit bonded to a PCB prior to start a FIBID process. For this purpose, a Gas Injection System (GIS) is used to introduce the desired precursor gas inside the chamber. The open end of the GIS needle is positioned close to the surface at a short distance (around 200 μm) to ensure that a sufficient precursor gas flux reaches the working area. The base pressure inside the vacuum chamber is 10^{-6} mbar increasing to about 4×10^{-6} mbar when the GIS valve is opened.

The ion acceleration voltage is 30 kV and the ion current ranges from 1 pA to 20 nA. The spot diameter of the FIB depends on the current, ranging from 7 nm at 1 pA to 450 nm at 20 nA. In principle, the highest resolution is achieved with small currents, but long patterning times must be avoided because they cause poor resolution due to the drift of the ion column. Therefore, the lowest current value is chosen such as to result in patterning times typically no longer than 5 min.

Before starting the FIBID process, the ion beam is first scanned to get a snapshot of the working area; on top of this image the patterns, which correspond to the desired material depositions, are precisely positioned. The patterning time is calculated as $t = V/(I \times V_{\mathrm{dose}})$, where V is the volume of the material to be etched or deposited, I is the ion current and V_{dose} is a calibration parameter known as the volume per dose. The beam is scanned over the selected area in a number of passes (see Fig. 1.17). The pitch scan (Δx, Δy), that is, the distance between two consecutive points, is selected to be equal to the spot diameter in the case of deposition (0% overlap) and half this value in the case of etching (50% overlap). The dwell time t_d, that is, the time that the FIB spends on every point, is adjusted to ensure that freshly adsorbed gas is in place when the beam reaches the point at the next pass. The refresh time t_r is the time between passes left for the system to recover fresh precursor gas molecules.

Chapter 2

On chip μSQUID Susceptometer: Design and Fabrication

2.1 Introduction

The research on the properties of magnetic materials at very low temperatures has been stimulated in the last fifteen years by the observation of fascinating quantum phenomena, such as quantum tunneling of spins [7,8,36], quantum coherence [4,27], and quantum entanglement [25,37]. Besides providing a direct hindsight on the not yet fully understood quantum-to-classical transition, these phenomena might also find application in the development of solid-state quantum information technologies [38].

These studies have fuelled the development of new magnetic sensors with improved performances that approach the experimental limits in terms of sensitivity and operation conditions. Experiments need to be performed at very low temperatures, when zero-point quantum fluctuations become dominant over classical thermal fluctuations. A very high spin sensitivity is also desirable to enable detecting the magnetic response of single layers of nanomagnets and eventually of individual ones. In addition, by magnetically diluting the samples, the decoherence caused by spin-spin interactions can be minimized. Another crucial point is the access to broader frequency bandwidths than those offered by commercial magnetometers, since the time scales of quantum dynamics can vary over many decades depending on the spin value, the magnetic anisotropy, and the couplings to the environment.

The many recent advances in this field include the development of miniature magnetometers, based on the use of either micro-Hall bars or micro- and nano Superconducting Quantum Interference Device (SQUID) sensors [39]. Another application with similar stringent performance is found in the use of metallic magnetic microcalorimeters as radiation detectors [40].

The measurement of the ac magnetic susceptibility of a magnetic material provides information on its equilibrium magnetic response as well as on the magnetization dynamics [41]. The technique consists of measuring the magnetization of the sample in response to an excitation ac magnetic field. Measurements as a function of frequency and temperature enable the determination of the spin-lattice relaxation time and the superparamagnetic blocking temperature, or studying the transition between different magnetic phases.

Our purpose has been to develop an ac magnetic susceptometer that combines high sensitivity and broad frequency bandwidth with operation down to very low temperatures and user friendliness. Commercial SQUID technology and readout electronics e.g., from Magnicon GbR, are now available with sensitivities near the quantum limit at mK temperatures and room temperature electronics adapted for operation with broad bandwidths [21]. We have taken advantage of such optimized devices as the starting point for the fabrication of our susceptometers. It turns out that, via a simple modification of the chips input wiring, a fully integrated thin-film μSQUID susceptometer can be obtained. This modification is carried out by focused ion beam etching and the subsequent in situ deposition of a superconducting material with nanoscale control [42–44]. The problem of achieving a good thermal contact at very low temperature has been solved by immersing the microsusceptometer inside the mixing chamber of a ^{3}He - ^{4}He dilution refrigerator Leiden Cyrogenics adapted to this end; this ensures a good thermalization of the sample down to 13 mK.

2.2 Superconducting Quantum Interference Device (SQUID)

SQUIDs are a consequence of the *macroscopic* quantum character of superconductivity. Their operation is based on two phenomena, i.e. the quantization of the magnetic flux and the Josephson effect. Let us first briefly introduce both of them.

In the simplest model of the hydrogen atom, that conceived by Bohr, the quantization condition for the electron angular momentum leads to well defined electronic orbitals. Quantum mechanically, this comes from the condition that electronic wave functions must not interfere destructively. The *macroscopic* wave function describing the whole ensemble of electrons (Cooper pairs) in a superconducting material shall not interfere destructively either. In the same way, this fact leads to the quantization of the magnetic flux threading a superconducting loop. This phenomenon was first devised by F. London [45]. Under the assumption that single electrons are the responsible for carrying the supercurrent, he proposed the flux quantum to be $\Phi_0 = h/e$, h being the Plank's constant and e the electron charge. The theory of superconductivity was later developed by J. Bardeen, L. N. Cooper, and J. R. Schrieffer (BCS-theory) [46].With the introduction of Cooper pairs, a factor 1/2 must be added to the early suggestion of London. In this way, the correct expression for the flux quantum becomes $\Phi_0 = h/2e \approx 2 \times 10^{-15}$ Wb.

The Josephson effect, on the other hand, was predicted by B. D. Josephson [47] in 1962 and later demonstrated experimentally by P. W. Anderson and J. M. Rowell [48]. To illustrate this phenomenon, let us use again the analogy with the hydrogen atom. The energy binding that holds a hydrogen molecule arises from the overlap of the electronic wave functions of both hydrogen atoms. In the same way, a finite coupling energy results from the overlap of the *macroscopic* wave functions of the electrons between two weakly connected superconductors. The weak link is usually thought to be an insulating layer but other configurations are also possible. For instance point contacts or normal conducting layers can also be used [49].

Let us define ϕ as the phase difference between the macroscopic wave functions describing the Cooper pairs of both superconductors. According to B. D. Josephson [47], the current threading the weak link (I) and the voltage drop across it (V) must satisfy the following relations

$$I(t) = I_0 \sin\phi(t) \tag{2.1}$$

$$V(t) = \frac{\Phi_0}{2\pi}\frac{\partial\phi}{\partial t} \tag{2.2}$$

For $I > I_0$, a voltage V arises, and the phase difference becomes time dependent. I_0 is therefore referred to as the critical Josephson current. As a consequence, when applying a constant voltage, the ac current will oscillate at the Josephson frequency $f_\mathrm{J} \approx 500$ MHz/μV.

2.2.1 The dc-SQUID

The most widely used device based on these ideas receives the name of direct current or dc-SQUIDS. These systems consist of two weak junctions connected in parallel on a superconducting loop. Dc- SQUIDS were invented by R. C. Jaklevic, J. Lambe, A. H. Silver, and J. E. Mercereau in 1964 [50].

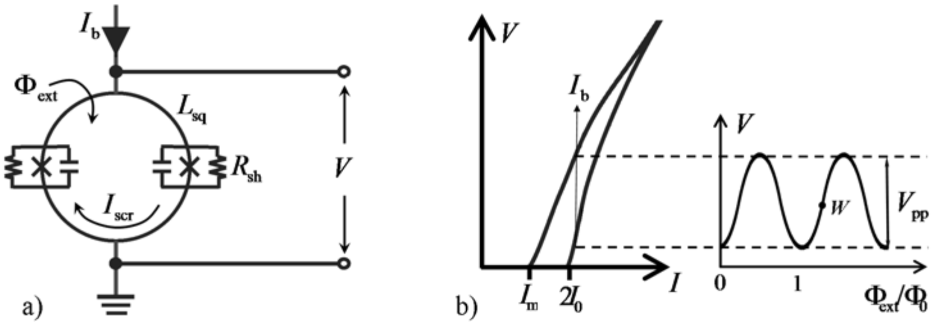

Figure 2.1: a) SQUID loop scheme where the two Josephson links are marked with crosses. Both weak links are resistively shunted in order to avoid hysteresis and can be characterized with two intrinsic capacitances. b) V-I curve. When the bias current I_b is chosen to be slightly larger than $2I_0$, where I_0 is the critical current of each one of the Josephson links, the maximum field modulation is obtained. The operation point W is chosen in the steepest part of the $V - \Phi_{\text{ext}}$ characteristic. Figures extracted from ref. [51]

Consider the scheme depicted in Fig. 2.1a. A superconducting loop, with autoinductance L_{sq}, is interrupted by two junctions, usually shunted with small resistors to remove hysteresis. Let us assume that the two Josephson junctions are identical and are characterized by the same critical current I_0. The SQUID loop is biased with an external current I_{b} that, in absence of any external magnetic flux, distributes symmetrically over the two SQUID branches.

Let us now suppose that, an external magnetic flux Φ_{ext} is coupled to the SQUID loop. Under these circumstances, an screening current I_{scr} will be generated in order to cancel this flux. The current distribution within the SQUID branches will no longer be symmetrical and one of the junctions will reach the critical current before the other does. As soon as that happens, a net voltage V will appear according to the second of Josephson's equations.

The total flux threading the loop must be equal to $n\Phi_0$ with n integer. If the external magnetic flux Φ_{ext} is further increased above $\Phi_0/2$, the SQUID energetically prefers to increase the total magnetic flux up to Φ_0 instead of screening it. The screening current will be therefore reversed and also does the Josephson voltage across the loop.

The transfer function defined as $V_\Phi = \partial V/\partial \Phi_{\text{ext}}$ has to be maximized in order to obtain the maximum sensitivity. In practice, an optimum working point is typically located at the steepest part of the $V - \Phi_{\text{ext}}$ characteristic (see Fig. 2.1b).

2.2.2 dc-SQUID readout

The sinusoidal voltage response to magnetic flux shall be linearized to obtain a larger dynamic range. This can be achieved operating in the so-called Flux Locked Loop (FLL) mode. Under this circumstances, the SQUID behaves as a *null-detector* of magnetic flux.

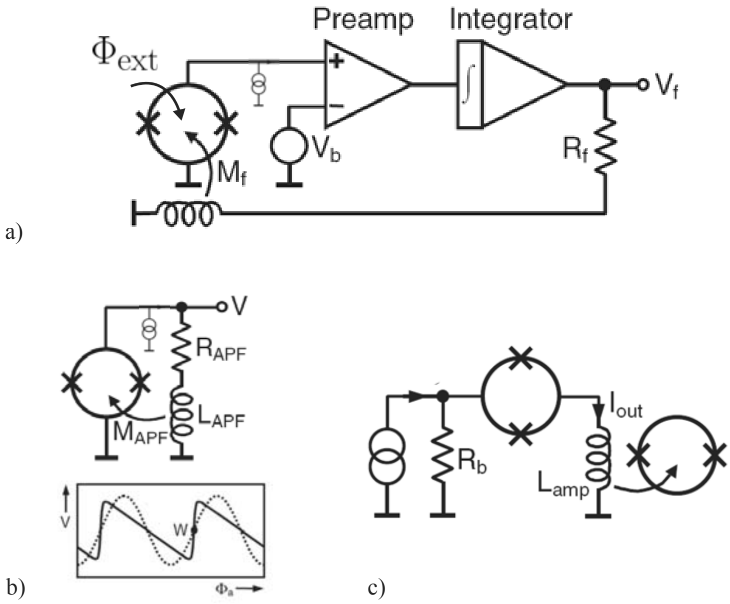

Figure 2.2: a) Operation in Flux Locked Loop (FLL) mode. b) dc-SQUID with Additional Positive Flux (APF). The latter leads to the distortion of the V-Φ_{ext} characteristic. c) Scheme of a two-stage configuration. The signal of the front-end SQUID is amplified with a second SQUID. Images obtained from ref. [51]

The operation in FLL mode is illustrated in Fig. 2.2a and summarized in the following. The SQUID is first biased at a working point W. A small variation of the external magnetic flux $\delta\Phi_{\text{ext}}$ leads to a variation δV of the total voltage. This small deviation from the working point is amplified at room temperature, integrated, and fed back into the SQUID via a feedback resistor R_f and a feedback coil, which is magnetically coupled to the SQUID via a mutual inductance M_f. The total flux threading the SQUID loop cancels when the following condition is satisfied

$$\Phi_{\text{tot}} = \Phi_{\text{ext}} - \frac{V_f}{R_f} M_f \approx 0 \tag{2.3}$$

Under these circumstances, the output voltage V_f will be proportional to the external flux Φ_{ext}.

Since the transfer function V_Φ is typically small, the overall electric noise in this configuration will be dominated by the room temperature amplifier. There are two possible ways of circumventing this problem, to use the flux modulation scheme with resonant transformer or to increase V_Φ in the low temperature region.

The first possibility is usually used in commercial SQUID magnetometers. The SQUID $V - \Phi_{\text{ext}}$ curve is flux modulated by an ac signal of peak-to-peak amplitude $\Phi_0/3$ and frequency $f_m \sim 100$ kHz. The resulting modulated SQUID response $V_m(t)$ is amplified and lock-in detected, using f_m as reference frequency. In this configuration, the output SQUID impedance and input preamplifier impedance have to be matched to have a good noise performance. This intermediate matching circuit (e.g. a transformer) is tuned at the modulation frequency thereby limiting the operable bandwidth of the system. Using suitable electronics a signal bandwidth of up to 100 kHz can be achieved. Commercial SQUID magnetometers, e.g. from Quantum Design, are usually limited to ~ 10 kHz.

On the other hand, there are different possible ways of increasing the transfer function at low temperatures. This option has the enormous advantage of enabling the direct readout of the signal, therefore preserving the full frequency bandwidth operability of the system.

One possibility is the use of Additional Positive Feedback (APF). This consists of using an APF coil magnetically coupled to the SQUID loop via a mutual inductance M_{APF} [52] (see Fig. Fig. 2.2b). Let us first suppose that the SQUID is biased at an operating point in the positive slope of the $V - \Phi_{\text{ext}}$ characteristic. In this case, a positive change in flux will cause an increase of the current in the APF coil that induces an additional, positive flux in the SQUID. On the other hand, the opposite effect occurs when the working point is chosen in the negative slope of the $V - \Phi_{\text{ext}}$ characteristic. The $V - \Phi_{\text{ext}}$ characteristic becomes therefore asymmetric leading on an increase of V_Φ in the positive slope.

Another widely used method of increasing the overall transfer coefficient is to use an additional SQUID as a low-noise preamplifier (see Fig. 2.2c) [53, 54]. Moreover, many identical SQUIDs connected in series can be used to amplify the overall transfer function [55, 56]. Under the appropriate circumstances, SQUID arrays exhibit a single SQUID-like overall $V - \Phi_{\text{ext}}$ characteristic. These two-stage configurations can also operate in FLL mode as a single SQUID with enhanced transfer function, enabling direct readout at room temperature.

On the other hand, also when using a direct readout method like those described above, the dynamical response is, when operating in FLL mode, limited by the SQUID's slew rate. This quantity gives the speed at which the feedback circuit can compensate for rapid flux changes at the input. The slew rate depends on the linear flux range of the SQUID (Φ_{lin}). The latter means, the flux range in which V varies linearly with Φ_{ext}. The linear flux range depends approximately on the transfer function as $\Phi_{\text{lin}} \approx V_{\text{pp}}/V_\Phi$ where V_{pp} is the peak-to-peak voltage of the $V - \Phi_{\text{ext}}$ characteristic (see Fig. 2.1b).

The use of APF leads on an increase of V_Φ while the value of V_{pp} remains the same. The linear flux range and, as a consequence, the frequency bandwidth, becomes therefore reduced. On the contrary, the use of SQUID arrays leads to an increase of both V_Φ and V_{pp} which does not compromise the dynamical performance. Under optimum conditions, the total bandwidth should be only limited by propagation delays between the room temperature feedback electronics and the low-temperature SQUID [57]. For a typical distance between these elements of ~ 1 m, one finds a theoretical limit of ~ 20 MHz.

2.2.3 SQUID applications

SQUIDs are widely used as magnetic flux detectors. Most commercial magnetometers and susceptometers are based on SQUID readout. SQUID-based susceptometry will be the topic of next section.

On the other hand, SQUIDs are often used as a low noise current amplifiers as occurs in the readout of superconducting transition-edge bolometers [58]. These are the most sensitive detectors of electromagnetic radiation available in the far-infrared and submillimeter regions of the spectrum.

Apart from SQUIDs, there are also many other applications of Josephson junctions. Quite recently, the macroscopic quantum behavior of Josephson junction circuits has been applied in the fabrication of artificial two-level systems. Single junctions and loops containing one or more junction are in fact very promising candidates for the physical realization of quantum bits [59–64].

2.3 μSQUID susceptometry

A susceptometer measures the magnetic susceptibility χ of a sample, i.e. the variation of the magnetization (M) with the external applied magnetic field (H)

$$\chi = \frac{\partial M}{\partial H}$$

SQUIDs behave effectively as very sensitive flux-to-voltage transducers. They can therefore be used to sense any physical quantity that can be converted into magnetic flux, e.g. magnetic susceptibility.

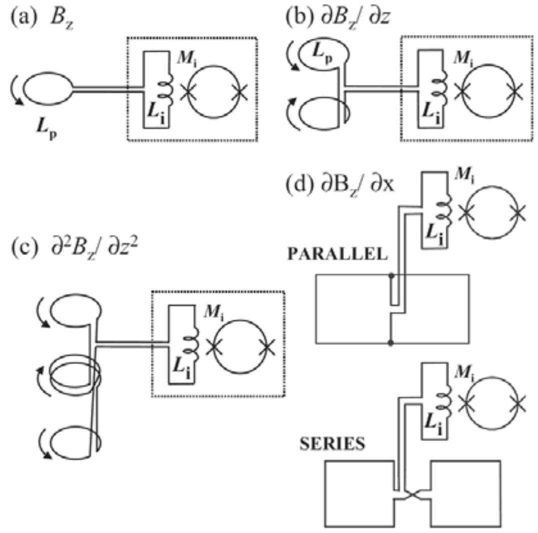

Figure 2.3: a) Magnetometer configuration. The pickup coil (L_p) couples the signal coming from the sample and then to a SQUID loop. The rest of the figures represent different gradiometric configurations. b) First order axial gradiometer. c) Second order axial gradiometer. d) Planar first order gradiometers with parallel and series connected pickup coils. Images from ref. [51]

In the most simple configuration, that of a magnetometer, a pickup coil (L_p) is used to couple an external flux to the SQUID loop (see Fig. 2.3a). Such magnetometers have the disadvantage of sensing not only the magnetic field coming from the sample but also any other external magnetic field, e.g. the Earth's field. In order to avoid this problem, gradiometric configurations shall be used.

A first-derivative order gradiometer consists of two coils wound in opposite directions (see Fig. 2.3b). When an homogeneous external magnetic field (H_0) is applied, it couples equally to both coils. A screening current appears therefore in each one of the loops but, since they have opposite directions, no net flux is coupled to the SQUID. The rejection of signals coming from outside can be improved by using a second order gradiometer (see Fig. 2.3c), third order, etc.

2.3.1 How does an ac susceptometer work?

A susceptometer consists of two circuits. On the one hand, the primary circuit, that creates the ac exciting magnetic field. On the other, the secondary circuit, that consists of two (or more) pickup coils designed in a gradiometric fashion. The latter circuit couples the magnetic signal coming from the sample (see

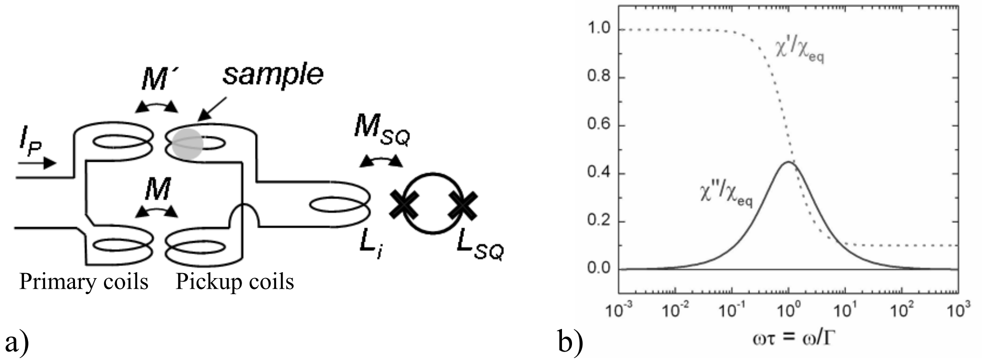

Figure 2.4: a) Scheme of a first order susceptometer coupled to a dc-SQUID. The primary coils create the excitation magnetic field and the secondary, or pickup coils couple the signal from the sample. b) Typical ac-susceptibility curve as a function of frequency. The drop of the real part of susceptibility coincides with the peak of the imaginary part and indicate the paramagnetic blocking of the susceptibility.

Fig. 2.4a).

When an oscillatory magnetic field ($H_{\mathrm{ac}} = H_0 \sin(\omega t)$) is used as the excitation magnetic field, two components will be obtained. One, going in-phase with H_{ac}, is proportional to the real part of the susceptibility χ', and the other, going out-of-phase with H_{ac}, is proportional to the imaginary part χ".

An example of the ac susceptibility of a magnetic material as a function of frequency, performed at constant temperature, can be seen in Fig. 2.4b. When the experimental frequency equals the inverse of the magnetic relaxation time (τ) of the sample, a peak appears in the imaginary component while the real one drops. Ac susceptibility measurements represent therefore a powerful tool in the study of spin dynamics.

2.3.2 Design considerations

Some considerations must be taken into account in order to improve the performance of a susceptometer. Consider the scheme shown in Fig. 2.3b where single-turn pickup coils are used. The sample couples a total flux Φ_{ext} to the pickup coils through the inductance L_p. This induces a screening current in the secondary circuit that couples a total flux Φ_{SQ} into the SQUID loop. Taking into account the property of conservation of flux in a superconducting circuit, and neglecting the effects of currents in the SQUID loop itself, this can be expressed as

$$\Phi_{\mathrm{SQ}} = \frac{M_{\mathrm{SQ}}}{L_p + L_i} \Phi_{\mathrm{ext}} \tag{2.4}$$

This equation must be maximized in order to find the optimum SQUID resolution. By doing so, and expressing the mutual inductance M_{SQ} as $k\sqrt{L_i L_{\mathrm{SQ}}}$ one finds that the maximum value

$$\Phi_{\mathrm{SQ,max}} = \frac{k}{2}\sqrt{\frac{L_{\mathrm{SQ}}}{L_p}}\Phi_{\mathrm{ext}} \tag{2.5}$$

is obtained for $L_i = L_p$.

Let us consider now the case of pickup coils consisting of n turns. Defining $l_{p,\mathrm{s}}$ as the inductance of a single turn coil, the total inductance of the pickup coil can be written as $L_p = n^2 l_{p,\mathrm{s}}$. Taking into account that the flux coupled to a n-turn coil is n times that coupled to a single-turn coil, equation 2.4 can be written as

$$\Phi_{\mathrm{SQ}} = \frac{nk\sqrt{L_i L_{\mathrm{SQ}}}}{n^2 l_{p,\mathrm{s}} + L_i}\Phi_{\mathrm{ext}}$$

this expression is maximum for $L_i = n^2 l_{\mathrm{st}}$ giving

$$\Phi_{\mathrm{SQ,max}} = \frac{k}{2}\sqrt{\frac{L_{\mathrm{SQ}}}{l_{p,\mathrm{s}}}}\Phi_{\mathrm{ext}}$$

That means that, providing that the matching condition $L_i = L_p$ is stratified, the sensitivity does not depend on the total inductance of the pickup coil but just on the single-turn inductance.

Finally, the pickup coil size also determines the sensitivity of the susceptometer. Let us consider in this discussion a point-like sample, i.e. a point dipole with magnetic moment μ. The total flux coupled to a circular coil when the sample is situated in the middle of the coil and μ points along the direction perpendicular to the coil plane, can be written as

$$\Phi_{\mathrm{ext}} = \frac{\mu_0 \mu}{2r}$$

where μ_0 is the permeability of free space and r is the loop's radius. Inserting this expression in Eq. 2.5 and taking into account that the pickup coil's inductance is proportional to the square of its radius r^2 one obtains

$$\Phi_{\mathrm{SQ}} = \frac{\mu_0 k}{4}\sqrt{\frac{L_{\mathrm{SQ}}}{c}}\frac{\mu}{r^2} \tag{2.6}$$

where c is a constant of proportionality. As we can easily see from Eq 2.6, smaller pickup coils, approaching the size of the sample, are desirable. This fact was first proposed by M. B. Ketchen and co-workers [65]. They were in fact the pioneers of the development of miniature SQUID-based susceptometers that we review in the next section.

2.3.3 Reduction to the micro- and nano-meter scale

μSQUID susceptometers are ultrasensitive magnetic detectors based on two ideas. The reduction of the SQUID loop's dimensions down to the dimensions of the sample, and the possibility of using the SQUID loop itself as the sensing pickup coil. As we said, these devices were pioneered by M. B. Ketchen and co-workers in the 80's [65] and continue to be the most sensitive sensors in the solid state.

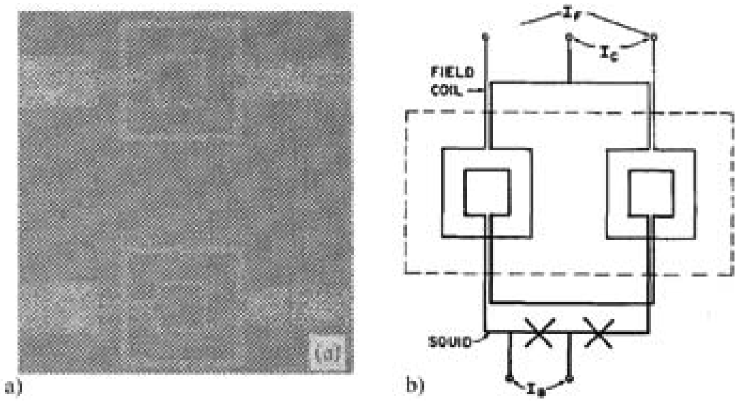

Figure 2.5: a) Image of one of the first thin-film integrated SQUID microsusceptometers fabricated by M.B. Ketchen, D. Awschalom and co-workers. From ref. [66] b) Scheme of the susceptometer circuit, obtained from ref. [67]

Figure 2.5 shows one of the first examples of such miniature susceptometers. In this case, the SQUID loop consisted of two pick up coils wound in opposite directions and connected in series giving rise to a susceptometer. The effective diameter of the pickup coils was ~ 15 μm giving a spin sensitivity of approximately 10^3 $\mu_{\mathrm{B}}/\mathrm{Hz}^{1/2}$. The secondary coils enabled to apply an excitation magnetic field that, in the absence of any sample, coupled no net flux to the SQUID loop. Furthermore, by passing part of the current into the center connector, a high degree of balance could be achieved. This device was able of operating up to frequencies of 1 MHz in open loop mode.

Much effort has been dedicated since then towards the further miniaturization of such devices. Figure 2.6 shows some recent examples. One of the most sensitive μSQUIDs, and one that has been successfully applied to the research of quantum phenomena in magnetic nanoparticles, can be seen in Fig. 2.6a. It was developed in the *Laboratoire Louis Néel* in 1995 as part of the thesis work of W. Wernsdorfer [68]. The inner SQUID loop diameter is approximately ~ 1 μm giving a spin sensitivity of $\sim 10^3$ $\mu_{\mathrm{B}}/\mathrm{Hz}^{1/2}$. The device shown in Fig. 2.6b represents a second step towards miniaturization. The development of this sensor was reported by S. K. H. Lam and co-workers in 2003 [69]. As they

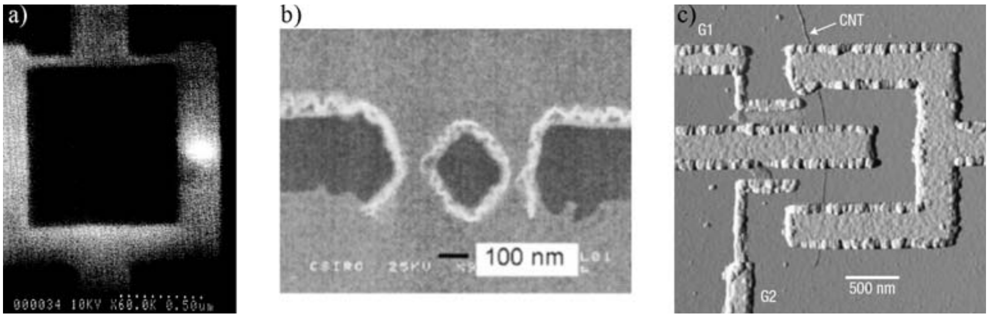

Figure 2.6: a) SQUID microsusceptometer developed by W. Wernsdorfer. Image taken from ref. [68] b) SQUID loop fabricated by S. K. H. Lam *et al*, from [69] c) In the 'nanosquid', the weak links are replaced with a carbon nanotube. Image taken from ref. [18]

showed, sensitivity increases up to $\sim 10^2\ \mu_{\mathrm{B}}/\mathrm{Hz}^{1/2}$ when the minimum SQUID wire width, that corresponds to the Josephson weak link, is reduced down to ~ 100 nm. Finally, in fig. 2.6c, we can see the ultimate effort directed towards the goal of single particle-detection. In this instrument, also developed in the *Laboratoire Louis Néel* [18], the Josephson junctions are implemented with carbon nanotubes, the diameter of which is close to that of a single molecule magnet like Mn_{12}. In this way, the 'nanoSQUID' is expected to be able of detecting $\sim 10\ \mu_{\mathrm{B}}$.

2.4 μSQUID susceptometer conception

Our purpose has been to develop a device similar to that fabricated by M.B. Ketchen, D. Awschalom and co-workers [66]. For this purpose we turned our attention to a new family of μSQUID sensors developed by D. Drung and co-workers [21]. We noticed that, just by rerouting some of the superconducting microwires conforming these sensors, a microsusceptometer coupled to the dc-SQUID could be obtained. In this section we describe some of the main characteristics of these devices and how we conceived the fabrication of our susceptometers.

2.4.1 Commercial μSQUID sensors from the PTB-Berlin and Magnicon GmbH

The Physikalisch-Technische Bundesanstalt (PTB) is the national metrology institute of Germany. It is distributed in two sites: Braunschweig and Berlin. The Cryosensors division from the PTB-Berlin is devoted to the development of μSQUID sensors and SQUID-readout electronics for measurement tech-

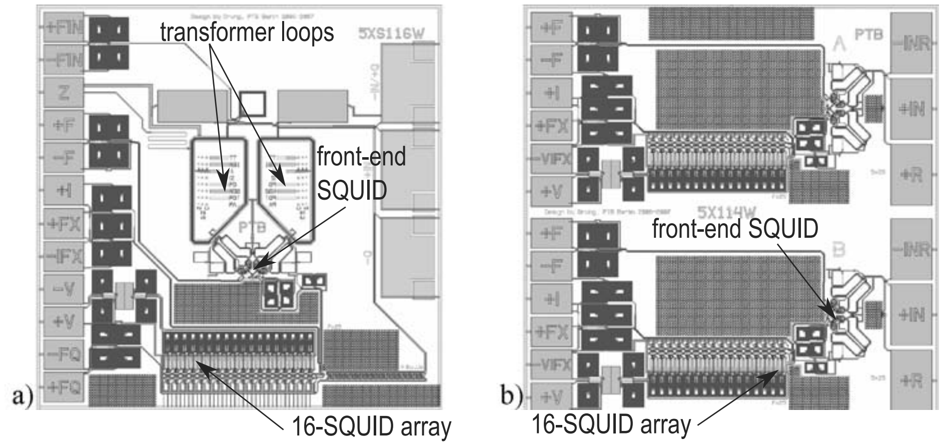

Figure 2.7: Scheme of two types of sensors fabricated at the PTB. a) High-input inductance sensor with $L_{\mathrm{in}} \approx 1.1$ μH. b) Low-input inductance sensor consisting of two devices, A and B, fabricated, respectively, at the top and bottom parts of the chip. Chip size is 3 mm × 3 mm. By courtesy of D. Drung.

niques such as biomagnetic diagnostics, nondestructive testing and evaluation and precision electrical measurements in metrology and research. In 2002 a license agreement was signed between the PTB-Berlin and Magnicon GmbH [22] to commercialize these devices.

PTB SQUID sensors are designed, fabricated and tested in Berlin. The fabrication technology of these sensors includes Nb wiring, SiO_2 insulators and Nb/Al/AlO_x/Al/Nb Josephson junctions. The area of the junctions is defined by anodization.

In Fig. 2.7 we can see two types of SQUID sensors fabricated at the PTB-Berlin. In both cases, the input signal is coupled to a low-inductance front-end SQUID with APF. The SQUID's output signal is then amplified with a second-stage array of 16 SQUIDs.

The first example in Fig. 2.7a corresponds to a sensor with high-input inductance. As we have seen in section 2.3.2, the optimum input inductance of the SQUID should approach the inductance of the device that is connected to it. For this reason, the PTB sensors incorporate an intermediate double transformer loop that provides an overall input inductance with practical values of ~ 1 μH. This transformer has a gradiometric design in order to couple no net flux coming from an external homogeneous magnetic filed, e.g. the Earth's field. The kind of sensors we will use during this thesis belong to the so-called XL type. In these devices, a 30-turn input double transformer loop is deposited on top of two single-turn pickup coils. The active area of each one of the pickup coils is, in our case, equal to 367 μm × 920 μm. The latter is inductively coupled to the SQUID loop through a second transformer. For the sake of clarity we will refer to this second transformer coils as the 'banana' coils.

Sensors with no intermediate loop (see Fig. 2.7b) have a lower input-coil inductance of about 2 nH. The input signal is then directly coupled to the front-end SQUID via the 'banana' coils the dimensions of which are 63 μm $\times$ 250 μm. The 'banana' coils consist of four rectangular shaped single turn coils connected in parallel and forming part of the SQUID loop itself (see Fig. 2.15).

The experimental flux noise of both kind of devices measured at $T = 4.2$ K is $S_\Phi^{1/2} = 800$ nΦ_0/Hz$^{1/2}$ which corresponds to a coupled energy resolution of 44 h. The total sensor size is 3 mm $\times$ 3 mm.

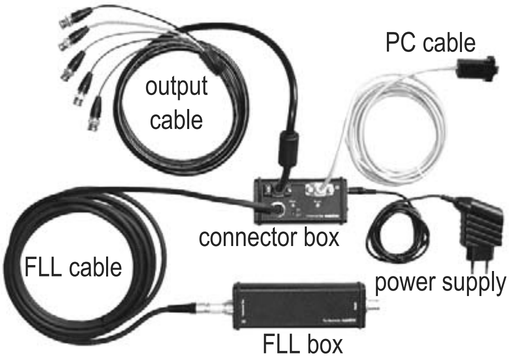

Figure 2.8: Readout SQUID electronics from the PTB-Berlin/Magnicon.

The PTB-Berlin has also developed one of the fastest dc SQUID readout electronics available to date [57]. The theoretical limit of FLL electronics operating in closed-loop is given by the propagation delay on the transmission lines. Taking a typical distance of ~ 1 m between the SQUID sensor and the room temperature electronics, the latter gives a theoretical maximum bandwidth of ~ 20 MHz. The readout electronics developed at PTB-Berlin have furnished this limit without degradation of the noise performance. This electronics consists of a FLL box containing up to three FLL boards that enable to use up to three different sensors. The FLL box is connected to the so-called connector box that gives the user control over SQUID parameters like the bias current I_b, the bias voltage V_b and the flux coupled to the SQUID loop via the feedback coils. This electronics can be easily manipulated through a *SQUIDviewer* software that enables an user-friendly use.

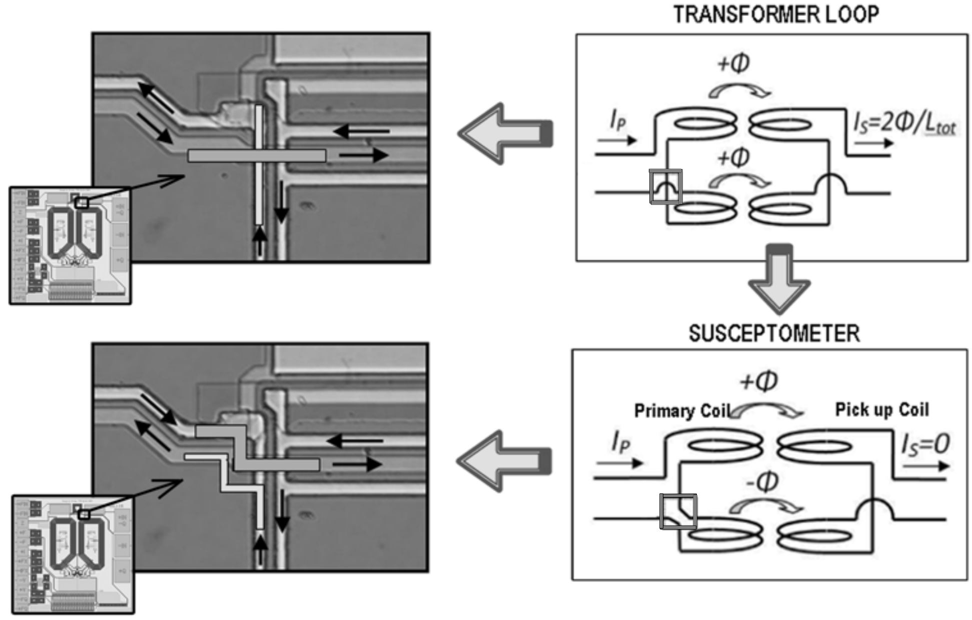

Figure 2.9: Modification of the SQUID wiring to fabricate a SQUID-susceptometer. (a) Initial state of the input flux transformer that is realized with two transformers connected as a first-order series gradiometer. (b) Final state of the input transformer in which the wiring has been modified to reverse the current direction in one half of the input coil resulting in no net flux coupled to the SQUID.

2.4.2 The Idea

All the coils in the chips layout of the PTB/Magnicon SQUID sensors are designed in a gradiometric fashion in order to minimize the sensitivity to external homogenous magnetic fields. We noticed that this property could be exploited to fabricate a microsusceptometer coupled to the SQUID loop in a straightforward way.

As we said in the previous section, an intermediate transformer with gradiometric design is used to match the low SQUID loop inductance to higher inductances of a few μH. In the top right panel of Fig. 2.9 we show an electrical scheme of the transformer loop. The resemblance between this circuit and that shown in Fig. 2.4a, i.e. that of a susceptometer, becomes evident. In fact, looking carefully at this scheme, one notices that the configuration of a real susceptometer could be easily attained just by undoing the wire-crossing marked within a red square. It therefore turns out that a simple rerouting in the superconducting circuitry of this transformer is sufficient to obtain a susceptometer that is coupled to the SQUID. This process could be effectively carried out by undoing the wire-crossing marked with yellow and green rectangles in the top left panel of Fig. 2.9.

Our goal is therefore to modify the sensor's wiring to reach the wire configuration represented in the bottom left panel of Fig. 2.9. For this purpose we need to modify a superconducting microcircuit, i.e. we need the ability of cutting superconducting microwires and creating new ones. We have overcome this challenge using focus ion beam etching and induced deposition of tungsten as we describe in the next section.

2.5 Circuit-edit of superconducting microcircuits

The basic principles of focused ion beam etching and deposition were introduced in the previous chapter (see section 1.5.1). The fabrication of micro and nano-wires of superconducting material is possible by using the appropriate precursor gas [42], as we will show. Furthermore, true superconducting connections to Nb wires are also feasible. These properties have provided us with the unique ability of repairing and modifying superconducting circuits like those of the PTB SQUID sensors.

2.5.1 FIB induced deposition (FIBID) of superconducting material

The combination of focused ion beam (FIB) etching and FIB induced deposition (FIBID) can also be used to perform a circuit edit, by which an integrated circuit is modified to obtain new prototype devices that simulate potential mask changes [70, 71]. The modifications consist of breaking some electrical connections and making new ones. Bridge connections can also be made because insulating materials (e.g. SiO_2), as well as conducting materials, can be deposited by choosing appropriate precursor gases. Compared with the effort of changing the masks, the modifications made using a circuit edit will take hours rather than weeks of work.

In 2004, E. S. Sadki and co-workers showed that FIBID of superconducting material was possible. When $W(CO)_6$ is used as precursor gas, the result is a composite material consisting of 40% C, 40% W and 20% Ga that is a superconductor with $T_c = 5.2$ K [42]. With this material being superconducting at liquid helium temperatures, the benefits of circuit edit can be extended to superconducting microcircuits. Therefore, it can be used to modify or repair highly valuable low-T_c superconducting devices such as SQUIDs, voltage standards based on Josephson junction arrays, or transition edge sensors. Furthermore, using this material the fabrication of 3D superconducting nanostructures and nanoSQUIDs at a desired place is also possible [72].

We used the commercial FEI Nova 200 Nanolab dual-beam system described in the previous chapter. As we said, it incorporates a scanning electron microscopy (SEM) column and a FIB column at 52°. For this work, two gas injection systems (GIS) have been used with $W(CO)_6$ and tetraethylorthosilicate (TEOS) precursor gases respectively.

2.5.2 Properties of W-FIBID at 4.2 K

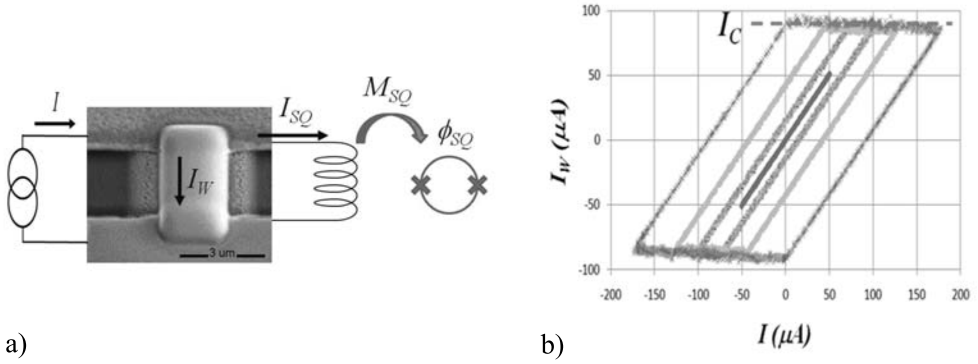

Figure 2.10: a) Schematics of the experiment performed to test the superconducting connection of amorphous W and Nb thin films. The SEM picture shows the actual W line connecting the two Nb terminals of the SQUID input coil. This image has been made at 52° b) Current across the W line as a function of the input current. The graphs show the results for input current amplitudes of 100 μA_{PP}, 200 μA_{PP}, 250 μA_{PP} and 350 μA_{PP}. It is seen that I_W does not increase above a limit value corresponding to the critical current of the W line, I_c.

W-FIBID is an amorphous material with an approximate atomic composition of 40% W, 40% C, and 20% Ga [42]. The typical resistivity at room temperature is 200 $\mu\Omega$cm and it is almost independent of temperature until the superconducting transition is reached. The RRR value, defined as RRR $= \rho(300\ K)/\rho(10\ K)$, is 0.98 [73]. The typical critical temperature is 5.2 K, although values of up to 6.2 K, depending on the deposition conditions, have recently been reported [74]. The nanoscale superconducting properties of the material have been studied [43, 44] and they have shown to be very homogeneous down to the atomic scale.

To study the properties of this amorphous W-based material the following experiment was performed at 4.2 K. A W FIBID line was deposited between the two Nb terminals of the input coil of a SQUID from the PTB. If the W line and the Nb-W line connections are superconducting, then the input coil is shortcircuited and no flux can be coupled to the SQUID. Figure 2.10a shows a scheme of the experimental setup and a SEM image of the deposited W-line, with dimensions 2 μm × 6 μm × 500 nm. The current through the W-line can be determined from the flux, $\Phi_{\rm SQ}$, measured by the SQUID as,

$$I_{\rm W} = I - I_{\rm SQ} = I - \frac{\Phi_{\rm SQ}}{M_{\rm SQ}} \tag{2.7}$$

Figure 2.10b shows the results of the experiment performed with the device immersed in liquid He. A 30 Hz triangular ac current with varying amplitude was applied to the input, and the resulting flux in the SQUID was continuously recorded. When the current was swept with a 100 μA peak-to-peak amplitude, the input current flowed through the W-line. For higher amplitudes, above a threshold value of 160 $\mu A_{\rm pp}$, a saturation of $I_{\rm W}$ and a hysteretic behavior was found. This result can be explained by considering that the critical current of the W-line is reached at $I_c = 80$ μA, and that a current is being trapped in the superconducting circuit formed by the Nb input coil and the W-line. Further, following the same idea, we have been able to trap 80 μA in this circuit. If we then disconnected the current source, we observed that the SQUID signal did not show any measurable decay in $\Phi_{\rm SQ}$ during 30 min.

This indicates that true superconducting connections between the Nb and W-lines are possible at 4.2 K. From this experiment, a critical current density of 8×10^3 A cm^{-2} is found, comparable to previously reported values of 1.5×10^4 A cm^{-2} at 4.4 K and 5 kOe [74], and 1.5×10^5 A cm^{-2} at 3 K without a magnetic field [42]. The low value of the critical current density of amorphous W compared with Nb thin films ($J_c > 10^6$ A cm^{-2}) shows that the technique will be appropriate mainly for low current applications.

2.5.3 Applications: beyond our expectations

Superconducting microcircuits are very sensitive devices that can be easily damaged by electrostatic discharges (ESD) when they are manipulated. Our ability of depositing superconducting as well as insulating material provides us the outstanding opportunity of repairing such devices. As an example, we show in the following how we have successfully repaired a damaged PTB SQUID sensor. Figure 2.11a shows a typical destructive effect of ESD on a cross connection of Nb lines forming part of the SQUID array. The top wire is open-circuited, the bottom wire is considerably affected and the insulation in between has disappeared.

The repair first starts with the deposition of a W-line with dimensions 2 μm × 8 μm × 200 nm that reinforced the bottom wire. Secondly, a SiO_2 layer with dimensions 5 μm × 8 μm × 200 nm was deposited on top. Thirdly, a W-line with dimensions 2 μm × 12 μm × 200 nm was deposited to reconnect

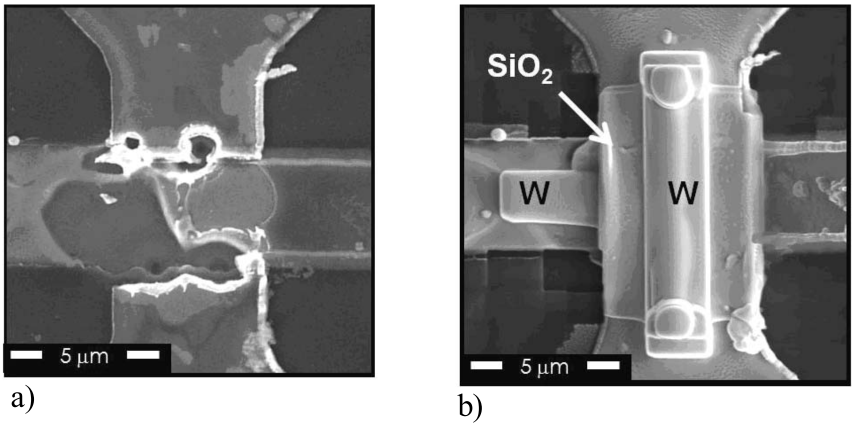

a) b)

Figure 2.11: SEM images of a (a) bridge Nb connection affected by electrostatic discharge and (b) the connection repaired after sequential deposit of W and SiO_2 using FIBID technique with $W(CO)_6$ and TEOS precursor gases respectively.

the top wire. Finally, smaller W squares were deposited at the ends of this line to ensure a good step coverage at the edges of the SiO_2 deposit. The whole process was completed within 2 h. It was checked that the device had become operational again with no observable changes on mutual inductances, SQUID critical current and V transfer function.

2.6 μSQUID susceptometer fabrication

In this section we describe the modification process of the PTB sensors. This has been possible thanks to FIB etching and W-FIBID, as described in the previous section. For this purpose, the sensor is connected to a printed circuit board (PCB) via bonding wires, which provide access to the electrical contacts during the modification process using feedthrough vacuum connectors. This fact enables us to monitor in situ the electrical resistance of the circuit being edited during the deposition and etching steps.

Two types of sensors have been obtained. The first generation consists of a microsusceptometer inductively coupled to the SQUID loop through the 'banana' coils. In a second step, we also noticed that the 'banana' coils that form part of the SQUID loop could be converted into a susceptometer as well, leading to our second generation of susceptometers. These sensors achieve better sensitivities due to two main reasons: the pickup coils are part of the SQUID loop itself, and the effective sensing area is reduced by approximately one order of magnitude. Our second generation belongs, in this way, to the original family of miniature SQUID susceptometers developed by M. B. Ketchen *et* *al* [65].

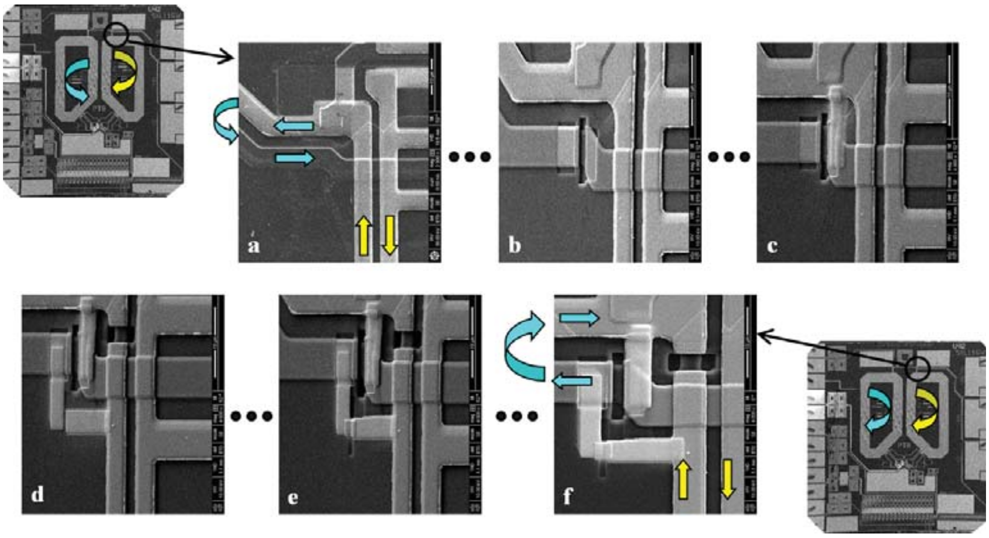

Figure 2.12: SEM images of the different steps performed during the modification process. a) Initial state of the circuit. Notice the sense of the current going to the left transformer (blue arrow) b) A window is opened in the insulating layer covering the superconducting microwires. In this step, also the first wire cut is made. c) A new connection is established between two microwires. d) The second wire cut is performed and the second wire deposition starts. d) The modification process finishes with the last wire deposition. f) At the end of the process, the sense of the current going to the left transformer loop has been effectively inverted (blue arrow) while the sense of the current going to the right transformer remains the same (yellow arrow).

2.6.1 First generation

We have used circuit edit to modify the superconducting circuit of SQUID sensors from the PTB. Figure 2.9 shows schematically how the SQUIDs have been transformed into integrated SQUID susceptometers. A modification of the superconducting wiring is made, such that the current flow in one of the primary coils loops of the input transformer is reversed. As we said in section 2.4.2, this goal can be achieved by undoing the wire-crossing shown in Fig. 2.9. The complete modification process is detailed in the caption of Fig. 2.12. After the modification, the bare SQUIDs are no longer sensitive to currents flowing through the input coil. More specifically, the measured sensitivity to such electrical currents changed from 0.3 μA/Φ_0 (which corresponds to a mutual inductance of 6.7 nH) to 1347 μA/Φ_0 (1.5 pH), the latter value being consistent with the expected deviations in the matching of the two symmetric loops forming the input transformer. By contrast, if a magnetic sample is located on one of the two halves of the input transformer, the mutual inductance

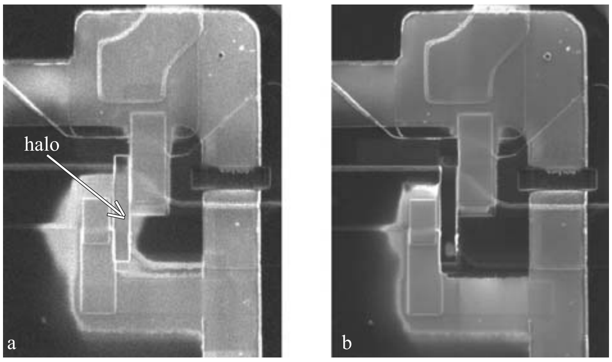

Figure 2.13: a) SEM image of the modified area showing the effects of the W halo. b) Same area after cleaning the halo by ion etching assisted with I_2 gas.

changes and a signal proportional to the magnetic susceptibility of the sample is detected by the SQUID.

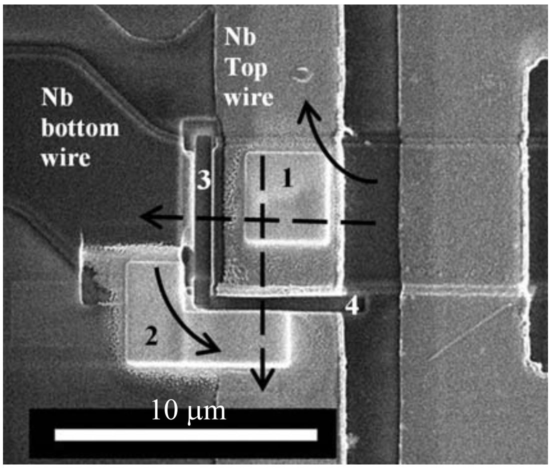

Figure 2.14: SEM picture of the modified area. (1) First connection between top and bottom wires at the crossing point. (2) Second connection. Note that the isolation layer was first removed to contact the bottom wire. (3, 4) Two trenches made with the FIB to break the original connections. Dashed arrows indicate the current flow before the modification while solid arrows represent the new current flow. Scale bar is 10 μm.

Our early attempts had a low yield of success, with the appearance of unexplainable short-circuits that ruined the device. By monitoring the process, measuring the electrical resistance in-situ, we concluded that this problem was caused by the uncontrollable halo formed around the W-FIBID deposit, outside the area where the FIB is scanned. The 'halo' arises from Ga$^+$ ions scattered along arbitrary directions by W nuclei, which are much heavier [75]. These short-circuits were eventually eliminated using a cleaning step with the

FIB as it can be seen in Fig. 2.13. However, the effects of the W-halo were often impossible to control leading to the damage of many sensors.

For this reason we developed later a high yield, reliable method of modifying the SQUIDs based on an alternative way of rerouting the connections between the two crossing lines. The resulting modification can be seen in Fig. 2.14 and the method is described in the following. A hole is first drilled with the FIB through the Nb top layer and the isolation layer to finally reach the Nb wire at the bottom. This step is easily controlled because one can actually see the Nb bottom layer using the ion column for the visualization (see section 1.5.2). The hole is subsequently filled with W-FIBID connecting the top and bottom wires. Almost no halo is produced in this step because most of the scattered Ga^+ ions are confined inside the hole and do not reach the surface. A second connection is made then, by using a minimum size for the W-FIBID deposits. Finally, two trenches are made with the FIB to break the original connections, thereby completing the modification process.

2.6.2 Second generation

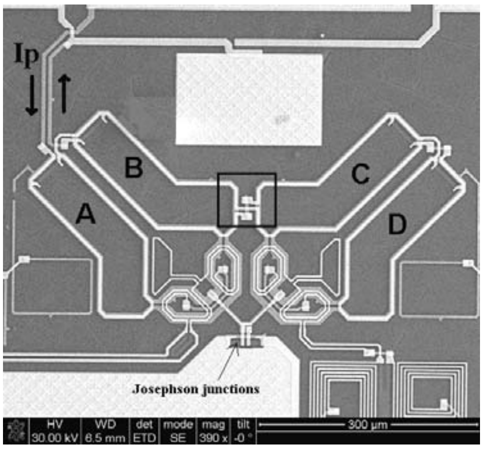

Figure 2.15: SEM picture of the front-end SQUID. The main contribution of the SQUID loop inductance comes from the four banana shaped coils A, B, C and D that are connected in parallel. These are the sensitive areas wherein the sample is placed. I_p is the primary current that creates the excitation magnetic field. The center square marks the modified region.

To achieve even better sensitivities, we have also modified low input coil inductance SQUIDs, which have no intermediate transformer. The SQUID loop (Fig. 2.15) consists mainly of four banana-shaped niobium coils, with effective areas of $63 \times 250\ \mu m^2$, connected in parallel. The input signal is inductively coupled to the SQUID loop through four pickup coils deposited on

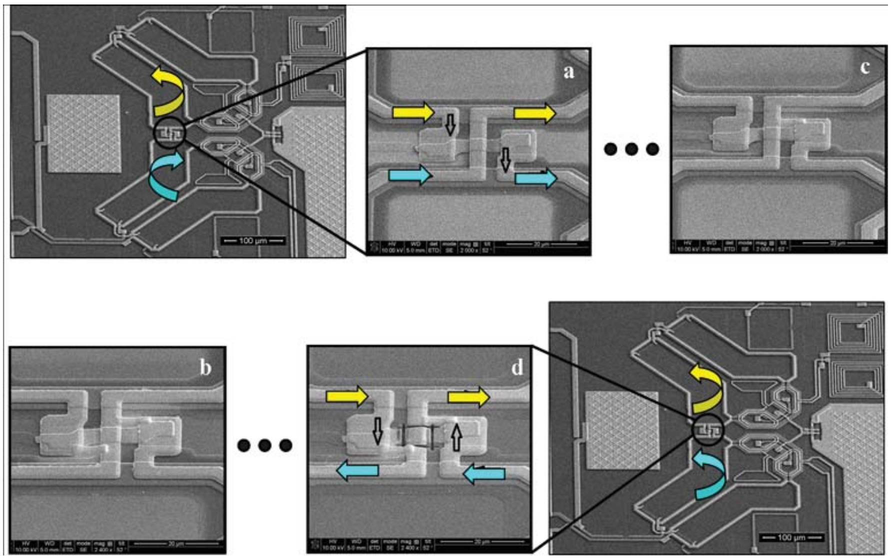

Figure 2.16: Transformation process for a SQUID susceptometer without intermediate transformer: a) original connection, b) first W-FIBID deposit, c) second W-FIBID deposit, and d) trenches produced with the FIB to break the original connections. Arrows indicate the direction of the primary current, note the difference in direction between a) and d).

top of the SQUID coil, therefore exactly matching the geometry of the latter. We noticed that these 'banana' coils could be transformed in a similar way as we did with the intermediate transformer loop in the previous section. In this second generation of susceptometers, the sample is directly placed on the SQUID loop, thereby improving the flux coupling between them.

A graphical sequence of the transformation process is shown in figure 2.16. It consists of the deposition of two W-FIBID connecting lines and the breaking of original connections using the FIB. The modification changes the sign of the mutual inductance between areas C+D and the primary coil, which is then reversed with respect to that of areas A+B. Under these conditions, a current I_p flowing through the primary coil (see Fig. 2.15) couples approximately no net flux to the SQUID. More specifically, the sensitivity to input current changes typically from 5.6 μA/Φ_0 (which corresponds to a mutual inductance of 360 pH) to 5882 μA/Φ_0 (0.34 pH). The sample to be measured can be located on either the left-hand side (areas A+B) or the right-hand side (areas C+D).

2.7 μSQUID susceptometer performance

Sensors are mounted on PCB holders and wire bonded to the copper pads using 25- μm aluminium wire. Sensors must be first characterized in order to ascertain wether the modification process has been successful or not. For this purpose we perform quick tests in liquid helium as we describe next. The temperature response of bare sensors has also been analyzed using a dilution refrigerator down to mK temperatures. In this section, we also describe a series of experiments that have enabled us to calibrate our sensors and determine their true spin sensitivity. Finally we present a few experiments performed on different samples that illustrate the enormously high dynamical capabilities of these sensors

2.7.1 Readout performance

FIRST GENERATION

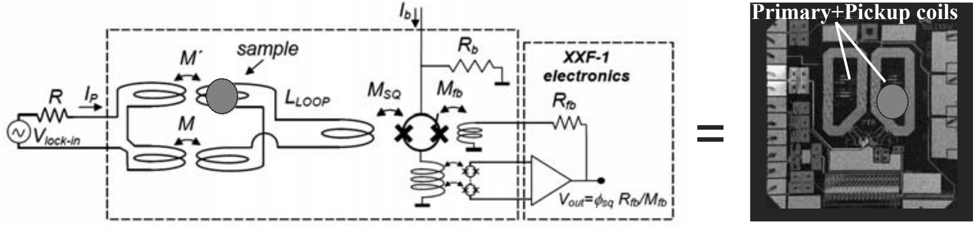

SECOND GENERATION

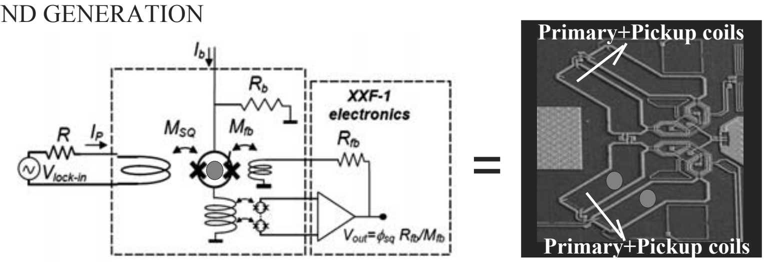

Figure 2.17: Schematic diagram of the SQUID susceptometer chip (inside dashed line) corresponding to the first (top) and second (bottom) generations.

Let us consider first the first generation of μSQUID susceptometers that we have developed (see Fig. 2.17 top). The input current I_P is controlled with the internal oscillator of the lock-in amplifier $\mathrm{V}_{\mathrm{Lock-in}}$ and a series resistance $R_{\mathrm{ext}\Phi}$. I_P couples flux to the first order gradiometer of the intermediate loop through mutual inductances M and M'. These mutual inductances have the same geometry and their values differ only when a magnetic sample is present, in that case $M' = M(1 + F'\chi)$ where χ is the magnetic susceptibility of the sample and F’ is a calibration factor usually referred to as the filling factor ($0 < F' < 1$). The flux coupled by the signal-SQUID is given by $\Phi_{\mathrm{SQ}} = I_P(M'-M)M_{\mathrm{SQ}}/L_{\mathrm{LOOP}} = I_P M M_{\mathrm{SQ}} F'\chi/L_{\mathrm{LOOP}}$. A second stage 16-SQUIDs array is used to read-out Φ_{SQ}. Magnicon XXF-1 electronics is used to operate the system in FLL mode. Finally, the in-phase and out-of-phase components of V_{out} oscillating at the driving frequency ω are read-out with the lock-in amplifier.

In the second generation, (see Fig. 2.17 bottom), one intermediate inductive coupling is avoided and the working principle is the same. Samples are deposited directly on the SQUID loop thereby modifying the mutual inductance M_{SQ}. The flux coupled by the SQUID is, in this case, given by $\Phi_{\mathrm{SQ}} = I_P M_{\mathrm{SQ}/2} F'\chi$, where $M_{\mathrm{SQ}/2}$ is the mutual inductance between half of the pickup coils and the SQUID loop.

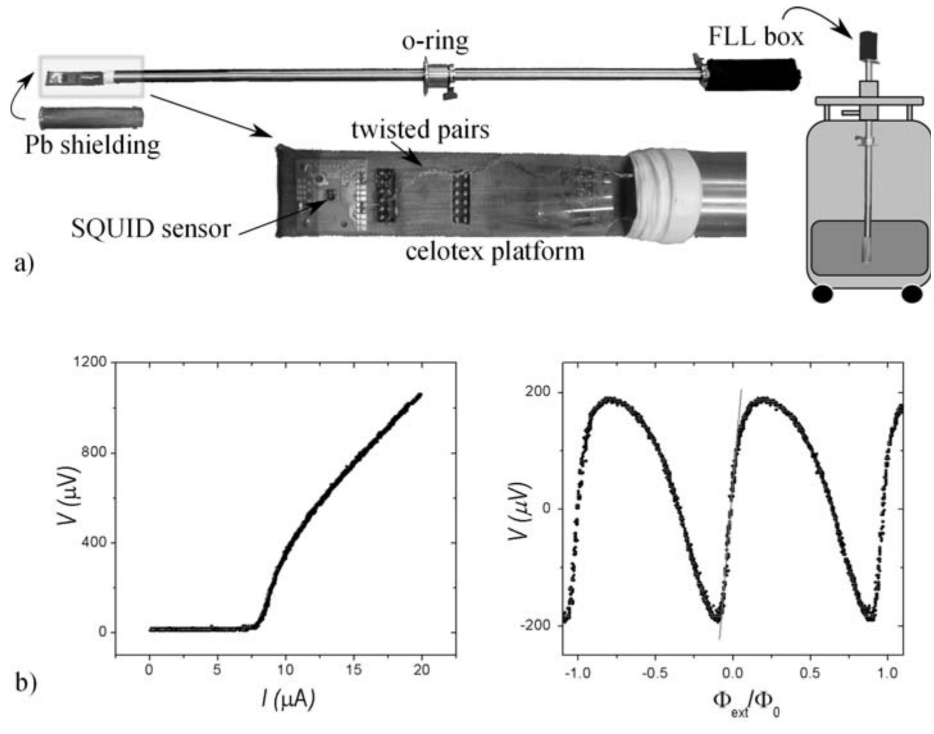

Figure 2.18: a) Image of the dipstick that enables us to perform quick sensor tests at helium temperatures using a transport dewar. The bottom part of the figure shows an enlarged view of the celotex part where sensors can be plugged or bonded directly to the twisted pars. b) $I-V$ and $V-\Phi$ characteristics of one two-stage high-input inductance SQUID sensor.

2.7.2 Sensor test at 4.2 K

The performance of our SQUID microsusceptometers has been tested at 4.2 K using a helium transport dewar. In this way, the use of the dilution refrigerator, which implies several days of work, will be reserved for measurements of magnetic samples below 4.2 K. Following the suggestion of D. Drung and coworkers, we have fabricated a so-called ”dipstick” . This instrument consists of a stainless steel stick terminated in a celotex platform where the sensors can be plugged (see Fig. 2.18)a. Sensors are magnetically shielded using a home-made superconducting cover fabricated with Pb sheets 125 μm thick ($T_c \sim 7$ K for Pb). The FLL box stays at the top of the stick connected to the bottom part through twisted cables. The dipstick is introduced directly into the helium dewar and held with an o-ring and a vacuum clamp.

The dipstick enables us to perform quick tests at liquid helium temperature. We can, for instance, analyze the main SQUID characteristics, e.g. the $I-V$ and the $V-\Phi$ curves, or check wether the modification process has been successful. Figure 2.18b shows an example of the $I-V$ curve corresponding to the maximum critical current of the 16-SQUID array of one of our sensors before its modification. From these measurements we can estimate the array-SQUID's critical current $2I_0 \approx 8$ μA, where I_0 corresponds to the critical current of one of the two Josephson junctions of each SQUID. The optimum bias current I_b will be therefore slightly larger than $2I_0$. Using $I_b \approx 9$ μA the overall $V-\Phi$ characteristic shown in the right part of Fig. 2.18b is obtained. The transfer function can be determined by a linear fit of the $V-\Phi_{\text{ext}}$ curve giving $V_\Phi \approx 3000$ μV/Φ_0. The linear flux range equals $\Phi_{\text{lin}} \approx 0.1$ Φ_0. Taking into account the excitation current applied to the feedback resistor to obtain a modulation corresponding to one flux quantum, the mutual inductance between the feedback coil and the SQUID loop can be calculated, giving $1/M_f = 41.3$ μA/Φ_0 (which corresponds to $M_f = 48$ pH).

2.7.3 Low-T characterization

Sensors are installed inside the mixing chamber of our dilution refrigerator previously described in chapter 1 (see Fig. 2.19). This chamber has been specially designed and fabricated with plastic to avoid any coupling with ac fields. It has 24 electrical connections with vacuum tight feedthroughs. To reduce the effect of electromagnetic interferences, a small Pb shield covers the SQUID holder inside the mixing chamber and a Cryoperm shield surrounds the whole inner vacuum chamber IVC of the refrigerator. In addition, special care has been taken to electrically isolate the cryostat and connecting tubes and to rf-filter all the lines used for thermometry. A commercial low-thermal

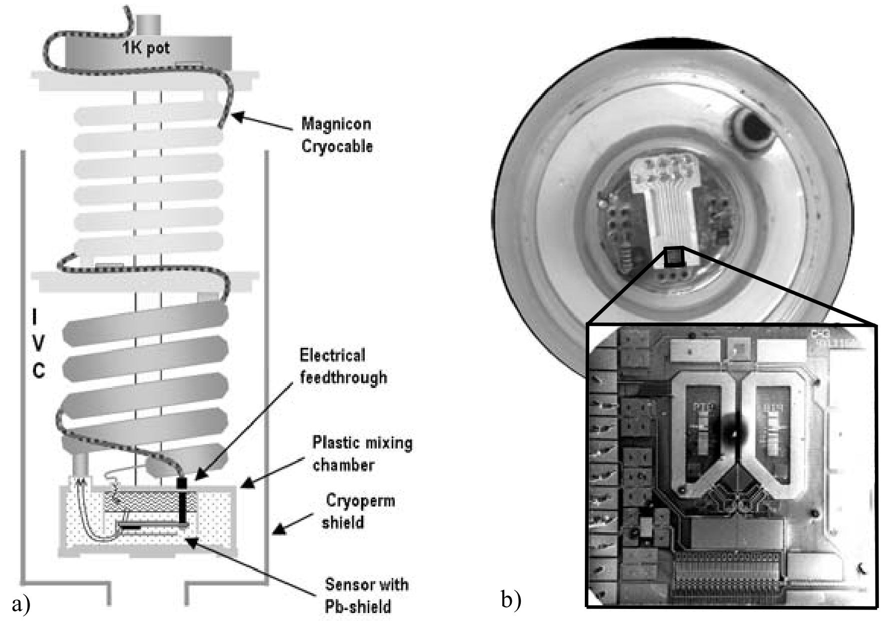

Figure 2.19: a) Representation of the lower part of the dilution refrigerator insert. The sensor lies inside the mixing chamber immersed in the ^{4}He rich phase, with the PCB holder plugged into electrical feedthroughs connected to the cryocable in the inner vacuum chamber. b) Bottom view of the mixing chamber with a SQUID-susceptometer chip mounted in place. The inset shows an enlarged view of the sensor, the size of which is 3 mm × 3 mm.

conductivity cryocable from Magnicon was used for the wiring from the mK region to 300 K at the top of the cryostat were the FLL box is connected.

The thermalization of the sensor and the sample is ensured by the direct contact with the helium bath. In this way, the heating of the sample due to the absorption of energy from the ac magnetic field when the imaginary susceptibility component is not zero, is also prevented since we profit the most from the cooling power of the dilution refrigerator. As it can be seen in Fig. 2.20, the cooling power and the base temperature 13 mK have not been affected.

Decreasing the temperature of the SQUID sensors also modifies some of their electronic properties. The critical current of the SQUID array increases a few 10% below 1 K. However, this change implies no distortion in the $V - \Phi$ curve at very low temperatures. More importantly, the flux noise spectrum, measured at different temperatures (see fig. 2.21), shows that the white noise decreases with the square root of temperature as predicted by the theory [76, 77]. This behavior saturates, below approximately 100 mK, probably due to "hot-electron" effects [78]. At 13 mK and 100 kHz, a typical uncoupled

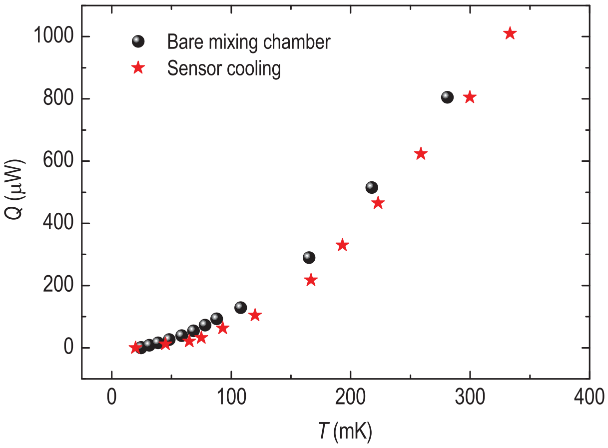

Figure 2.20: Cooling power of the dilution refrigerator measured with the bare mixing chamber and after wirings and one μSQUID sensor covered with a Pb shielding was installed in it.

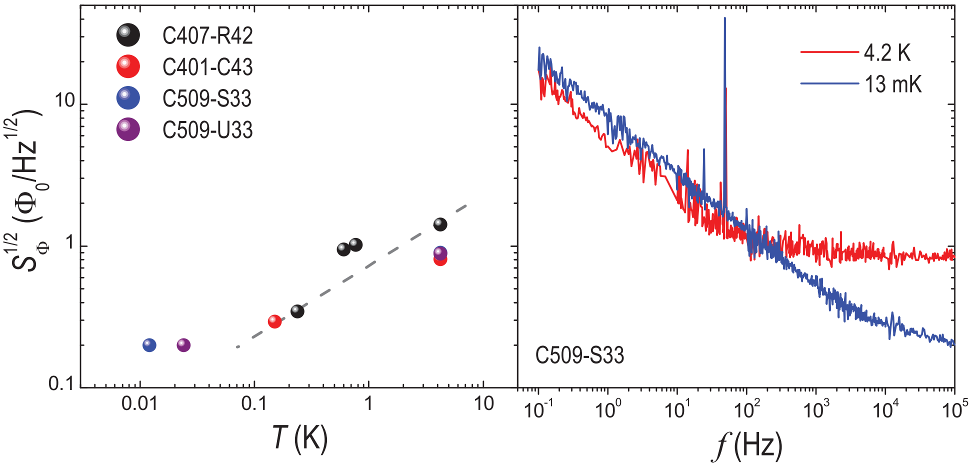

Figure 2.21: High frequency flux noise (white noise) measured at different temperatures on different sensors (left). The white noise depends on temperature as expected from the theory ($S_\Phi^{1/2} \propto T^{1/2}$) down to $\sim$ 100 mK when it saturates. On the right we can see the whole flux noise spectra measured on one sensor at 4.2 K and 13 mK. The white noise decreases when decreasing the temperature whereas the $1/f$ noise remains nearly the same.

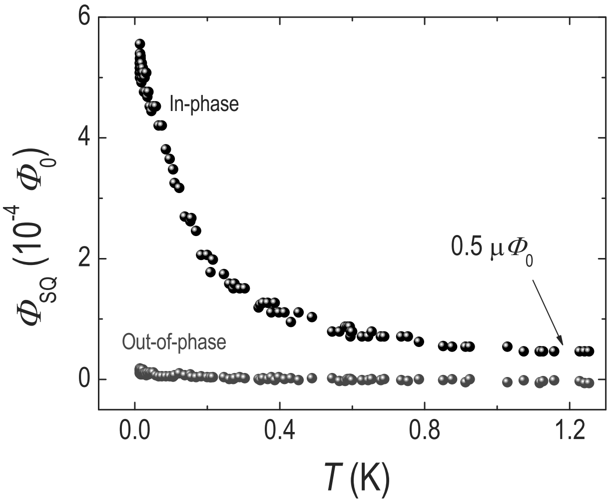

Figure 2.22: $1/T$-dependent background flux signal of a bare sensor when applying an excitation current of 500 μA. Solid circles correspond to the in-phase response and open circles to the out-of-phase.

energy sensitivity $S_\Phi/2L = 7\hbar$ is obtained, where $S_\Phi^{1/2} = 0.20\ \mu\Phi_0/\mathrm{Hz}^{1/2}$ is the magnetic flux noise, $L = 115$ pH is the inductance of the front-end SQUID, and $\hbar = h/2\pi$ is the Planck constant.

The intrinsic response of the bare sensors has been characterized down to very low temperatures (see Fig. 2.22). After subtracting the constant background due to the misbalance of the pickup coils, a weak $1/T$-dependent signal shows up below 800 mK. The existence of such signal was checked in different experiments in which we found that it does not vary from run to run. Similar results have been reported by Sendelbach *et al* in a dc experiment, the origin of which was attributed to the effect of unpaired surface spins [79]. Thanks to the thorough characterization performed here, this background can be easily subtracted from the signal generated by a sample.

2.7.4 Calibration and spin sensitivity measurements

We have performed a calibration of the sensors following the procedure developed by D. D. Awschalom *et al* [66]. Small Pb filings were obtained from a 99.99% Pb foil. By melting these filings under Ar atmosphere, we got small Pb spheres, which are stabilized by their surface tension. A Pb sphere with radius $R = 45\ \mu$m was placed at different locations over the pickup coil of our sensors. The corresponding variation of the input mutual inductance ($\Delta M/M$) was measured at 4.2 K. The latter is proportional to the magnetic susceptibility of the Pb sphere. Below the critical temperature of Pb ($T_c = 7$ K),

Figure 2.23: Image of the sensor used for the calibration experiment. For this purpose, a 45 μm-in-diameter Pb sphere (indicated with an arrow) was positioned at different locations within the pickup coils and the variation of the mutual input inductance was measured. The chip was first covered with a thin layer of vacuum grease, this helps to maintain the sphere at the desired position and to manipulate it.

the sphere becomes superconducting and behaves as a perfect diamagnet with $\chi = -1$ providing then a direct method to convert the variation of mutual inductance into magnetic units.

The total flux coupled to the pickup coils strongly depends on the sphere position. This fact becomes even more evident as the size of the calibration sample decreases (this question will be analyzed in more detail in chapter 6). We found that the maximum sensitivity is obtained when the sphere is placed close to one of the pickup coil corners. We describe first the calibration process of one of our first-generation susceptometers (see Fig. 2.23) with sensing area of 367 μm × 920 μm.

The calibration Pb sphere is positioned as shown in Fig. 2.23. The device is then cooled through the transition temperature of Pb by introducing it inside a helium transport dewar. Under these circumstances, we measure a relative inductance variation of $\Delta M/M = 3 \times 10^{-3}$, consistent with the geometrical estimations done by M. B. Ketchen *et al* [65].

The calibration factor F is defined as the variation of the sample's magnetization sufficient to couple one flux quantum to the SQUID loop. For small applied magnetic fields, F can be obtained by doing

$$F = \frac{\delta\chi}{\delta\Phi} H V \tag{2.8}$$

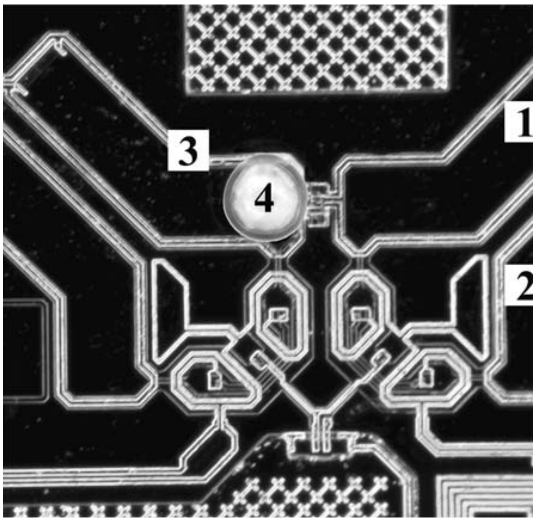

Figure 2.24: Image of the Pb sphere used for the calibration of a second generation μSQUID susceptometer. The sphere occupies position 4. Numbers correspond to the different positions on which the sphere was positioned. The image was taken with the dark-field mode of an optical microscope.

where χ is the volume susceptibility of the sample, H is the magnetic field and V is the volume of our sample. H is reduced with respect to the applied magnetic field H_{app} due to the demagnetization field that appears in the sample. In this way, H is given by

$$H = \frac{H_{\mathrm{app}}}{4\pi + D\chi} \tag{2.9}$$

where D is the demagnetization factor that, for the case of an sphere equals $D = 4\pi/3$. The calibration factor can be therefore obtained using the formula

$$F = \frac{4\pi R^3}{3} \frac{H_{\mathrm{app}}}{(4\pi + D\chi)\delta\Phi} \tag{2.10}$$

Here, R is the radius of the sphere and $\delta\Phi$ is the variation of the flux in the SQUID caused by the superconducting transition of the Pb sphere.

H_{app} can be estimated by taking into account the input excitation current that flows through the primary coils and their geometry. For this purpose, we perform numerical calculations of H_{app} using a finite element method. The result of this computation gives $H_{\mathrm{app}} \approx 60$ mOe for $I_p = 50\ \mu$A. Inserting this value and the experimental variation of magnetic flux $\delta\Phi = 0.274\ \Phi_0$ in Eq. 2.10 we obtain $F = 10^{-8}$ emu/Φ_0. Using, for instance, a feedback resistance of $R_f = 30$ kΩ and taking into account the mutual inductance between the SQUID loop and the feedback coil of these sensors $1/M_f \approx 42\ \mu$A/Φ_0, the calibration factor can be expressed as $F = 8.6 \times 10^5 \mu_{\mathrm{B}}/\mu$V

Taking into account the measured flux noise of these sensors, we can estimate their spin sensitivity, that is, the figure of merit proposed by Ketchen *et al* [80]. Our spin sensitivity (each spin having a moment of μ_{B}, where μ_{B} is the Bohr magneton) is $s_\mu \approx 9.6 \times 10^5$ $\mu_{\mathrm{B}}/\mathrm{Hz}^{1/2}$ at 4.2 K and $s_\mu \approx 2.1 \times 10^5$ $\mu_{\mathrm{B}}/\mathrm{Hz}^{1/2}$ at 13 mK.

The sensitivity of one of the second-generation SQUID susceptometers, with sensing area of 63 μm × 250 μm, was determined in a similar way. The Pb sphere was placed at different locations as indicated in Fig. 2.24. For each of these, the corresponding variation of the input mutual inductance $\Delta M/M$ was measured at 4.2 K. We find that the flux created by the sphere is positively coupled to the SQUID when it is located on the A or B areas, and negatively when it is located on the C or D areas (cf. Fig. 2.15). As we said, the variation of ΔM is very sensitive to the sample position, being maximal when the sphere is located at position 4 of Fig. 2.24. At this point, we find $\Delta M/M = 4.7 \times 10^{-3}$.

The experimental calibration factor was measured using an excitation current $I_p = 250$ μA which produces approximately $H_{\mathrm{app}} \approx 1.6$ mOe at the sample position. The measured variation of magnetic flux was $\delta\Phi = 0.062$ Φ_0 giving $F = 1.15 \times 10^{-9}$ emu/Φ_0. Again, considering a feedback resistance of $R_f = 30$ kΩ and $1/M_f \approx 42$ μA/Φ_0, the latter leads to 9.8×10^4 μ_{B}/μV. Under these circumstances, the spin sensitivity is $s_\mu \approx 2.4 \times 10^4$ $\mu_{\mathrm{B}}/\mathrm{Hz}^{1/2}$ at 13 mK.

As we can see, the experimental sensitivity of the second generation of μSQUID susceptometers is enhanced by one order of magnitude compared to the first generation. This is in agreement with the rule that better sensitivities are achieved for smaller dimensions [80]. These results can be compared with those reported in the literature for similar devices. An experimental spin sensitivity of $s_\mu \approx 2 \times 10^2$ $\mu_{\mathrm{B}}/\mathrm{Hz}^{1/2}$ at 200 mK was reported by M. E. Huber *et al* using a sensing area with 4.6 μm diameter [81]. Another example is that reported by C. Granata *et al* who obtained $s_\mu \approx 10^2$ $\mu_{\mathrm{B}}/\mathrm{Hz}^{1/2}$ at 4.2 K for a sensing area of 200 nm × 200 nm [82].

2.7.5 Background subtraction and signal scaling

As we have showed in sections 2.6.1 and 2.6.2, the balance between the pickup coils is not optimum. This problem is inherent to the fabrication process. Two coils fabricated by optical lithography differ typically by a 0.1%, approximately. In addition, our coils are not fabricated in a completely symmetric way. Superconducting circuit elements surrounding both coils differ, increasing considerably the misbalance. These facts lead on a net background signal that we must characterize first in order to subtract it from the signal coming from a sample. Figure 2.25 shows a measurement of the background performed at 4.2 K as a function of the frequency.

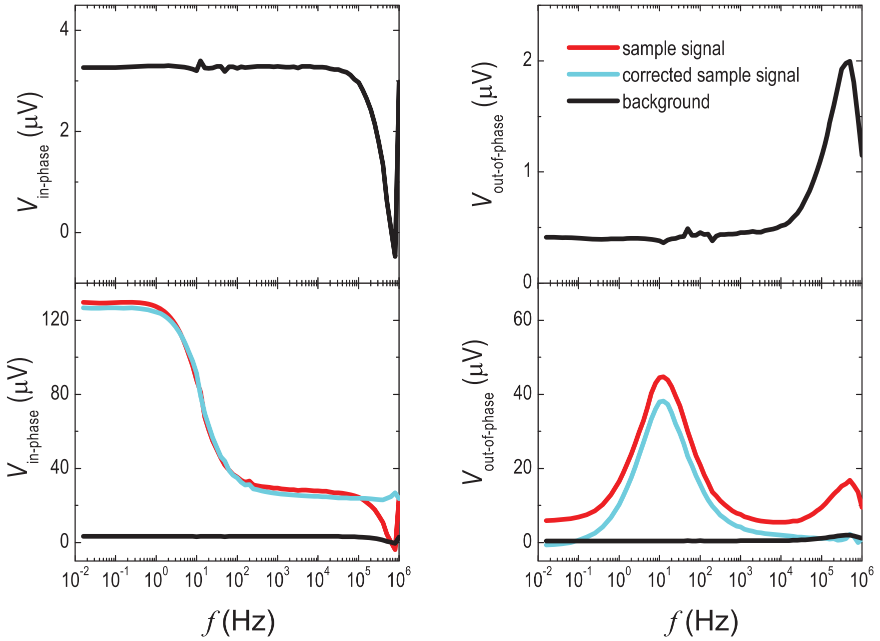

Figure 2.25: In-phase (left) and out-of-phase (right) components of the SQUID output voltage vs. frequency. Upper panels show the response of the bare sensor whereas the bottom panels show the signal coming form a sample of HoW_{10} clusters.

As it can be seen in the top panels of Fig. 2.25, the dynamical response of the system degrades considerably at high frequencies. This is probably due to the fact that we are using the same cables for the input (excitation) and output currents.

It is however possible to extract information about the susceptibility response above 100 kHz by a proper background correction. The latter is illustrated in the bottom panels of Fig. 2.25 and described in the following. Let us denote $\rho_{\text{exp}}(f)$ and $\theta_{\text{exp}}(f)$ to the modulus and phase, respectively, of the experimental SQUID output. These quantities are obtained from

$$\rho_{\text{exp}}(f) = \sqrt{V'^2(f) + V''^2(f)} \tag{2.11}$$

$$\theta_{\text{exp}}(f) = \tan^{-1}\left(V''(f)/V'(f)\right) \tag{2.12}$$

where V' is the output response going in-phase with the excitation magnetic field and V'' is the out-of-phase component. On the other hand $\rho_{\text{BG}}(f)$ and $\theta_{\text{BG}}(f)$ are, respectively, the modulus and phase of the output background measured in the absence of any sample. Let us additionally denote the low frequency limit of $\rho_{\mathrm{BG}}(f)$ as $\rho_{\mathrm{BG}}(0)$. The high-frequency dependence can be corrected and the background can be subtracted from the experimental signal by doing

$$\rho_{\mathrm{corr}}(f) = \rho_{\mathrm{exp}}(f)\frac{\rho_{\mathrm{BG}}(0)}{\rho_{\mathrm{BG}}(f)} - \rho_{\mathrm{BG}}(0) \tag{2.13}$$

$$\theta_{\mathrm{corr}}(f) = \theta_{\mathrm{exp}}(f) - \theta_{\mathrm{BG}}(f) \tag{2.14}$$

and finally

$$\chi\text{'} = F/H\rho_{\mathrm{corr}}(f)\cos\left(\theta_{\mathrm{corr}}(f)\right) \tag{2.15}$$

$$\chi\text{"} = F/H\rho_{\mathrm{corr}}(f)\sin\left(\theta_{\mathrm{corr}}(f)\right) \tag{2.16}$$

where F is the calibration factor and H is the magnetic field. In the example shown in Fig. 2.25 we can see the in-phase and out-of-phase voltage responses corresponding to the experimental SQUID output with a sample positioned in the pickup coils, the output background measured in the absence of any sample and the corrected signal. The sample used was, in this case, a crystal of HoW_{10} clusters measured at 200 mK. More details about this sample can be found in next section.

The experimental calibration factor F obtained in the previous section enables us to convert the SQUID voltage output into magnetic units. This parameter depends however on geometrical considerations, like the sample size, shape and position. For this reason, it will be better to calibrate the voltage signal obtained from each sample separately. This calibration can be easily performed by measuring the susceptibility response of the sample in a commercial SQUID magnetometer that, knowing the sample's mass, provides absolute susceptibility units. In this way, comparing the signal obtained with the μSQUID susceptometer and with the commercial SQUID magnetometer in a coincident temperature range, it is possible to scale the former signal.

2.7.6 Dynamical response

Our susceptometer inherits the extremely broad bandwidth capabilities of the PTB readout electronics. This property enables us to perform ac susceptibility measurements covering more than eight decades (1 mHz - 1 MHz). Figure 2.26a illustrates the extreme performance of our integrated susceptometers. The top panel shows susceptibility data measured at 4.2 K on a micron-sized crystal of $\mathrm{Mn}_{12}\mathrm{Bz}$ single molecule magnets [83] placed directly on the SQUID loop (second generation of susceptometers). These measurements take typically $\sim$ 2 hours for the whole range of frequencies studied. In a single run, the frequency dependent susceptibility enables measuring, under identical conditions, the very different magnetic relaxation times (τ) of the two species of

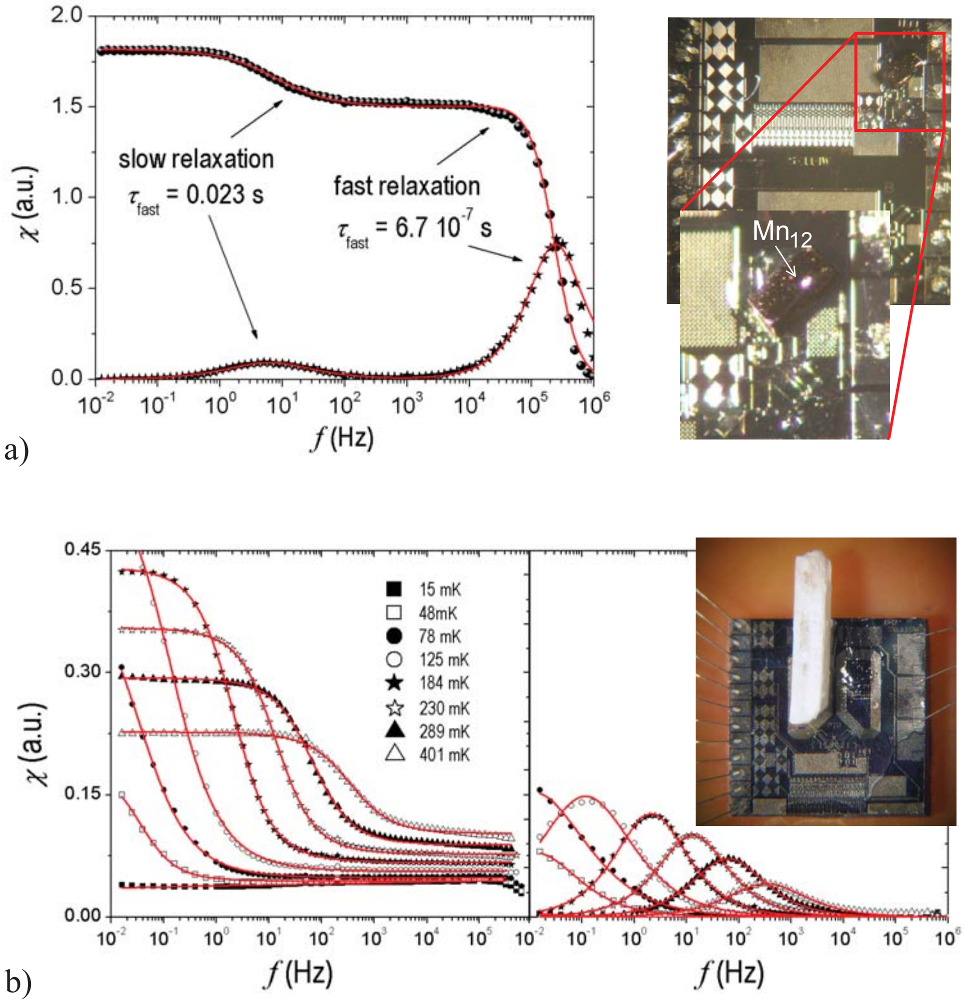

Figure 2.26: a) In-phase and out-of-phase ac susceptibility components of a 200 μm $\times$ 100 μm $\times$ 20 μm single crystal of $Mn_{12}Bz$ single-molecule magnets at $T = 4.2$ K. Measurements within the whole bandwidth of the system performed using one of our second-generation susceptometer enable us to observe the magnetic relaxation of the two molecular species present in this sample. The respective relaxation times have been determined by fits of a combination of two Cole-Cole laws (solid lines) to the experimental data (scatter). On the right hand we can see an image of the sensor and the sample attached to it with vacuum grease. b) Real and imaginary components of the susceptibility of a larger 2.5 mm $\times$ 500 μ m $\times$ 200 μ m crystal of HoW_{10} measured using one of our first-generation susceptometers down to 15 mK. Experimental data (scatter) have been fitted to Cole-Cole functions (solid lines). The inset shows an image of the sensor and the sample. The Cole-Cole law will be introduced in the next chapter (section 3.7.3).

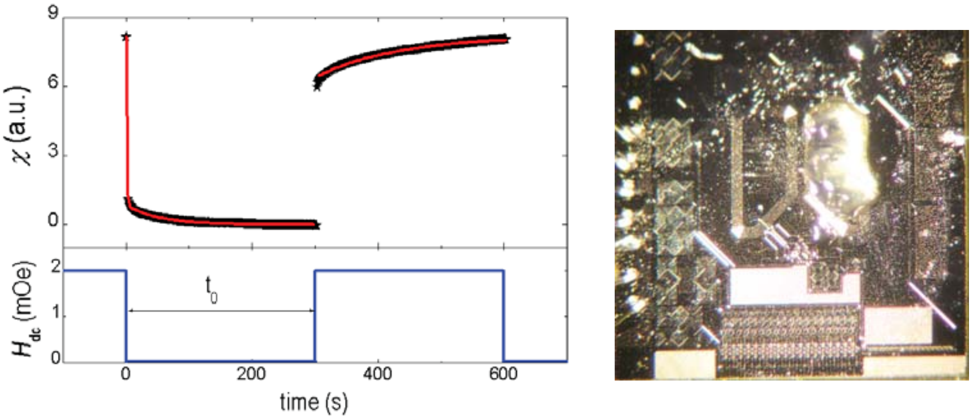

Figure 2.27: Dc magnetic response of $\mathrm{LiHo_{0.167}Y_{1-0.167}F_4}$. For this experiment, we used a powdered sample mixed with vacuum grease. From these measurements, the mean relaxation time at 200 mK was determined in 10 minutes giving $\tau = 50$ s.

$\mathrm{Mn_{12}}$ clusters present in this sample. On the one hand, the fast relaxing species that represents approximately a 90% of the clusters in this compound, with relaxation times of order $\tau = 3 \times 10^{-7}$ s at 4.2 K. On the other, the remaining 10% of standard, or slow relaxing, $\mathrm{Mn_{12}}$ molecules, for which $\tau = 0.026$ s.

Figure 2.26b shows measurements performed using the dilution refrigerator down to very low temperatures. In this case, we have used one of our first-generation SQUID microsusceptometer to measure the susceptibility response of a single crystal of $\mathrm{HoW_{10}}$ clusters. These samples consist of single holmium ions encapsulated within two polyoxometalate molecules [16] and exhibit the typical features attributed to single-molecule magnets. The relaxation rate of these nanomagnets remain sufficiently large even down to the close vicinity of the absolute zero, which our powerful dilution refrigerator enables us to explore.

On the other hand, the relaxation time of single molecule magnets and magnetic nanoparticles becomes usually extremely large at very low temperatures. In order to characterize this ”slow” region it is very convenient to study the sample’s magnetic response to a dc magnetic filed. This kind of measurements can be easily performed with our susceptometer in the following way. A current pulse (I_p) is applied to the primary coils during a time interval t_0. This current creates a dc magnetic field H_{dc}. The current is then switched off and the relaxation response of the magnetization is monitored as a function of time (relaxation sequence). After that, the excitation current is switched on again and the recovery of the magnetization is monitored (recovery sequence). In this way, it is possible to estimate the equilibrium value of the susceptibility at $H = H_{dc}$ by extrapolating the voltage response to $t \to \infty$ in the recovering sequence. Fitting the susceptibility response in the relaxation sequence to an exponential law of the form $(1 - e^{-t/\tau})$ it is possible to obtain an estimation of the relaxation time τ. This method enables an accurate determination of very long relaxation times within reasonable experimental times. An example of such measurements, performed on a holmium fluoride salt, is shown in Fig. 2.27

2.8 Conclusions

The μSQUID susceptometer developed by us combines the high sensitivity and broad bandwidth of the Magnicon/PTB SQUID sensors with the possibility of measuring samples in direct contact with the ^{3}He-^{4}He mixture of a dilution refrigerator. The fabrication of these devices, by a simple modification of the electrical circuit, has been carried out in our laboratories thanks to the superconducting properties of W-FIBID.

The deposition of a superconducting material with nanometric control using FIB tools opens up the possibility of extending the very useful 'circuit edit' concept to superconducting microchips. We have demonstrated that superconducting connections between W FIBID lines and Nb films can be fabricated and that they are operative at 4.2 K. FIBID then provides a powerful technique that can be used to fix errors of design in devices, or to carry out modifications very quickly without the need of onerous changes in the masks and new fabrication runs. Furthermore, the described method enables the repairing of valuable low-T_C superconducting microcircuits with high resolution; this was previously impossible.

Two kind of sensors have been obtained. In the so-called first generation of SQUID microsusceptometers, the sensors consist of two pickup coils designed in a gradiometric way with an effective area of 367 μm × 920 μm. On top of the latter, two 30-turn primary coils produce an average magnetic field of $H_0[\text{mOe}] \sim 0.05 I_p[\mu\text{A}]$, where I_p is the excitation current. The pickup coils are inductively coupled to a dc-SQUID the signal of which is then amplified in a second stage that includes an array of 16-SQUIDs. Small crystals of a few hundred μm or powdered samples mixed with vacuum grease can be placed on top of the pickup coils without the assistance of any mechanical setup. The sensitivity of these devices has been determined experimentally giving $s_\mu \approx 2.1 \times 10^5\ \mu_\text{B}/\text{Hz}^{1/2}$ at 13 mK.

On the other hand, a second-generation of SQUID microsusceptometers with enhanced sensitivity has been fabricated as well. These consist of four pickup coils connected in parallel with gradiometric design that forms part of the SQUID loop itself. The effective sensing area of each one of these coils is 63 μm × 250 μm. On top of them, four single-turn primary coils connected in series create a mean field of $H_0[\text{mOe}] \sim 0.01 I_p[\mu\text{A}]$. The signal coming from the sample is therefore directly coupled to the SQUID loop and amplified with the 16-SQUIDs array. The sample manipulation becomes more difficult since only crystals of a few μm can be used and also because of the smaller size of the pickup coils. For these reasons, these sensors will only be used in those cases where the sensitivity must be maximized.

The development of these instruments has opened many possibilities for the study of spin dynamics at low temperatures in our laboratory. We have, for instance, investigated the intriguing phenomena of spin quantum tunneling and its relevance for the mechanisms of spin-lattice relaxation (see chapter 7) or the influence of the molecular symmetry on the anisotropy of single molecule magnets (see chapter 6). These experiments show that we have a powerful and versatile technique for the characterization of different solid state candidates for quantum computing (molecule-based qubits). Our second-generation of microsusceptometer has also enabled the detection of the magnetic susceptibility of submonolayer arrangements of magnetic nanoparticles deposited directly onto the SQUID sensor via Dip Pen Nanolitography (DPN) (see chapter 5). The latter provides the opportunity to ascertain to what extent the properties of molecule nanomagnets are influenced by the surface where they are patterned and therefore the reliability of hybrid structures. Our work also provide an experimental method of determining the energy coupling between these patterns and superconducting circuits. We have demonstrated how this coupling can be enhanced by more than three orders of magnitude by controlling the particle distribution down to the micro/nanometric scale.

Part I

The classical world

Chapter 3

Theoretical Considerations: Magnetic Nanoparticles

3.1 Introduction

On December, 1950, Richard Feynman challenged the scientific community to go into a new world: the world of smallness. In his talk ”There’s Plenty of Room at the Bottom” [84], the famous physicist pointed out that exciting and unknown properties would arise as a consequence of size reduction. The humankind had been however taking advantage of this world many years before. Glassworkers in the ancient Rome already knew that colloidal gold nanoparticles can be used as pigment to stain glasses with different colors like yellow, red or mauve. The concept of understanding and exploiting the properties of materials under the micron scale received later the name of ”nanotechnology” and has brought many surprises to scientists. As Richard Feynman envisaged, roles are reversed in the nanoscopic scale. The outstanding forces that dominate our macroscopic conception of the world, like gravity, becomes negligible, whereas weak interactions like Van der Waals forces gain prominence. Finite-size and surface related properties, irrelevant in bulk materials, are the responsible of many of the characteristics exhibited by nanoparticles. Their electronic, optical, electrical, magnetic, chemical and mechanical behavior is found to vary from that of their macrosized counterparts, opening new opportunities for applications.

Here, we will focus our attention on magnetic materials and the effects coming along with size reduction starring superparamagnetism [85,86]. Within these effects stand out the decrease of the Curie (Néel) temperature [87] or the enhancement of the magnetic anisotropy. Surface effects including magnetic disorder, spin canting or frustration, usually leads to a decrease (increase) of the net magnetic moment of ferro or ferrimagnetic (antiferromagnetic) particles [88]. These contributions become more noticeable as size decreases since the percentage and influence of atoms lying at the surface of the crystal increases.

Magnetic nanoparticles are of especial interest in different fields such as (bio)chemistry, medicine, data storage and environmental sciences. Much effort has been devoted to the synthesis of biocompatible magnetic particles able of moving through living organisms and being remotely manipulated by means of an external magnetic field. These are the basis of future medical treatments like drug delivery, hyperthermia or medical diagnostics like magnetic resonance image (MRI) [89]. Magnetic anisotropy is another well-known characteristic of magnetic materials that stabilizes the magnetic moment against thermal fluctuations. This property, enhanced in nanosized crystals, would enable the recording and storing of information in high density storage media [90]. In this regard, the combination of ferro and antiferromagnetic nanocomposites could eventually lead to an increase of the anisotropy thereby assisting the magnetization stability [91].

The magnetic response of nanoparticles is usually analyzed within the framework of superparamagnetism. Since their size is too small to sustain more than one magnetic domain, these particles are characterized by a net magnetic moment locked along the easy axis of the magnetization. Hence, particles are treated as classical paramagnetic compounds with ”giant” spins. The latter is governed by the well-known Langevin law, describing the magnetization dependence with the applied magnetic field, and the Curie law, describing the response of the magnetic susceptibility as a function of temperature.

Although being a good approximation to the problem, fundamental differences between paramagnetic substances and real systems of nanoparticles can lead to an erroneous interpretation of the results. To begin with, whatever the used synthesis method might be, practical nanoparticles are not morphologically equal between them. That leads to a distribution of sizes ($f(D)$), magnetic moments ($f(\mu)$) activation energy barriers ($f(U)$) or magnetic relaxation times ($f(\tau)$) within the sample. It is found that the magnetic susceptibility response is very sensitive to the width of $f(\mu)$ whereas magnetization isotherms are well accounted for by the mean value of the distribution. Under these circumstances, a combined analysis including the effects of the distribution of magnetic moments would be desirable.

Although the influence of $f(\mu)$ in the magnetization response vs. applied field has been taken into consideration in several works [92–96], the same does not happen with the magnetic susceptibility (except for [95]). The first purpose of this chapter is to develop a systematized methodology to perform such combined analysis in a straightforward way. In addition, we will introduce some algebra that will enable us to obtain information about $f(U)$ and $f(\tau)$ from the non-equilibrium susceptibility data.

On the other hand, the problems mentioned above are even more important when dealing with nanoparticles made of antiferromagnetic materials. In this case, the influence of anisotropy must be cautiously taken into account and the classical Langevin function may not provide a good description of the magnetic response. In addition, the magnetic moment of antiferromagnetic nanoparticles has been found to depend on temperature on an unexpected way [97–101] that has been ascribed to a thermoinduced magnetization [102]. These questions will be pointed out in more detail in this chapter, providing the main theoretical notions that we will use in the following chapters, when we study a real sample of antiferromagnetic particles.

3.2 Superparamagnetism and the monodomain state

Magnetic atoms owe their properties to the spin and orbital momenta of the unpaired electrons present in their structure. Such atoms can usually be treated as permanent magnetic moments ($\mu_{\mathrm{at}} = g\mu_{\mathrm{B}}S$), the strength of which depends not only on the spin and orbital electronic momenta, but also on the electric field created by neighbouring atoms when they are combined to form a crystal. In some materials, interactions between magnetic atoms (exchange interactions) can favor different momenta alignment configurations giving rise to magnetic order.

In ferromagnetic materials, the formation of magnetic domains is energetically preferred, in such a way that the total magnetization of the material is reduced and the energy cost of magnetic flux lines coming out of the surface is saved (see Fig. 3.1a). The formation of magnetic domains has however other energy expenses; boundaries between domains must be created. The latter are the so-called domain walls where the orientation of μ is progressively tilted (see Fig. 3.1b). Exchange interactions will favor large domain walls to avoid unalignment, on the contrary, small domain walls contribute to maintain the crystallinity and benefit the anisotropy energy balance. In this way, the total length of the domain wall (d_w) results from the competition between the exchange interactions constant J and the anisotropy constant K

$$d_w \propto \sqrt{J/K}$$

When the size of the crystal is reduced below d_w, the formation of domains has no longer energetic advantages and the particle consist of just one domain.

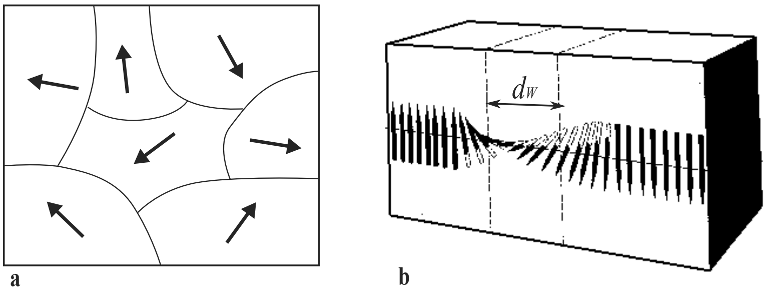

Figure 3.1: a) Drawing of a magnetic material consisting of domains. b) These domains are separated by domain walls the width of which depends on the exchange and anisotropy energies.

Monodomain particles respond as ”giant” spins and receive for this reason the name of ”superparamagnets”.

3.3 Magnetic order: the Curie temperature

Spontaneous magnetization of ferro- and ferrimagnetic nanoparticles occurs as long as the magnetic order within the particle can be sustained. As temperature increases, thermal energy is favored in the competition against exchange energy and the magnetic order is progressively destroyed. Above the Curie temperature (T_C) the response of the material is paramagnetic and the spontaneous magnetization falls to zero. The bulk saturation magnetization (M_{sb}) dependence with temperature is usually described by a power law

$$M_{sb} = M_{sb}(0)\left[1 - \left(\frac{T}{T_\mathrm{C}}\right)^{\lambda}\right] \tag{3.1}$$

where $M_{sb}(0)$ is the saturation magnetization at temperature $T = 0$ and the exponent λ depends on the material but it is typically of the order of 3/2.

3.4 Magnetic anisotropy

When the magnetic moment of an ion composing a solid is free to rotate, the material is said to be isotropic in terms of magnetic response. This is not, however, the most common situation in magnetic crystals in which there is usually one (or more) preferred directions along the space. The latter is defined as the easy axis of the magnetization and we will denote it as the z axis.

There are at least three sources of anisotropy in nanoparticles. (a) The magnetocrystalline anisotropy arises from the electrostatic interaction between the electron and the crystalline field, plus the spin-orbit coupling. Ubiquitous for any crystal-size, this effect depends only on the crystal structure. (b) In the case of non-spherical particles there will also be a term due to the shape anisotropy. The latter arises from the demagnetizing factor which is not equal for every direction of the space giving rise to a preferred axis. (c) The last contribution is the surface anisotropy. This is of great importance in nanoparticles and it is responsible of some of their characteristics. Surface anisotropy has the same origin as the magnetocrystalline anisotropy but its influence is usually stronger since the particle surface exhibits poor crystallinity. The lack of neighbouring atoms, spin canting and other effects strongly affect the magnetic anisotropy of small clusters. As the particle size decreases, the surface to volume ratio increases, leading to an enhancement of such "surface effects".

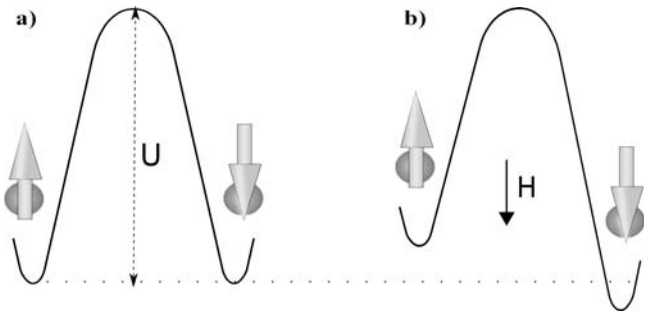

Figure 3.2: a: Schematic drawing of the energy barrier created by anisotropy characterized by the activation energy (U). b: In the presence of an applied magnetic field, the degeneracy is broken and a metastable state appears.

For a particle with an easy magnetization axis z, there will be two preferred directions of the magnetic moment. This can be schematized by a classical double well potential energy landscape. The magnetic moment reversal implies overcoming an energy barrier or activation energy U (see Fig. 3.2a). If a magnetic field is applied, one of the two directions will be favored (see Fig. 3.2b). The anisotropy constant K is defined as

$$K \equiv U/V \tag{3.2}$$

3.5 Equilibrium magnetic response

The magnetic response of a compound with ρ_n magnetic atoms (per unit of mass or volume) with spin S in the presence of a magnetic field H and a thermal bath T is well described by the Brillouin function

$$M = \rho_n g\mu_{\mathrm{B}} S \mathscr{B}_{\mathrm{S}}\left(\frac{g\mu_{\mathrm{B}} SH}{k_{\mathrm{B}}T}\right) \tag{3.3}$$

Where

$$\mathscr{B}_{\mathrm{S}}(x) = \frac{2S+1}{2S}\coth\left(\frac{(2S+1)x}{2S}\right) - \frac{1}{2S}\coth\left(\frac{x}{2S}\right)$$

In the case of superparamagnets, the net magnetic moment per particle (μ) is usually large, and the Brillouin function can be replaced by its classical limit, the Langevin function

$$M = n\mu\mathscr{L}\left(\frac{\mu H}{k_{\mathrm{B}}T}\right), \qquad \text{where } \mathscr{L}(x) = \coth(x) - \frac{1}{x} \tag{3.4}$$

n being in this case the density of magnetic particles. The product $M_{sb} = n\mu$ is the saturation magnetization, that is the magnetization of the particle for $\mu H \gg k_{\mathrm{B}}T$.

The latter expressions are valid if we consider a sample containing magnetic nanoparticles with their anisotropy axis randomly distributed and only if the thermal energy is much larger than the anisotropy energy $U \ll k_{\mathrm{B}}T$ [103]. There is no analytical expression in the case of large anisotropy and a numerical computation of M is required.

The Curie law accounts for the equilibrium magnetic susceptibility of a compound of free paramagnetic atoms

$$\chi_T = \frac{n\mu^2}{3k_{\mathrm{B}}T} \tag{3.5}$$

This expression also describes the magnetic response of a sample containing superparamagnetic clusters with their anisotropy easy axis distributed at random and providing that $U \ll k_{\mathrm{B}}T$ [103].

3.6 Magnetic relaxation

The expressions given above are valid under the assumption that particles attain thermal equilibrium with the thermal bath. The process that leads to the equilibrium response is called magnetic relaxation and it is related to the rate at which the magnetic moment is able to overcome the energy barrier created by anisotropy (U). At high temperatures, the relaxation will be fast since thermal fluctuations assist the magnetic moment to visit all the possible energy configurations. On the other hand, a large anisotropy barrier, as compared with $k_{\mathrm{B}}T$, will frustrate any attempt of attain thermal equilibrium. This situation is well described by the Ahrrenius law

$$\tau = \tau_0 e^{U/k_{\mathrm{B}}T} \tag{3.6}$$

where τ is the relaxation time, that is, the time that the magnetic moment needs to change its state from one energy minima to another and τ_0 is a characteristic attempt time usually around 10^{-13}–10^{-9} s.

For temperatures above a certain threshold called blocking temperature (T_B), magnetic response will be that of equilibrium, whereas, at $T < T_B$, the magnetic response will show non-equilibrium typical features like hysteresis or blocking of the magnetic susceptibility. T_B strongly depends on the experimental time, therefore, it can be obtained from dynamic magnetic measurements like the ac-susceptibility response to an applied oscillating magnetic field. Let us suppose that the external field makes an angle Ψ with the z axis, we can then divide it into two components: the longitudinal component ($H_{\parallel}$), parallel to the easy axis, and the transversal component ($H_{\perp}$). The effect of $H_{\parallel}$ is that depicted in Fig. 3.2b, that is, it favors the spin inversion within a characteristic time ($\tau_{\parallel} = \tau$) given by Arrhenius law. On the other hand, $H_{\perp}$ does not lead to a break down of minima degeneracy but it modifies slightly the moment orientation. That means that the energy of the particle is increased within the well and the response just implies the reorganization of the levels populations. The latter is usually so fast ($\tau_{\perp}$ is of the order of the prefactor τ_0 of Eq. 3.6) that can hardly ever been measured experimentally. The magnetic susceptibility can be also divided into two components, one corresponding to the response to $H_{\parallel}$, and one corresponding to $H_{\perp}$

$$\chi(\omega, T) \;=\; \frac{\chi_{\parallel}^{eq}(T)}{1 + i\omega\tau_{\parallel}} \cos^2 \Psi + \frac{\chi_{\perp}^{eq}(T)}{1 + i\omega\tau_{\perp}} \sin^2 \Psi \tag{3.7}$$

where $\chi_{\parallel}^{eq}(T)$ and $\chi_{\perp}^{eq}(T)$ are the equilibrium responses along and perpendicular to the applied magnetic field. If we consider a system of nanoparticles with their easy axis distributed at random, we can substitute $\cos^2 \Psi$ and $\sin^2 \Psi$ with their spatial averages $\langle \cos^2 \Psi \rangle = 1/3$ and $\langle \sin^2 \Psi \rangle = 2/3$.

The response to an oscillatory magnetic field $H_{ac} = H_0 \cos(\omega t)$ has two components: the component oscillating in-phase with the field, defined as the real part of the susceptibility (χ'), and the out-of-phase or imaginary part (χ"). Since usually $\tau_{\perp} \ll 1/\omega$, we can assume that the perpendicular susceptibility is always that of equilibrium. Then, rewriting Eq. 3.7 in terms of the real and imaginary part one obtains the Debye equations

$$\chi\text{'}(\omega, T) = \frac{1}{3}\frac{\chi_{\|}^{eq}(T)}{1+\omega^2\tau^2} + \frac{2}{3}\chi_{\perp}^{eq}(T) \tag{3.8}$$

$$\chi\text{"}(\omega, T) = \frac{1}{3}\frac{\chi_{\|}^{eq}(T)\omega\tau}{1+\omega^2\tau^2} \tag{3.9}$$

where $\tau = \tau_{\|}$. In the case of small anisotropy energy compared to the thermal energy ($U \ll k_{\mathrm{B}}T$) $\chi_{\|}^{eq}(T)$ is that given by Eq. 3.5 and $\chi_{\perp}^{eq}(T) = M_{\mathrm{sb}}^2/K$. The real part follows therefore Curie's law down to a temperature close to T_B where it falls down to a value given by $\chi_{\perp}$. The imaginary part remains very small but shows a peak at the blocking temperature. In this way, the anisotropy constant K can be obtained by fitting the values of T_B at different frequencies ω using the relation

$$\ln(1/\omega) = \ln(\tau_0) + \frac{KV}{k_{\mathrm{B}}T_B} \tag{3.10}$$

3.7 Size/moment distribution effect

The magnetic response of a real nanoparticle system differs from the theoretical predictions due to several reasons. In our special case, one of the main issues to take into account is the particles size and moment distribution. For instance, the magnetization saturation strongly depends on the particle moment ($M_{\mathrm{s}} = n\mu$). Larger moments saturate at lower magnetic fields giving rise to a distorted Langevin function.

In ferromagnetic (ferrimagnetic) clusters, a simple relation between particle size and magnetic moment (magnetic moment per unit formula) is usually established

$$\mu = \rho_n V g \mu_{\mathrm{B}} S \tag{3.11}$$

where ρ_n is the volume density of magnetic atoms (unit formulas) in the particle and V is the volume. This relation turns to be too naive when dealing with real nanoparticles. Surface effects, degradation of the crystallinity or spin canting, can lead to a decrease of the real magnetic moment compared to that predicted by Eq. 3.11. Therefore, it is paramount to include the effects of distribution of magnetic moments in the data analysis.

3.7.1 Equilibrium response considering the distribution function of magnetic moments

Let us first introduce the most commonly used distribution functions in nanoparticle analysis. The normal or Gaussian distribution is used to describe a wide

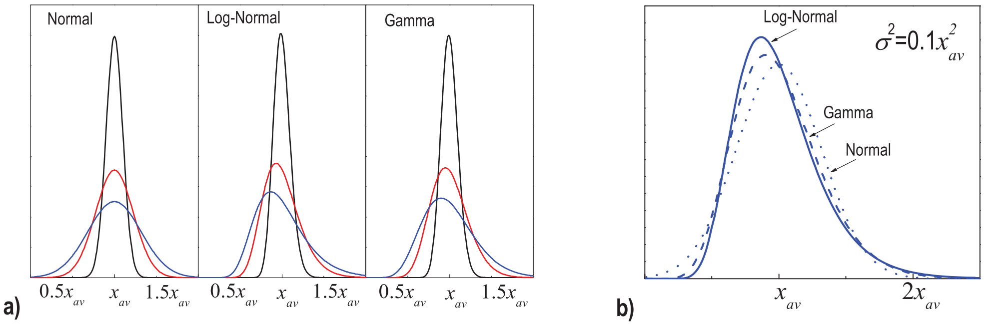

Figure 3.3: Plot of three different distribution functions that can be used to fit the experimental size or moment distributions of nanoparticles. a) Comparison of the Gaussian, Log-Normal and Gamma functions for three values of the variance, $\sigma^2 = 0.01x_{av}^2$ (black line), $\sigma^2 = 0.05x_{av}^2$ (red line) and $\sigma^2 = 0.1x_{av}^2$ (blue line). b) Differences between the Log-Normal and Gamma functions are visible for high values of σ^2.

variety of natural systems in which the data tend to accumulate around the mean value leading to the well-known bell shape (see Fig. 3.3a). It has the standard form

$$f_{\mathrm{N}}(x) = \frac{n}{\sqrt{2\pi}\sigma} \exp\left(\frac{-(x - x_{av})^2}{2\sigma^2}\right) \tag{3.12}$$

Where n is the number of particles counted in the distribution. x_{av} is the mean or average value which is also equal to the median value x_p, and σ^2 is the variance.

The log-normal and the gamma distribution are quite similar but present slight differences for large values of the variance as we can see in Fig. 3.3b. The log-normal function is described by

$$f_{\mathrm{LN}}(x) = \frac{n}{\sqrt{2\pi}Sx} \exp\left(\frac{-\ln\left(x/x_p\right)^2}{2S^2}\right) \tag{3.13}$$

Where x_p is the median value. The mean value is $x_{av} = x_p e^{S^2/2}$, and the variance equals $\sigma^2 = x_{av}^2(e^{S^2} - 1)$. The gamma function is described by

$$f_{\Gamma}(x) = \frac{n}{\theta}\left(\frac{x}{\theta}\right)^{\beta} \frac{e^{x/\theta}}{\Gamma(\beta + 1)} \tag{3.14}$$

In this case, $x_{av} = \theta(\beta + 1)$, $x_p = \theta\beta$ and $\sigma^2 = x_{av}^2(\beta + 1)$.

Let us now determine the influence of a given particle moment distribution on the magnetic response. For this purpose we need to average the magnetization or the susceptibility over the function given by Eq. 3.4 or Eq. 3.5. Defining $f(\mu)$ as the distribution of number of particles having a magnetic moment equal to μ, the magnetization will be given by

$$M = \int_0^\infty f(\mu)\mu\mathscr{L}(\frac{\mu H}{k_\mathrm{B}T})d\mu \tag{3.15}$$

where $f(\mu)$ refers to that given by Eq. 3.12, 3.13 or Eq. 3.14. This expression can not be solved analytically and numerical fits must be performed. For the equilibrium magnetic susceptibility one obtains

$$\chi_T = \int_0^\infty \big(f(\mu)\mu^2/3k_\mathrm{B}T\big)d\mu$$

In the case of considering the Normal distribution $f(\mu) = f_\mathrm{N}(\mu)$, the latter expression can be solved by extending the integration limits as

$$\int_0^\infty \big(f_\mathrm{N}(\mu)\mu^2/3k_\mathrm{B}T\big)d\mu \approx \int_{-\infty}^\infty \big(f_\mathrm{N}(\mu)\mu^2/3k_\mathrm{B}T\big)d\mu$$

this approximation holds true in most of the cases since, for real nanoparticles distributions, $f_\mathrm{N}(\mu \leq 0) \leq f_\mathrm{N}(0)/20$ typically. That means that the density for negative values of x, which has no physical meaning, can be neglected. By changing the variable $x = \mu - \mu_{av}$ one obtains

$$\chi_T = \tfrac{n/\sqrt{2\pi}\sigma}{3k_\mathrm{B}T}\left(\int_{-\infty}^\infty x^2 e^{-x^2/2\sigma^2}dx + \mu_{av}\int_{-\infty}^\infty xe^{-x^2/2\sigma^2}dx + \mu_{av}^2\int_{-\infty}^\infty e^{-x^2/2\sigma^2}dx\right)$$

Where the second term cancels since the function xe^{-a} is antisymmetric. The latter expression can be rewritten as a function of the gaussian integral $I_n(a)$ defined as

$$I_n(a) = \int_{-\infty}^\infty x^n e^{-ax^2}dx = \sqrt{\pi}\frac{\partial^{n/2}}{\partial a^{n/2}}a^{-1/2}$$

By doing so, after some straightforward algebra one obtains

$$\chi_T = \frac{n}{3k_\mathrm{B}T\sqrt{2\pi}\sigma}\big(I_2(1/2\sigma^2) + \mu_{av}^2 I_0(1/2\sigma^2)\big) = \frac{n}{3k_\mathrm{B}T}\big(\sigma^2 + \mu_{av}^2\big)$$

On the other hand, the log-normal and gamma distribution functions equal zero at $\mu = 0$ and the resulting integral can be solved without any approximation. For the case of the log-normal distribution one obtains

$$\chi_T = \frac{n}{3k_\mathrm{B}T\sqrt{2\pi}S}\int_0^\infty \frac{1}{\mu}\exp\left(\frac{-\ln\big(\mu/\mu_p\big)^2}{2S^2}\right)d\mu = \frac{n\mu_{av}^2 e^{S^2}}{3k_\mathrm{B}T}$$

And finally, for the case of the gamma distribution the susceptibility equals

$$\chi_T = \frac{n}{3k_\mathrm{B}T\theta^{\beta+1}\Gamma(\beta+1)}\int_0^\infty \mu^\beta e^{x/\theta}d\mu = \frac{n\mu_{av}^2(\beta+2)}{3k_\mathrm{B}T}$$

The latter integrals can be founded in any integration textbook.

The susceptibility can therefore be expressed in a more general way as

$$\chi_T = \frac{n\mu_{av}^2\delta}{3k_\mathrm{B}T} \tag{3.16}$$

where the value of δ depends on the selected distribution. In the case of the normal function $\delta_\mathrm{N} = \sigma^2/\mu_{av}^2 + 1$, for the log-normal function $\delta_\mathrm{LN} = \exp(S^2)$ whereas $\delta_\Gamma = (\beta+2)$ for the gamma distribution.

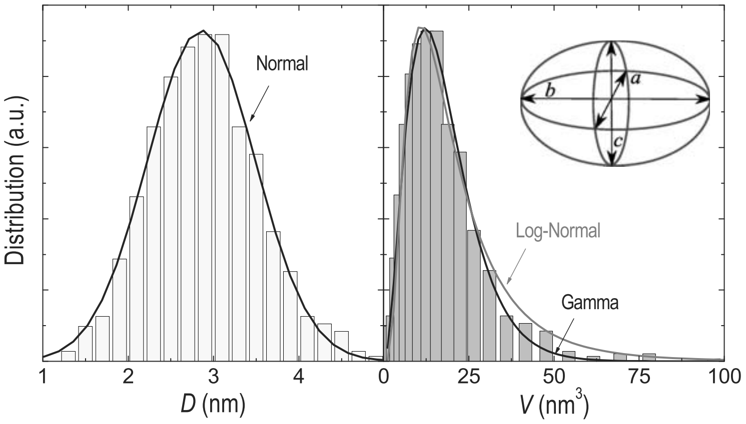

Figure 3.4: Typical example of the diameter (D) and effective volume (V) distribution of a real sample of maghemite nanoparticles. V has been obtained from TEM images by approximating each cluster to an ellipsoid with axis a, b and $c = a$ (see inset). D is calculated as the effective diameter of an sphere of volume V. The D experimental data is well described by a Normal distribution function whereas V, and subsequently the moment distribution, present a quite asymmetrical shape that can be better accounted for a Log-Normal or Gamma distribution functions.

Susceptibility measurements close to the Curie temperature can however provide erroneous information about the moment distribution. As temperature approaches T_C, the magnetic moment per particle is reduced due to thermal fluctuations that destroy magnetic order. It is therefore convenient to take these effects into account in order to correctly interpret the data, especially at high temperatures. Eq. 3.1 accounts for the saturation magnetization reduction with temperature, the latter can be calculated by doing

$$M_{sb} = \int_0^\infty f(\mu)\mu d\mu$$

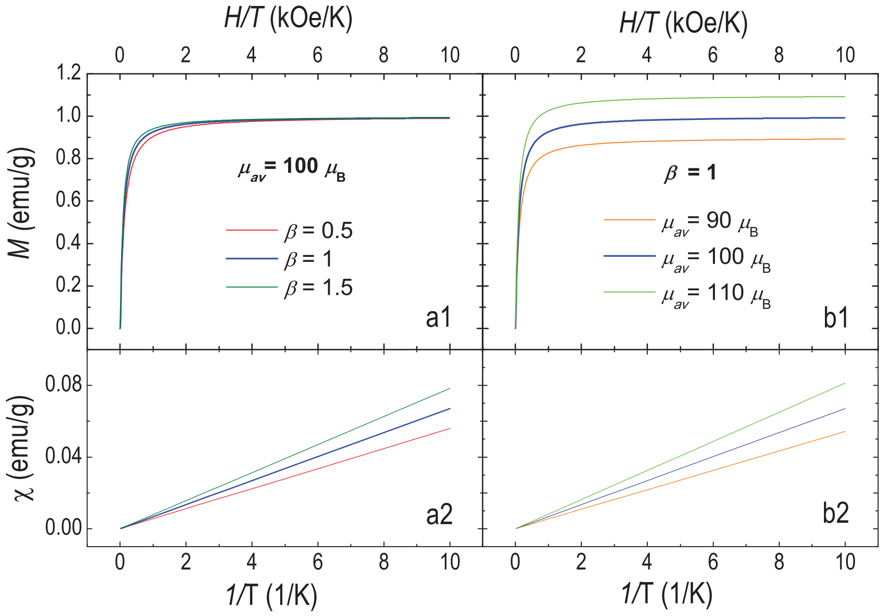

Figure 3.5: Numerical calculations of M and χ averaging over a Gamma distribution function considering a sample of 10^{18} particles per gram. a1) and 2) show the influence of the β parameter on the magnetic response whereas b1) and 2) show the curves for different values of μ_m

which can be analytically integrated giving

$$M_{sb} = n\mu_{av} \tag{3.17}$$

independent of the distribution function used in the integration. Therefore, the dependence of M_{sb} with temperature can be taken into account by inserting Eq. 3.17 and Eq. 3.16 in Eq. 3.1, giving

$$\chi T = M_{sb}(0)^2 \frac{\delta}{3k_{\mathrm{B}}} \left[1 - \left(\frac{T}{T_{\mathrm{C}}}\right)^{\beta}\right]^2 \tag{3.18}$$

The latter expression will be valid for temperatures well above the blocking temperature, that is, temperatures where susceptibility response is that of equilibrium and therefore follows Curie law.

Usually, a Normal function does not account well for the particle moment distribution determined experimentally. Although the typical distributions of particle diameter (D) is rather bell-shaped, the volume distribution (V) and therefore, the moment distribution, is no longer symmetrical. Since the moment distribution is directly related to the volume distribution, the Log-Normal or the Gamma account better for the experimental distribution shape. In these cases, the mean and the median value of the moment distribution are not the same, leading to a tail that decreases slower for high values of the moment and better reproduce the experimental data as we can see in the example of Fig. 3.4.

To summarize, from a combined analysis of the magnetization and susceptibility data it is possible to determine experimentally the magnetic moment distribution of a given sample of magnetic nanoparticles. From numerical simulations it can be shown that the magnetization is not very sensitive to the distribution variance (see Fig. 3.5a1). In fact, the saturation magnetization is independent of the function used and the values obtained from a simple fit to a Langevin law are quite similar to the mean value of the magnetic moment (see Fig. 3.5b1). On the other hand, large magnetic moments strongly affect the experimental susceptibility, and the latter is therefore, very sensitive to both variables: the mean value μ_m and the variance σ^2 (see Fig. 3.5a2 and b2) [95].

3.7.2 Ac susceptibility analysis

The magnetic anisotropy of a nanoparticle also depends on its size. Therefore, we should also consider a distribution of activation energies ($f(U)$) in the analysis of ac-susceptibility data. The expressions of real and imaginary susceptibility can be calculated by summing up the contribution of every particle to the expressions given by Eq. 3.8 and 3.9

$$\chi'(\omega, T) = \frac{1}{3}\int_0^\infty \frac{\chi_\parallel^{eq}(T,U)}{1+\omega^2\tau^2} f(U)dU + \frac{2}{3}\int_0^\infty \chi_\perp^{eq}(T,U) f(U)dU \quad (3.19)$$

$$\chi''(\omega, T) = \frac{1}{3}\int_0^\infty \frac{\chi_\parallel^{eq}(T,U)\omega\tau}{1+\omega^2\tau^2} f(U)dU \quad (3.20)$$

Larger particle size entail larger anisotropy energy, therefore larger particles will become "blocked" at higher temperatures. In this way, the dependence of χ" with temperature will reproduce the activation energy distribution of the sample. Let us define U_b as the activation energy of those particles the relaxation time of which equals the experimental time for a given temperature.

$$U_b = k_\mathrm{B} T \ln\left(\frac{1}{\omega\tau_0}\right) \quad (3.21)$$

As the relaxation time depends exponentially on U, we can assume that, at a given temperature, particles with $U > U_b$ will be completely blocked whereas those with $U < U_b$ are in equilibrium. χ" will be therefore roughly zero for those particles having $U < U_b$ and we can approximate

$$\chi''(\omega, T) = \frac{1}{3}\int_{U_b}^\infty \frac{\chi_\parallel^{eq}(T,U)\omega\tau}{1+\omega^2\tau^2} f(U)dU \quad (3.22)$$

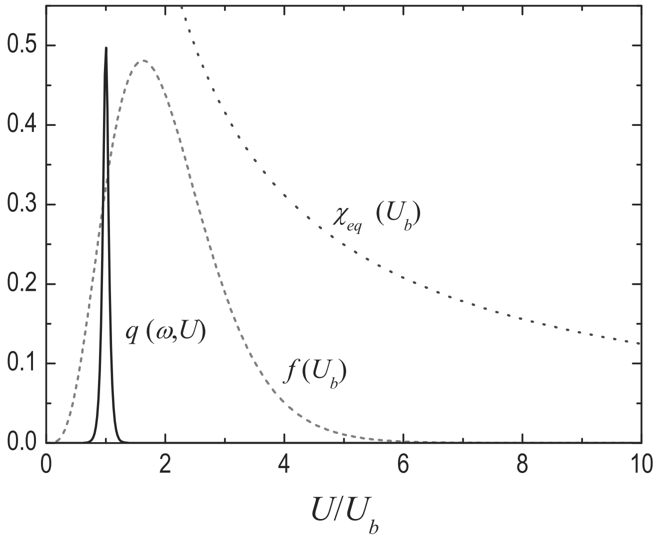

Figure 3.6: Function $q(\omega, U)$ determines the dependency of χ" with frequency. Arrhenius law relates the activation energy with the frequency making possible to plot $q(\omega, U)$ vs. the variable U/U_b that gives a maximum at $U = U_b$. The plot of $f(U_b)$ and $\chi_{eq}(U_b)$ is obtained considering real values of systems of nanoparticles and normalizing the resulting functions. In this case, a Gamma distribution function has been chosen with $U_{av} = 2U_b$ K and $\beta = 4$

The function defined by $q(\omega, U) = \omega\tau/(1 + \omega^2\tau^2)$ is plotted in Fig. 3.6 vs. U/U_b. Comparing it with a typical activation energy distribution function we can see that the latter is much broader. We can therefore take $\chi_{\|}^{eq}(T, U)f(U)$ out of the integral by evaluating it at $U = U_b$ and then solve the integral of $q(U, \omega)$. After some calculations one finds that [104, 105]

$$\chi\text{"}(\omega, T) \simeq \frac{\pi}{3} k_{\mathrm{B}} T \chi_{\|}^{eq}(T, U_b) f(U_B) \tag{3.23}$$

In this way, the activation energy distribution function can be easily obtained by plotting the χ" experimental data as a function of the scaling variable U_b and considering $f(U_b)$ that defined in Eq. 3.13 or Eq. 3.14.

3.7.3 Magnetic relaxation: distribution of τ

Debye equations describe the relaxation process of an ideal system consisting of identical particles. There are however different mechanisms that lead to the presence of distinct relaxation times for every particle, giving rise to a distribution of τ ($f(\tau)$). The most evident of these mechanism, is a distribution of sizes or magnetic moments, as we have discussed during this chapter. Another possibility would be to deal with a system in which every particle feels a different magnetic field caused for instance by a a distribution of dipolar magnetic fields within the sample. The effect of a distribution of relaxation times can be taken into account by considering the phenomenological Cole-Cole function. This expressions were initially introduced to describe dielectric measurements [106] and can be written as

$$\begin{aligned}
\chi'(\omega) &= \chi_s + \frac{(\chi_T - \chi_s)\left[1+(\omega\tau)^{1-\beta}\cos\left(\frac{\pi}{2(1-\beta)}\right)\right]}{\left[1+(\omega\tau)^{1-\beta}\cos\left(\frac{\pi}{2(1-\beta)}\right)\right]^2+\left[(\omega\tau)^{1-\beta}\sin\left(\frac{\pi}{2(1-\beta)}\right)\right]^2} && (3.24)\\
\chi''(\omega) &= \frac{(\chi_T - \chi_s)\left[(\omega\tau)^{1-\beta}\sin\left(\frac{\pi}{2(1-\beta)}\right)\right]}{\left[1+(\omega\tau)^{1-\beta}\cos\left(\frac{\pi}{2(1-\beta)}\right)\right]^2+\left[(\omega\tau)^{1-\beta}\sin^2\left(\frac{\pi}{2(1-\beta)}\right)\right]^2} && (3.25)
\end{aligned}$$

Where $0 \leq \beta \leq 1$ is the Cole-Cole parameter that characterizes the width of the distribution of relaxation times. Equations 3.24 and 3.25 provide a good description of the magnetic relaxation for small values of β, i.e. when dealing with narrow distributions of relaxation times. In the limit $\beta = 0$, the Cole-Cole equations equal the Debye approach.

The distribution function of τ can be, however, rather complex (e.g. spin glasses). In those cases it is still possible to define a "mean" relaxation time $\bar{\tau}$ independent of the distribution function. In a general case, the quotient χ''/χ' can be written as [107]

$$\frac{\chi''(\omega)}{\chi'(\omega)} = \frac{\int_0^\infty \frac{f(\tau)\omega\tau}{1+\omega^2\tau^2}d\tau}{\int_0^\infty \frac{f(\tau)}{1+\omega^2\tau^2}d\tau}$$

The latter is essentially the mean value of $f(\tau)$ multiplied by the frequency ω and weighted by the "cut off" function $(1+\omega^2\tau^2)^{-1}$ [107]. Under the condition $\omega\tau \ll 1$, the quotient $\chi''/\chi'\omega$ will no longer depend on the frequency giving [107]

$$\frac{\chi''(\omega)}{\chi'(\omega)}\frac{1}{\omega} = \bar{\tau} \qquad (3.26)$$

3.8 Antiferromagnetic nanoparticles

Whereas the magnetic properties of ferri- and ferromagnetic (FM) nanoscopic crystals are quite well understood, the magnetic state in an antiferromagnetic (AFM) material is much more intriguing. For instance, the magnetic ground state of such a crystal at $T = 0$ is usually described as a configuration with two parallel sublattices of atoms (e.g. A and B), each of them pointing along opposite directions (see Fig. 3.7). This state is not, however, a stationary state of the Hamiltonian describing the interaction.

The situation becomes even more complicated when reducing the size of these crystals to the nanometric scale. It has been found that the magnetization of such particles is often larger than the bulk value [108–113]. Louis Néel proposed in 1961 [114–116] that a non zero magnetic moment (μ_{unc}) should arise in AFM nanoparticles due to uncompensated spins at the surface or in the interior. However, the magnetic response, and, specially the temperature dependence of μ_{unc}, has been a puzzle for a long time. Numerous authors reported experiments in which μ_{unc} was found to increase with temperature within a certain temperature range where it was expected to decrease [97–100]. Besides, it has been theoretically predicted that AFM nanoparticles are more likely to exhibit collective quantum behavior such as macroscopic quantum tunneling of the Néel vector than FM particles [117]. These questions are briefly reviewed in this section.

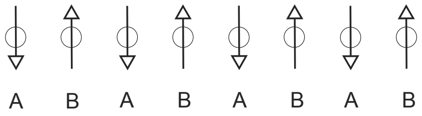

Figure 3.7: Classical representation of the ground state in antiferromagnetic chains

3.8.1 The antiferromagnetic state

Above the Néel temperature (T_{N}), the magnetic response of the material is paramagnetic. Thermal fluctuations are, under these circumstances, stronger than the exchange interaction that sustain the magnetic order through the crystal. A simple expression for T_{N} can be obtained from the molecular field theory relating the latter to the exchange constant J, the atomic spin S and the number of nearest neighbours Z [118].

$$T_{\mathrm{N}} = \frac{2S(S+1)JZ}{3k_{\mathrm{B}}} \tag{3.27}$$

In the paramagnetic range the magnetic susceptibility follows Curie-Weiss law (see Fig. 3.8 (a)) given by

$$\chi(T > T_\mathrm{N}) = \frac{N_\mathrm{A} n_\mathrm{at} \mu_\mathrm{at}^2}{3k_\mathrm{B}(T - \theta)} \tag{3.28}$$

Where N_A is the Avogadro number, μ_at is the magnetic moment per ion, n_at is the number of magnetic atoms per particle or unit formula and θ is a characteristic temperature that often differs from the Néel temperature due to interactions within the sublattice (non-nearest neighbours interactions [119]). $\theta > 0$ for the case in which ferromagnetic interactions are predominant whereas $\theta < 0$ when antiparallel alignment is preferred.

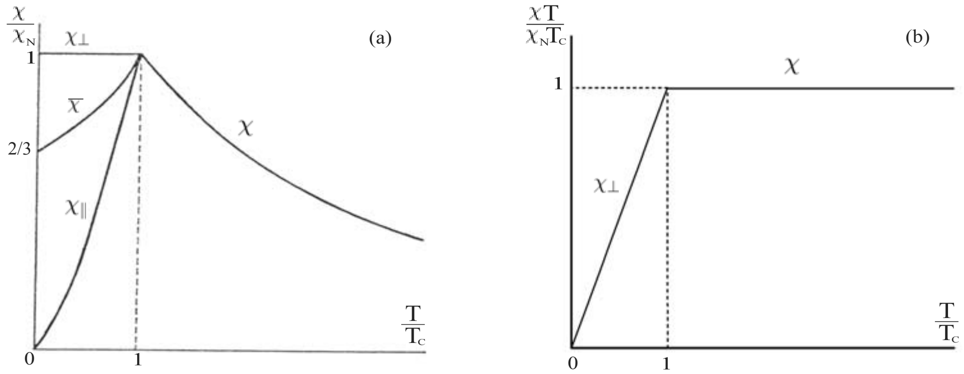

Figure 3.8: Magnetic response of an antiferromagnetic material vs. temperature obtained from the molecular-field model [118]. (a) Magnetic susceptibility follows Curie-Weiss law above the Néel temperature and the perpendicular component remains constant below the transition. When plotting χ_AF multiplied by temperature (b) one obtains a temperature-independent term above T_N and a term going to zero below T_N as temperature decreases.

Below T_N, the magnetic susceptibility has two direction-dependent components with respect to the easy magnetization axis. The parallel susceptibility ($\chi_\parallel$), which tends to zero as temperature decreases and the perpendicular component ($\chi_\perp$) wich does not depend on temperature (see Fig. 3.8 (a)). The latter also receives the name of antiferromagnetic susceptibility (χ_AF) and can be approximated from the mean field theory formulae as

$$\chi_\mathrm{AF} = M_\mathrm{s}/H_\mathrm{E} \tag{3.29}$$

Where M_s is the sublattice magnetization and H_E is defined as an effective exchange field consequence of the exchange interactions between the magnetic atoms. The influence of anisotropy, on the other hand, can be included as an effective anisotropy field H_A that depends on the anisotropy constant K.

These quantities are given by

$$\begin{aligned} H_E &= \frac{2JZS}{g\mu_\mathrm{B}} = \frac{3k_\mathrm{B}T_\mathrm{N}}{g(S+1)\mu_\mathrm{B}} && (3.30) \\ H_A &= K/M_s && (3.31) \end{aligned}$$

When a magnetic field is applied along the preferred axis, there is a sublattice (A) pointing in the direction of the field but the other one (B) points in the opposite direction. The susceptibility of the B lattice will increase linearly with the field. For sufficiently large applied field, there will be a critical value (H_sf) at which the spontaneous magnetization of both sublattices will "flop" to the transversal direction. This is said to be the spin-flop transition in antiferromagnets and H_sf only depends on the anisotropy and exchange field through

$$H_\mathrm{sf} = \sqrt{2H_\mathrm{A}H_\mathrm{E}} \tag{3.32}$$

3.8.2 AFM nanoparticles: the uncompensated magnetic moment

As L. Néel pointed out in 1961, in AFM nanoparticles there may be a difference in the total number of spins in the two sublattices due to the random occupancy of the lattice sites. This effect leads to the apparition of an uncompensated magnetic moment μ_unc. If we consider a random occupancy of all the lattice sites, the number of uncompensated spins will be of the order of $N^{1/2}$. Therefore, $\mu_\mathrm{unc} = N^{1/2}\mu_\mathrm{at}$, where μ_at is the magnetic moment per atom. If we suppose the core of the particles to be defect-free, the number of uncompensated spins will be of the order of $N^{1/3}$ and thus, $\mu_\mathrm{unc} = N^{1/3}\mu_\mathrm{at}$ [114].

In many studies of AFM nanoparticles, the analysis of the magnetization data was based on a modified Langevin function [97, 99, 100]. In this model, particles are treated as if they were FM, but replacing the magnetic moment μ in Eq. 3.4 with μ_unc, and adding a linear term that account for the effect of the antiferromagnetic susceptibility χ_AF.

$$M = n\mu_\mathrm{unc}\mathscr{L}\left(\frac{\mu_\mathrm{unc}H}{k_\mathrm{B}T}\right) + \chi_\mathrm{AF}H \tag{3.33}$$

However, this kind of analysis can lead to erroneous estimations of μ_unc and its variation with temperature. The reason is that the anisotropy energy is usually larger than the Zeeman energy due to the smallness of μ_unc. Then, for relatively low fields, the sublattice moments and hence μ_unc, are not free to fluctuate randomly but only along the anisotropy axis. Therefore, the

Langevin function will no longer provide a good approximation of the magnetic response. Besides, in AFM particles, the distribution can differ from the volume distribution due to surface disorder and spin canting making the analysis even more difficult [120]

It is, however, possible to avoid these problems, by means of the initial magnetic susceptibility. It can be shown that the parallel susceptibility is independent of the anisotropy and the specific moment distribution used [121]. In a sample with the easy axis of anisotropy randomly distributed, the spatially averaged susceptibility will be equal to

$$\chi = \frac{1}{3}\chi_{\shortparallel} + \frac{2}{3}\chi_{\perp} \tag{3.34}$$

where $\chi_{\shortparallel}$ is the susceptibility along the applied magnetic field and $\chi_{\perp}$ is the perpendicular susceptibility. The latter will be equal to χ_{AF} neglecting the contribution to the perpendicular susceptibility from the uncompensated atoms. Then, the initial susceptibility in the limit $T \to 0$ can be written as

$$\chi = \frac{1}{3}\frac{n\mu_{\mathrm{unc}}^2}{k_{\mathrm{B}}T} + \frac{2}{3}\chi_{\mathrm{AF}} \tag{3.35}$$

3.8.3 Spin waves and the thermoinduced magnetic moment

Exchange interactions between magnetic atoms are often described by the Heisenberg-Dirac Hamiltonian, if we consider interactions only between nearest neighbours, the latter can be formulated as [118]

$$\mathscr{H} = -2J \sum_{n,m\in\{\mathrm{n.n.}\}} \mathbf{S}_n \cdot \mathbf{S}_m \tag{3.36}$$

For $J > 0$, configurations with all the spins pointing in the same direction are favored and FM order appears. For $J < 0$, anti-parallel order is energetically preferred and the configuration is AFM. However, the classical image of an antiferromagnetic chain of spins with $S = \frac{1}{2}$ described as [118]

$$\Psi_{\mathrm{AFM}} = \psi_1(\uparrow)\psi_2(\downarrow)\psi_3(\uparrow)...\psi_n(\downarrow)\psi_m(\uparrow)...\psi_N(\downarrow) \tag{3.37}$$

is not even a stationary state of the hamiltonian as it does not satisfy Schrödinger equation. To form stationary states, a lineal combination of 3.37 such as [118]

$$\Psi^{\pm}_{\mathrm{AFM}} = \frac{1}{\sqrt{2}}\big(\psi_1(\uparrow)\psi_2(\downarrow)\psi_3(\uparrow)...\psi_N(\downarrow) \pm \psi_1(\downarrow)\psi_2(\uparrow)\psi_3(\downarrow)...\psi_N(\uparrow)\big) \tag{3.38}$$

must be considered. In the case of an antiferromagnetic chain, Ψ^{-}_{AFM} will be the minimum energy state with energy $E_{\mathrm{AFM}} = -\frac{3|J|N}{4}$.

3.8.3.1 Excited states: spin waves

For the sake of simplicity, let us analyze fist the case of a ferromagnetic chain of atoms. At low temperatures, the thermodynamic magnetic properties of a system are determined by the low-lying excited states, i.e. the states close to the ground state. Bloch and Slater showed that these states can be described as waves of spin reversal (spin waves). The latter can be represented from a classical point of view as depicted in Fig. 3.9. In this illustration, each spin S precesses around the easy axis z with an amplitude such that the total magnetization will decrease by $g\mu_\mathrm{B}$ if the first mode is excited ($n_1 = 0$), $2g\mu_\mathrm{B}$ for the second mode ($n_1 = 1$) and so forth.

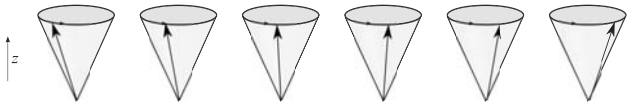

Figure 3.9: Spin-wave representation in a ferromagnetic ion chain

The dispersion relationship of such spin waves can be calculated under the condition $aq \ll 1$, where a is the distance between magnetic atoms and q is the wavevector. The result of this calculation gives [118]

$$E_q^{\mathrm{FM}} = 2JSa^2q^2 + g\mu_\mathrm{B}H_A = \hbar\omega_q \tag{3.39}$$

Here, the term $g\mu_\mathrm{B}H_A$ takes into account the effect of the anisotropy field. The total energy of the system will be given by

$$E = \sum_q \left((n_q + \frac{1}{2})\hbar\omega_q \right) \tag{3.40}$$

where the quantum number n_q takes integer values 0, 1, 2... and is the number of quanta or ”magnons” excited on each mode.

The situation becomes much more complicated in the case of antiferromagnetic materials. In order to form states that satisfy Schrödinger equation, combinations of spin waves must be created. On the one hand, linear combinations such as that described by 3.38 will be possible, but they will not contribute to the magnetic moment and they will not be considered in the following calculations. Another possibility to form a normal mode will be the combination of two spin waves with different values of n_q in each sublattice. This situation can be classically illustrated as depicted in Fig. 3.10. In this image, the spin of the two sublattices precess with unequal amplitudes around the anisotropy axis (z).

Therefore, in some excited states, the two sublattice magnetization directions will form different angles θ_A and θ_B with the easy axis z (see Fig. 3.11).

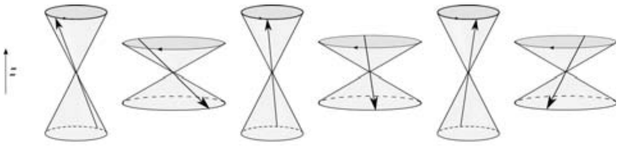

Figure 3.10: Spin-wave representation in an antiferromagnetic ion chain

The relation between the two angles depends on the anisotropy field and the exchange field. Taking into account that usually $H_A \ll H_E$ one finds that

$$\frac{\sin\theta_A}{\sin\theta_B} \simeq 1+\delta, \qquad \text{where } \ \delta = \pm\sqrt{2\frac{H_A}{H_E}} \tag{3.41}$$

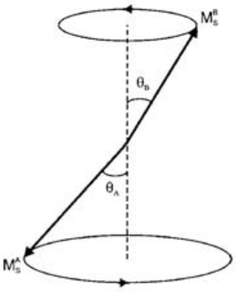

Figure 3.11: Uniform mode in an antiferromagnet. The magnetization vectors of the two sublattices M_s^{A} and M_s^{B}, precess with different precession angles, θ_{A} and θ_{B} around the anisotropy axis z.

The dispersion relation for such spin waves in an antiferromagnet can also be calculated and is given by

$$E_q^{\mathrm{AFM}} = g\mu_{\mathrm{B}}\left[(H_E+H_A)^2 - H_E^2\left(1-\frac{2q^2a^2}{Z}\right)\right]^{1/2} = \hbar\omega_q \tag{3.42}$$

The total energy of the crystal can also be obtained from Eq. 3.40.

The former calculations are valid for any cubic crystal, let us focus now on nanometric-sized particles. Considering for simplicity a nanoparticle with cubic shape, being d the side length, the allowed values of the wavevector will be given by

$$q = k\pi/d, \qquad k = 0,\, 1,\, 2,\, 3...$$

The energy gap between the mode with $q=0$ and the modes with $q \neq 0$ will increase as the size of the particle, namely d, decreases. For this reason, the modes with $q \neq 0$ will play a smaller role at low temperatures in nanoparticles.

In this case, considering just the modes with $q = 0$ and assuming that usually $H_A \ll H_E$, Eq. 3.42 can be reduced to

$$E_{q=0}^{\mathrm{AFM}} = g\mu_{\mathrm{B}}\sqrt{2H_E H_A} = \hbar\omega \tag{3.43}$$

Nevertheless, there are striking differences between spin waves in antiferromagnets and ferromagnets. If we compare expression 3.43 with Eq. 3.39, in the antiferromagnetic case, we find a contribution not only from anisotropy but also of exchange energy, even for $q \to 0$. The latter means that the formation of a spin wave implies a higher energy cost in AFM since neighbouring spins are no longer (anti)parallel.

3.8.3.2 Thermoinduced magnetic moment

S. Mørup *et al* [102] proposed recently that the different precession angles of the two sublattices will lead to an additional, temperature dependent, net magnetic moment (μ_{th}) in AFM nanoparticles. The absolute value of μ_{th} will be given by (see Fig. 3.11)

$$|\mu_{\mathrm{th}}| = M_s V |\cos\theta_{\mathrm{A}} - \cos\theta_{\mathrm{B}}|$$

The thermal average of μ_{th} will vanish if no external field is applied since precession states with magnetic moments up and down are degenerated. In the presence of an external field, the degeneracy is lifted, and a finite magnetization can be observed. S. Mørup *et al* obtained an expression for the thermoinduced susceptibility (χ_{th}) due to the thermoinduced magnetization using Boltzmann statistic. In this derivation, χ_{th} is found to increase linearly with temperature as

$$\chi_{\mathrm{th}} \approx \frac{4N_{\mathrm{A}}k_{\mathrm{B}}T}{H_A H_B} \tag{3.44}$$

We have also obtained an expression for the thermoinduced susceptibility using quantum statistical mechanical formulae, as follows. The energy of the uniform mode when a magnetic field (H) is applied is be given by

$$E_{n,\pm} = \hbar\omega_0 \mp g\mu_{\mathrm{B}}H = (n + 1/2)\hbar\omega_{0,\pm}$$

where $\hbar\omega_0$ is the dispersion relationship given in Eq. (3.42) for the case of $q = 0$. The partition function can be calculated as

$$Z = \sum_{n=0}^{N-1}\left(e^{-\beta(n+1/2)\hbar\omega_{0,+}} + e^{-\beta(n+1/2)\hbar\omega_{0,-}}\right)$$

The number of modes (N) are obtained in Mørup derivation as $N = 1/\xi$, where ξ is the smallest allowed change in $\cos\theta$, θ being the precession angle of the spin along the easy anisotropy axis. For $N \to \infty$ the partition function can be approximated by

$$Z \simeq \frac{e^{-\beta\hbar\omega_{0,+}/2}}{1-e^{-\beta\hbar\omega_{0,+}}} + \frac{e^{-\beta\hbar\omega_{0,-}/2}}{1-e^{-\beta\hbar\omega_{0,-}}} \tag{3.45}$$

The thermoinduced susceptibility can then be obtained as

$$\chi_{\text{th}} = \left.\frac{\partial M}{\partial H}\right|_{H=0} = \left.\frac{\partial}{\partial H}\left(\frac{1}{\beta Z}\frac{\partial Z}{\partial H}\right)\right|_{H=0} = \frac{1}{\beta}\frac{\frac{\partial^2 Z}{\partial H^2}\big|_{H=0} Z_0 - \left(\frac{\partial Z}{\partial H}\big|_{H=0}\right)^2}{Z_0^2}$$

where Z_0 is the partition function defined in Eq. 3.45 for $H = 0$. The previous expression reduces to

$$\chi_{\text{th}} = \frac{1}{\beta}\frac{\frac{\partial^2 Z}{\partial H^2}\big|_{H=0}}{Z_0^2}$$

since the term $\frac{\partial Z}{\partial H}\big|_{H=0}$ cancels at $H = 0$ when $\omega_{0,+} = \omega_{0,-} = \omega_0$. After some straightforward algebra we find

$$\chi_{\text{th}} T \approx \frac{N_{\text{A}}(g\mu_{\text{B}})^2}{4k_{\text{B}}}\frac{1}{1-\kappa}\left(1 + 3\kappa + 4\kappa\frac{1+\kappa}{1-\kappa}\right) \tag{3.46}$$

where $\kappa = \exp(\hbar\omega_q/k_{\text{B}}T)$. This expression is valid only at sufficiently low temperatures, where just the uniform mode is populated. In this derivation, the zero point energy has been taken into account, therefore, the temperature dependence of the susceptibility at very low temperatures will be more accurate.

The thermoinduced magnetic moment is parallel to the easy axis of the magnetization. Therefore, for a sample of AFM nanoparticles with randomly distributed easy axis, one can obtain an approximated expression in the limit $T \to 0$ using Eq. 3.34

$$\chi \approx \frac{1}{3}\left(\frac{N_{\text{A}}\mu_{\text{unc}}^2}{k_{\text{B}}T} + \chi_{\text{th}}\right) + \frac{2}{3}\chi_{\text{AF}} \tag{3.47}$$

where χ_{th} refers to that obtained in Eq. 3.44 or Eq. 3.46. In this expression, we have neglected that, the thermoinduced magnetic moment μ_{th} will also contribute to the Curie term, giving a $1/T$ dependence. According to Eq. 3.47 andSQUIDzoomSQUIDzoom 3.44, there will be threshold temperature (T_{th}) above which the contribution of the thermoinduced magnetic moment will be dominant over the uncompensated magnetic moment

$$T_{\text{th}} > \mu_{\text{unc}}\frac{\sqrt{H_A H_B}}{2k_{\text{B}}} \tag{3.48}$$

Finally, it is important to highlight that the former expressions are only valid at low temperatures where just the uniform mode is populated. The contribution of μ_{th} is progressively canceled at high temperatures when successively higher energy modes are populated.

3.8.4 Macroscopic Quantum Tunneling

J. A. Swanson predicted 40 years ago that quantum effects could manifest in nanomagnets with sizes below a certain threshold (< 20 nm) [122]. A. Caldeira and A. J. Leggett [2] proposed later that a relatively large number of atoms strongly coupled by exchange interactions can coherently tunnel through the energy barrier created by anisotropy. These phenomena received the name of macroscopic quantum tunneling (MQT) of the magnetic moment. Since then, numerous authors have reported MQT of the magnetization in nanoparticles of ferro- and ferrimagnetic materials [123–127]. In 1990, B. Barbara and M. Chudnovsky [117] concluded from theoretical calculations that this behavior will be enhanced in nanoparticles of antiferromagnetic materials (MQT of the Néel vector). This can be easily understood taking into account the dispersion relation for FM and AFM spinwaves (3.39 and 3.43 respectively). At low temperatures where $q \to 0$, the energy of the FM spinwaves depends on the anisotropy field whereas the energy of the AFM spinwave is enhanced by the exchange field. This effect has been defined as an *exchange enhancement of the anisotropy*. The tunneling of the magnetic moment (or Néel vector) is due to the terms which do not commute with the hamiltonian. Therefore, quantum fluctuations will be much stronger in AFM particles than in FM particles. B. Barbara and M. Chudnovsky calculated theoretically the temperature below which quantum transitions dominate the magnetic response of a FM particle (T^*_{FM}) and an AFM particle (T^*_{AFM}) giving

$$\begin{aligned} T^*_{\mathrm{AFM}} = \frac{\mu_{\mathrm{B}}}{k_{\mathrm{B}}}\sqrt{\frac{K}{\chi_\perp}} &\propto \left(\frac{H_{\mathrm{A}}}{H_{\mathrm{E}}}\right)^{1/2} T_{\mathrm{N}} \\ T^*_{\mathrm{FM}} &\propto \left(\frac{\langle H_{\mathrm{A}}\rangle}{H_{\mathrm{E}}}\right) T_{\mathrm{C}} \end{aligned}$$

where T_{N} is the Néel temperature, T_{C} is the Curie temperature and $\langle H_{\mathrm{A}}\rangle$ is the geometrical average for the longitudinal and transversal anisotropy. Since usually $H_{\mathrm{A}} \ll H_{\mathrm{E}}$, the crossover temperature $T^*_{\mathrm{AFM}} > T^*_{\mathrm{FM}}$. The tunneling rate in the AFM case is also expected to be much larger. Besides, the magnetic moment of FM particles, μ, is much larger than μ_{unc}. Interactions between particles will be therefore more important in FM, implying a reduction in the probability of observing quantum phenomena. AFM particles are less affected by decoherence.

Chapter 4

Size Dependent Magnetic Properties of Ferritin Based Nanoparticles

4.1 Introduction

Ferritin is a very well-known protein used since the 90's to synthesize nanoparticles of different compounds [128]. Ferritin-based nanoparticles exhibit very attractive properties like high size homogeneity, solubility in water or low aggregation. In addition, these particles are promising candidates for applications due to their biocompatibility [129] and capability to form ordered superstructures [130] or even crystals [131, 132].

Any work involving the artificial synthesis of nanocrystals inside ferritin usually begins with the synthesis of iron oxide particles. The result are nearly spherical nanoparticles of varying diameter (up to 8 nm) that consist of either maghemite, magnetite or, in most of the cases, an amorphous oxide made of maghemite/magnetite. The latter constitutes the best-known example of ferritin-based nanoparticles and receive for these reason an especial name: magnetoferritin [133–135].

From a fundamental point of view, the intrinsic properties of magnetic oxide nanoparticles are known to deviate from those of the bulk material [88]. More specifically, nanoparticles usually present lower saturation magnetization [136–139] and enhanced magnetic anisotropy [139–145]. These changes are attributed to the lower symmetry of the surface sites, as well as to the presence of disorder and broken exchange bonds, all of which become increasingly important as the size decreases [142, 146, 147]. In this respect, magnetoferritin represents a particularly interesting case of study since the effective surface to volume ratio and the intrinsic disorder can become rather high, as a result of the mechanism that leads to the particle nucleation and growth. However, no detailed analysis of the dependence with size of the magnetization and magnetic anisotropy has been carried out on magnetoferritin to date. The aim of our work was to fill this gap. For this purpose, a series of γ-Fe_2O_3 particles of different diameters have been prepared inside ferritin. By varying the quantity of iron that is added to a solution of apoferritin it is possible to control the size of the particle between 1.5 and 8 nm. A detailed magnetic study has been performed taking into account the influence of the particle size distribution as we have described in the previous chapter (see section 3.7). From the latter we are able of obtaining a structural and magnetic model of magnetoferritin. As we will show, these particles exhibit very high magnetic disorder that is not only restricted to the surface but results from their irregular growth inside the protein cavity.

On the other hand, in these chapter we present a thorough magnetic study of ferritin-based nanoparticles made of an antiferromagnetic (AFM) material. Unlike their ferro or ferrimagnetic (e.g. maghemite and magnetite) counterparts, antiferromagnetic nanoparticles should exhibit exciting properties as a consequence of quantum mechanic laws. For instance, they have been proposed as good candidates for the observation of macroscopic quantum tunneling of the magnetic moment since they are more robust against decoherence than their ferro or ferrimagnetic analogues [117]. As it was introduced in the previous chapter, another consequence of antiferromagnetism in nanoparticles should be the emergence of the thermoinduced magnetic moment predicted by Mørup *et al* in 2005 [102]. The spins belonging to a magnetic lattice precess as a consequence of thermal energy leading to the so called "spin waves". The uniform mode ($q = 0$, q being the wavevector) is of especial interest in nanoparticles since it is the only state populated at low temperatures. In the case of an AFM material, spin precession occurs with unequal amplitudes in each sublattice in order to fulfill Schrödinger equation. In such unbalanced lattice, a net thermoinduced magnetic moment arises, increasing with temperature as the precession amplitude of the uniform mode increases. The latter contribution is however canceled above a certain temperature threshold due to the population of successive non-uniform modes with $q \neq 0$. [102]

The experimental confirmation of such effects is however a hard task. Different authors claimed the observation of a temperature-dependent magnetic moment in ferrhydrite nanocrystals, including natural ferritin [97,98] or chemically synthesized ferrhydrite particles [99–101], but the experimental method followed in the determination of the net magnetic moment has been later questioned [103,120,148]. In addition, these works did not dedicated especial attention to the theory developed by Mørup *et al* and, to our knowledge, there is only one example in the literature showing experimental results devoted to clarify this question [149].

The system of magnetic nanoparticles presented here constitutes an excellent case of study. In this chapter we will present the magnetic characterization performed and show how these data unambiguously support the existence of the thermoinduced magnetic moment. Moreover, at the end of next chapter, we will present an extended study at very low temperatures in which we are able of observing the temperature range in which the response of the system is purely dominated by the uncompensated magnetic moment. That is to say, we have directly measured the intrinsic magnetic moment of the nanoparticles which arises solely from finite size effects.

4.2 Biological moulds

In the same way as chemist use bakers to contain reactions and keep them isolated from the outside, nature has also developed a variety of cage shaped proteins to provide the electrochemical and environmental conditions to perform reactions inside the cells. Ferritin for example, is the iron storage protein of living beings. Iron is simultaneously toxic and necessary for the organism, i.e. it is essential for the correct performance of hemoglobin, the protein that transports oxygen through blood, but free iron would result very toxic to cells. Ferritin proteins act as an iron buffer, storing it in a non-toxic form, and transporting it to the areas where it is required. Ferritin is a spherical hollow shell with 12(8) nm outer (inner) diameter, respectively. Iron is stored as an hydrated iron oxide (or phosphate), predominantly as a nanomineral of ferrhydrite containing about 4500 Fe atoms.

Researchers realized that the properties of ferritin and other protein cage architectures could be exploited to synthesize nanoparticles in an artificial way. These include the series of ferritin-like proteins known as Dps (DNA-binding proteins for starved cells), the cowpea chlorotic mottle virus (CCMV) or a small heat-shock protein (sHsp).

4.2.1 Brief history of protein cages

Ferritin was the first protein used as a biological template for the artificial synthesis of nanomaterials. In 1937, V. Laufergberg isolated a protein extracted from horse spleen and found that it contained 20% iron [150]. He named it ”ferritin” from the Latin ”ferratus” or ”bound with iron”. Between 1942 and 1946,

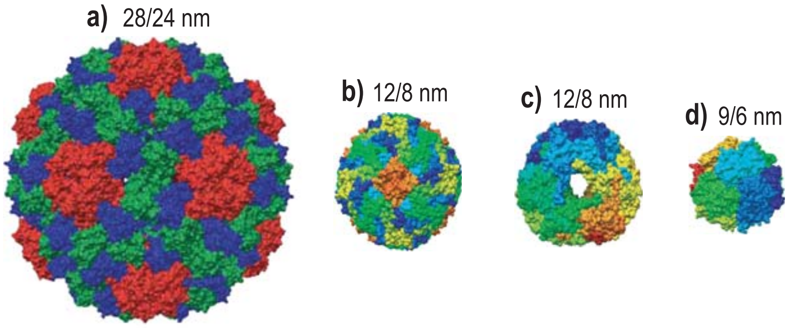

Figure 4.1: Image reconstruction of some of the most used protein cage architectures for nanoparticle synthesis and their outer/inner diameter size. a) cowpea chlorotic mottle virus (CCMV). b) Horse spleen ferritin. c) small heat-shock protein (sHsp). d) DNA-binding proteins for starved cells (Dps).

Granick and Michaelis published a series of papers on ferritin and suggested that this protein could consist of a small iron oxide micelle surrounded by a proteic part [151–158]. The cage like shape of ferritin was finally confirmed in 1991 when its crystal structure was resolved by X-Ray diffraction [159] (see Fig. 4.2). Although the most popular ferritin-based nanoparticle is magnetite/maghemite (Fe_3O_4/γ–FeO_3), the first time that ferritin was used as a reaction vessel was to synthesize a Mn(II) nanoparticle [128]. It was in 1991 when N. Meldrum and S. Mann reported the formation of Mn(O)OH inside ferritin. A year later the same group reported the successful synthesis of maghemite and the resultant artificial molecule was called magnetoferritin [133]. Since then, a wide variety of nanoparticles have been synthesized inside ferritin. Apart from Fe_3O_4/γ–FeO_3 and Mn(O)OH other oxides like Mn_3O_4, Co(O)OH [160], Co_3O_4 [161], as well as Eu, Fe, and Ti hydroxide [162] have been reported. Metallic and semiconductor nanoparticles have also been prepared, like Cu [163], Pd [164], Ni, Co [165], Ag [166], CoPt [167] or In_2O_3 [168]. Given the enormous success of ferritin-based nanosynthesis, researchers envisaged the use of other cage-like proteins looking for new properties and particle sizes. For instance, The Dps from *listeria innocua* have been used in the formation of 4.5–6.0 nm Fe_3O_4 [169] and 3.5 nm Co_3O_4 particles [170]. The CCMV virus have used for the crystallization of polyoxometalate species like Vn, Mb and W [171]. A mutant constructed version of CCMV has been also used to synthesize 24–nm particles of γ–FeOOH [172]. The sHsp from *Methanococcus jannaschii* performs a similar reaction as ferritin that can lead to the formation of encapsulated ferrhydrite [173].

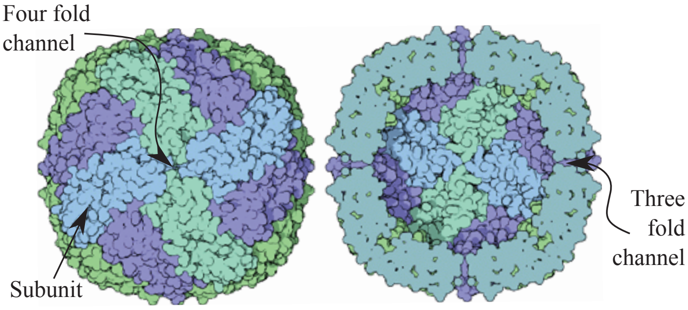

Figure 4.2: Image reconstruction of ferritin and ferritin cross section.

4.2.2 Applications of protein-encapsulated nanoparticles

Protein encapsulated nanomaterials provide unique advantages in material science. Due to its biological origin, they are suitable to be produced in large scale and each cage type exhibits narrow size distributions. These systems present three distinct surfaces, the inner part, the subunit interface and the outer part. All of them can be chemically or genetically engineered to reach different functionalizations. The inner part has been successfully used for nanoparticle crystallization with potential applications in high density storage media . For instance room-temperature ferromagnetic CoPt ferritin-based nanoparticles have been fabricated [174]. A genetically engineered CMMV has been recently reported with peptides in its subunit structure able to metal bind Gd chelators. These are well-known contrast agents with MRI capabilities [175]. Reactive sites present in the protein surface can be used to couple organic and inorganic links with high symmetry. This provides th

e opportunity of synthesizing cell-specific targets that, combined with the capability of nanoparticle storage could be used in drug delivery [176] or cancer treatment by hipertermia [129]. Recent results also indicate that these protein structures are biocompatible and could be used in the future as *in vivo* medicaments [177].

4.3 Magnetoferritin: size-dependent properties

In this section we report a detailed experimental study of maghemite nanoparticles, with sizes ranging from 1.6 up to 6 nm. Samples have been synthesized in the Instituto de Nanociencia de Aragón (INA) by R. de Miguel [178] following the protocol described in ref. [135].

We introduce first some intrinsic properties of iron oxides, more specifically maghemite and magnetite. The morphological and physical characterization of the nanoparticles, including TEM and X-Ray diffraction, is then described. Finally, the magnetic response of the maghemite cores is presented. The latter has been performed by combining ac susceptibility and dc magnetization measurements. From the equilibrium magnetic response, we have determined the distribution of magnetic moments as described in the previous chapter (see section 3.7.1). In addition, we have also determined, the distribution of the activation energies required for the magnetization reversal and, from this, the size-dependent magnetic anisotropy constant K. The results presented here reveal a highly disorder crystal and magnetic structure of the magnetic cores, accordingly, a simple picture of magnetoferritin consisting of different crystalline domains will be suggested.

4.3.1 Iron Oxides: bulk properties

The term "ferromagnetism" was historically used for those materials that showed spontaneous magnetization. That is, materials that could attract other metals like iron. Magnetite, a mineral produced naturally by aerobic weathering of magmatic rocks, was the first example that showed magnetic properties to the humankind. There are many legends about the very earliest discovery of magnetite, but all of them agree that such deed was done either by the Greeks or the Chinese. In any case, it seems that the mineral was named after Magnesia, a region of ancient Thessaly. The Chinese benefited from its properties to build the most primitive compasses used by fortune tellers and later for navigation orientation [179]. However, this iron oxide is not strictly speaking a ferromagnet. Materials in which exchange interactions favor antiparallel alignment can also exhibit permanent magnetization if the opposed magnetic moments on both sublattices are unequal. This kind of magnetic order, called ferrimagnetism, results in very similar characteristics than that of ferromagnets and is found in many iron oxides. Magnetite and maghemite are two well known examples of ferrimagnetic materials.

Magnetite is a black mineral with chemical formula Fe_3O_4 that exhibits an inverse spinel crystal structure [180] with unit cell parameter $a = 0.8396$ Å. Iron is present on two oxidation states, Fe^{2+} occupying octahedral sites and Fe^{3+} occupying both octahedral and tetrahedral sites. Magnetite is however usually found to be non-stoichiometric, having a ratio of $Fe^{2+}/Fe^{3+} \approx 0.5$. Regarding the magnetic order, spins occupying octahedral and tetrahedral sites are antiferromagnetically coupled. Since the magnetization of both sublattices is different, the crystal is ferrimagnetic below the Curie temperature $T_{\mathrm{C}} \approx 850$ K. Saturation magnetization of bulk samples is found to be $M_{sb} = 82$ emu/g.

Maghemite is very similar to magnetite but all or most of the iron is in

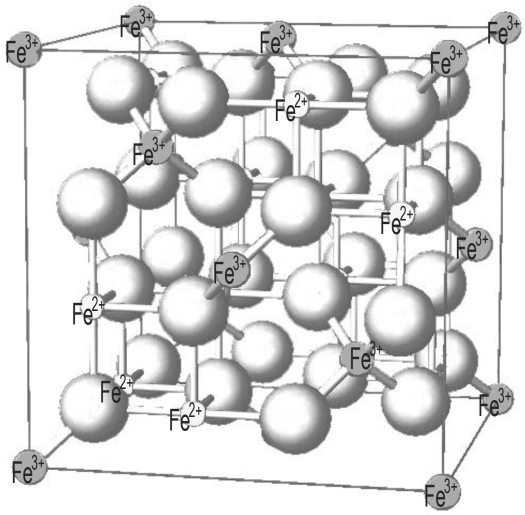

Figure 4.3: Crystal structure of magnetite. That of maghemite is exactly the same but including a certain number of cation vacancies.

the trivalent state compensated with cation vacancies. The degree of vacancy order depends strongly on the size of the crystal. Its chemical formula is usually written as $\gamma{-}Fe_2O_3$ and the unit cell parameter is $a = 0.8347$ Å. This material is ferrimagnetic as well with Curie temperature $T_C \approx 820 - 986$ K but the magnetic moment per unit formula is slightly smaller giving a saturation magnetization of $M_{sb} = 74$ emu/g.

These similarities make it very difficult to distinguish between the two iron oxides through spectroscopic techniques. Magnetic measurements also give similar results in both cases. Therefore, the proper identification of magnetite or maghemite is not a trivial issue and can not always been accomplished.

4.3.2 Synthesis of Magnetoferritin

Magnetoferritin nanoparticles have been synthesized in the Instituto de Nanociencia de Aragón (INA) by R. de Miguel [178] following the protocol described in ref. [135]. Briefly, 500 ml of a 50 mM AMPSO [1] (3-[(1,1-Dimethyl-2-hydroxyethyl)amino]-2-hidroxy-propanesulfonic acid) solution, buffered to pH 8.6 with 2.0 M NaOH, were stirred with a magnetic stirrer and de-aerated with Ar for 1 hour. After de-aeration, this solution was kept stirring under Ar atmosphere and warmed up to 65°C. Once this temperature was reached, an apoferritin solution (100 mg/500 ml) was added and the reaction solution

---

[1] The reagents AMPSO and ammonium ferrous sulfate as well as apoferritin and ferritin from horse spleen, were purchased from Sigma.

was left stirring for 10 minutes. 5 ml of a 0.1 M $(NH_4)_2Fe(SO_4)_2 \cdot H_2O$ solution were prepared and de-aerated with Ar for at least 30 minutes and aliquots of this solution were added every 15 minutes to reach the final theoretical load of 3000 Fe atoms per protein, being the first 2 additions of 66 μl and the rest, until 23, of 185 μl, corresponding to a theoretical load of 50 and 140 Fe atoms per protein, respectively. Samples of 100 ml each, corresponding to theoretical loads of 50, 240, 500 and 1000 Fe atoms per protein were taken out during the reaction time. The five final solutions (named N50, N240, N500, N1000 and N3000) were dialyzed against distilled water, concentrated to a volume of approximately 5 ml each and then lyophilized. Lyophilized samples can be kept at 4°C or -20°C for longer storage. The concentration of iron concentration in the nanoparticles was determined by microanalysis or inductively coupled plasma (ICP) atomic emission spectrometry. To perform the microanalysis, the lyophilized nanoparticles were dissolved in water, reaching a concentration of 2–3 mg/25 ml. If necessary, some drops of concentrated hydrochloric acid (HCl) are added drop-wise to the solution in order to dissolve aggregates. Usually, 2 mg of lyophilized sample are needed for a regular elemental analysis experiment.

4.3.3 Characterization by TEM

Transmission Electron Microscopy (TEM) images have been taken for all samples by R. de Miguel and C. Carbonera. These images are shown in Fig. 4.4. As we can see, the size of the black spots that correspond to the iron oxide core, increases with the iron loading. Their shape is however not round or spherical. Often, and especially for low iron contents, we find particles that are ”moon-like” or ”horseshoe”, see for instance the insert of Fig. 4.4c. The latter can bee understood due to the special mechanism of crystal grown inside ferritin. As it has been reported, there are several iron nucleation centers in the inner cavity of the protein [181], this fact leads to different starting points for the maghemite crystal to start growing and the resultant particle evolves from the outside towards the center of the cavity.

Fig. 4.4e shows a typical TEM image of stained particles. In these images it is possible to distinguish between the magnetic core (in black) and the protein shells (a white circle around the iron oxide core) indicating that the nucleation process takes place inside the cavity of apoferritin. We also observe that not all the proteins are equally filled. In fact, some virtually empty proteins appear as well. This inhomogeneous filling has been attributed [135] to the catalytical activity of the surface of already nucleated iron oxide clusters for the oxidation of Fe(II). This increases the rate of iron uptake and growth in some proteins at the expense of others. For the N3000 sample, the images reveal also a

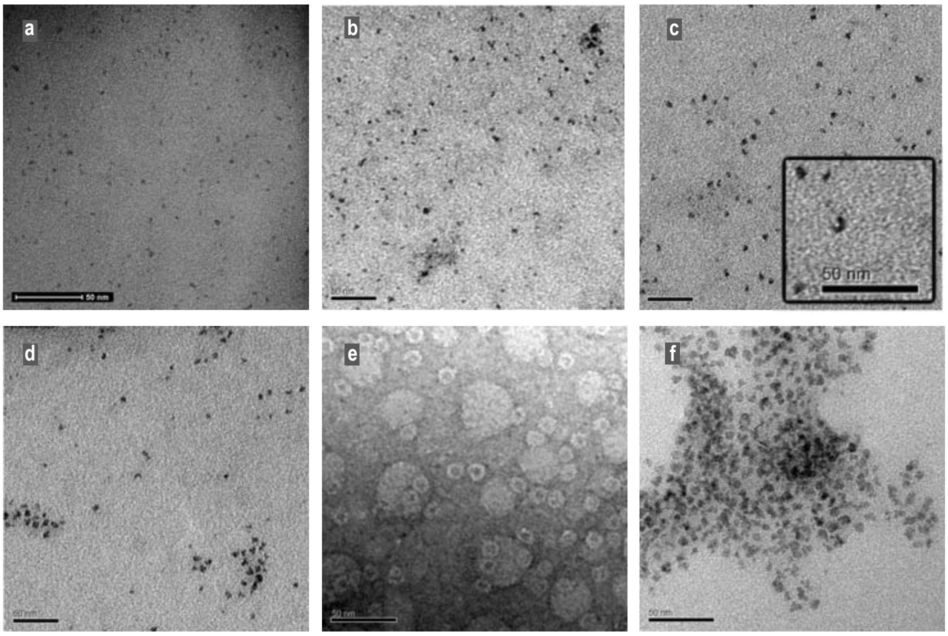

Figure 4.4: Typical TEM images of samples with increasing nominal iron loading per protein N: (a) N = 50; (b) N = 240; (c) N = 500; (d) N = 1000; (e) N = 1000 stained; (f) N = 3000. The inset in (c) is an enlarged picture showing irregular nanoparticle shapes found in the N500 sample. The image showed in (e) was taken on a stained N1000 sample, to show the contrast of the proteic shell (in white). The bar length is 50 nm in all these images

clustering of nanoparticles, probably resulting from protein shells which are overfilled.

The size distribution for all the synthesis has been obtained by measuring the diameters of a large number of particles (between 500 and 1000 depending on the sample) selected from different representative areas of the grid. For this purpose we have approximated the shape of the particles to an ellipsoid with axis a and b. The effective diameter is obtained by making the volume of the ellipsoid ($V = \pi/6a^2b$) equal to the volume of an sphere of diameter D. We have also calculated the ellipticity ε of every particle defined as the ratio between the shorter and longer axis. These distributions are depicted in Fig. 4.5. The diameter (ellipticity) distribution are bell-shaped and can be fitted to normal distributions characterized by the mean value D_{av} ($\varepsilon_{\mathrm{av}}$) and variance σ_D (σ_ε), respectively. However, the volume distribution function is no more symmetrical since large diameters have a bigger contribution as the volume goes with the cube power of D. These distributions can bee reasonably well fitted by Gamma distribution functions. The latter has been introduced in the previous chapter (Section 3.7.1) and can be characterized by a mean value of

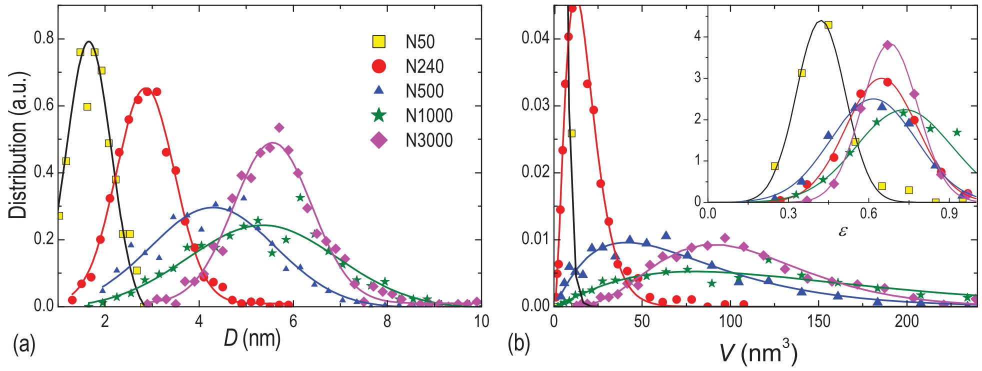

Figure 4.5: Size distributions as obtained from the TEM image analysis (scatter) fitted to the corresponding distribution functions (lines). (a) The effective diameter distribution exhibit typical Gaussian shape. (b) The volume distribution can be better described by a Gamma distribution function. The inset shows the distribution of ellipticities ε fitted to Gaussian function.

Sample	D_{av} (nm)	σ_D/D_{av}	V_{av} (nm^3)	σ_V/V_{av}	ε_{av}	$\sigma_\varepsilon/\varepsilon_{\text{av}}$
N50	1.65	0.25	2.7	0.7	0.4	0.21
N240	2.86	0.22	17.7	0.6	0.6	0.20
N500	4.29	0.31	77.6	0.7	0.6	0.26
N1000	5.35	0.30	153.1	0.7	0.8	0.25
N3000	5.56	0.15	109.7	0.4	0.7	0.15

Table 4.1: Parameters of the Gaussian distribution of particle diameters, Gamma distributions of particle volumes and Gaussian distribution of particle ellipticities. The latter approaches unity as particle volume increases indicating that the spherical shape is only reached when the protein is nearly full.

the volume (V_{av}) and the variance (σ_V). These values are given in Table 4.1 and confirm that iron-oxide cores grow with increasing N and that their shapes tend to be rather irregular, with the average ε ranging between 0.4 and 0.8. It transpires that the spherical shape is only approached when the molecule becomes nearly fully loaded. In the case of the N3000 sample, the distribution shown in Fig. 4.5 does not include the sizes of very large aggregates observed in the TEM images, but only the sizes of isolated nanoparticles.

Electron diffraction patterns were also measured. These results reveal a clear degradation of the crystallinity as the size of the magnetic core decreases. However, the obtained rings (not shown here) correspond closely to the indexation of magnetite or maghemite crystallographic planes. A detailed description of these results can be found in Ref. [182].

4.3.4 X-Ray characterization

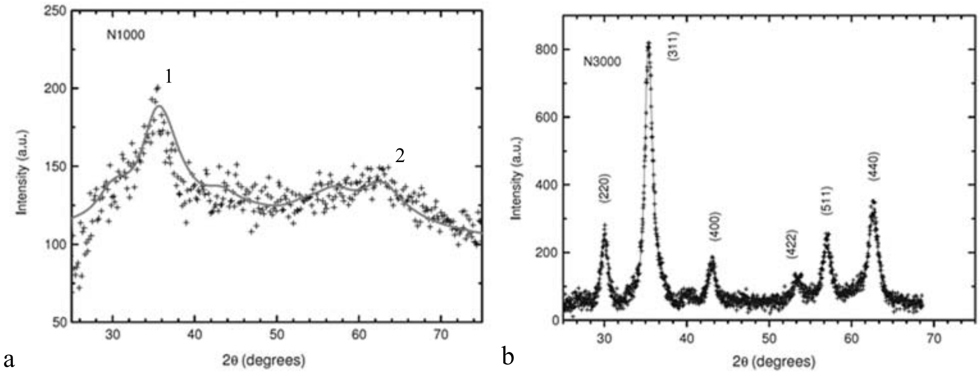

Figure 4.6: X-ray diffraction patterns of N1000 and N3000 samples, after subtraction of the apoferritin contribution to the background. a) N1000 sample. Peak 1 contains contributions from (220), (311) and (400) magnetite or maghemite Bragg reflections whereas peak 2 reflects the superposition of (422), (511) and (440) reflections. b) N3000 pattern, indexed with the magnetite or maghemite powder diffraction pattern.

The crystal structure of the particles was also studied by means of X-Ray diffraction by J. Bartolomé. The reflections observed agree both with the calculated patterns for maghemite or magnetite (see Fig. 4.6). An average diameter D_{X-ray} can be derived from these data giving $D_{X-ray} = 2$ nm in the case of the N1000 sample, much smaller than the average size $D = 5.3$ nm obtained from TEM. This fact indicates that the crystalline disorder in magnetoferritin inorganic cores increases with decreasing size. For N3000 a value $D_{X-ray}14\pm1$ nm is obtained, which shows the formation of an important fraction of nanoparticles with dimensions exceeding those of the apoferritin cavity (8 nm). A more complete description of these experiments can be found in Ref. [182].

4.3.5 Magnetic characterization of magnetoferritin

Magnetic measurements have been performed using a commercial SQUID magnetometer from Quantum Design as described in chapter 1. Two types of measurements are presented in this section. First, equilibrium magnetization measurements, that enable us to obtain information about the distribution of magnetic moments. And, second, ac magnetization measurements that provide much information abouth the dynamical response of the magnetic nanoparticles. From the latter, we are able to determine experimentally the distribution of activation energies in this sample. A complete Mössbauer spectroscopy study of all samples has been performed by C. Piquer. The obtained spectra (not shown here) agree well with those corresponding to maghemite or magnetite. A detailed description of these results can be found in Ref. [182].

4.3.5.1 First consideration: superparamagnetic behavior

In first place, let us see whether the nanoparticles exhibit superparamagnetic character. Fig. 4.7 shows magnetization hysteresis loops measured on two representative samples, namely N240 and N1000, at $T = 2$ K, as well as field-cool and zero-field-cool (FC-ZFC) measurements. Both measurements exhibit typical features of superparamagnetic behavior.

At $T = T_{\mathrm{B}}$ defined as the blocking temperature, a maximum appears in the ZFC response from both samples. The latter indicates the superparamgnetic blocking of the magnetic moment for the corresponding measurement time of the experiment. The largest sample (N1000) becomes blocked at higher temperatures (22.4 K compared to 12.9 K) indicating that the activation energy increases with size.

At low temperatures, well below the blocking temperature of each sample, anisotropy dominates the magnetic response and the magnetization shows hysteresis. The coercitive field (B_{c}) is slightly larger in the case of the smallest sample (0.145 T compared to 0.086 T). Since the low-T limit of B_{c} is proportional to the average anisotropy constant K, this result indicates larger anisotropy for decreasing size, as usual in nanoparticles.

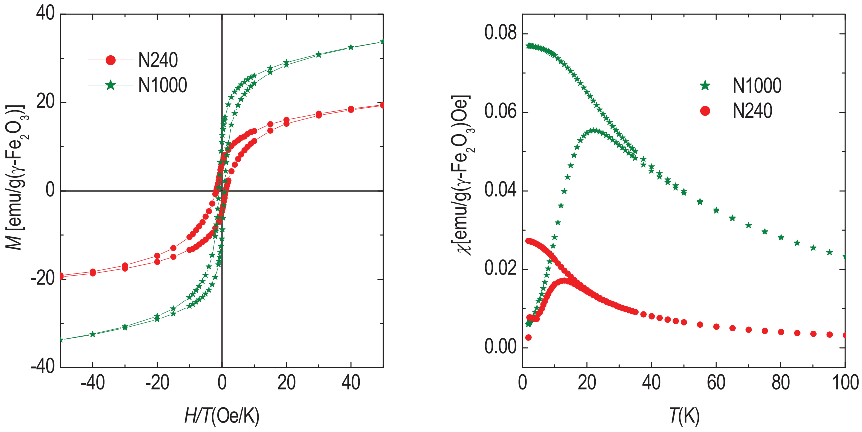

Figure 4.7: Magnetization hysteresis loop measured at T = 2 K (a) and field-cool and zero-field-cool (b) measurements of magnetoferritin samples N240 and N1000.

4.3.5.2 Equilibrium magnetization and susceptibility: size-dependent magnetic disorder

Above the blocking temperature, the magnetization reflects the equilibrium response of the ensemble of nanoparticles. The latter implies that the magnetization vs. field isotherms will show no hysteresis (see Fig. 4.8). In addition, M vs. H data measured well above T_{B} and M vs. T data measured under strong magnetic fields (5 T for some data shown in Fig. 4.8) scale on a single curve when they are plotted as a function of H/T. The latter property indicates that the magnetic anisotropy affects little the magnetization for sufficiently high temperatures or sufficiently high magnetic fields, as expected [148]. By contrast, at lower temperatures the magnetization isotherms deviate from the scaling plot, flattening at intermediate fields. In this section, we use the equilibrium susceptibility and the magnetization to extract information about the internal magnetic structure of magnetoferritin inorganic cores. Using the method described in the previous chapter (Section 3.7.1) the distribution of magnetic moments can be determined for each magnetoferritin sample. Using equations 3.15, 3.17 and 3.18, the simultaneous fit of the magnetization isotherms and susceptibility data enables us to accurately determine the distribution of superparamagnetic moments $f(\mu)$. We have chosen for the latter a Gamma function (see Section 3.7.1) since it accounts reasonably well for the volume distribution function. This function is completely described by the mean value of the magnetic moment (μ_{av}) and the variance (σ_{μ}).

Results obtained by this method for magnetoferritin samples with different iron loadings are shown in Fig. 4.8, while Fig. 4.9 shows the magnetic distributions $f(\mu)$ derived from the fits. The distribution parameters as well as other structural and magnetic data are also listed in Table 4.2. The average magnetic moment decreases with decreasing size, as expected.

In order to gain a deeper insight into the magnetic structure of magnetoferritin, it is useful to compare these magnetic moments with those calculated using the bulk magnetization $M_{sb} = 363$ emu/cm^3 (74 emu/g) of maghemite. For this, we employ the volume distribution $f(V)$, extracted from the analysis of TEM images (see Fig. 4.5, table 4.1 and 4.2), and calculate the magnetic moments as $\mu = M_{sb}V$. We observe (see Fig. 4.9) that μ_{av} is about ten times smaller than $M_{sb}V$, showing that the saturation magnetization of magnetoferritin cores is strongly reduced with respect to that of bulk maghemite.

Reduced magnetic moments are commonly observed in maghemite nanoparticles [136, 137, 139, 146]. They have been associated with the canting of Fe spins caused by disorder. Kodama and co-workers [95,146] proposed a model in which the rupture of exchange bonds near the particle's boundaries, together

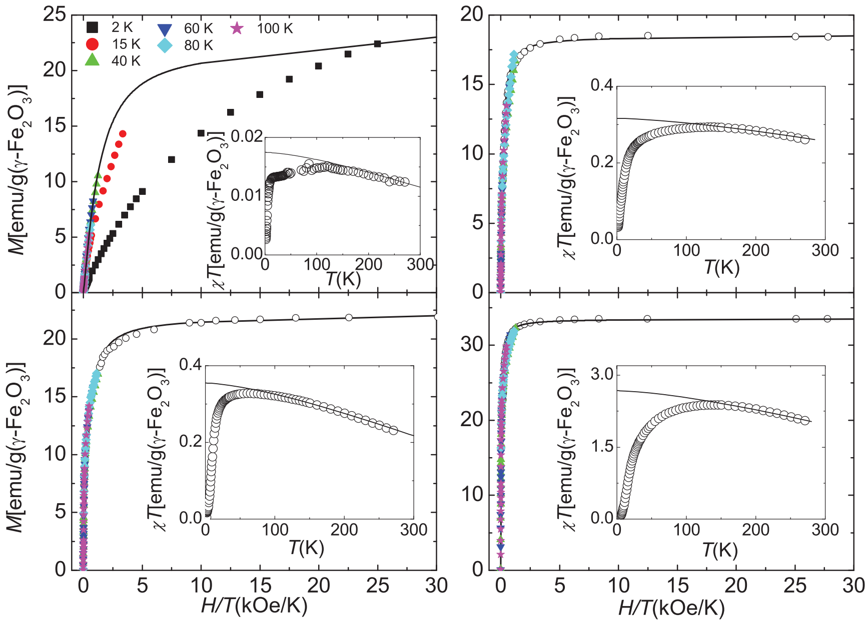

Figure 4.8: Magnetization data of magnetoferritin samples with varying nominal iron content per molecule. The insets show the susceptibility response multiplied by temperature. Left: top, N50; bottom, N240. Right: top, N500; bottom N1000

with the strong magnetic anisotropy of these sites, lead to a magnetically frozen surface layer. This model accounts for the low saturation magnetization and the high saturating magnetic fields measured experimentally. However, the saturation magnetization is also predicted to decrease with decreasing particle size, as the fraction of surface to core atoms increases. In the case of magnetoferritin, by contrast, the saturation magnetization depends weakly on D, at least for $D < 5.5$ nm, showing that the spin disorder is not restricted to a surface atomic layer of constant width

Magnetic disorder is probably enhanced in magnetoferritin by the especial conditions and the environment in which inorganic cores grow inside the cavity of apoferritin. Since iron can nucleate at multiple sites, the nanoparticles result from the growth of several nanocrystals that merge together. This interpretation is supported by the irregular particle shapes observed in TEM images (see for instance the inset of Fig. 4.4c) as well as by X-ray diffraction data described in section 4.3.4.

This mechanism of particle growth is clearly different from the situation usually met in nucleation/precipitation methods. It is therefore reasonable

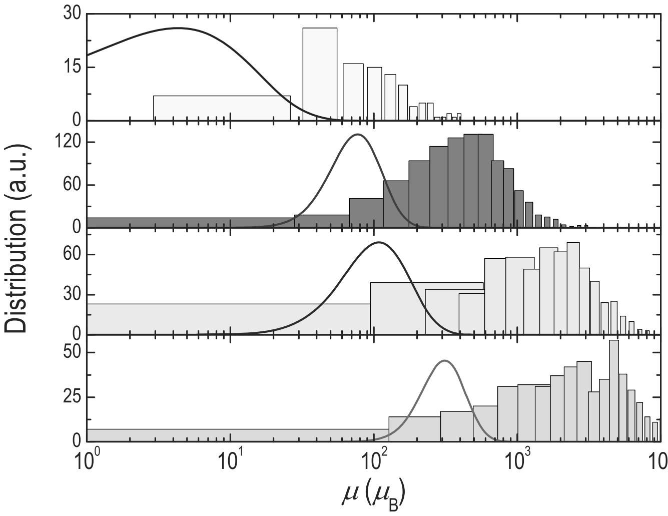

Figure 4.9: Distributions $P(\mu)$ of magnetic moments μ for samples of magnetoferritin with varying iron content. Top, N50; second panel, N240; third panel, N500; bottom N1000. Solid lines, distributions obtained from the fit of the equilibrium magnetic susceptibility and magnetization; bars, data obtained from the distribution of particle volumes assuming that $\mu = M_{sb}V$, with $M_{sb} = 363$ emu/cm^3 being the saturation magnetization of bulk maghemite

to expect that magnetoferritin cores are less crystalline or, equivalently, that they possess a larger effective surface to core ratio. From a structural point of view, magnetoferritin cores present some similarities with hollow maghemite nanoparticles, which consist also of several crystalline domains [183]. There are also similarities between their magnetic behaviours. More specifically, the saturation magnetization of 8 nm maghemite nanoshells is nearly 20 times smaller than M_{sb} [183], comparable to the values we estimate for magnetoferritin cores. Exploiting this analogy, we suggest that spins in different crystalline domains of magnetoferritin point along different directions, determined by their local anisotropy axes. This effect, which strongly reduces the net magnetic moment per particle [183], is enhanced if, as it is the case with magnetoferritin (see next section 4.3.5.3), surface or interfacial spins posses a strong magnetic anisotropy. A simple picture of the magnetic structure of magnetoferritin cores that emanates from the experiments is shown in Fig. 4.10. It is worth mentioning that also the natural form of ferritin, which contains an antiferromagnetic crystal of ferrihydrite, has been found to be highly disordered from a magnetic point of view. In fact, the uncompensated magnetic moment of ferritin agrees with a random orientation of all the spins and not only of those located at the core's surface [99, 105].

A different situation is met in the N3000 sample which, according to the

Sample	$\mu_{\mathrm{av}}(\mu_{\mathrm{B}})$	$\sigma_{\mu}/\mu_{\mathrm{av}}$	$U_{\mathrm{av}}/k_{\mathrm{B}}(\mathrm{K})$	σ_U/U_{av}	U/k_{B}	$K(\times 10^6\ \mathrm{erg/cm^3})$
N50	13	0.8	25	0.7	44	127
N240	90	0.4	155	0.7	240	121
N500	140	0.5	283	0.4	347	50
N1000	350	0.3	381	0.5	499	37

Table 4.2: Parameters of the Gamma distributions of magnetic moments and activation energies of magnetoferritin obtained from the analysis of magnetic data measured on samples with varying iron content. U is the slope of the Arrhenius plots for the blocking temperatures. K is the magnetic anisotropy constant

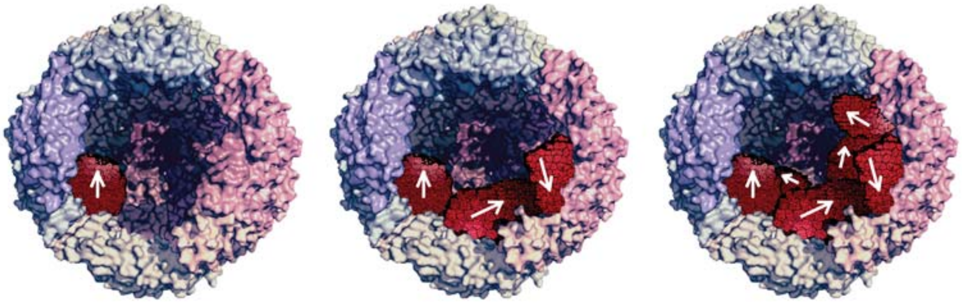

Figure 4.10: Illustrative picture of the magnetoferritin growth process. Crystallization begins at different points of the protein's internal surface leading to the formation of different crystalline domains. The white arrows represent the magnetization vectors of each of the crystalline domains that form the nanoparticle. They are strongly pinned along different directions by the strong anisotropy of surface spins. The frustrated interactions between different domains give rise to a strong reduction of the net magnetic moment per molecule

TEM characterization, contains large aggregates arising probably from the merging of several overfilled proteins. The magnetic response of this sample shows evidences of strong interparticle magnetic interactions. For this reason, the method described in this section cannot be applied to determine the distribution $f(\mu)$ of magnetic moments. The saturation magnetization of this sample, estimated from the high field limit of magnetization isotherms, agrees with M_{sb}, suggesting that its magnetic structure becomes closer to that of bulk maghemite.

4.3.5.3 Ac-susceptibility scaling: size-dependent magnetic anisotropy

In this section, we consider the dynamical magnetic response of magnetoferritin, that is, the response under the non-equilibrium conditions that charac-

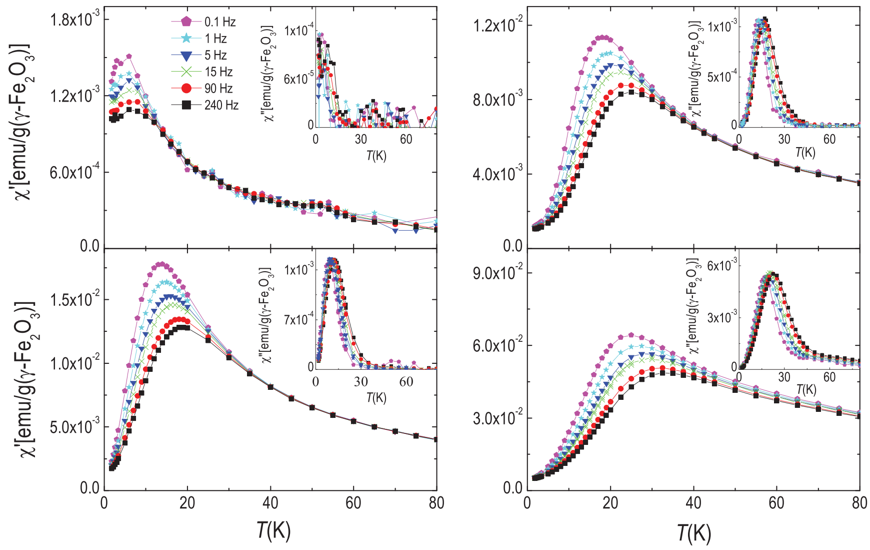

Figure 4.11: Frequency-dependent ac susceptibility of four samples of magnetoferritin with different nominal iron loading per molecule. Left: top, N50; bottom, N240. Right: top, N500; bottom N1000. The main panels show the real susceptibility component χ'. The insets show the imaginary susceptibility component χ" of each sample

terize the temperature region close to or below the blocking temperature T_{B}. This response provides information on the magnetic anisotropy and how this parameter depends on size. The progressive freezing of the magnetic moments by the magnetic anisotropy barriers gives rise to a dependence of the ac susceptibility on the frequency ω of the excitation ac magnetic field, as it is indeed observed experimentally (see Fig. 4.11). For a given ω, T_{B} is usually defined from the maximum of the imaginary susceptibility component χ". We observe that T_{B} increases with ω, according to Arrhenius law that is characteristic of a thermally activated relaxation, with a characteristic activation energy U and a characteristic attempt time ω_0. We have found that U increases with particle size, as expected.

In principle, it is possible to estimate the anisotropy constant K from the relationship $U = KV_{\mathrm{av}}$. However, in a sample with a distribution of particle sizes (thus also of activation energies), the characteristic U governing the blocking temperature is not equal to $U_{\mathrm{av}} \equiv U(V_{\mathrm{av}})$ [183]. A more precise determination of the anisotropy constant can be achieved as described in the previous chapter, by performing a scaling analysis of the full $\chi"(T)$ curves measured at all frequencies. The scaling is indeed observed for all samples of magnetoferritin (cf Fig. 4.12), with the exception of N3000. In the latter sample, χ"(T) curves show a very large and flat response extending from T_{B} to well above room temperature. This response can be associated with the bulk-like magnetic behavior of large aggregates. For the other four samples, the scaling function provides a direct picture of the distribution of activation energies, which can be well described by a Gamma function. The parameters U_{av} and σ_U of these distributions are listed in Table 4.2, which also contains the same information for the distributions of magnetic moments. Once the distributions of U and V (see Table 4.1) are known, the anisotropy energy constant K can be determined simply as the ratio $K = U_{\mathrm{av}}/V_{\mathrm{av}}$.

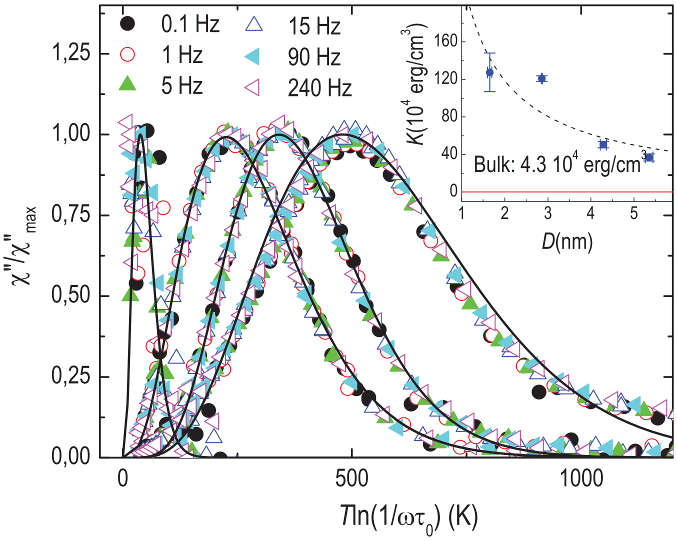

Figure 4.12: Scaling plots of the imaginary susceptibilities of magnetoferritin samples with varying nominal iron content. The inset shows the magnetic anisotropy constant as a function of the average particle diameter. The solid blue line is a least-squares fit of Eq. 3.23 to the data. The dotted red line shows the bulk anisotropy of maghemite

The anisotropy constants determined by this method are also listed in Table 4.2 and plotted in the inset of Fig. 4.12 as a function of the average diameter. They are between one and two orders of magnitude larger than the anisotropy $K_{\mathrm{bulk}} \approx 4.7 \times 10^4$ erg/cm^3 of bulk maghemite and increase with decreasing D. The size-dependent anisotropy constant K can be fitted with the following expression

$$K = K_{\mathrm{bulk}} + \frac{6K_{\mathrm{s}}}{D} \tag{4.1}$$

where K_{s} is a surface anisotropy constant. The last term in Eq. 4.1 accounts for the different anisotropy of iron sites located near the particle boundaries and for their increasing relative fraction for decreasing sizes [95,144,145,184].

The very strong pinning of surface spins dominates the activation energy of magnetoferritin cores. This result is compatible with the magnetic structure shown in Fig. 4.10. In fact, the strong anisotropy of each crystalline domain can compete against their mutual interactions, giving rise to a nearly frustrated magnetic structure and therefore accounting for the very low magnetic moments found experimentally.

From the fit, we estimate $K_{\mathrm{s}} = 0.04\ \mathrm{erg/cm^2}$. This value is two times larger than the surface anisotropy reported in [144] for maghemite nanoparticles that were also synthesized inside biological moulds. Besides the differences in experimental methods and particle sizes covered by the two studies (in [144] $4.9\ \mathrm{nm} < D < 19\ \mathrm{nm}$), we think that this difference might be attributed to differences in the particles morphologies. The nanoparticles studied in Refs. [144, 145] were synthesized by fully loading nanomoulds of varying size. In the present study, by contrast, we have varied the iron loading of apoferritin. As we discuss in section 4.3.3 and 4.3.4, the partial filling of apoferritin gives rise to highly irregular inorganic cores, for which the effective surface to volume ratio can be enhanced with respect that of fully loaded proteins.

These results confirm that the magnetic properties of magnetoferritin are largely determined by the particle's surface. The enhanced anisotropy is due to the existence of low-symmetry atomic sites at the particle's surface and inside it, which in the present case can be associated not only with surface sites, but also with the structural disorder of magnetoferritin cores

4.3.6 Conclusions: size effects in magnetoferritin

We have reported the results of a detailed study of magnetoferritin nanoparticles with average sizes ranging from 1.6 to 8 nm. From a structural point of view, magnetoferritin cores are poorly crystalline and irregular in shape, probably consisting of several crystalline domains merged together. The particular morphology of the inorganic cores probably results from their irregular growth inside the apoferritin nanocavity.

The structural disorder leaves also its mark on the magnetic properties. Our data reveal the existence of a strongly reduced magnetism, with magnetic moments per particle that are about ten times smaller than expected for crystalline maghemite particles of the same size. For the smallest nanoparticles investigated, which consist of barely 50 iron atoms, the magnetic moment per particle amounts to barely 16 μ_{B}.

A scaling analysis of the frequency-dependent ac susceptibility has enabled us to extract the distribution of activation energy barriers, and from this the magnetic anisotropy constant K. It is found to be between one and two orders of magnitude larger than the anisotropy of bulk maghemite and to increase with decreasing D. The enhanced anisotropy is probably due to the existence of low-symmetry atomic sites.

Our data reveal that magnetoferritin molecules behave as highly disordered magnetic nanoparticles, whose net magnetic moment results from the superposition (and near cancellation) of the magnetization vectors of different crystalline domains. Similar results have been recently reported from magnetic measurements performed in hollow maghemite nanoparticles [183]. The activation energies that control the magnetization switching rates are determined by the strong anisotropies of those spins located at the nanoparticle interfaces.

4.4 CoO-ferritin: the thermoinduced magnetic moment

In this section we present the physical and magnetic characterization of cobalt oxide nanoparticles synthesized inside ferritin. Samples have been synthesized by R. de Miguel [178] following the protocol described by Tsukamoto *et al* but introducing some variations [161] in order to achieve different results in cobalt loading rates, size and even composition of the resulting nanoparticles.

We discuss first some basic properties of bulk CoO. A morphological characterization by TEM has been performed as well revealing very small particle sizes of just 2 nm in average. Energy-dispersive X-ray (EDX) and X-ray photoelectron spectroscopy (XPS) studies support the formation of CoO although the presence of OH groups can not be ruled out as a consequence of the intrinsic tendency of ferritin to produce hydroxides. We present a detailed magnetic study performed at temperatures between $T = 1.8$ up to 400 K. These are also consistent with the magnetic characteristics of CoO. Still typical consequences from size reduction like the decrease of the Néel temperature are observable. From the analysis of the magnetization isotherms, it is possible to quantify the value and dependence with temperature of the antiferromagnetic susceptibility. Measurements of the initial magnetic susceptibility have been performed as well. The latter enables us to avoid problems related with the magnetic anisotropy and to confirm the influence of the thermoinduced magnetic moment in these particles. The temperature range of susceptibility measurements will be extended down to very low temperatures ($T = 13$ mK) in the next chapter revealing a new exciting clue that supports our arguments.

4.4.1 The CoO oxide: bulk properties

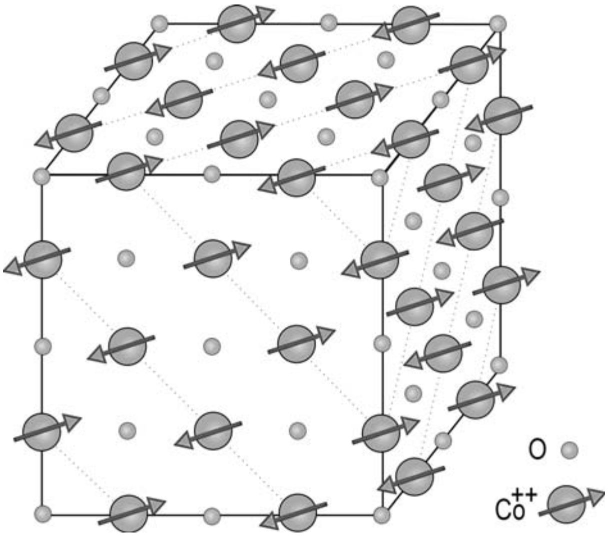

Figure 4.13: Crystal (circles) and magnetic (arrows) structure of CoO. On the crystal structure each atom has six nearest neighbours with octahedral geometry. On the magnetic structure each atom has 4 nearest neighbours and 12 next nearest neighbours, both exhibiting antiferromagnetic interactions

Cobalt(II) oxide (CoO) is an antiferromagnetic material below $T_{\mathrm{N}} \simeq 291$ K. In 1950, N. C. Tombs and H. P. Rooksby solved its crystal structure by means of X-Ray diffraction [185]. They found that, above the Néel temperature, CoO crystallizes in the same structure of NaCl, with lattice constant $a = 4.25$ Å (see Fig. 4.13).

Unlike other oxides (i.e. magnetite, maghemite...), the magnetic properties of CoO have not been so extensively studied. That comes partly from the fact that Co(II) tends to Co(III) at room temperature, leading to the formation of Co_3O_4. It is therefore difficult, to obtain single-phase and stoichiometric bulk samples. The Néel temperature was determined in the 50's by dilatation [186] and magnetic susceptibility studies [187]. Its magnetic structure was also resolved at that time by means of neutron diffraction measurements [188,189]. It was found to be f.c.c. with the Co magnetic moments along [111] direction and with opposite directions in the successive layers (see Fig. 4.13).

In the following years, some authors reported the magnetic moment per cobalt atom (μ_{Co}). In 1951 H. la Blanchetais obtained a value of $4.96\mu_{\mathrm{B}}$ from high temperature susceptibility measurements [187]. N. Elliot reported three years later a moment of $4.2\mu_{\mathrm{B}}$ [190] and W. L. Roth obtained $3.80\mu_{\mathrm{B}}$ by means of neutron diffraction in 1958 [189]. The exchange constants were obtained experimentally by means of magnetic susceptibility measurements

[191] and molecular field analysis developed by Kanamori [192] and they were found to be $J_1 = -6.9$ K for nearest neighbours and $J_2 = -21.6$ K for next nearest neighbours. Interactions between next nearest neighbours are therefore antiferromagnetic as well and quite large. The latter explains the fact that the experimental values of θ differ from the observed T_{N}. For instance J. R. Singer reported $\theta \approx -332$ K from susceptibility measurements above the Néel temperature of bulk CoO [193].

A spin-flop transition at $H_{\mathrm{sf}} \approx 120$ kOe was measured by K. Inagawa *et al* [194]. Inserting this value in Eq. 3.32, and considering the magnetic moment per Co atom obtained by W. L. Roth, the Néel temperature, the lattice constant and the fact that there are 4 Co atoms per unit cell, we obtain a value of the magnetic anisotropy constant of $K = 1.6 \times 10^6$ erg/cm^3 for bulk CoO.

4.4.2 Characterization by TEM

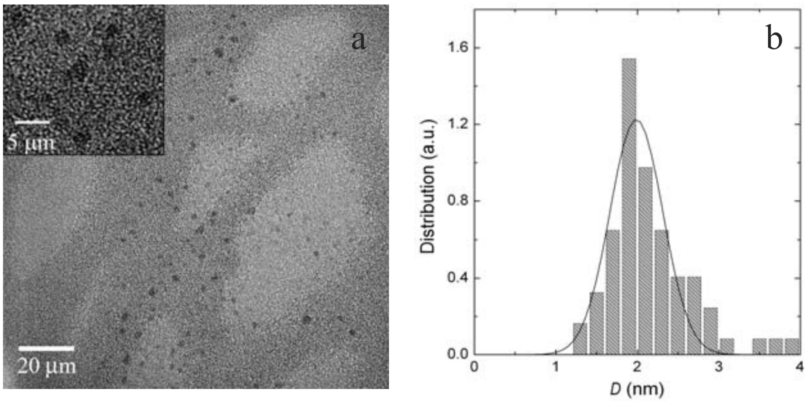

Figure 4.14: a: Typical TEM images of a sample of cobalt oxide nanoparticles in ferritin. The inset is an enlarged picture showing the homogeneity in spherical shape. Black spots represent the inorganic cores, whereas the protein shell is not visible. b: Particle diameter distribution obtained from the analysis of TEM images. The solid line is a Gaussian fit that gives an average diameter of $D = 2.0$ nm and $\sigma = 0.3$

The particle size and shape inside the cavity of the ferritin protein has been studied by means of TEM. These images were acquired by R. de Miguel. Fig. 4.14.a shows a representative TEM image of the particles. As it can be seen, most of CoO inside the nanoparticles is in the form of a unique particle with spherical-like shape. However, in a very limited number of cases with nanoparticle diameters over 3.0 nm, (not-shown in the figure) bean-shaped or several small cores inside a single ferritin can be distinguished. This fact indicates that in the case of the larger nanoparticles the growth takes place from two or three different nucleation centres placed on the inner cavity of the apoferritin. The particle size distribution of the sample was obtained after a thorough analysis of the images obtained by TEM (Fig. S2). The diameter of the nanoparticles ranges from 1.2 to 3.0 nm, with a maximum number of particles (peak of the Gaussian curve) near 2 nm.

4.4.3 Energy-dispersive X-ray (EDX) and X-ray photoelectron spectroscopy (XPS)

Energy-dispersive X-ray (EDX) and X-ray photoelectron spectroscopy (XPS) was performed by R. de Miguel [178]. The EDX analysis enables to determine the average load of cobalt per particle giving an average number of 108 cobalt atoms per protein molecule. On the other hand, the oxidation state of the cobalt can be determined by means of XPS analysis. Clear differences in the experimental spectra obtained on metallic Co (0), Co^{2+} in CoO, and Co^{3+} have been reported [195, 196] providing therefore useful fingerprints for determining the oxidation state of Co. From the experiments performed by R. de Miguel and co-workers it is evidenced that cobalt atoms in our ferritin-based nanoparticles are clearly in the 2+ formal oxidation state occupying octahedral sites, which suggests the formation of CoO. For a more detailed description of this characterization see ref. [197].

4.4.4 Magnetic characterization of CoO-ferritin: the thermoinduced magnetic moment

Magnetic measurements have been performed using a commercial SQUID magnetometer from Quantum Design as described in chapter 1 down to 1.8 K. The region of very low temperatures (down to 13 mK) will be explored in the next chapter where we analyze these questions further. Magnetic measurements shown in this section are presented in units of emu per mol of ferritin-based particle.

4.4.4.1 First considerations: Nanoparticles vs. bulk magnetic properties

In the previous sections we have shown that the properties of our nanoparticles are consistent with the formation of cobalt monoxide. Let us see now what happens with the magnetic properties. The magnetic response of surface atoms differs from that of bulk (or core) atoms due to different effects such as the reduction of the number of neighbours, surface magnetic disorder, spin canting or frustration. Surface effects are strongly influenced by the crystal size, since the surface to core ratio increases as the size is reduced. As a result, the magnetic properties that characterize the bulk material are usually found to be size-dependent. For instance, the decrease of T_{N} and the enhancement of the anisotropy constant are well-known to occur in nanoparticles and have been very often reported in the literature. For instance S. N. Klausen *et al* found that the Néel temperature of AFM disk-shaped NiO nanoparticles with average diameter of 12 nm and thickness of 2.9 nm decreased from the bulk value of $T_{\mathrm{N}}(\mathrm{bulk}) = 523$ K to $T_{\mathrm{N}}(\mathrm{NP}) \approx 460$ K [198]. A. Punnoose *et al* reported that T_{N} of a set of CuO AFM nanoparticles with diameters ranging form 9.1 to 37 nm was also size-dependent giving $T_{\mathrm{N}} \approx 228$ and $T_{\mathrm{N}} \approx 207$ K respectively whereas $T_{\mathrm{N}}(\mathrm{bulk}) \approx 230$ K for bulk CuO [199].

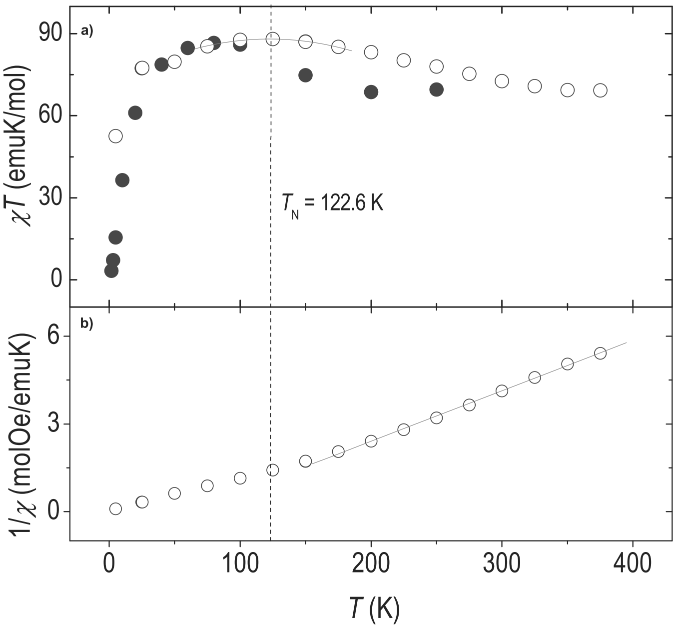

Figure 4.15: Susceptibility of the CoO-ferritin sample vs. temperature. (a) The peak that arises at $T \approx 122.6$ K indicates the transition from the antiferromagnetically ordered regime to the paramagnetic one. (b) Above the Néel temperature, the response of the sample is that of a compound of paramagnetic Co atoms following Curie law.

In order to ascertain wether the antiferromagnetic character of the magnetic structure is preserved, let us first analyze the susceptibility measurements. Fig. 4.15.a shows the antiferromagnetic susceptibility data multiplied by temperature ($\chi_{\mathrm{AF}}T$). This quantity is obtained from the isotherm magnetization measurements using a method described in next section. The plot of $\chi_{\mathrm{AF}}T$ vs. T enables us to determine the transition temperature and also to distinguish between ferromagnetic and antiferromagnetic order. We attribute the broad maximum observed near 100 K to the transition from the paramagnetic to the antiferromagnetic state. The susceptibility of an AFM material tends to a constant value $[\chi_{\mathrm{AF}}(T \rightarrow 0)]$ below T_{N}, therefore $\chi_{\mathrm{AF}}T$ will tend to zero as observed in our data. Above this temperature, $\chi_{\mathrm{AF}}T$ tends to the value corresponding to the susceptibility of the paramagnetic Co ions. Theoretical calculations of such a transition predict an abrupt elbow rather than a maximum (see Fig. 3.8 b). We attribute these differences to surface effects which will be discussed at the end of the chapter.

The Néel temperature is defined at the maximum slope of $\chi(T)$. Since there are too few points at temperatures around the transition, we use the data obtained from magnetization measurements at $H = 100$ Oe and use the temperature at the maximum as the transition temperature. Adjusting the resulting peak to a second order function we obtain $T_{\mathrm{N}} \approx 122.6$ K. Thus, the Néel temperature is ~ 2.4 times lower than T_{N} of bulk CoO. Such reduction is typically attributed to size effects but in our case, additional phenomena must be taken into consideration. As we show in section 4.3, crystalline and magnetic disorder is especially enhanced in ferritin based nanoparticles. Also structural differences with respect to the bulk CoO can appear due to the presence of OH groups. These effects will be discussed in more detail at the end of the chapter (section 4.4.5).

Above the Néel temperature, the magnetic response of the material is paramagnetic (Fig. 4.15.b). It is therefore possible to obtain the value of the net magnetic moment per Co atom μ_{Co} by fitting the high temperature region of the susceptibility with a Curie-Weiss law (Eq. 3.28) Taking $n_{\mathrm{at}} \approx 108$ as the number of Co atoms conforming the nanoparticle, as estimated by the EDX analysis (see section 4.4.3), we obtain $\mu_{\mathrm{Co}} \approx 2.1\ \mu_{\mathrm{B}}$ in quite good agreement with the value reported in the literature for bulk CoO. From this fit we obtain $\theta \approx -54$ K consistent with the fact that antiferromagnetic interactions are preferred between nearest and next nearest neighbours but very different from the value reported by J. R. Singer [193]. This discrepancy will be examined on section 4.4.5.

We can also extract some information about the anisotropy constant from the ac susceptibility data. Following the method described in section 3.6 it is possible to obtain a mean relaxation time ($\bar{\tau}$) by dividing the imaginary part of the susceptibility by the real part and the angular frequency. $\bar{\tau}$ has been determined using the experimental data corresponding to the lowest frequency measured (0.1 Hz), and the data are shown in Fig. 4.16. At low temperatures, the relaxation time remains approximately constant. This is usually found in systems of particles where the magnetic relaxation is dominated by quantum tunneling of the magnetization. Above ~ 3 K the mean relaxation time depends on temperature as one would expect from a classical thermally assisted

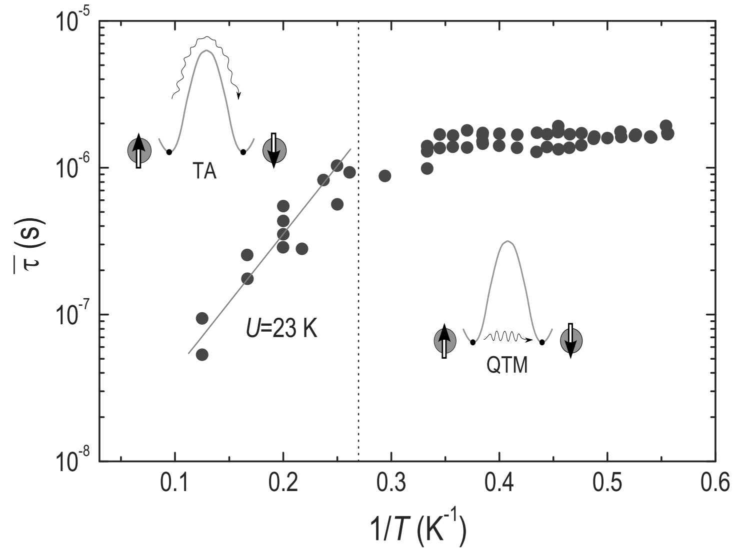

Figure 4.16: Mean magnetic relaxation time obtained from the quotient $\chi''/\chi'\omega$. Fitting the latter to an Arrhenius law it is possible to obtain an estimation of the energy barrier created by the anisotropy ($U \simeq 23$ K).

relaxation process. The fitting of these data to an Arrhenius law (see Eq. 3.6) provides an estimation of the anisotropy constant giving $K = 0.8 \pm 0.1 \times 10^6$ erg/cm^3. however, the latter result must be cautiously taken into consideration. As we discussed in section 3.6, the described method can fail in giving accurate values of τ, especially when there are many or unknown mechanisms involved in magnetic relaxation.

4.4.4.2 Isothermal magnetization measurements: determination of $\chi_{\mathbf{AF}}$

Magnetization isotherms have been measured up to 50 kOe and at temperatures $T = 1.8$, 5, 10, 20, 40, 60, 80, 100, 150, 200 and 250 K. The experimental results are shown in Fig. 4.17. As usual in magnetic nanoparticles, the magnetization increases with the magnetic field, but it does not saturate even for the largest applied fields because of the intrinsec antiferromagnetic susceptibility (χ_{AF}).

The same magnetization data are shown in Fig. 4.18 as a function of H/T. As we argued in section 3.8.1, the complete set of curves does not collapse into one because of the effects of χ_{AF} and the anisotropy field. It is however possible

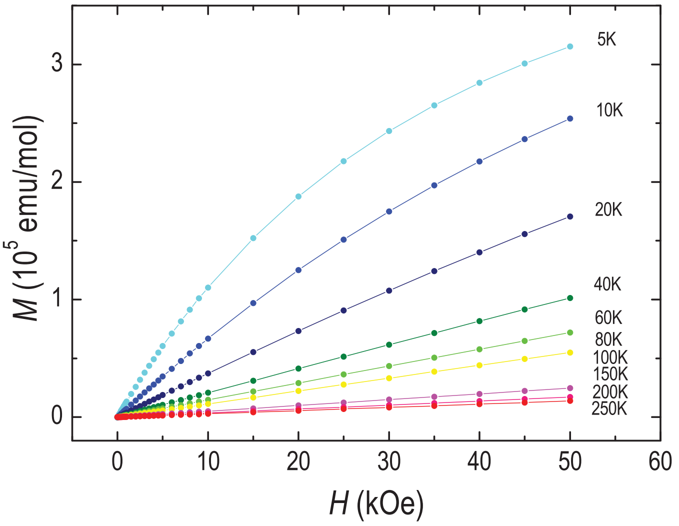

Figure 4.17: Magnetization isotherms measured at different temperatures. Magnetization increases linearly with the field even at the highest temperature studied as a consequence of the antiferromagnetic susceptibility.

to extract information about χ_{AF} from these data as described by [120]. For sufficiently high fields, eq. 3.4 reduces to

$$M \approx \chi_{\mathrm{AF}} T \frac{H}{T} + \mu_{\mathrm{unc}} N \tag{4.2}$$

since the derivative of the Langevin function ($\mathscr{L}(x)$) tends to zero for high values of x. We can therefore obtain the value of χ_{AF} as a function of temperature by a linear fit of the the high field data. The value of χ_{AF} when $T \to 0$ can be calculated by the extrapolation of $\partial M(H)/\partial(H/T)$ to $1/(H/T) \to 0$. By doing so, at $T = 1.8$ K, we obtain $\chi_{\mathrm{AF}}(T \to 0) = 0.70 \pm 0.09$ emu/molOe (see the inset of Fig. 4.18). This value is in quite good agreement with that obtained from a simple mean field theory. The antiferromagnetic susceptibility is then given by $\chi_{\mathrm{AF}} = M_{\mathrm{s}}/H_{\mathrm{E}}$, where H_{E} is the exchange field defined in Eq. 3.30 and M_{s} is the sublattice magnetization in units of emu/mol, defined as $M_{\mathrm{s}} = \mu_{\mathrm{Co}} N_{\mathrm{A}} n/2$ being N_{A} the Avogadro number and n the number of Co atoms conforming the particle. Inserting experimental values in these equations leads to $\chi_{\mathrm{AF}} = 0.55$ emu/molOe.

4.4.4.3 Magnetic susceptibility

The analysis of the initial susceptibility (χ) provides a way to circumvent problems associated with the finite magnetic anisotropy (see section 3.8.1). Dc and ac susceptibility data measured at different frequencies are shown in

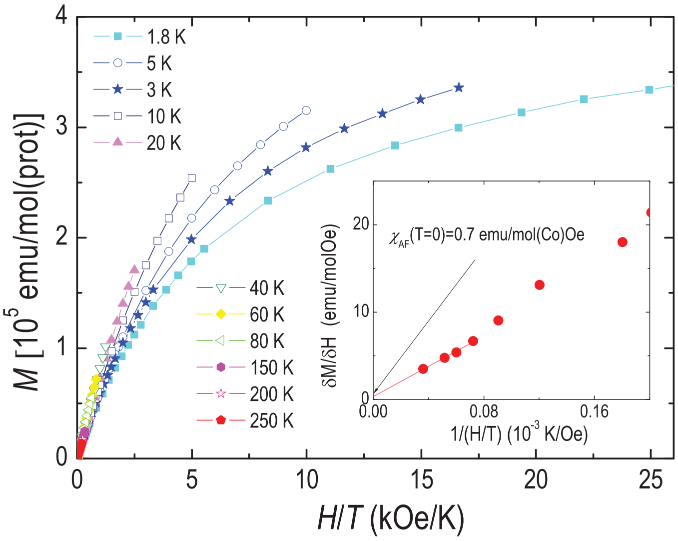

Figure 4.18: Magnetization curves do not scale into one when plotted vs. H/T as an evidence of the strong influence of anisotropy in these particles. The derivative of the magnetization with respect to the magnetic field allows for the determination of the antiferromagnetic susceptibility at $T = 0$ by extrapolating it to $1/(H/T) \rightarrow 0$.

Fig. 4.19. There are no signs of a fully superparamagnetic blocking of the susceptibility down to 1.7 K, although a weak imaginary component (χ") shows up below $\sim$ 10 K. The real part of susceptibility (χ') also shows an appreciable dependence with frequency below this temperature. The latter indicates that thermal fluctuations are no longer sufficient to assist the magnetic moment to overcome the energy barrier created by the anisotropy field. At each temperature, there is a characteristic time for the susceptibility to relax. As frequency increases, the experimental time (τ) decreases and these effects become evident with the reduction of χ' and the emergence of χ". At $T = 1.8$ K and 0.1 Hz ($\tau = 10$ s), the imaginary part represents just a 0.01 % of the total signal indicating that the magnetic response is very close to equilibrium. The experimental time in the dc measurements is one order of magnitude larger ($\tau \approx 200$ s). We can therefore assume that these data correspond to the equilibrium magnetic response of the sample (χ_{T}).

4.4.4.4 Thermoinduced magnetic moment

Let us first analyze qualitatively the magnetic response of our system of CoO-ferritin particles. In Fig. 4.20 we plot the experimental susceptibility, measured at different frequencies, multiplied by temperature (χT). Dc susceptibility data measured at relatively high magnetic fields ($H = 100$ Oe) are

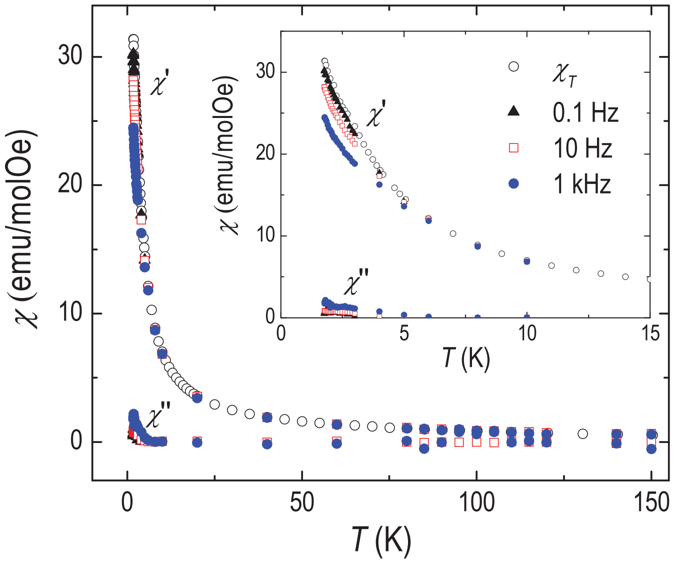

Figure 4.19: Initial susceptibility measurements as a function of temperature. There is no sign of a total blocking of the susceptibility down to 1.8 K, this question will be addressed at the end of next chapter.

shown as well ($\chi_{\mathrm{T}}T$). Experimental data converge above 30 K with $\chi_{\mathrm{AF}}T$ as the Néel temperature is approached. However, at low temperatures the existence of a net magnetic moment gives rise to a large contribution. As temperature decreases, $\chi_{\mathrm{AF}}T$ tends to zero and χT, should therefore tend to a constant value determined by μ_{unc}. By contrast, the experimental data show a pronounced dependence with temperature, which becomes especially noticeable below $T \sim 3$ K. This anomaly strongly suggest the existence of a thermoinduced magnetic moment.

In order to clarify the existence of μ_{th} in our nanoparticles, let us refer to section 3.8.3.2. Eq. 3.47 describes the initial susceptibility response of AFM particles as the sum of three terms. The first two terms contribute to the parallel susceptibility. These are originated by the uncompensated magnetic moment (μ_{unc}) and the thermoinduced magnetic moment (μ_{th}). And the last term arises from the antiferromagnetic susceptibility (χ_{AF}) and contributes to the perpendicular susceptibility. Inserting the expression of the thermoinduced susceptibility obtained by Mørup and coworkers (see Eq. 3.44) in Eq. 3.47 one obtains

$$\chi T \approx \frac{N_{\mathrm{A}}\langle\mu_{\mathrm{unc}}^2\rangle}{3k_{\mathrm{B}}} + \frac{4N_{\mathrm{A}}k_{\mathrm{B}}T}{3H_{\mathrm{A}}H_{\mathrm{B}}} + \chi_{\mathrm{AF}}T \tag{4.3}$$

The latter is valid only at sufficiently low temperatures where just the

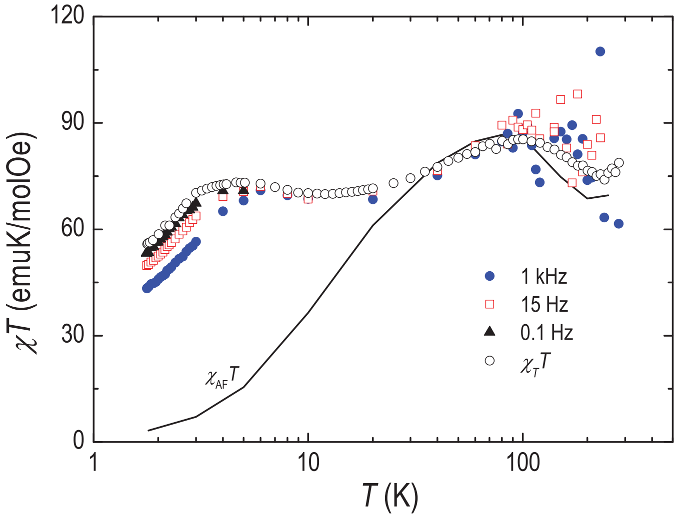

Figure 4.20: Magnetic susceptibility multiplied by temperature. Three regimes are visible; at low temperatures up to ~ 3 K, susceptibility increases considerably with temperature in agreement with that predicted by the thermoinduced magnetic moment theory. Above this temperature, such contribution disappears and susceptibility is only influenced by the uncompensated magnetic moment and the antiferromagnetic susceptibility. The later increases as well with temperature up to the Néel temperature when the response of the sample is that of a compound of paramagnetic Co atoms.

homogeneous ($q = 0$) mode is populated. The energy of this mode (E_0) will be given by Eq. 3.43. Inserting the expression of E_0 in Eq. 4.3 and multiplying it by temperature one gets

$$\chi T \approx \frac{N_\mathrm{A} \langle \mu_\mathrm{unc}^2 \rangle}{3 k_\mathrm{B}} + \frac{8}{3} N_\mathrm{A} k_\mathrm{B} \left(\frac{g \mu_\mathrm{B}}{E_0} \right)^2 T^2 + \chi_\mathrm{AF} T \tag{4.4}$$

Thus, the uncompensated magnetic moment gives a constant contribution to χT. On the other hand, the dependence of $\chi_\mathrm{AF} T$ with T is not trivial but it has already been experimentally determined in section 4.4.4.2. The latter can be subtracted from the experimental data to obtain the intrinsic magnetic response of the nanoparticles $\chi^\mathrm{NP} T = \chi T - \chi_\mathrm{AF} T$. The resulting data are depicted in Fig. 4.21 as a function of temperature. As we can see, $\chi^\mathrm{NP} T$ follows the dependence deduced from Mørup's theory (see Eq. 4.4) up to 3 K when it dramatically falls to zero. These data clearly evidence that μ_th is playing a significant role below 3 K

Up to now, the theory of the thermoinduced magnetic moment had provided a good qualitative explanation of the experimental data. Let us see now

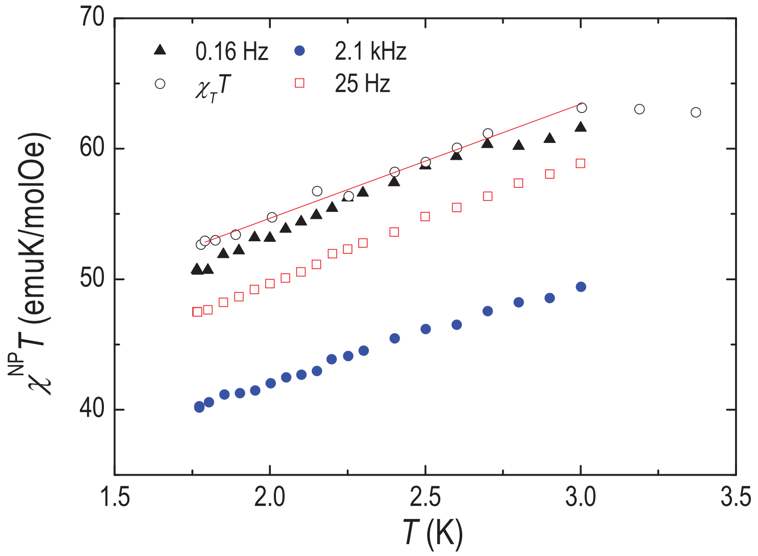

Figure 4.21: Intrinsic magnetic response of the nanoparticles ($\chi^{\mathrm{NP}}T$). This is obtained by subtracting the antiferromagnetic susceptibility from the experimental data shown in Fig. 4.20. $\chi^{\mathrm{NP}}T$ increases linearly with T^2 as predicted by Mørup's theory.

whether it can provide a quantitative account for the experimental results as well. As we explained in section 3.8.1, the existence of μ_{th} is related with the fact that only the ground state is populated in nanoparticles of antiferromagnetic materials, having energy E_0. The energy of this state depends on the size of the particle since modes with wave length larger than the particle size can not be sustained. This energy can be calculated by using the dispersion relation given by Eq. 3.42 for $q = \pi/d$, considering for simplicity a cubic nanoparticle with side length d. The population of the first non-homogeneous mode ($q = 1\pi/d$) will occur above a certain temperature that depends on the energy of the first excited state (E_1) and so on. The contribution of μ_{th} disappears as inhomogeneous states of progressively higher energy are populated. Using the values for the Néel temperature and anisotropy constant that we obtained experimentally in section 4.4.4.1, we can now determine the value of these energies and therefore the temperature threshold for the apparition and vanishing of the thermoinduced susceptibility. The values of the exchange and anisotropy fields can be calculated from Eq. 3.30 and 3.31 respectively. Inserting these values, the lattice parameter $a = 4.25$ Å and the number of nearest neighbours $nn = 12$ in Eq. 3.42, we obtain $E_0 = 12$ K, $E_1 = 62$ K and $E_2 = 122$ K. Using Eq. 3.48 we obtain $T_{\mathrm{th}} = 41$ K as the threshold temperature above which the contribution of the thermoinduced magnetic moment to the susceptibility dominates over the contribution due to the uncompensated magnetic moment. The theory of spin waves in antiferromagnets would therefore account for the apparition of the thermoinduced susceptibility at temperatures above $T_{\mathrm{th}} = 41$ K where only the uniform mode is populated followed by an increasing of the latter until a temperature of ~ 60 K in which μ_{th} is progressively canceled leading to a decrease of the experimental net susceptibility. What we actually observe in our system is that the thermoinduced susceptibility shows up below 1.7 K and disappears at about 3 K. Concluding, the experimentally determined energies of the magnetic excitations spectra are, by more than one order of magnitude, smaller than those predicted by the classical theory of spin waves in antiferromagnets.

To finish this section let us extract some information about the uncompensated magnetic moment μ_{unc}. According to Eq. 4.4, we can do that by a linear fit of $\chi^{NP}T$ vs. T^2 giving $\mu_{\mathrm{unc}} = 17\ \mu_{\mathrm{B}}$. As we introduced previously, L. Néel proposed that this moment could be accounted by the imperfect sublattice compensation in small particles. The relation between μ_{unc} and the atomic magnetic moment μ_{Co} is given by

$$\mu_{\mathrm{unc}} = \mu_{\mathrm{Co}} n_{\mathrm{at}}^{\gamma} \tag{4.5}$$

where n_{at} is the number of magnetic ions conforming the particle, and the exponent γ varies between 1/3 and 2/3 depending on the degree of disorder. Values close to 1/2 have been reported for ferritin particles with varying Fe content [99, 134]. This result is explained by the fact that the spin disorder, which gives rise to the net magnetic moment, is not restricted to the surface, but extends to the whole particle [114]. For the case in which disorder only affects the particle surface, a value of 1/3 will be expected [114]. Taking into account that our clusters consist of a nominal number of $n_{\mathrm{at}} = 108$ Co atoms, and using the experimental magnetic moment of Cobalt $\mu_{\mathrm{Co}} \approx 2.1$ μ_{B}, we obtain a value of $\gamma = 0.45$ suggesting that the magnetic order of the core is also disturbed. As we have seen in section 4.3.5, magnetic disorder in magnetoferritin particles is also quite large and affects not only the surface but the core as well. These results suggest that disorder enhancement is a general feature of ferritin-based nanoparticles and it is a consequence of the characteristic growth mechanism employed by the protein.

4.4.5 Conclusions: size effects

Nanoparticles undergo a magnetic transition at a temperature ~ 2.4 times smaller than the bulk material. Such effect is very commonly founded in systems of nanoparticles of ferro or antiferromagnetic materials [198, 199]. The reduction of T_{N} is a direct consequence of the increase of the surface to volume ratio when size is diminished. Atoms lying at or close to the surface are lacking in nearest and next nearest neighbours. The effective exchange coupling of all the atoms conforming the whole particle is therefore reduced leading in a decrease of T_{N}. Our nanoparticles are so small that they consist of just ~ 108 Co atoms. That means that approximately $\sim 71\%$ of the atoms lie at the surface having non-complete number of nearest neighbours. In addition, exchange interactions can be particularly affected in our especial case for two reasons: first, the enhanced magnetic disorder found in ferritin based nanoparticles (see section 4.3 and Fig. 4.10), and secondly, the possibility of structural changes in the oxide due to the presence of OH groups. Under these circumstances, a considerable reduction of the effective exchange constant is expected. The same arguments apply to the change of θ. This parameter is very sensitive to interactions within the sublattice, that is, to interactions with next nearest neighbours. The experimental value of θ is still negative but it is considerably increased from the bulk one, meaning that non-nearest neighbour interactions are still effectively antiferromagnetic but there is a ferromagnetic contribution. This fact would be responsible as well for the slight increase of χT as temperature decreases down to the Néel temperature (see Fig. 4.15). Anion vacancies at the surface and spin canting can lead to ferromagnetic interactions to be energetically preferred on the surface.

Finally, the observation of the thermoinduced magnetic susceptibility constitutes an important size effect as well. The influence of μ_{th} becomes apparent at low temperatures, when just the ground state of AFM spin waves is populated. The gap between the ground and the excited states increases when decreasing the size of the crystal, for this reason, the latter effect plays a more important role in nanoparticles, becoming measurable. Notice that the magnitude of μ_{th} does not depend on size but the possibility to observe this contribution indeed does.

The energy scales of the spin excitations involved in the rising of μ_{th} found experimentally deviate however drastically from those expected using the classical theory of spin waves in bulk AFM materials. This quantitative disagreement could be associated with the influence of finite-size effects in the magnetic excitations of nanoscaled systems as it has been theoretically predicted. [200, 201] In particular, the lifetime of low energy wavemodes, and especially the uniform mode $q = 0$, seems to be strongly reduced in nanoparticles of CoO compared with their analogues in the bulk material. [202] This fact leads to the existence of new pairs of excitations having $q \neq 0$ that can account for the premature cancelation of μ_{th} observed here.

Chapter 5

Magnetic Measurements on 2-D Arrays of Magnetic Nanoparticles

5.1 Introduction

Single molecular magnets (SMM) and magnetic particles under the micron scale are promising candidates for many applications and are also very interesting from a scientific point of view due to its rich physical behavior [9, 203]. Applications cover very different fields from medicine to information technology and very often demand multi- or monolayer patterns, e.g. in quantum computation or high density storage media [204]. Although much effort has been done, the preservation of their magnetic properties under these circumstances remains still unclear and the reason is the lack of appropriate characterization techniques. Traditional bulk techniques are pointless since they do not fulfill the high sensitivity required for these measurements. To illustrate this, let us take as an example the SMM $\mathrm{Mn_{12}Ac}$ and let us assume that its magnetic behavior is not modified when it is arranged as a monolayer. These clusters present a net magnetic moment of 20 μ_B arising from non compensated spins on their structure. The ac magnetic susceptibility of $\mathrm{Mn_{12}Ac}$ at 4.2 K and 1 Hz is of about 10 emu/molOe. If we prepare a monolayer of this material, covering an area of 10 μm × 10 μm, it would produce a signal of just 10^{-14} emu when an ac magnetic field of 10 Oe is applied. This signal is far below the sensitivity of commercial SQUID magnetometers, which is usually of the order 10^{-8} emu.

The use of synchrotron-based techniques like X-ray absorption spectroscopy

(XAS) and X-ray magnetic circular dichroism (XMCD) at low temperatures provides enough sensitivity to overcome these problems. For instance, M. Mannini *et al* measured successfully the magnetic properties of Mn_{12} [205] and Fe_4 monolayers [206] on gold surfaces. However, these techniques imply the use of very sophisticated facilities and the analysis of the experimental data is not straightforward. Local magnetic probes like spin-polarized scanning tunneling microscopy [207,208] or magnetic force microscopy [209] provide excellent spatial resolution but time dependent measurements are difficult due to the sample tip interaction. Direct characterization techniques like micro-Hall or microSQUID magnetometers show much more attractive capabilities. These sensors enable simple measurements, low temperatures characterization and provide a direct measurement of the magnetic moment or magnetic susceptibility. For instance, using a micro Hall gradiometer, Y. Li *et al* [210] reported measurement of the magnetization switching of a single Fe nanoparticle ($\mu \sim 5 \times 10^5\ \mu_{\rm B}$). Unfortunately, the field sensitivity deteriorates rapidly when Hall sensors are reduced to the submicron size. SQUID-based sensors are promising candidates to be the most sensitivity magnetometers in the solid state. Energy sensitivity is not theoretically restricted down to the quantum limit ($\mu_{\rm B}$), however, it strongly depends on spatial and fabrication considerations [211]. The smallest spin population successfully measured to date was a single 1000-atom cobalt cluster with $\mu \sim 10^3\ \mu_{\rm B}$ [19].

As we just advance, another major issue that should be considered is the coupling between sample and sensor. The flux coupled to a coil strongly depends on the particle location with respect to the coil boundaries [17]. Therefore, depositing the sample with a high spatial resolution is crucial, since it is critically related to the magnetic sensitivity. This motivation and many other applications, like molecular electronics or biosensors [204], stimulated the use of several micro- and nano- fabrication techniques, i.e. electron beam lithography [212], electrodeposition [213], scanning tunneling microscope lithography [214], manipulation via atomic force microscopy tip [215] or dip pen nanolithography (DPN) [24]. The last one has been used here to deliver ferritin particles with nanoscale precision over pre-selected areas of the sensor. Ferritin acts not only as a confined reaction vessel for the synthesis of nanoparticles but, it also provides an excellent carrier which can be easily patterned and immobilized over different substrates [23].

On the other hand, the interest of optimizing the coupling between magnetic particles and superconducting microcircuits is not restricted to the detection of minute magnetic signals. Recent efforts directed towards the development of feasible and practical quantum computers have driven researchers to explore hybrid quantum architectures [216]. The latter are based on the combination of different elements that have been up to now independently surveyed: artificial superconducting qubits and spin ensembles connected via microwave photons or superconducting microcircuits [217]. In the latter case, measuring and maximizing the magnetic coupling between spins and the superconducting microwires becomes a matter of paramount importance since it is related with the rate at which a quantum operation can be performed.

In this chapter we present magnetic measurements performed on 2 dimensional arrays of magnetic nanoparticles fabricated by DPN. For this purpose, ferritin-based antiferromagnetic nanoparticles of CoO described in the previous chapter have been chosen as model system. We demonstrate that magnetic nanoparticles can be easily deposited on the most sensitive areas of the sensor and that direct magnetic measurements are feasible. Furthermore, we will extract new information supporting the existence of the thermoinduced magnetic moment and its dependence with temperature. Measurements from high temperature ($>$ 100 K) down to the vicinity of absolute zero (13 mK) enable us to observe all the regimes predicted theoretically.

5.2 Dip-pen Nanolithography and ferritin-based particles: an ideal combination

Dip-pen nanolithography (DPN) is a direct-writing technique that enables the immobilization of different particles on pre-selected areas of a wide variety of surfaces. First, we present the basic operation of DPN and its application to deposit ferritin particles over the surface of our sensor with microscopic space control [23]. A relatively accurate number of deposited proteins is also possible [218] giving us the opportunity to study the relation between the flux coupling per particle and its position.

5.2.1 Introduction to DPN

The writing instrument that dominated for the longest period in History (over one-thousand years) was the quill pen. On the 19th century, this tool was replaced by the dip pen, based on the same idea as its precursor. A dip pen consists of a metal nib with capillary channels. The ink is recharged from an ink bowl and is then drawn from the nib to the paper via a combination of gravity and capillarity [219]. In 1999, R. D. Piner *et al* [24], applied the same technique to develop a new lithography method to direct-write collections of molecules on surfaces. This technique was called ”Dip-Pen” Nanolithography (DPN) because of the analogy with the traditional dip pen writing method. DPN uses an atomic force microscopy (AFM) tip as a ”nib”, a solid-state substrate as ”paper”, and a solution containing the molecules as ”ink”. The AFM

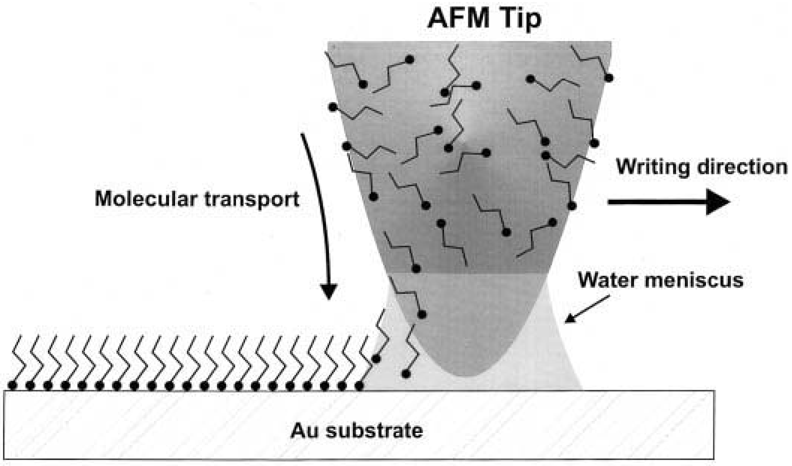

Figure 5.1: Illustration of the DPN writing procedure. Figure extracted from reference [24]

tip is first coated with the desired solution and then brought into contact with the surface. Capillarity transport of the molecules from the tip to the surface via a water meniscus enables the successful deposition of small collections of molecules in submicrometer dimensions (see Fig. 5.1). R. D. Piner *et al* reported experiments showing the successful deposition of 1-octadecanethiol (ODT) molecules on Au surfaces. For instance, arrays of 25 dot-like features 0.46 μm diameter, spaced 0.54 μm were prepared. DPN appeared as a simple but very powerful deposition method. It enables the creation of arbitrary shapes (see Fig. 5.2) or the deposition of several kind of molecules on surfaces [220] without the necessity of arduous patterning steps. The writing speed can be increased by the use of several tips for parallel writing [221]. A wide variety of biomolecules have been patterned with the use of DPN while preserving their biological activity, e.g. functional proteins [222], antibodies [223] and DNA molecules [224]. DPN deposition has also been extended to different surfaces like silicon or gallium arsenide [225] and metallic (Pt, Au, Ge, Ag, Cu and Pd) and semiconductor nanostructures have also been reported [226]. The best reported feature resolution to date, is $\approx$ 15 nm for alkanethiol inks on single-crystal gold surfaces [221].

5.2.2 Application to ferritin

Ferritin behaves as an ideal carrier to be used in combination with the direct-writing capabilities of DPN. Ferritin proteins have been indeed successfuly immobilized on a wide variety of surfaces (gold, silicon. niobium and aluminium) [23] by E. Bellido and co-workers [227]. In these experiments, the

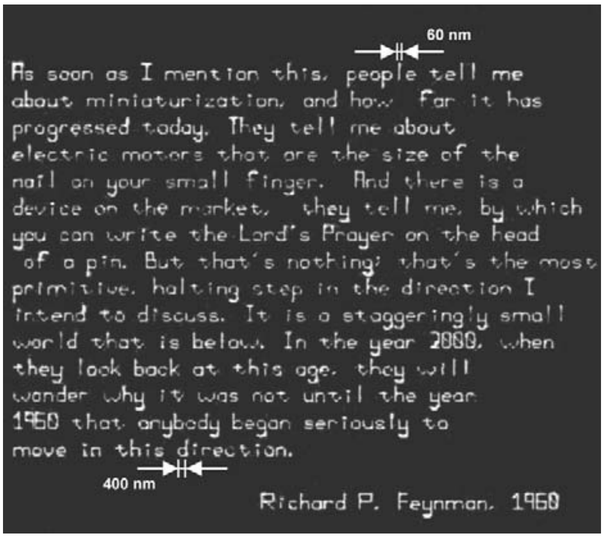

As soon as I mention this, people tell me
about miniaturization, and how far it has
progressed today. They tell me about
electric motors that are the size of the
nail on your small finger. And there is a
device on the market, they tell me, by which
you can write the Lord's Prayer on the head
of a pin. But that's nothing; that's the most
primitive, halting step in the direction I
intend to discuss. It is a staggeringly small
world that is below. In the year 2000, when
they look back at this age, they will
wonder why it was not until the year
1960 that anybody began seriously to
move in this direction.

Richard P. Feynman, 1960

Figure 5.2: Feynman's speech written with organic molecular ink on a gold surface via dip pen nanolithography in 1999

protein ink solution was prepared with a mixture of 80% commercial horse spleen ferritin with 20% glycerol. The use of glycerol enhances the molecular ink viscosity, favoring the tip coating and the transference from the tip to the surface. It also enhances the ink activity by inhibiting dehydration. The AFM tip is coated by dipping it into a microwell containing the latter solution. Bringing the coated tip in contact with the substrate, dot-like features of the protein solution are created on pre-selected areas of the surface. The resulting arrays have been characterized by optical microscope (Fig. 5.3 (a)) and AFM (Fig. 5.3 (b)). Tapping mode AFM (TMAFM images) reveal an averaged height per dot of 10 ± 2 nm (see Fig. 5.3 (c)), consistent with the size of a single ferritin (12 nm), confirming that proteins form a (sub)monolayer. Adjusting the tip-substrate contact time, it is possible to control the size of the dot-like feature miniaturizing it down to 100 nm in diameter.

5.2.3 Controlling the number of deposited proteins

The experimental determination of the number of deposited proteins per dot is not a trivial issue due to the limited resolution of characterization techniques to identify individual molecules deposited by DPN. To overcome these problems, E. Bellido *et al* [218] developed recently a novel strategy to directly quantify the number of particles written with DPN. By writing the ferritin dot-like features directly on the surface of transmission electron microscopy (TEM) grids, the identification of individual proteins becomes possible thanks

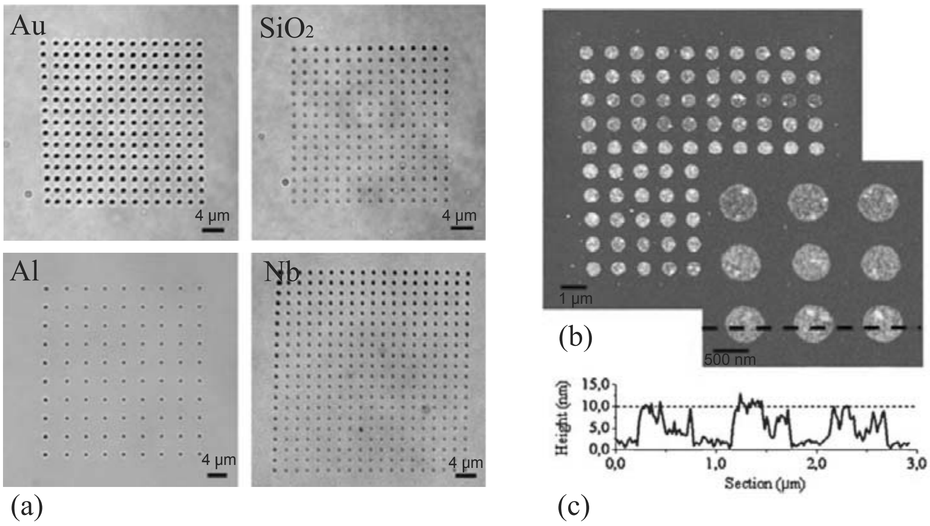

Figure 5.3: Ferritin arrays fabricated by DPN. (a) Optical images of the dot-like features on different substrates. (b) AFM image of a ferritin array printed on gold with 500 nm-in-diameter dot-like features. (c) Height profile that corresponds to the last row of the 3 × 3 dot magnification on (b).

to the ferric core of natural ferritin. E. Bellido *et al* found that the number of ferritin particles per dot (N) depends on two experimental parameters: the concentration of the ferritin solution used to coat the AFM tip and the dimension of the dot-like feature generated by DPN. N will be given by the formula

$$N = 1.389 \times 10^{-6} C r_b^3 \tag{5.1}$$

where C is the concentration and r_b is the radius of the dot-like feature. The validity of Eq. 5.1 was experimentally confirmed with the fabrication of numerous arrays in which the number of proteins was controlled by means of C or r_b variation. For instance, by considering the dot-like features with a diameter of 150 nm, they calculated the theoretical ferritin concentration to immobilize 10, 5 and eventually 1 units from Eq. 5.1. These experiments were performed and the average number of particles founded was 10.5 ± 1.5, 4.9 ± 1.4 and 1.4 ± 0.2 (see. Fig. 5.4). For the latter case, 100 dots were studied, 36 of them contained only one particle, and none of them contained more than 4 particles.

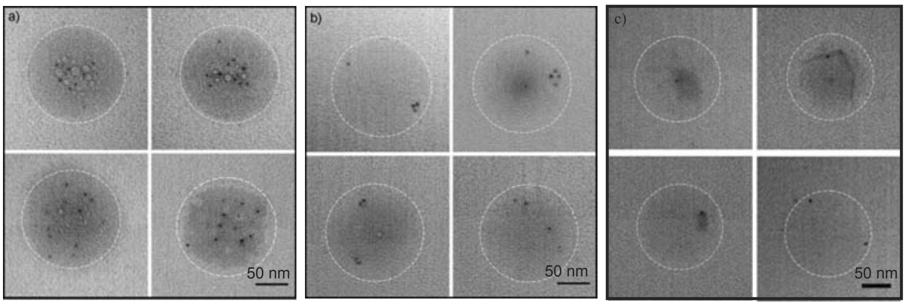

Figure 5.4: TEM images of the dot-like features generated by DPN using different concentrations to obtain a) 10 particles per dot, b) 5 particles per dot and c) 1 particle per dot.

5.3 Fabrication of ferritin arrays on the surface of the μSQUID sensor

The extraordinary direct-writing capabilities of DPN have been used to fabricate 2 dimensional dots containing ferritin on the surface of one of our first-generation μSQUID susceptometers. The tiny magnetic signal produced by this arrangement will challenge the sensitivity of the sensor to its limit. For this reason, it is very important to determine first the regions in which ferritin particles will couple the most flux into the pickup coils. In this section we describe first the theoretical calculations we have performed in order to determine these 'most active' areas. We describe next the fabrication process of the ferritin dots that has been carried out by E. Bellido. The ferritin samples used in these experiments are those containing nanocrystals of CoO. The reasons for this choice will be described at the end of this section.

5.3.1 Array design: coupled flux optimization

The magnetic susceptibility is detected by means of the variation of the mutual inductance (ΔM) between the primary coil and the secondary (pickup) coil originated by the presence of a magnetic moment μ in the neighborhood of these coils. ΔM is proportional to the susceptibility through

$$\Delta M = MF'\chi \tag{5.2}$$

where M is the mutual inductance of the empty susceptometer, χ is the volume magnetic susceptibility of the sample and F' is a geometrical factor usually called filling factor (see Chapter 2 for more details). The geometry of the device plays therefore a major role on the susceptometer performance. Measurements shown in chapter 2 (see section 2.7.6) were carried out on large crystals, in the sense that their size was comparable with the size of the pickup coil loop. Since our aim is to perform measurements on a monolayer particle array, we should examine first some geometrical considerations that are relevant to achieve the ultimate goal of maximizing the coupling between sample and coil.

We need to calculate the magnetic field originated by a magnetic moment μ and hence, the magnetic flux coupled to the pickup coil ϕ_{coupled}. Calculations appear much easier if we take into account the fact that sources and fields can be interchanged (see Fig. 5.5). This relationship can be formulated as [1]

$$\phi_{\text{coupled}} \cdot i_{\text{P}} = |\vec{\mu} \cdot \vec{B}_{\text{P}}| \tag{5.3}$$

The latter means that we can also solve the equivalent problem of evaluating the magnetic field created at the sample position (B_{P}) by a current i_{P} flowing through the pickup coil.

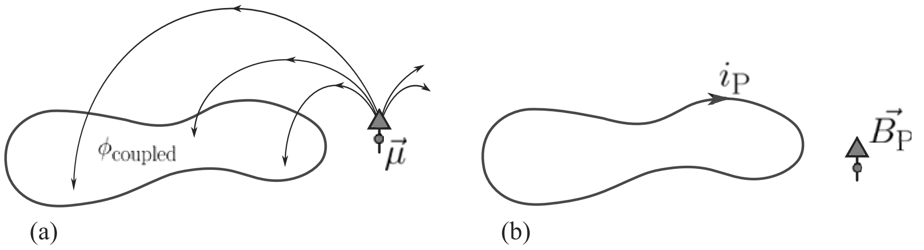

(a) (b)

Figure 5.5: Schematic representation of expression 5.3. (a) We consider first a dipole with magnetic moment μ and a coil of arbitrary form. A magnetic flux ϕ_{coupled} will be coupled to the coil as a consequence of the magnetic field created by μ. (b) The equivalent problem would be to evaluate the magnetic field B_{P} created at the dipole position by a current i_{P} flowing thorough the coil.

Let us introduce now the concept of loop/dipole coupling factor α as the coupled flux per unit of magnetic moment. Using formula 5.3 and using the fact that $\vec{\mu}$ is, under the conditions of our interest, parallel to $\vec{B}_{\text{P}}$, α can be calculated as

$$\alpha = \frac{\phi_{coupled}}{\mu} = \frac{B_{\text{P}}}{i_{\text{P}}} \tag{5.4}$$

First we will examine a very simple situation, in order to understand the strong relation between α and the location of the magnetic dipole with respect to the pickup coil. Let us consider the situation depicted in Fig. 5.6.a where a magnetic dipole is placed at the center of a loop. The total magnetic flux coupled to the coil is evaluated by means of the integration of the magnetic

---

[1] Expression 5.3 can be demonstrated in a straightforward way by expressing the magnetic flux coupled to the pickup coil as $\phi_{\text{coupled}} = \oint \vec{A} \cdot d\vec{l}$ where $\vec{A}$ is the vector magnetic potential which, in the case of a magnetic dipole, equals $\vec{A} = \vec{\mu} \times \vec{r}/r^3$. Expression 5.3 can be easily obtained by using the vectorial identity $(\vec{\mu} \times \vec{r}) \cdot d\vec{l} = (\vec{r} \times d\vec{l}) \cdot \vec{\mu}$ and the Biot-Savart law.

field lines going through the area inside the coil. Lines labeled 2–11 will not contribute to the integral since they traverse the area twice in opposite directions. Only lines labeled 1 and 12 will have a non-zero contribution to the net flux. Under conditions depicted in Fig. 5.6.b only lines 7–12 are canceled whereas lines 1–6 contribute to the net magnetic flux. From these arguments we can expect that α increases as samples are placed closer to the coils.

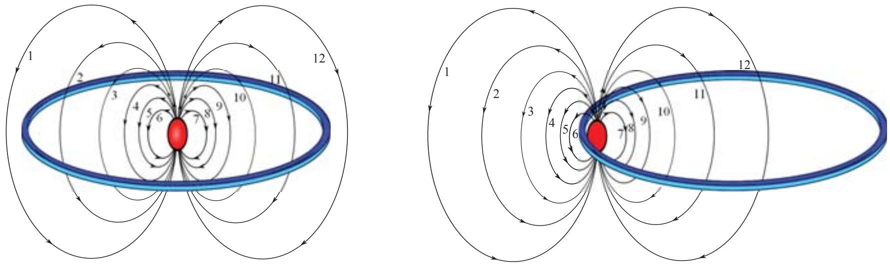

(a) (b)

Figure 5.6: Scheme of magnetic flux lines coupled to a circular coil in two situations. (a) The dipole is placed on the center of the loop. (b) The dipole is placed close to the coil wire.

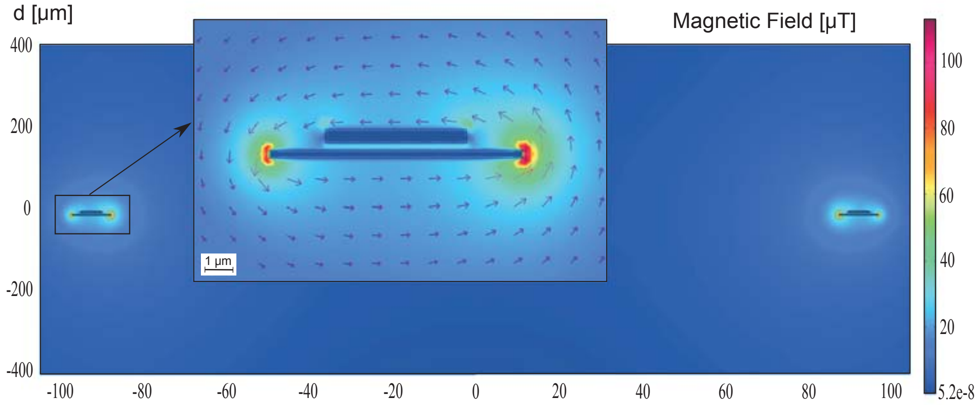

Figure 5.7: Cross section view of the magnetic field created by a current $i = 500$ μA passing through the pickup coil. The inset shows an amplification of the region near to the wire.

We can now determine quantitatively the value of α taking into account the actual geometry of our susceptometer as mentioned before. This problem is reduced to the evaluation of the magnetic field created by a current flowing through the pickup coil. For the sake of simplicity, we approximate the actual shape of the pickup coils to a circular loop with effective radius $r_{eff} = (A/\pi)^{1/2}$ where A is the area of the coil. Inserting real values for A one obtains $r_{eff} =$ 85 μm. The pickup coil (cross section dimensions 9 μm $\times$ 300 nm) is covered with a SiO_2 250 nm-thick layer and finally with the primary coil (5 μm $\times$ 500 nm). With these considerations we can simulate the magnetic field on a plane perpendicular to the coils using COMSOL Multiphysics software[2]. As we can see in Fig. 5.7, the magnetic field becomes largest in the vicinity of the coils, which implies an enhancement of α. We will therefore, refer to these region as the "active area" of the sensor. Now we can obtain α from Eq. 5.4 as a function of the distance from the pickup coil wire towards center of the coil. As we can see in Fig. 5.8, the value of α is enhanced nearly by two orders of magnitude when the samples are deposited on the closest position to the pickup coil wire's edges.

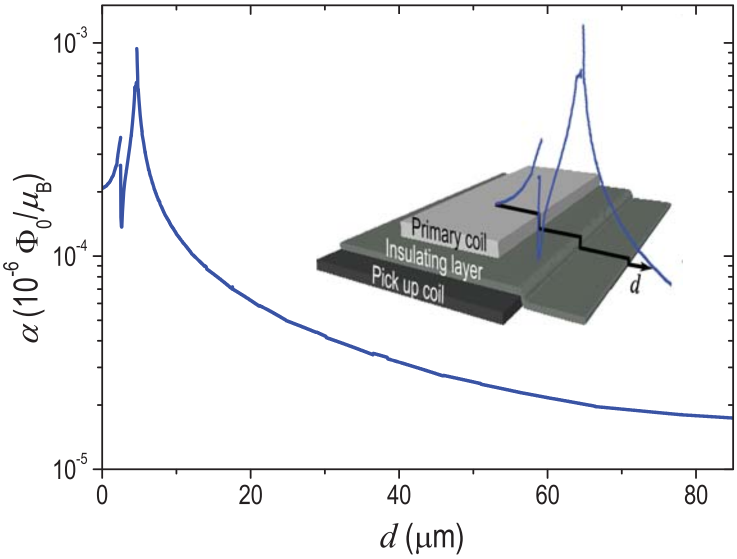

Figure 5.8: Coupling factor α as a function of distance from the center of the pickup coil wire towards the center of the coil. The inset shows a 3-D illustration of the cross section of the pickup and primary coil wires where the α profile has been superimposed (blue line). The black line indicates the region over which α has been computed.

As we introduced in Chapter 2, a susceptometer provides a signal proportional to the susceptibility of a sample located within the pickup coils, that is to say, to the magnetic moment induced in the sample by the field created by the primary coil (B_{P}) along its direction. For these reasons, it will be more convenient to introduce the concept of coupling factor in terms of susceptibility α_{χ}. the latter can be defined as the coupling factor α multiplied by $B_{\mathrm{P}}/i_{\mathrm{P}}$ to account for the fact that the magnetic moment is induced by the

---

[2] To simulate superconductivity we impose the magnetic potential A to be constant inside the coils. Setting $A_{\mathrm{pu}} = 2.99 \times 10^{-14}$ Wb/m in the pickup coil and $A_{\mathrm{P}} = 2.93 \times 10^{-14}$ Wb/m in the primary coil, results in the raising of a current $i_{pu} = 500$ μA and $i_{\mathrm{P}} \approx 0$ μA [228].

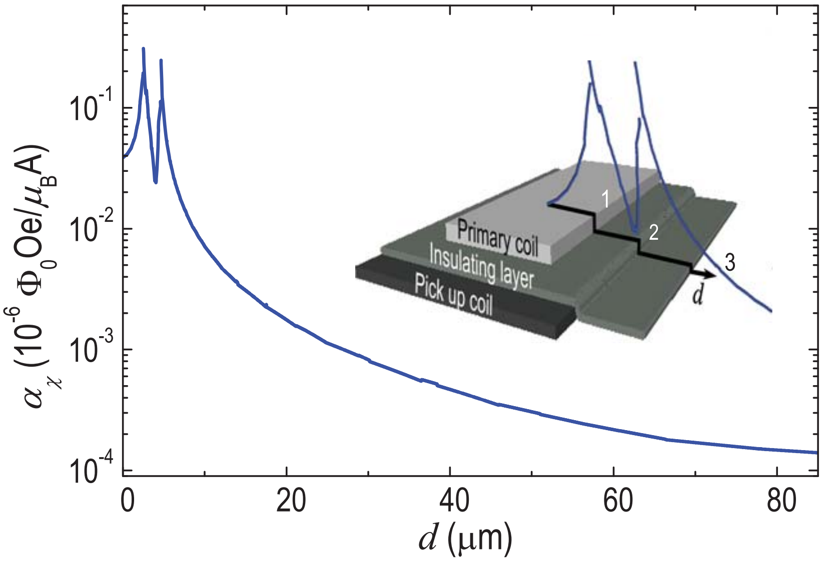

Figure 5.9: Numerical calculations of the coupling factor α_χ as a function of distance from the center of the pickup coil wire towards the center of the coil. The inset shows a 3-D illustration of the cross section of the pickup and primary coil wires where the α_χ profile has been superimposed (blue line). The black line indicates the region over which α_χ has been computed. The most "active" areas corresponds to the regions of maximum α_χ denoted as 1 and 2 in the inset.

magnetic field B_{P} created by a current that circulates through the primary coil (i_{P}). For small values of the applied field, the induced magnetic moment will grow linearly with B_{P}, and the proportionality constant will be the initial susceptibility of the sample χ. Taking into account this relation, α_χ can be written as

$$\alpha_\chi = \frac{\phi}{N\chi i_P} = \frac{B_{pu}B_P}{i_{pu}i_P} \tag{5.5}$$

Where N is the number of particles and χ is the magnetic susceptibility given in emu/mol. The magnitude of B_{P} has been computed using COMSOL software as well. In this case, it must be taken into account that a screening current will rise in the pickup coil since it is a superconducting close circuit. The effect of such current will be the reduction of the net magnetic field created by the primary coil [3]. Theoretical calculations of α_χ are shown in Fig. 5.9. α_χ has been evaluated over the surface where the particles will be actually

---

[3] In this case setting $A_{\mathrm{P}} = 7.9 \times 10^{-15}$ Wb/m in the primary coil and $A_{\mathrm{pu}} = 5.6 \times 10^{-15}$ Wb/m in the pickup coil results in the raising of a current $i_{\mathrm{P}} = 500$ μA and $i_{pu} = -413$ μA.

deposited. As we can see, the coupling is enhanced by more than three orders of magnitude when the samples are deposited on the closest position to the pickup coil and primary coil's edges meaning an enhancement of the electrical signal of the same order. Achieving the goal of detecting the magnetic signal of a particle monolayer implies that our sensor will work close to its limit of sensitivity. For this reason, a micrometric control over the particle deposition will be the decisive factor, since only particles located on the active areas of the sensor will have an appreciable contribution to the net signal.

5.3.2 Ferritin arrays fabricated by DPN on the sensor surface

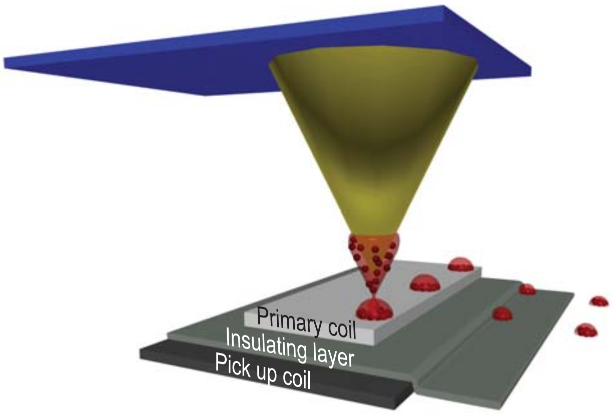

Figure 5.10: Schematic of the DPN deposition process onto the most active areas of the sensor, as it has been determined from the calculations shown in Fig. 5.9.

CoO-ferritin nanoparticles have been deposited as described in 5.3.2 by E. Bellido [227] onto the most active areas of the sensor that have been previously determined (see Fig. 5.9 and 5.10). Three rows have been patterned, each one composed of a series of dot-like features separated by 4 μm, that means that we have $\sim$ 150 dots per row approximately. The first row lies over the pickup coil (region 1 in Fig. 5.9) and every dot furnishes approximately 2×10^4 proteins. The second and third row have been deposited at $\sim$ 500 nm and $\sim$ 4.5 μm from the inner part of the pickup coil, corresponding to regions 2 and 3 in Fig. 5.9 respectively. These dots are smaller in size as it can bee seen in the image and furnish approximately 10^4 proteins. Thus, the total number of patterned proteins is about 10^7. Taking this into account and the positions of these dots with respect to the coil boundaries, the theoretical estimated average value of the coupling factor per particle will be of the order of $\bar{\alpha}_\chi = 0.10(1)$ μmΦ_0Oe/μ_BA.

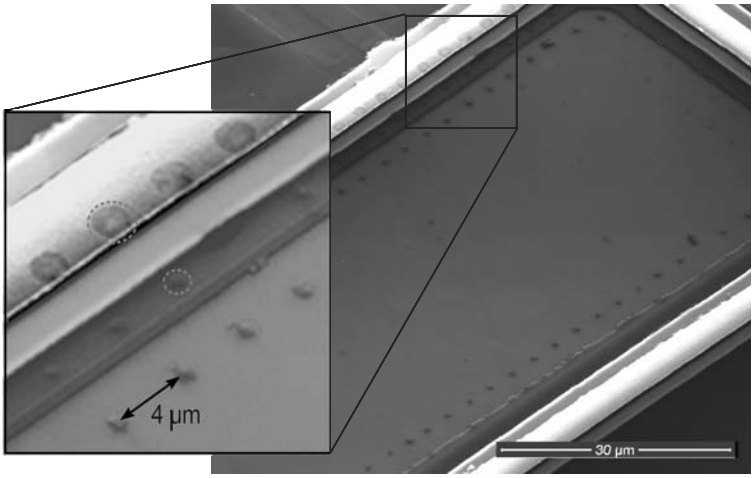

Figure 5.11: SEM image of the ferritin arrays fabricated on the most sensitive areas of the sensor surface. The inset shows an enlarged view of the dot like features.

5.3.3 Sample choice: CoO-ferritin

DPN-based deposition of ferritin provides the opportunity to study different aspects. In the first place, we want to demonstrate that direct magnetic measurements on monolayer particle are feasible, thanks to the high magnetic sensitivity of our susceptometer. For this reason, the most suitable samples will be chosen depending on their magnetic properties. CoO-ferritin particles do not exhibit blocking of the magnetic susceptibility down to 1.8 K (the minimum temperature reached by the experiments described in Chapter 3) and will therefore provide an appreciable temperature dependent signal at the operation temperatures of the dilution refrigerator ($\lesssim$ 5 K).

Besides, the low-temperature magnetic properties of these samples are very interesting from a physical point of view. First of all, these particles constitute a beautiful example of system lying near the fuzzy borderline between the classical and the quantum world. Two ingredients favor the observation of quantum effects: the size of these particles (consisting of 108 Co atoms), very close to the atomic scale dominated by quantum physics, and the antiferromagnetic character of their magnetic core. As we pointed out in section 3.8.4, quantum fluctuations are much stronger in antiferromagnets. Therefore, collective quantum effects like macroscopic quantum tunneling of the Néel vector (MQT) are more robust against temperature fluctuations than in ferromagnetic materials. One must however, have in mind that these particles are grown inside apoferritin, a biological protein consisting of more than 10^4 atoms. The interaction of the magnetic core with this ”environment” should tend to estabilize a classical response [229].

Antiferromagnetic nanoparticles are also very attractive from a theoretical point of view. It has been predicted that, a net magnetic moment per particle will arise due to the thermal excitation of non-uniform spin waves (see section 3.8.3.2). The thermoinduced magnetic moment is expected to decrease as temperature decreases down to a limiting value which corresponds to the net magnetization of non-compensated spins at the surface of the particle. To achieve this limit, very low temperature studies are required. To the best of our knowledge, there is no other example in the literature in which this limit has been explored.

5.4 Magnetic measurements at very low temperatures

In this section we present magnetic measurements performed on the CoO-ferritin submonolayer. The experimental awkwardness of this task demands a careful characterization of the sample magnetic response and sensor background at low temperatures. The latter will enable us to obtain the magnetic signal produced exclusively by the samples and the corresponding experimental coupling factor defined in section 5.3.1. In addition, this measurements will add some relevant information supporting the existence of the thermoinduced magnetic moment discussed on the previous chapter (see section 4.4.4.4). Finally we will compare the response of the CoO-ferritin particles with that of the magnetoferritin (sample N50). Whereas the latter exhibit a ”classical” behavior, the magnetic relaxation of CoO-ferritin seems to be dominated by quantum rules at low temperatures. These differences and their sources will be discussed.

5.4.1 Bulk characterization down to 13 mK

In order to scale and compare the signal obtained from the measurements carried out on the monolayer, we need to characterize first the samples at mk temperatures in a bulk-like experiment. For this purpose, we prepared a mixture of CoO-ferritin particles and Apiezon-N grease. We will refer to the latter sample as bulk-sample. A small quantity of the bulk-sample ($\sim 1\ \mu$g) was positioned on the microsusceptometer pickup coils and cooled inside the mixing chamber of the dilution refrigerator unit. The resulting signal is transformed to magnetic units by scaling it with the measurements obtained from the commercial magnetometer in a convenient temperature range where both measurements overlap (1.8–4.5 K). The susceptibility increases with decreasing temperature down to ~ 50 mK following Curie law as it can be seen in Fig.

5.14. However, below 300 mK, the in-phase (real) part of the susceptibility becomes frequency dependent and an out-of-phase (imaginary) component of the susceptibility arises indicating blocking of the magnetic moment due to anisotropy or other non-equilibrium effects.

5.4.2 Measurements on the monolayer: background substraction and signal scaling

The magnetic signal produced by the monolayer was measured using the dilution refrigerator down to very low temperatures. In these experiments an ac excitation current of $i_{\mathrm{P}} = 500\sin(\omega t)$ μA was applied to the primary coils. That produces an oscillatory magnetic field at the sample position of approximately $B_{\mathrm{P}} \approx 0.3\sin(\omega t)$ Oe (see section 5.4.3 below). The voltage response produced by the sample is however very small. It is therefore very important to characterize the background of the sensor properly, in order to distinguish it from the signal coming from the samples. For this reason, the electrical response produced by a bare susceptometer was measured down to 13 mK under the same conditions as the experiment performed on the monolayer. This characterization results are shown in chapter 2 (see Fig. 2.22).

In Fig. 5.12 we can see that both responses are comparable down to ~ 400 mK where the signal coming from the monolayer rises up as temperature decreases. This is a clear evidence that, below this temperature, the measured signal comes actually from the sample and it is not an electronic or background-originated artifact. Only the in-phase response has been depicted since the out-of-phase one is comparable to the background signal indicating that it lies below the limit imposed by sensitivity. For this reason we will concentrate on the in-phase component. The series of insets in Fig. 5.12 shows the resulting signal once the background has been subtracted.

The voltage data shown in Fig. 5.12 can be converted to magnetic units by scaling it with the magnetic response of the bulk-sample in a coincident temperature range. We have chosen for this purpose a temperature range going from 100 to 400 mK. Lower temperatures have been avoided since, as we will show in the following sections, small differences are evident at low temperatures between both measurements. The resulting data are shown in fig. 5.13 in units of emu per mol of particle.

5.4.3 Experimental determination of the coupling factor

In the previous section we have obtained the magnetic response of the monolayer-sample converting the output signal (V) to magnetic units (emu/mol per fer-

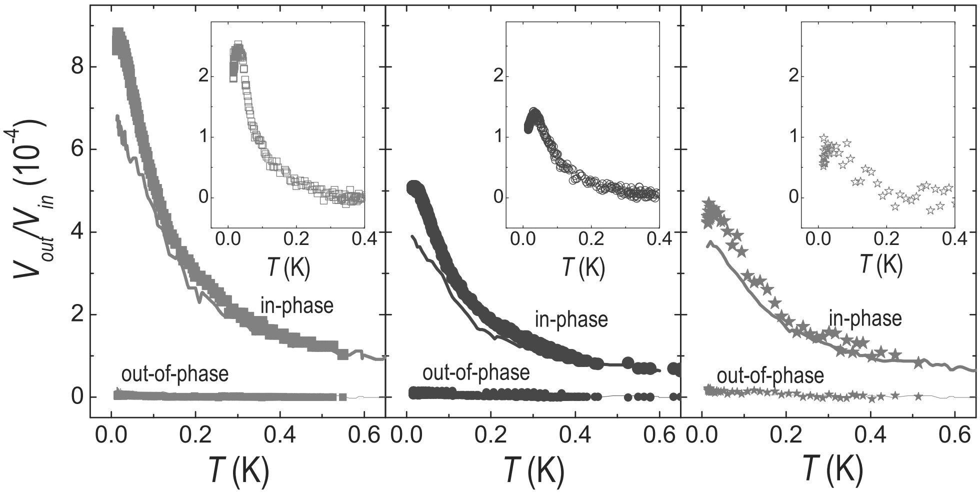

Figure 5.12: Output in-phase and out-of-phase voltages divided by the input voltage corresponding to the bare sensor (solid lines) and the monolayer of CoO-ferritin nanoparticles (scatter). The latter rises over the background below ∼ 400 mK. The insets show the output in-phase response once the background has been subtracted.

ritin particle) by scaling it with measurements performed in a commercial magnetometer. As we have a pretty good estimation of the number of deposited particles (N), we can obtain now an experimental estimation of the coupling factor α_χ defined in Eq. 5.5. In this equation, $\phi_{coupled}$ refers to the flux coupled to the SQUID which can be calculated from the output voltage, since these two quantities are related trough fabrication parameters as $\phi_{coupled} = V_{\rm out} M_f / R_f$. Here R_f is the feedback resistance and M_f is the mutual inductance between the SQUID and the feedback coil. The current flowing through the primary coil ($i_{\rm P}$) can be obtained from the input voltage $V_{\rm in}$ taking into account the value of the external flux resistance ($R_{\rm ext\Phi}$) used (see section in chapter 2). With these considerations, α_χ will be given by

$$\alpha_\chi = \frac{\Delta V_{\rm out}}{V_{\rm in}} \frac{R_{{\rm ext}\phi} M_f}{R_f} \frac{1}{N \Delta\chi} \tag{5.6}$$

Here, $\Delta V_{\rm out}$ and $\Delta\chi$ are referred to the susceptibility and subsequent voltage variation in a given temperature range. By inserting real values in Eq. 5.6 we obtain $\alpha_\chi = 0.36(1) \times 10^{-6}\ \phi_0 {\rm Oe}/\mu_{\rm B}{\rm A}$, in quite good agreement with the theoretical calculations shown in Fig. 5.9.

Let us analyze the physical meaning of this value. Taking into account the estimated excitation magnetic field at the sample position the latter means that the total flux coupled to the SQUID loop equals $6 \times 10^{-10}\ \phi_0$ per $\mu_{\rm B}$.

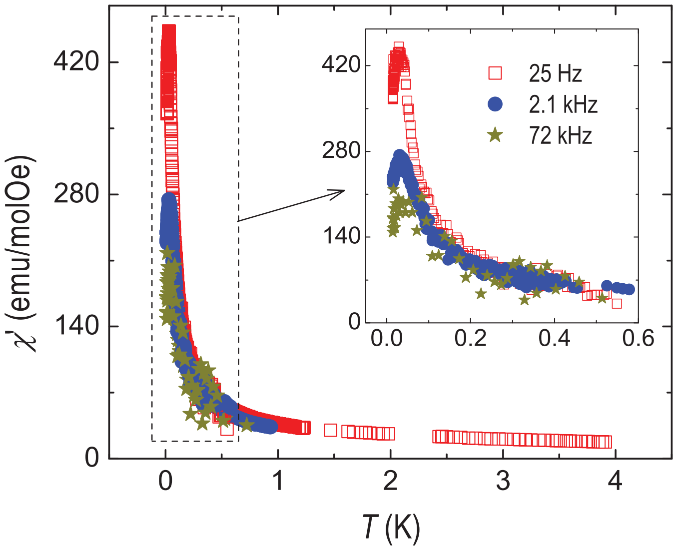

Figure 5.13: Real susceptibility of the monolayer sample. Above 400 mK the data corresponds to the measurements performed on the bulk-sample.

In chapter 2 we measured experimentally the flux noise of our sensors giving 0.2 $\mu\phi_0/Hz^{1/2}$ at mK temperatures. With these considerations we found that the experimental sensitivity in these conditions is enhanced giving ~ 300 $\mu_{\mathrm{B}}/Hz^{1/2}$. This value is nearly two orders of magnitude better than what we obtained using a lead sphere of ~ 45 μm in diameter (see Chapter 2). The reduction of the sample size together with the exceptional capabilities of DPN of manipulating the spatial distribution of samples enable us to exploit the most of the sensitivity of our sensors.

The experimental value of the flux coupled to the SQUID enables us to determine also the energy coupling between the array of ferritin-based particles and the SQUID loop, a quantity that can be of relevance for the application of hybrid architectures in quantum computing. The energy coupling ε per unit of magnetic moment is

$$\varepsilon = \frac{\Phi^2_{\mathrm{coupled}}}{2L_{\mathrm{SQUID}}}\frac{1}{\mu_i} \tag{5.7}$$

where $L_{\mathrm{SQUID}} = 112$ pH is the self-inductance of the SQUID loop. According to our experimental data, $\Phi_{\mathrm{coupled}} = 1.8 \times 10^{-4}$ Φ_0 at $T = 50$ mK. At this temperature, the experimental thermally averaged magnetic moment induced in our sample by the excitation magnetic field is $\mu_i = 2.3 \times 10^5$ μ_{B}. The latter gives $\varepsilon/\hbar \sim 30$ Hz/μ_{B} comparable with $\varepsilon/\hbar \sim 6$ Hz/μ_{B} (4 Hz/μ_{B}) reported recently for the coupling between electron spins of nitrogen-vacancy centers (Cr^{3+} ions) in single crystals of diamond (ruby) and superconducting planar resonant cavities [230, 231].

5.4.4 The virtue of improving the thermalization

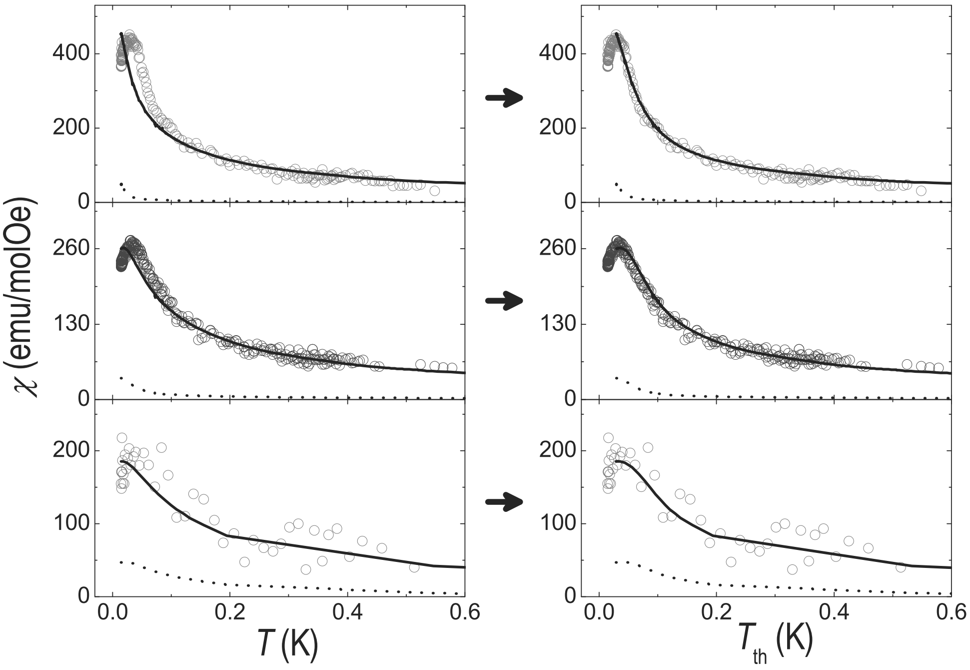

Figure 5.14: Left panel: magnetic response of the monolayer sample (open circles) scaled to the calibrated measurement performed in a bulk-like sample (lines) at different frequencies. Solid lines represent the real part of the susceptibility and dot lines the imaginary part. Slight differences between the two measurements become apparent below ∼ 100 mK due to a poor thermalization of the bulk-like sample. Right panel: bulk and monolayer-sample response versus the scaling variable $T_{\rm th}$, both measurements coincide by choosing the appropriated function $T_{\rm th} = f(T)$.

As we pointed out in section 5.4.2, magnetic measurements performed on the monolayer differ from that of the bulk-sample in the sense that the latter seems to be "shifted" to lower temperatures below ∼ 100 mK (see Fig. 5.14). This behavior could be accounted for by a poor thermalization of the bulk-sample, a very well-known effect in very low temperature experiments. The heating of the sample due to an out-of-equilibrium response, or a bad transfer of heat between the latter and the bath can lead to the apparition of a temperature gradient. As a consequence, the temperature read out by the thermometer will slightly differ from the actual temperature of the sample leading on the data shift that we observe experimentally.

The thermalization of samples at mK temperatures strongly depends on the heat flux transfer between the helium bath and the sample, the quality of which is quantified by a constant R_{K} referred as the Kapitza resistance. There are two main contributions to decrease R_{K}, namely the capability of phonons to be transmitted from the bath to the sample and the contact interface between them. In crystalline lattices, low energy phonons are usually those with long wavelengths, commonly larger than a typical nanoparticle. The dispersion relationship of phonons in amorphous solids can be however very different. For those materials, with non-periodic arrangement of atoms, new low-energy modes with short wavelength are allowed. These modes help the system to attain thermal equilibrium with the bath of just a few mK. Indeed, this idea forms the basis for the design of heat exchangers in cryogenic systems. The fact that the Kaptiza resistance of the monolayer sample is lower than that of the mixture of ferritin and Apiezon-N grease (bulk-like) could be accounted for by a better phonon transference from the helium bath to the former. In addition, the ratio of the contact surface to the sample volume of the monolayer sample with the bath is much higher than that of the bulk-like one, implying a decrease of R_{K} and an enhanced thermalization.

Since the degradation of the thermalization is proportional to the temperature, we can find a scaling variable T_{th} such that by plotting the magnetic response of the bulk-sample versus T_{th}, the latter coincide with the magnetic response of the monolayer-sample. We assume that $T_{\mathrm{th}} = f(T)$ is a function of the temperature exclusively and does not depend on the frequency. By doing so, we can compensate the lack of thermalization of the bulk-sample and correct the low temperature data of the latter. In this way, we can ”recover” the data corresponding to the imaginary part of the susceptibility measured on the bulk-sample that we were not able to measure with the monolayer-sample.

5.4.5 The thermoinduced magnetic moment revisited

As we showed in the previous chapter, the magnetic moment of the CoO-ferritin samples exhibits a dependence with temperature that can be accounted for by the existence of a thermoinduced magnetic moment, a concept that was introduced by S. Mørup and co workers [102]. The latter effect leads to an increase of the effective magnetic moment above the intrinsic uncompensated magnetic moment (μ_{unc}), typical of AFM nanoparticles. Measurements performed on the bulk and monolayer-samples of Co-magnetoferritin provide an excellent opportunity of observing experimentally the temperature range where the response of the particles is purely dominated by μ_{unc}. That is to say, we are able of measuring the intrinsic magnetic moment of an antiferromagnetic particle and distinguish it from other contributions, something that had not been achieved to date.

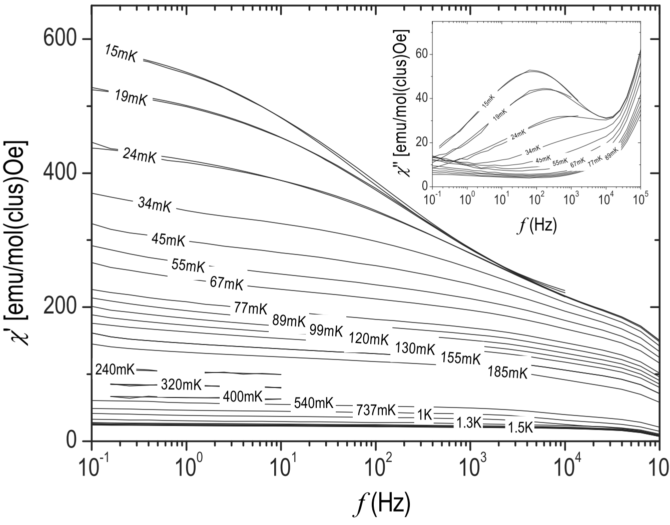

Figure 5.15: Real part of the susceptibility measured at different temperatures as a function of frequency. The inset shows the imaginary part where a clear peak rises up below $T \sim 40$ mK indicating superparamagnetic blocking of the magnetic moment. At high frequencies we can observe the influence of a different contribution to the relaxation.

Let us first extract some information about the equilibrium response of the nanoparticles. For this purpose we consider the frequency dependent susceptibility measurements performed on the bulk-sample (see Fig. 5.15). By fitting this data to a Cole-Cole function defined in section 3.7.3, we obtain the equilibrium susceptibility χ_T at each temperature. Plotting χ_T as a function of the scaling variable T_{th}, we obtain the equilibrium response of our system of antiferromagnetic particles. In this way, the magnetic data presented in the previous chapter (see Fig. 4.20) can be extended down to very low temperatures.

Fig. 5.16 shows the equilibrium and frequency dependent susceptibility data multiplied by T_{th}. As we can see, the equilibrium response decreases as T decreases down to ≈ 400 mK as predicted by S. Mørup et al. Below this temperature $\chi_T T_{\text{th}}$ is found to become independent of temperature down to $T \approx 100$ mK where it falls down again. The ac-susceptibility exhibits a qualitatively similar behavior. χT_{th} shows a plateau below a given temperature, which however depends on frequency. We attribute the plateau to the transition from the thermoinduced regime to the one dominated by the intrinsic uncompensated magnetic moment which is independent of temperature.

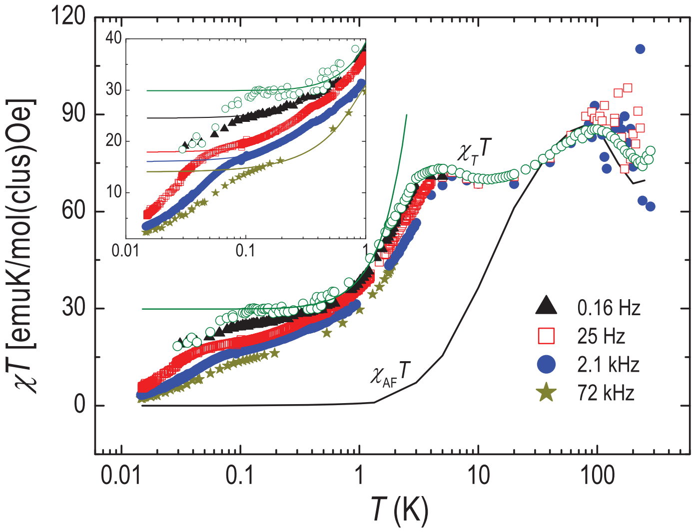

Figure 5.16: Real susceptibility multiplied by the scaling variable T_{th}. The inset shows an amplification of the low temperature region where the frequency-dependent plateaus described on the text are clearly visible. The lines represent the fittings to Eq. 5.8 and 5.9 performed at each frequency.

Let us, for the sake of completeness, rewrite here the expressions that we obtained in chapter 3 and 4 for the equilibrium magnetic susceptibility

$$\chi T \approx \frac{N_{\text{A}} \langle \mu_{\text{unc}}^2 \rangle}{3k_{\text{B}}} + \chi_{\text{th}} T + \chi_{\text{AF}} T \tag{5.8}$$

Now, since our experiments have been performed down to mK temperatures, it will be more convenient to use the expression for χ_{th} obtained by us in section 3.8.3.2. In this derivation, the zero point energy was taken into account providing therefore a better description of the very low temperature data

$$\chi_{\text{th}} T \approx \frac{N_{\text{A}} (g\mu_{\text{B}})^2}{4k_{\text{B}}} \frac{1}{1-\kappa} \left(1 + 3\kappa + 4\kappa \frac{1+\kappa}{1-\kappa} \right) \tag{5.9}$$

where $\kappa = \exp(\hbar\omega_q / k_{\text{B}} T)$.

The experimental data shown in Fig. 5.16 have been accurately fitted to these expressions showing that the equilibrium response agrees well with the predictions that follow from the theory of the thermoinduced susceptibility indeed. The fit enables us to obtain a more accurate estimation of the uncompensated magnetic moment $\mu_{\text{unc}} = 16\ \mu_{\text{B}}$, and of the energy of the uniform mode $E_0(\exp) = 385$ mK. This energy can be compared with the value predicted by the theory of spin waves in AFM $E_0(\text{teo}) = 17$ K. The present results clearly support the existence of a thermoinduced magnetic moment in antiferromagnetic nanoparticles. Despite the quantitative disagreement found with the theory, the latter would be essentially correct. The approach developed by Mørup and co workers predicts a dependence of the magnetic moment with temperature that is actually observed experimentally. The data suggest, however, that the energy spectra of magnetic excitations, and probably the nature of these, must be reconsidered in the case of nanoparticles as it was already discussed in the previous chapter (see section 4.4.5).

5.4.6 The intrinsic magnetic moment comes to light: spin dynamics

Below ≈ 400 mK, the magnetic response of the CoO-ferritin particles is solely dominated by the uncompensated magnetic moment. The latter provides the exceptional opportunity to study the behavior of the bare intrinsic magnetic moment of an antiferromagnetic particle avoiding the influence of any other contribution. In the present case, the magnetic data shown in Fig. 5.16 reveal some intriguing behavior at low temperatures that demands especial attention.

As we shown in the previous chapter (see section 4.4.4.1), magnetization reversal is assisted by quantum tunneling below ≈ 3 K. However, susceptibility drops dramatically to zero at ≈ 100 mK. More precisely, the drop that corresponds to the high frequency data (i.e. 25 Hz, 2.1 kHz and 72 kHz) occurs at lower temperatures as frequency increases. The latter is typically ascribed to the magnetic blocking of the susceptibility, consequence of a classical thermally activated relaxation process. The transition from thermally activated relaxation regime at high temperatures to one dominated by quantum tunneling of the magnetization at low temperatures is a quite common phenomena that has been often found in magnetic molecules and also nanoparticles. The decrease of the temperature implies a reduction of the mechanisms that lead to decoherence thereby favoring the emergence of quantum phenomena. Our system of nanoparticles exhibit surprisingly a completely different behavior; here we observe the transition from a quantum to a classical regime as temperature decreases. In addition, the equilibrium response ($\chi_T T$) and that corresponding to the lower frequency ($f = 0.16$ Hz) describe a narrow step at $T \approx 100$ mK but does not drop to zero. The latter is equivalent to a reduction of the intrinsic magnetic moment from 16 μ_B to 12 μ_B.

Let us analyze more carefully this response by studying the behavior of the magnetic relaxation time down to very low temperatures. In Fig. 5.15 we

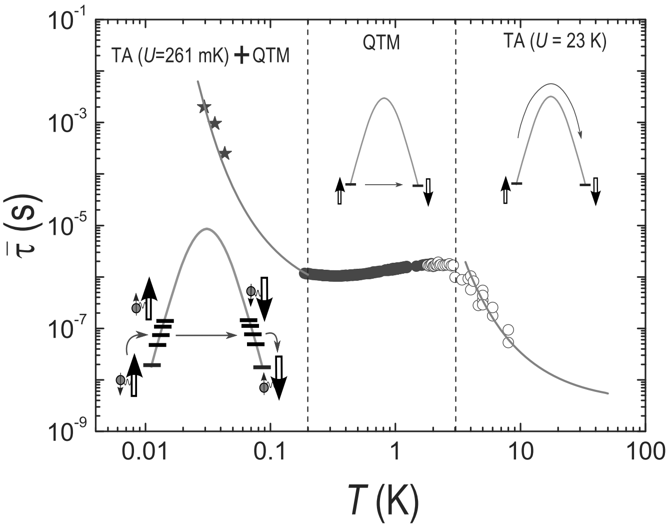

Figure 5.17: Relaxation time of the cobalt particles as a function of temperature. Three different regions are clearly appreciable. Above ≈ 3 K, magnetization reversal is assisted by thermal energy. Below this temperature and down to ≈ 200 mK, the relaxation process occurs via Quantum Tunneling of the Magnetization (QTM). Surprisingly, magnetic relaxation appears to be Thermally Activated (TA) again at very low temperatures. The data corresponding to both regions of TA relaxation have been fitted to an Arrhenius law. The insets show an illustrative scheme of the relaxation process associated to the three regions. That corresponding to the lowest temperature region is depicted in more detail in Fig. 5.18

can see that the condition $\omega\tau \ll 1$ (i.e. χ' independent of frequency) holds at low frequencies down to $T \sim 200$ mK. Thus, the mean relaxation time $\bar{\tau}$ defined in section 3.6 as the quotient χ"/χ'ω will provide a good description of the relaxation of the magnetic moment at temperatures above $T \gtrsim 200$ mK. At lower temperatures, τ can be obtained by fitting the susceptibility data shown in Fig. 5.15 to a Cole-Cole law (see section 3.6). The obtained values of $\bar{\tau}$ are depicted in Fig. 5.17. As we can see, there are three clearly different regimes. Above ~ 3 K, the relaxation time decreases exponentially with temperature following Arrhenius law. Below this temperature, τ remains nearly constat down to ~ 100 mK indicating that the relaxation process is assisted by quantum tunneling of the magnetization. At very low temperatures a new thermally activated process shows up.

We attribute this unusual reentrant behavior to the effect of interactions between the cobalt oxide nanoparticle and neighbouring spins. The origin of these "environmental" spins is unknown; they can be (groups of) cobalt atoms bound to the core via OH molecules or (groups of) iron atoms that are inherent to the protein structure of ferritin. The AFM coupling between

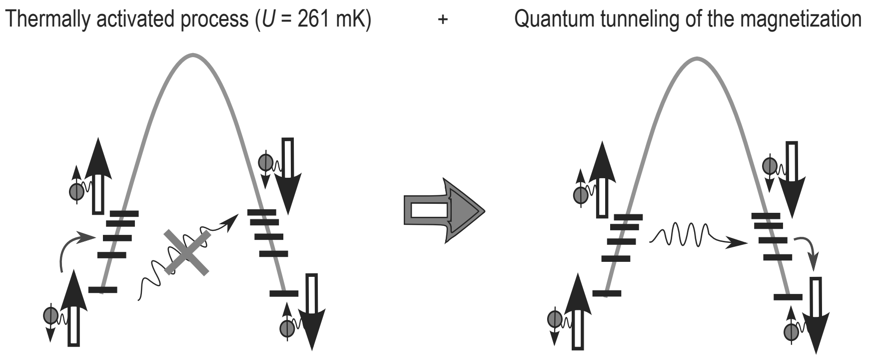

Figure 5.18: Below $\sim$ 100 mK, the relaxation of the magnetic moment of the CoO-ferritin particles occurs in three steps: (a) thermally assisted relaxation of the ”environmental” spin (represented as a small arrow), quantum tunneling of μ_{unc} (big arrow), magnetic relaxation of the coupled system.

the cobalt core and such spins would also lead to the net magnetic moment reduction observed in the response of $\chi_T T$ at $T \approx 100$ mK. As it was pointed out previously, $\chi_T T$ describes a narrow step equivalent to a reduction of the intrinsic magnetic moment from 16 to 12 μ_{B} (see Fig. 5.16).

The coupling of the CoO core to these ”environmental” spins blocks the direct tunneling processes since the final and initial state related by the reversal of the nanoparticle's magnetic moment do not have the same energy. Under these circumstances, the relaxation can take place via a process that is schematically depicted in Fig. 5.18. First, the ”environmental” spin is flipped by a thermally activated fluctuation. The energy of the latter equals the energy of the coupling with the nanoparticle. From this excited state, the magnetic moment of the cobalt core is allowed to relax via a direct tunneling process to a second excited state of the same energy. Finally, the group of coupled particles relaxes to the ground state providing the flipping of the ”environmental” spin. This mechanism provides a more efficient relaxation path for the coupled system than the direct tunneling between the ground states. The latter would imply the simultaneous tunneling of both magnetic moments, i.e. that of the CoO nanoparticle and that of the ”environmental” spin.

5.4.7 Quantum effects: Ferri vs. antiferromagnetic particles

Let us finally compare the response of the cobalt oxide particles with that observed in the magnetoferritin samples in the previous chapter. As we said, the magnetic relaxation of the CoO-ferritin sample at high temperatures is well described by a thermally activated process over an energy barrier created by anisotropy of $U \sim 22$ K. However, relaxation occurs assisted by quantum tunneling of the magnetization below ≈ 3 K.

Magnetoferritin sample labeled as N50 contain 1.65 nm sized particles with an energy barrier estimated to be $U \sim 25$ K. However, these samples did exhibit superparamagnetic blocking of the susceptibility at the expected temperatures ($T_B \sim 4-9$ K) meaning that we do not observe the influence of any quantum process.

These particles are very similar in terms of size and magnetic anisotropy energy. The only big difference between them lies in the fact that the Fe-magnetoferritin particles consist of maghemite, a ferrimagnetic material, whereas, interactions between the magnetic ions conforming the CoO-ferritin sample are antiferromagnetic. The latter is exactly the key factor here. As we introduced in chapter 3, particles made of antiferromagnetic materials are more likely to exhibit quantum behavior than ferro or ferrimagnets since quantum fluctuations in AFM materials are more robust against thermal fluctuations than in the case of FM materials. The systems presented here are very interesting candidates for further studies on the influence of size and magnetic order on the quantum behavior of magnetic particles.

5.4.8 Conclusions

In this chapter we have reported the successful deposition of nanoscopic magnetic particles with $S \sim 10$ on the most active areas of the μSQUID susceptometer by dip pen nanolithography. We have shown that magnetic measurements within the whole bandwidth and down to very low temperatures are feasible. In this sense, our μSQUID sensors combined with DPN capabilities appear as a very promising tool for direct particle monolayer characterization. Furthermore, single monolayer particle arrangements exhibit a better thermalization with the helium bath at mK temperatures, which implies an additional advantage with respect to traditional bulk measurements.

The evolution from commercial bulk characterization techniques to micro-sized particle measurements demands some basic concepts to be reconsidered. The success of nanoparticle detection using a μSQUID susceptometer depends on the capability of the pickup coil to couple the most of the magnetic flux produced by the sample. This coupling can be enhanced by matching the pickup coil size to the sample size [65]. However, a technological limit appears when the size of the particle is reduced below the lithographic limits of superconducting wire fabrication. In our special case, the wires composing the pickup coils are micrometric whereas the samples are just 2 nm diameter sized. In these circumstances, the study and the capability of manipulating the spatial distribution of particles becomes paramount. The excellent agreement between the coupling factor calculated theoretically and the experimental value is an evidence of the capability of DPN to exploit the high sensitivity of the sensor. Our results could also provide an efficient way of testing, quantifying and optimizing the coupling between magnetic particles and a wide variety of superconducting microcircuits such as superconducting microstrip cavities or flux qubits.

On the other hand, the novel measurements presented here provide the experimental confirmation of the existence of the thermoinduced magnetic moment. We are able to observe the transition from the temperature range dominated by the latter to the one dominated by the uncompensated magnetic moment. That is, the intrinsic magnetic moment originated by size effects in AFM nanoparticles. We have observed experimental evidences of quantum effects as well. The existence of such effects has very interesting consequences in comparison with the magnetic response of ferrimagnetic nanoparticles with similar characteristics. These systems seem to be ideal models for further studies of the relation between magnetic order and quantum fluctuations. In other words, the robustness of a magnetic system to remain ”quantum” against thermal fluctuations.

Part II

The quantum world

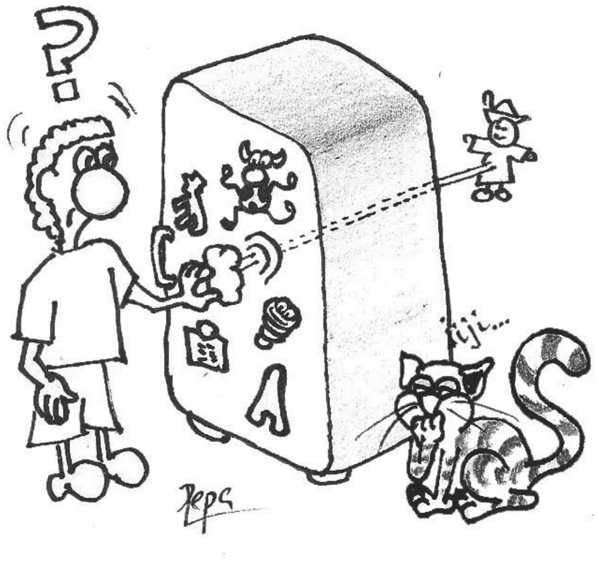

Chapter 6

Molecular design of spin-based qubits

6.1 Introduction

Since their discovery, Single Molecule Magnets (SMMs) have become a favorite subject of study for many researchers. The reason is simple: their enormously rich physical behavior. SMMs are for instance amongst the most complex magnetic entities that show quantum phenomena like tunneling, quantum coherence or quantum interference. On the other hand, it is exactly their rich physical behavior what makes their study very difficult from an experimental point of view. The latter requires the use of very versatile instruments, apart form the commercial magnetometers. In our case, this problem has been solved thanks to the broad band capabilities of the μSQUID susceptometer developed as part of this thesis work. Without the aid of this instrument it would be impossible to observe the interesting phenomena that we will describe in the present and next chapter.

Most experimental studies have focused on polynuclear magnetic molecules like the archetypes Mn_{12} and Fe_8 [7–11, 232–234]. However, their quantum spin dynamics is still far from being well understood. For this reason, we have turned our attention to a new family of even simpler SMMs consisting of just one isolated magnetic center. The latter is a lanthanide ion encapsulated in different polyoxometalate architectures [16] that have an enormous influence on its anisotropy and therefore on its magnetic response as well.

These molecules appear as excellent candidates for their integration as reliable quantum bits (qubits) for quantum computing. There are several arguments that support this idea. First, the quantum coherence of a given system is known to decrease as the number of degrees of freedom increases. It can be intuitively understood that clusters consisting of just one magnetic atom will have a higher probability of surviving in a pure quantum state than their polynuclear counterparts. Secondly, mononuclear-based SMMs enable their magnetic dilution, i.e. the synthesis of crystals containing both magnetic and non-magnetic molecules. The average distance between the magnetic entities can therefore be varied at wish. In this way, dipolar interactions can be minimized while conserving the crystallinity. Finally, these polyoxometalates moieties consist mainly of tungsten and oxygen. The former ion has stable isotopes with zero nuclear magnetic moment and the latter carries no nuclear spin. Hence, nuclear spin-free molecules can be prepared thereby maximizing their quantum coherence.

In this chapter, we introduce the family of compounds that will be the subject of our study. As we will see, the complete series of lanthanides can be obtained but in the present chapter we will concentrate on clusters with gadolinium. As a free ion, Gd^{3+} is an isotropic atom with a $L = 0$ ground state configuration. However, when it is introduced in a crystal field, this isotropy becomes distorted. Gadolinium appears therefore as a model crystal field probe. When it takes part of a crystal or a molecule, its electronic wavefunction must adapt itself to the surrounding symmetry. This phenomenon provides then an indirect characterization of the structural properties of the crystallographic site.

In this chapter we present a combination of specific heat measurements, electron paramagnetic resonance spectroscopy and ac magnetic susceptibility measurements. This characterization has enabled the accurate determination of the ligand field parameters that describe the hamiltonian of these systems.

Our work shows how the crystal anisotropy of this family of SMMs can be tailored by means of chemistry. Playing with the POM structure in which the lanthanide ion is encapsulated, it is possible to design the hamiltonian of these molecules *à la carte*. These results open the door for a novel kind of molecular engineering. Combining the control on the chemical synthesis and physical characterization, new molecules could be designed and optimized for different applications such as quantum computing, high-density information storage or magnetic refrigeration.

6.2 Single Molecule Magnets (SMMs)

As we introduced in Chapter 3, magnetic nanoparticles are of much technological interest. However, the control over the crystallinity and homogeneity at the nanometric level is extremely difficult. One possible way of circumventing these problems is the bottom-up approach, i.e. the synthesis of completely identical molecules characterized by a large magnetic moment. These systems appeared at the beginning of the 1980s and attracted much interest from both the physics and chemistry communities, especially after the finding of the coexistence of classical and quantum behaviors in Mn_{12}. In this section we will first provide a short description of the generally accepted definition of SMMs. We will then dedicate a few words to the most popular and other less known molecules. And finally, we will present a recently developed family of magnetic molecules that consist of individual lanthanide atoms encapsulated in polioxometalate (POM) moieties that also exhibit the general properties of SMMs.

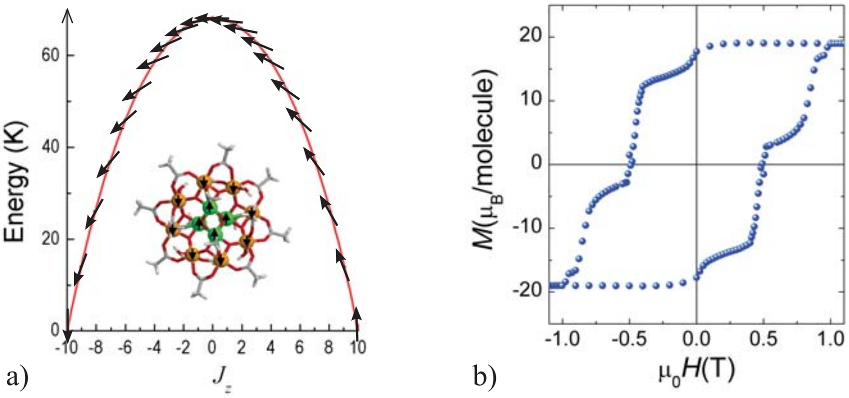

Figure 6.1: a) Energy level structure of Mn_{12} corresponding to the possible projections of its spin along the easy magnetization axis. The inset shows a representation of a Mn_{12} cluster. b) Typical hysteresis loop measured on a Mn_{12} single crystal at $T = 2.5$ K.

6.2.1 What is a SMM?

A high-spin cluster is a molecule that consists of a relatively small number of magnetic ions (~ 10) strongly coupled between them giving rise to a net magnetic moment [235]. When these systems exhibit the general properties of superparamagnetic nanoparticles, they receive the name of single molecule magnets [1]. These properties include phenomena like the blocking of the susceptibility or the magnetic hysteresis (see Fig. 6.1b). The magnetic anisotropy that drives these phenomena is of purely molecular origin; no interaction between them is necessary for these phenomena to occur. Therefore, SMMs can be dissolved in different solvents [236, 237], prepared in amorphous crystals [238] or encapsulated in different matrices, like polymers [239], and they still retain these properties.

The molecule that represents the paradigm of SMMs is Mn_{12}. Figure 6.1a shows the classical potential energy corresponding to the possible spin projections (S_z) along its easy magnetization axis. Having a $S = 10$ ground state configuration, the classical projections of S become quantized into 21 allowed states corresponding to $S_z = -S$, $-(S-1)$, ..., $S-1$, S. The spin reversal can take place by climbing up and down all the 21 allowed states assisted by thermal energy [240] or through a quantum tunneling process between quasi-degenerate states located on opposite sides of the barrier [241–243]. The resonant character of this tunneling process leads to the famous steps observed in the hysteresis loops of Mn_{12} (see Fig. 6.1b).

6.2.2 Applications of high-spin clusters and SMMs

The strong uniaxial magnetic anisotropy exhibited by some SMMs makes them ideal candidates for high density magnetic storage applications. The ground state doublet is separated by the energy barrier created by the anisotropy (see Fig. 6.1a) thereby stabilizing the spin orientations $\pm S$ at low temperatures. These energy levels correspond therefore to two effective spin states that can be used to store information in a binary code [244].

High-spin clusters have also been proposed as suitable materials for low temperature magnetic refrigeration [245]. The latter happened after the discovery that the magnetocaloric effect (MCE) can be enhanced in these materials. MCE describes the relation between the magnetic entropy (and therefore temperature) and the applied magnetic field. It is of great technological interest for both commercial refrigeration and ultralow temperature scientific research [246].

Finally, one of the most exciting potential applications of SMM is their integration as the building blocks of quantum computers [14]. Quantum information processing exploits the abilities of quantum systems, namely entanglement and superposition of states, to perform computational tasks at rates inaccessible for classical computers [15]. Efficient integer factorization, data search in arbitrary large databases, generation of true random numbers or the simulation of quantum systems are just some examples of the extraordinary tasks that such a computer could perform. The physical realization of quantum computers is however extremely difficult. D. DiVincenzo enumerated in 1997 a series of requirements that should be fulfilled in order to achieve this goal [247]. These criteria can be summarized as follows: i) One needs an scalable number of well-defined quantum bits (qubits), ii) the ability to prepare a given state of the whole system, iii) sufficiently large decoherence time to perform quantum error correction, iv) the ability to realize a universal set of quantum gates and v) the possibility to measure the quantum state after the computation.

Many systems have been proposed for practical realization of qubits, e.g. photons, trapped ions, nuclear spins, quantum dots, dopants in solids, or superconducting structures based on Josephson junctions (for a recent review see Ref. [248]). The first examples in the list exhibit very large decoherence times but are difficult to manipulate. On the other hand, solid state candidates enable efficient qubit interactions to perform gate operations but the decoherence times are short. In addition, the scalability of superconducting qubits implies some technical problems to get identical unities. SMMs, would lie in the middle of this list providing: i) the scalability supplied by chemical synthesis, ii) well defined quantum spin states that can be initialized in their ground state by cooling and manipulated through microwave radiation, iii) adequate decoherence times that could be eventually enhanced, iv) intercluster exchange interactions that enable the realization of quantum gates and, finally, v) the possibility of reading out the final state via magnetic flux coupling thanks to their relatively large magnetic moment [38].

6.2.3 Some outstanding examples

SMMs are usually made of transition metal ions like manganese, iron or vanadium [249]. These elements are chosen since they can provide large ground spin states. Typically used chemical ligands are O^{2-}, OH^-, OCH^{3-}, F^-, Cl^- and $RCOO^-$. These linkers mediate the strong superexchange interactions that couple the spins inside the cluster. The set of organic ligands surrounding the magnetic cluster shields it from neighbouring ions, preventing for instance intercluster exchange interactions. Moreover, they also influence the molecule chemical and structural properties that will determine their solubility, their symmetry when organized into single crystals or their ability to form self-assembled monolayers [250].

6.2.3.1 The story begins with the Mn_{12} acetate

The $[Mn_{12}O_{12}(CH_3COO)_{16}(H_2O)]_4 \cdot 2CH_3COOH \cdot 4H_2O$, usually shortened as $Mn_{12}Ac$, is beyond any doubt the archetype of SMMs. Its molecular structure is depicted in Fig. 6.2a. As it can be seen there, it consist of eight external Mn^{3+} ions and an internal tetrahedron of four Mn^{4+}. Antiferromagnetic interactions are predominant between the inner and outer rings of ions leading to a spin $S = 10$ ground state. It was synthesized for the first time in 1980 by T. Lis as a product of the reaction of Mn^{2+} and MnO_4^- in the presence of acetic acid [251]. Not much attention was paid to this unexpected discovery until one decade later. In 1991, a group of the Laboratory for Molecular Magnetism at the University of Florence (Italy) performed ac magnetic susceptibility measurements on Mn_{12} down to 4.5 K [252] and observed the onset of an imaginary component of the susceptibility in the paramagnetic phase, that is, in the temperature range where the spin system was expected to be in thermal equilibrium. This phenomenon was interpreted as a thermally assisted relaxation process that becomes blocked when the experimental time (the inverse of the frequency) is shorter than spin reversal characteristic time, as occurs in magnetic nanoparticles (see Section 3.6). Mn_{12} would therefore also exhibit hysteresis of the magnetization below 4 K, as it was experimentally evidenced soon afterwards by the same group [1]. It was understood that these properties had an underlying different origin than the magnetic hysteresis observed in bulk ferromagnets. The latter is due the motion of domain walls in a long-range ordered magnetic material whereas the former is a property of individual molecules.

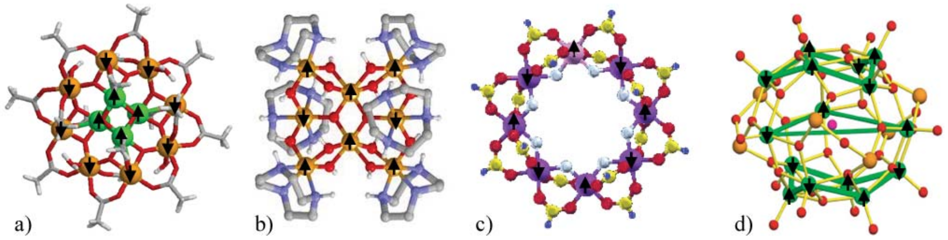

Figure 6.2: Some well-known examples of SMMs are the $Mn_{12}Ac$ (a) and Fe_8 (b). Other interesting low-spin clusters for quantum computing applications are the Cr_7Ni (c) and the V_{15} (d).

Another breakthrough came in 1997 with the observation of pronounced steps in the hysteresis cycle of $Mn_{12}Ac$ as well as maxima in ac susceptibility curves [7–9]. These phenomena were ascribed to a resonant tunneling process that occurs when levels associated to spin states on opposite sides of the anisotropy barrier coincide in energy.

Finally, a most striking quantum phenomena was also observed in this compound: quantum coherence. This is evidenced by the energy difference that separates the superposition states ($|\uparrow + \downarrow\rangle$ and $|\uparrow - \downarrow\rangle$) that would classically remain degenerated ($|\uparrow\rangle$ and $|\downarrow\rangle$). This energy difference, known as the tunnel splitting Δ, was experimentally determined on $Mn_{12}Ac$ and Fe_8 by means of EPR and specific heat measurements [10, 11]. The latter compound will be the subject of the next section.

6.2.3.2 The Fe_8 and the Berry phase

Fe_8, brief for $[Fe_8O_2(OH)_{12}(tacn)_6]Br_8(H_2O)_9$, (tacn=1, 4, 7-triazcyclononane), was also first synthesized in the 1980s [253]. However, its SMM character was not discovered until 1996 by means of ac magnetic susceptibility and Mössbauer spectroscopy [254]. Its molecular structure is depicted in Fig. 6.2.b. It consists of a butterfly structure of eight ^{3+}Fe ions having three different coordination symmetries. As a result, a ground state with spin $S = 10$ is obtained.

Fe_8 gained much popularity since it was the first SMM for which pure quantum tunneling of the magnetic moment was observed between the ground states [232]. But even more interesting, the effects of quantum interferences on the tunnel splitting were also experimentally evidenced in Fe_8. The latter effect had been theoretically predicted by D. Loss *et al* and J. von Delft *et al* in 1992 [233, 234] and attributed to the constructive and destructive interference that appears when the spin reverses through paths with opposite windings.

6.2.3.3 Novel qubit candidates: Heterometallic rings and V_{15}

Currently, the main problem for the physical realization of quantum computers is decoherence. Although SMM are very attractive candidates, their decoherence times (T_2) are short compared with those of other candidates like nuclear spins or photons. Much effort is being devoted now to identify the mechanisms responsible for lowering T_2 in these systems. Recent advances have been reported in two low-spin clusters: heterometallic antiferromagnetic wheels of Cr_7Ni and Cr_7Mn and a three-dimensional cluster of V_{15}. The first and last examples have $S = 1/2$ ground states providing therefore ideal two-level systems.

The first type of clusters is schematically depicted in Fig. 6.2.c. They consist of a ring of Cr ions coupled antiferromagnetically. One of these ions is replaced by a Ni or Mn atom giving rise to a non-zero spin ground state with $S = 1/2$ and $S = 1$ respectively. Its synthesis [255] was stimulated by theoretical predictions about the increase of the decoherence time in antiferromagnetic wheels with excess spin [256]. Rabi oscillations were observed in both compounds and the magnitude of T_2 was experimentally determined by means of EPR spectroscopy [257]. This experiment evidences the negative influence of hyperfine interactions on the lifetimes of quantum states, finding an enhancement in the decoherence rate from ≈ 3 μs to ≈ 1 ms when substituting hydrogen for deuterium.

The synthesis of the second cluster mentioned above, V_{15}, had been described more than 20 years ago [258]. It consists of three layered rings of V antiferromagnetically coupled resulting in a ground state $S = 1/2$. Rabi oscillations were also observed by means of EPR measurements and a maximum decoherence time of 800 ns was measured [27].

6.2.4 Mononuclear SMMs

A different approach has been the synthesis of simpler and simpler SMMs, down to the limit of developing molecules consisting of individual magnetic atoms. This was the goal of N. Ishikawa and co-workers that reported the synthesis and magnetic characterization of double decker compounds based on single lanthanide (Ln) atoms [259]. These systems consist of two phthalocyanine molecules encapsulating a Ln ion in the trivalent state. Different lanthanide atoms were studied including Ln = Tb, Dy, Ho, Er, Tm, and Yb that provide large spin states due to strong spin-orbit coupling ($J = 6$, 15/2, 8, 15/2, 6 and 7/2 respectively). These double decker molecules exhibit SMM typical features like slow relaxation of the susceptibility and magnetic hysteresis.

Following this trend, AlDamen *et al* reported later the synthesis of a similar family of compounds based on polioxometalates (POMs) [260]. Moreover, AlDamen *et al* also showed that these ions can be encapsulated in different ligand fields. The latter leads to a beautiful series of mononuclear SMMs exhibiting very different dynamical properties.

These systems are very promising candidates for quantum computing since they can be prepared as total nuclear spin free systems [261]. In this way, it is possible to prevent the hyperfine interaction between the POM cluster and the magnetic atom, known to be a source of decoherence [257]. Their simplicity can also contribute to improve their stability against decoherence. Unlike other polynuclear candidates like Cr_7Ni and $V_{15}Mn$, the magnetic moment of one of these POM-based SMM is associated with a single atom. As the robustness of a quantum state decreases with the system's number of degrees of freedom, simple molecules, like those presented here, are desirable. In addition, magnetically diluted crystals can be easily prepared. Starting from a solution containing both magnetic and non-magnetic, e.g. Y, lanthanide ions and following the normal crystallization procedure, it is possible to control the average spin-spin distance in the lattice at will. The same does not apply to polynuclear SMMs with which the distance between molecules can be only controlled in solution. These new compounds will be the subject of the present and next chapters.

6.3 The spin hamiltonian: anisotropy and quantum spin tunneling

The spin hamiltonian is the usual formalism for describing the hamiltonian of SMMs. Its introduction will be very useful for the discussion that follows.

The total spin of a magnetic ion having n unpaired electrons is $S = n/2$ with $2S+1$ corresponding possible S_z projections along the easy magnetization axis z. As a first approximation, we can write

$$\mathcal{H} = DS_z^2 + E(S_x^2 - S_y^2) + \mathcal{H}_{\text{zeeman}} \tag{6.1}$$

where $\mathcal{H}_{\text{zeeman}}$ is due to the Zeeman effect and vanishes at zero applied field. Subtracting the constant $DS(S+1)/3$ and rewriting S_x and S_y in terms of the ladder operators S_+ and S_- we obtain for zero applied field

$$\mathcal{H} = D\left[S_z^2 - \frac{1}{3}S(S+1)\right] + \frac{E}{2}(S_+^2 + S_-^2) \tag{6.2}$$

which has the advantage that it satisfies $\text{Tr}\mathcal{H} = 0$, Tr being the trace of the tensor. The D parameter contributes to define the anisotropy along the z axis, being $D < 0$ for easy-axis symmetry and $D > 0$ for easy-plane symmetry. In the former case, the ground states correspond to the highest spin projection along the z-axis and are separated by an energy barrier $U \simeq DS^2$. In the second case, the ground state corresponds to the lowest values of S_z .

An easy way to visualize the effect of D and E is to make a surface tridimensional plot of the classical magnetic energy in cartesian coordinates. In this representation, the distance from the origin to the surface equals the potential energy of a classical spin. Figure 6.3a shows the case for $D < 0$ and $E = 0$, i.e. pure axial symmetry. In Fig. 6.3e we can see an example of planar symmetry obtained with $D > 0$ and $E = 0$. On the other hand, the E parameter contributes to define an easy axis in the xy plane as it can be seen in Fig. 6.3b and 6.3f. The inclusion of this term adds a preferred axis along the x axis for $E < 0$ and along the y axis for $E > 0$. Values of E/D larger than 1/3 are not considered since it is physically equivalent to rename the reference axis.

Equation (6.2) represents the simplest crystal field hamiltonian, but in practice higher order terms are usually needed. Fortunately, only even-terms up to order $k = 2, 4, 6...2S$ must be included since odd-terms give zero matrix elements. The most convenient way of evaluating the matrix elements of a crystal field hamiltonian is the "operator equivalents" method described by

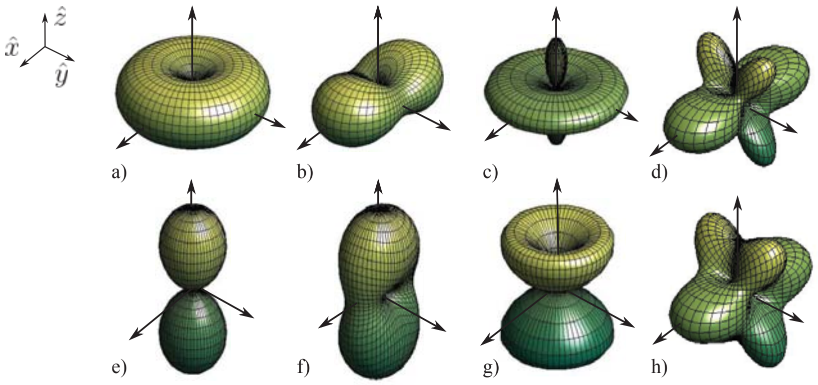

Figure 6.3: Classical potential energy corresponding to all possible spin orientations in space. The first row shows different examples with axial symmetry along the z axis ($D < 0$) whereas the second row corresponds to planar symmetry on the xy plane ($D > 0$). In b and f, a transversal $E = |D|/3$ term is added. The effect of a positive diagonal fourth order term $B_4^0 = |D|/6$ and $B_4^0 = |D|/3$ can be seen in c and g, respectively for $E = 0$. Finally, the consequences of a transversal fourth term $B_4^2 = |D|/3$ are depicted in d and h for $E = B_4^0 = 0$.

Stevens [262] and Bleaney and Stevens [263]. The spin hamiltonian can be written as

$$\mathcal{H} = \sum_{q,k} A_k^q \langle r^k \rangle \theta_k \mathbf{O}_k^q \tag{6.3}$$

where the sum in q and k runs up to $2S$. A_k^q are the zero field splitting parameters to be determined for each ion and crystal symmetry. The coefficients θ_k are multiplicative factors that were tabulated by Stevens [262]. The product $A_k^q \langle r^k \rangle \theta_k$ is usually also abbreviated using the B_k^q parameters. Finally, the $\mathbf{O}_k^q$ matrices are the so-called Stevens operators.

In Fig. 6.3 the effects of some fourth order terms can be seen. The B_4^0 parameter produces a distortion of the potential energy surface. This is illustrated in Figs. 6.3c, with $D < 0$ and $B_4^0 = |D|/6$, and 6.3g, with $D > 0$ and $B_4^0 = |D|/3$. The term B_4^4 produces similar results as the E parameter, i.e. it defines an easy axis in the xy plane, but rotated 90° with respect to that produced by the E term. The rest of the fourth order B_4^q parameters set different preferred axis along the space. For instance the effect of a positive $B_4^2 = |D|/3$ is depicted in Figs. 6.3d and 6.3h for axial and planar symmetry respectively.

One advantage of this method is that it exploits the most from the point group symmetry of the ion providing a rational way of discerning beforehand which energy terms cancel. For instance, the hamiltonian corresponding to the C_4 point group (see Fig. 6.6a below) can be written as

$$\mathcal{H} = B_2^0\mathbf{O}_2^0 + B_4^0\mathbf{O}_4^0 + B_4^4\mathbf{O}_4^4 + B_6^0\mathbf{O}_6^0 + B_6^4\mathbf{O}_6^4 \tag{6.4}$$

During this thesis, we will only need to use five operators whose explicit form is given below.

$$\mathbf{O}_2^0 = \left[3J_z^2 - J(J+1)\right] \tag{6.5}$$

$$\mathbf{O}_2^2 = \frac{1}{2}\left(J_+^2 + J_-^2\right) \tag{6.6}$$

$$\mathbf{O}_4^0 = \left[35J_z^4 - 30J(J+1)J_z^2 + 25J_z^2 - 6J(J+1) + 3J^2(J+1)^2\right] \tag{6.7}$$

$$\mathbf{O}_4^4 = \frac{1}{2}\left(J_+^4 + J_-^4\right) \tag{6.8}$$

$$\begin{aligned}\mathbf{O}_6^0 = {} & \left[231J_z^6 - 315J(J+1)J_z^4 + 735J_z^4 + 105J^2(J+1)^2J_z^2 - 525J(J+1)J_z^2\right. \\ & \left. +294J_z^2 - 5J^3(J+1)^3 + 40J^2(J+1)^2 - 60J(J+1)\right]\end{aligned} \tag{6.9}$$

where J_+ and J_- are the ladder operators. Here we have replaced the spin angular moment S with the spin-orbit number $J = S + L$ since this quantum number is more convenient to, describe rare earth ions where L is not quenched. Comparing Eqs. 6.2, 6.4, 6.5 and 6.6, it can be easily seen that $B_2^0 = 1/3D$ and $B_2^2 = E$.

6.3.1 Quantum Tunneling in SMMs

The B_k^0 terms are diagonal on the basis defined by $|m\rangle$, i.e. the eigenvectors of S_z, defined as $S_z|m\rangle = m|m\rangle$, being $m = -S$, $-(S-1)$, ..., $(S-1)$, S. On the other hand, the $q \neq 0$ terms are off-diagonal in this basis, and the states $|m\rangle$ are no longer the eigenvectors of the hamiltonian. When these terms are present, the new eigenvectors are symmetric and antisymmetric superpositions of the type $(|m\rangle \pm |-m\rangle)$ that are no longer degenerate. The energy difference between these levels is defined as the tunnel splitting Δ. Physically, the latter means that pure $|m\rangle$ states are not stationary but evolve in time from $|m\rangle$ to $|-m\rangle$ at a frequency given by $\Delta/\hbar$. The tunnel splitting is a measure of the delocalization of the wavefunction on both sides of the potential well, and it therefore determines the probability of going from $|m\rangle$ to $|-m\rangle$ via a direct tunneling process.

The addition of a second order transverse term B_2^2 mixes states with $\Delta m = \pm 2$. A fourth order transverse term like B_4^4 mixes states with $\Delta m = \pm 4$ and so on. For this reason, ions having half-integer-spin number (Kramers ions) should exhibit no quantum effects like tunneling at zero field.

However, there is an alternative way of inducing quantum transitions between the spin states via the application of an external magnetic field perpendicular to the easy magnetization axis. The Zeeman term in Eq. 6.1 has the following form

$$\mathcal{H}_{\text{zeeman}} = -g\mu_{\text{B}}\left(H_x J_x + H_y J_y + H_z J_z\right)$$

that can be rewritten as

$$\mathcal{H}_{\text{zeeman}} = -g\mu_{\text{B}}\left[\frac{1}{2}(J_+ + J_-)(H_x - iH_y) + J_z H_z\right]$$

The effect of a transverse magnetic field along the x or y directions is therefore the mixture of all the spin states of the system. Spin tunneling between the ground states of a Kramers ion can therefore occur when it is assisted by a transverse magnetic field. In a similar way, the tunneling probability of integer-spin systems can become suppressed.

These effects can be seen in the following example. We have calculated numerically the tunnel splitting by diagonalizing a realistic hamiltonian. For this purpose we have chosen

$$\mathcal{H} = B_2^0 \mathbf{O}_2^0 + B_4^4 \mathbf{O}_4^4$$

with $B_2^0/k_{\text{B}} = -0.059$ K and $B_4^4/k_{\text{B}} = 4 \times 10^{-4}$ K. These values correspond to the GdW_{10} single molecule magnet that we will describe later in this chapter. Gadolinium is in its trivalent state corresponding to $S = 7/2$. Since the term B_4^4 only connects states with $\Delta m = \pm 4$ no tunneling should be observed (see Fig. 6.4a). However, as we increase the transverse applied field, the tunnel splitting increases up to $\Delta/k_{\text{B}} = 2 \times 10^{-6}$ K at $H_x = 130$ Oe.

On the other hand, the effect of a longitudinal magnetic field along the easy magnetization axis is to block the tunnel probability. This magnetic field receives the name of bias field since it brings the degenerate spin ground states *out-of-resonance*.

These arguments have important consequences on the dynamics of SMMs that inevitably suffer the presence of an inhomogeneous magnetic field originated by the dipolar interactions. Let us consider a crystal of SMMs in the paramagnetic phase. Under these circumstances, each molecule feels a net dipolar field that can be described by a distribution $P(H_{\text{dip}})$ of width $\sigma_{H_{\text{dip}}}$. This is equivalent to a net dipolar energy bias distribution $P(\xi_{\text{dip}})$ of width $\sigma_{\xi_{\text{dip}}}$ that is shown in Fig. 6.4b, in which real values corresponding to the dipolar field distribution of GdW_{10} have been considered.

If a spin satisfies the "tunnel window" condition $-\Delta/2 \leq \xi_{\text{dip}} \leq \Delta/2$, its relaxation rate ($\tau^{-1}$) will be given by the tunneling frequency $\tau^{-1} = \Delta/\hbar$. For

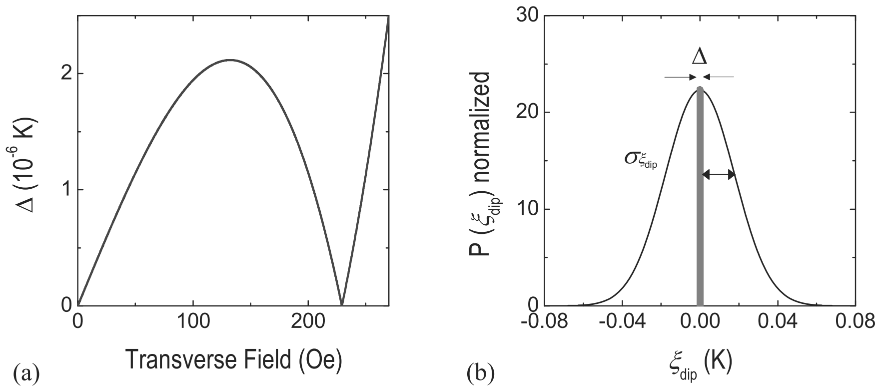

Figure 6.4: (a) Tunnel splitting of a $S = 7/2$ system as a function of the transverse applied magnetic field. (b) Energy bias distribution function corresponding to GdW$_{10}$. The bias field of dipolar origin plays the role of a longitudinal magnetic field that brings the tunnel probability *out of resonance*. Only those spins that satisfy the condition $-\Delta/2 \leq \xi_{\text{dip}} \leq \Delta/2$ are allowed to tunnel.

the rest of the cases $\tau^{-1} \approx 0$. We can therefore obtain a mean relaxation rate τ_{av}^{-1} integrating within the window defined by Δ

$$\tau_{\text{av}}^{-1} = \int_{-\Delta/2}^{+\Delta/2} (\Delta/\hbar) P(\xi_{\text{dip}}) d\xi_{\text{dip}}$$

Since usually $\Delta \ll \sigma_{\xi_{\text{dip}}}$ we can approximate

$$\tau_{\text{av}}^{-1} \approx \frac{\Delta^2}{\hbar} P(\xi_{\text{dip}} = 0) \tag{6.10}$$

If we assume the dipolar energy bias distribution $P(\xi_{\text{dip}})$ to be gaussian, the latter leads to

$$\tau_{\text{av}}^{-1} \approx \frac{\Delta^2}{\hbar\sqrt{2\pi}\sigma_{\xi_{\text{dip}}}} \tag{6.11}$$

If the energy bias of a given spin satisfies the window condition it will flip through quantum tunneling. The inversion of this spin leads to a redistribution of dipolar fields along the crystal. In this way, some of the spins that had negligible tunnel probability can eventually "enter" into the tunnel window. In 1998, N. V. Prokof'ev and P. C. E. Stamp demonstrated that this process evolves in time giving the opportunity to all spins to flip by tunneling [264]. In their derivation, they considered also the influence of fluctuations in the hyperfine bias originated by "flip-flop" processes of the nuclear spins. These fluctuations lead to a time-varying net energy bias that increases the effective energy window for the tunneling to occur. Anyway, these calculations lead to the same relation defined by Eq. 6.11, which is independent of the hyperfine fields.

To conclude, let us emphasize that dipolar bias fields slow down the average tunneling rate by a factor $\Delta/\sqrt{2\pi}\sigma_{\xi_{\mathrm{dip}}} \ll 1$. On the other hand, dipolar interactions also enable the quantum relaxation of Kramers ions that otherwise would exhibit a very small tunneling probability.

6.3.2 Mononuclear lanthanide SMMs based on POMs

Polyoxometalates are molecules based on high valence transition metal atoms like V, Mo or W. Their structure consists normally of a series of polyhedra that, combined with O, share vertex or edges to form a larger polyanion. As we said in section 6.2.4, AlDamen *et al* have recently reported the successful synthesis of different families of POM-based molecules containing individual lanthanide atoms that exhibit the typical features of SMMs [16, 260].

In this thesis, we will deal with two of the different families of compounds reported by AlDamen and co-workers, namely the $[\mathrm{Ln(W_5O_{18})_2}]^{9-}$, briefly $\mathrm{LnW_{10}}$, and the $[\mathrm{Ln\ (P_5W_{30}O_{110})}]^{12-}$, shortened as $\mathrm{LnW_{30}}$. The synthesis has been carried out by S. Cardona-Serra [265] including Gd, Tb, Dy, Ho, Er, Tm, Yb and Y. The structure of both families, as determined by X-Ray diffraction, is schematically shown in Fig. 6.5.

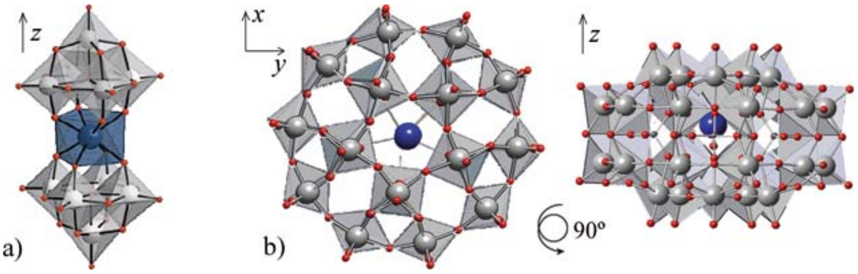

Figure 6.5: Structure of two lanthanide polioxometalate SMMs, the $\mathrm{LnW_{10}}$ (a) and the $\mathrm{LnW_{30}}$ (b).

The clusters of the first family consist of an individual lanthanide atom sandwiched by two anionic $[\mathrm{W_5O_{18}}]^{6-}$ moieties (see Fig. 6.5a). Each ligand coordinates the central Ln ion with tetragonal-pyramidal symmetry (C_4 point group as depicted in Fig. 6.6a). However, each moiety is twisted by an angle $\alpha = 44.2°$ with respect to the other. The coordination can be therefore considered a distorted square-antiprismatic symmetry (C_{4d} point group as depicted in Fig. 6.6a). Electrical neutrality is obtained through the addition of hydrated sodium cations leading to the introduction of a large number of water molecules in the lattice. As a result, the Ln trivalent ions are quite well isolated giving a minimum Ln-Ln distance of ≈ 1 nm.

In the second family, the individual Ln trivalent cation is encapsulated inside a tungstophosphate anion $[P_5W_{30}O_{110}]^{15-}$. This moiety exhibits doughnut shape with a central cylindrical cavity used for housing the lanthanide with C_{5v} symmetry (as depicted in Fig. 6.6a). The result is a disk shaped molecule, the structure of which can bee seen in Fig. 6.5b. In this case, the minimum Ln-Ln distance equals ≈ 2 nm.

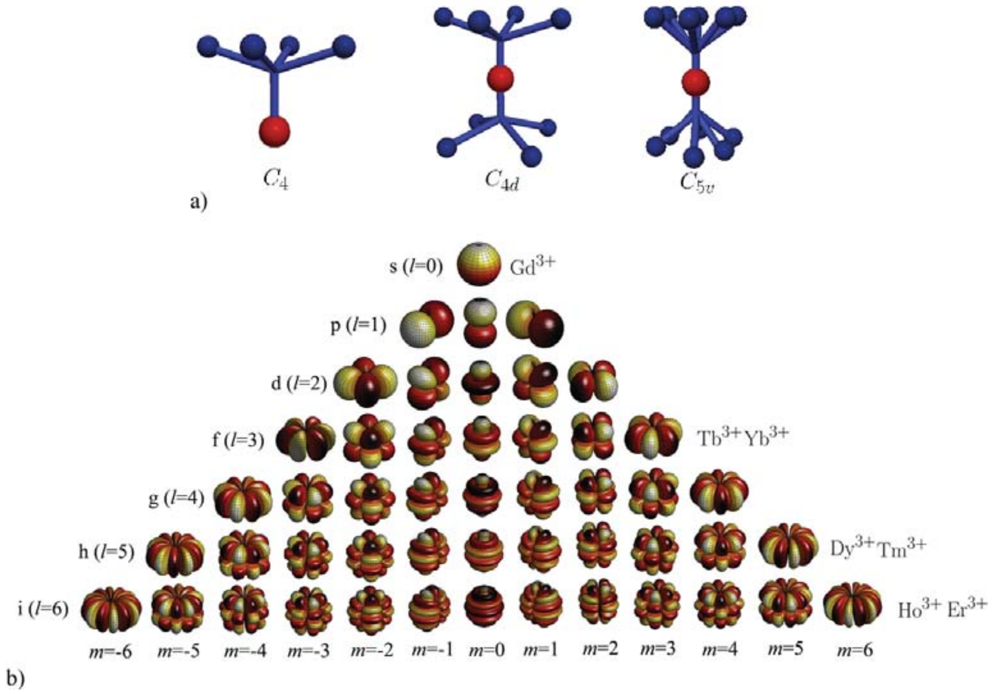

Figure 6.6: Molecular anisotropy is ultimately determined by the point group symmetry of the site in which the lanthanide is housed and the anisotropy of the ion itself. The figure shows three examples of point symmetry groups (a) and the possible electron orbital configurations (b).

The anisotropy of these molecules results from the combination of the crystal symmetry induced by the POM architecture (see Fig. 6.6a) and the orbital electronic configuration of the lanthanide ion itself (see some examples in Fig. 6.6b). This anisotropy determines the energy level structure corresponding to the different projections of the spin that will ultimately govern the magnetic dynamical properties. For this reason, N. Ishikawa also developed a numerical method to determine the values of the different $A_k^q\langle r^k\rangle$ parameters defined in Eq. 6.3. This method was based on the simultaneous least-square fit of the magnetic susceptibility data and H^1 NMR paramagnetic shifts for the whole series of compounds under the assumption that they are isostructural and that the $A_k^q\langle r^k\rangle$ coefficients can be expressed as a linear function of the number of f electrons [266]. This method describes well the magnetic properties of the series of double decker compounds studied by them [267]. For this reason, the same procedure has been applied for determining as a first approximation the zero field splitting parameters of the series of POMs-based single molecule magnets [260].

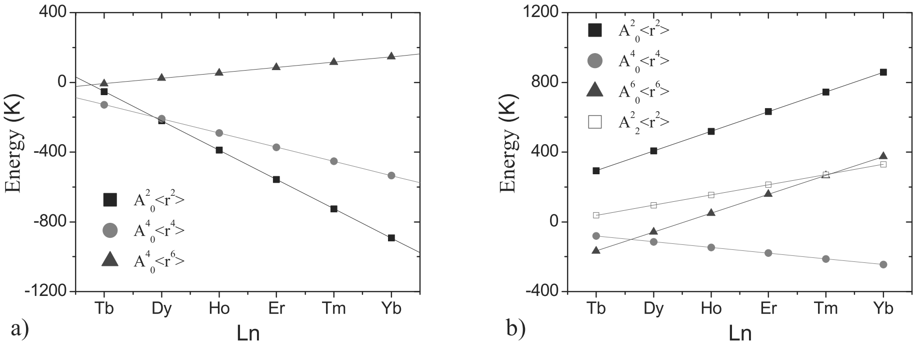

Figure 6.7: Values of the $A_k^q\langle r^k\rangle$ parameters for the series of the different compounds synthesized and corresponding to the two families. (a) LnW$_{10}$ (from Ref. [265]). (b) LnW$_{30}$ by courtesy of M. Clemente and S. Cardona-Serra.

The ligand field parameters have been determined by S. Cardona-Serra and co-workers [265]. For the LnW$_{10}$, an ideal D_{4d} point group symmetry has been considered the spin Hamiltonian of which consists only of diagonal terms:

$$\mathcal{H}_{\mathrm{LnW}_{10}} = A_2^0\langle r^2\rangle\theta_2\mathbf{O}_2^0 + A_4^0\langle r^4\rangle\theta_4\mathbf{O}_4^0 + A_6^0\langle r^6\rangle\theta_6\mathbf{O}_6^0 \qquad (6.12)$$

Constants $A_k^q\langle r^k\rangle$ are the parameters to be determined while the coefficients θ_2, θ_4 and θ_6 are the constants tabulated by Stevens [262]. A simultaneous fit of the susceptibility data from 2 K up to room temperature corresponding to Ln=Tb, Dy, Ho, Er, Tm, Yb has been performed (for more details see [265]). The set of parameters are depicted in Fig. 6.7.a. As it can be seen there, the $A_0^2\langle r^2\rangle$ parameters are negative for all the ions studied indicating uniaxial anisotropy along the z axis. The latter axis corresponds to the line connecting both POM molecules that surround the lanthanide (see Fig. 6.5.a).

Regarding the LnW$_{30}$ family, there is no specific hamiltonian corresponding to a C$_{5v}$ symmetry. However, it is possible to ascertain in a first approximation which contributions are more important. By performing some simple calculations, S. Cardona-Serra and co-workers have found that the hamiltonian that better describes the system can be approximated by that of Eq. 6.12 plus a second order transverse term giving

$$\mathcal{H}_{\mathrm{LnW}_{30}} = A_2^0\langle r^2\rangle\theta_2\mathbf{O}_2^0 + A_2^2\langle r^2\rangle\theta_2\mathbf{O}_2^2 + A_4^0\langle r^4\rangle\theta_4\mathbf{O}_4^0 + A_6^0\langle r^6\rangle\theta_6\mathbf{O}_6^0 \quad (6.13)$$

Following the same procedure as before (see [265]), the set of ligand field parameters that accounts simultaneously for the susceptibility data of the LnW_{30} family (with Ln=Tb, Dy, Ho, Er, Tm, Yb) has been determined. These parameters are plotted in Fig. 6.7.b. Interestingly, the $A_2^0\langle r^2\rangle$ parameters are all positive in this case indicating a preferred easy-plane symmetry. The xy easy plane corresponds to plane of the disk-like molecules (see Fig. 6.5.b).

6.4 Gadolinium: a model crystal field probe

As it might have been noticed by the reader, gadolinium has not been included in the discussion presented above. The reason is that Gd is an isotropic ion in its trivalent state. The J_z states should be therefore degenerate at zero applied field enabling the magnetic moment to attain thermal equilibrium at any temperature. Under these circumstances, no trace of the typical features ascribed to SMMs should be observed. However, the magnetic susceptibility of GdW_{10} and GdW_{30} exhibits superparamagnetic blocking at very low temperatures as it can be observed in Fig. 6.8.

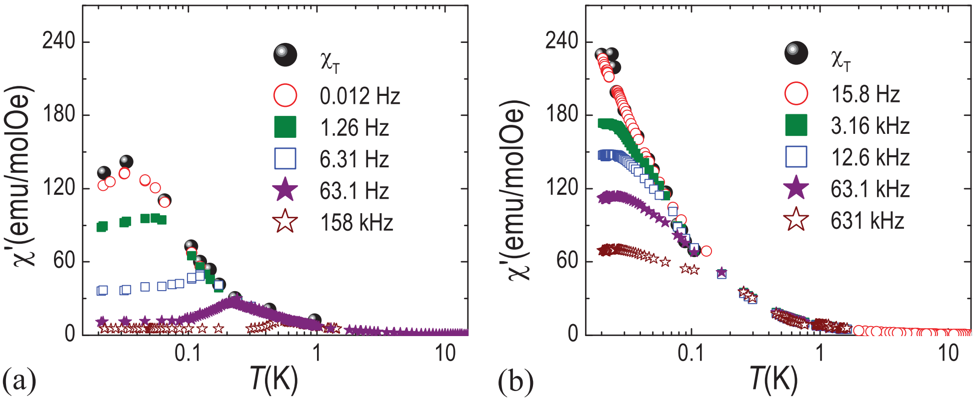

Figure 6.8: Real part of the susceptibility of GdW_{10} (a) and GdW_{30} (b) as a function of temperature. Measurements obtained for different frequencies are shown in both cases together with the equilibrium susceptibility (χ_T). The latter is determined as the $f \to 0$ limit of the real susceptibility data shown in Figs. 6.15a and 6.17a fitted to a Cole-Cole law.

The ideal isotropy of the Gd^{3+} ion becomes distorted by the presence of the surrounding crystal field. In this way, gadolinium appears as an excellent probe to explore the symmetry induced when encapsulating these magnetic ions in different POM structures. In this chapter we will study the differences in the dynamical magnetic response of the LnW_{10} and the LnW_{30} families, which follows as a consequence of their different ligand field architectures. For this purpose, a combination of specific heat measurements, EPR spectroscopy and ac magnetic susceptibility has been used. The results are described in the following.

6.4.1 Gadolinium as a free ion and as part of a crystal

Gadolinium is a rare earth element belonging to the group of lanthanides (f-block in the periodic table). It is paramagnetic at room temperature providing one of the most commonly used Magnetic Resonance Image (MRI) contrast agents. Apart from its medical application, gadolinium is of much technological interest for the development of adiabatic magnetic refrigerators thanks to its large magnetocaloric effect. In fact, gadolinium and its alloys are the most-used materials for room temperature adiabatic refrigeration.

The electronic configuration of Gd corresponds to [Xe], $4f^7$, $5d^1$, $6s^2$. In the trivalent cationic state this turns to [Xe], $4f^7$ where half of the 4f shell is fully occupied. According to Hund's rules, this configuration results in a total spin momentum of $S = 7/2$ and angular momentum of $L = 0$, i.e. the fundamental state is ^{8}L in the spectroscopic notation. The g factor of gadolinium will be therefore that of a free electron, i.e. $g = 2$. The latter has been confirmed experimentally by several groups, like W. Low and D. Shaltiel that found $g = 1.991 \pm 0.001$ in a EPR experiment on gadolinium in thorium oxide [268].

The distortion induced by a crystal field on the isotropy of this ion has been previously studied in crystals containing gadolinium. B. Bleaney *et al* studied Gd^{3+} ions located in a six fold symmetry crystal field [269]. They found that the interaction between the ideal ^{8}S state and the crystal field leads to a level splitting at zero field of ~ 0.35 K. W. Low and K. Shaltiel found an overall splitting of ~ 0.25 K in Gd^{3+} ions located in a cubic field [268]. One of the largest splitting was reported by S. Geschwind *et al* in a sample of Al_3O_4 doped with Gd^{3+} impurities. In this case, gadolinium is in a three fold symmetry giving a total splitting of ~ 1.8 K [270].

6.4.2 Magnetic characterization at $T > 1.8$ K

GdW_{10} and GdW_{30} samples have been characterized in a commercial MPMS magnetometer from Quantum Design as described in chapter 1. The magnetization response to the applied magnetic field has been measured on powdered samples of both compounds.

As we can see in Fig. 6.9, magnetization curves measured at three different temperatures merge into one when plotted vs. H/T, indicating that the molecular spins are able to attain thermal equilibrium and that anisotropy effects are relatively weak at these temperatures. The saturation magnetization of both samples coincides with the expected value of a spin $S = 7/2$, i.e. $M_{sb} = gS = 7\ \mu_B$.

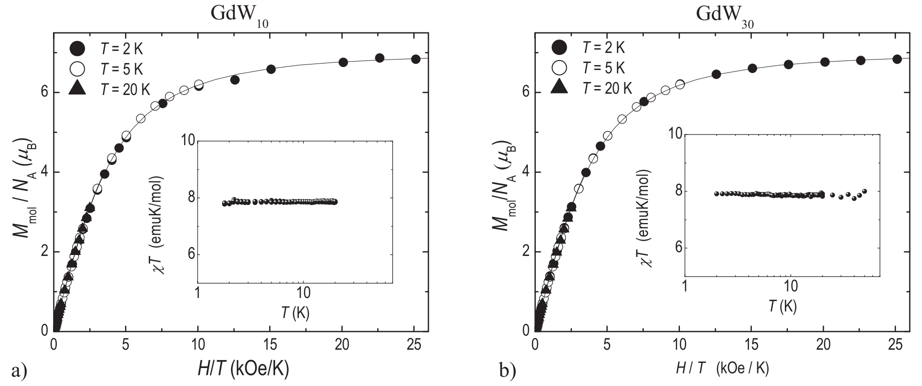

Figure 6.9: Magnetization of GdW$_{10}$ (a) and GdW$_{30}$ (b) plotted vs. H/T at different temperatures. The insets show the value of χT vs. temperature corresponding to GdW$_{10}$ (a) and GdW$_{30}$ (b) that remains constant indicating no influence of anisotropy.

Magnetic susceptibility is inversely proportional to temperature, following Curie's law (see Eq. 3.5). In the insets of Fig. 6.9.a and b, we can see the product χT vs. temperature corresponding to GdW$_{10}$ and GdW$_{30}$, respectively. χT remains independent of temperature down to 1.8 K giving a value of $C = N_A g^2 \mu_B^2 S(S+1)/3k_B = 7.9$ emuK/mol. The latter gives $S \approx 3.5$ in very good agreement with the results obtained from the saturation magnetization.

From these analyses we can conclude that GdW$_{10}$ and GdW$_{30}$ behave as effective spins equal to 7/2 indeed. These measurements will also serve us to scale the data obtained at very low temperatures using our μSQUID susceptometer.

6.4.3 Specific heat

The specific heat of GdW$_{10}$ and GdW$_{30}$ was measured as a function of temperature and under different applied fields. For this purpose, we employed a few mg of powdered sample and performed the measurements using a PPMS from Quantum Design as described in chapter 1.

The contribution from the lattice dominates the specific heat measured at high temperatures ($T \geq 20$ K) and can be easily subtracted from the experimental data. In this way we can concentrate on the magnetic contribution that varies with the applied field as shown in Fig. 6.10. The fact that the specific heat shows a Schottky-like anomaly already for $H = 0$ suggests the presence of a finite zero-field splitting.

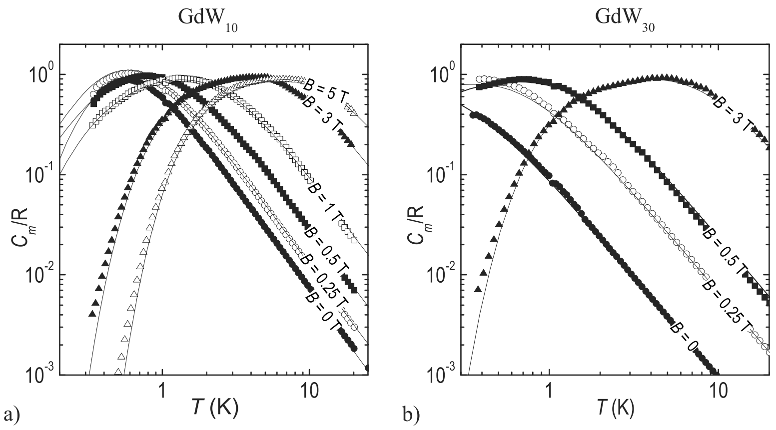

Figure 6.10: Magnetic specific heat (scatter) of GdW$_{10}$ (a) and GdW$_{30}$ (b) as a function of temperature measured unter different magnetic fields. The contribution form the lattice has been subtracted from these data and the resulting curves have been fitted to a theoretical computation of C_m (solid lines).

In the same figure, we show calculations of the magnetic specific heat performed with the anisotropy parameters of each compound. For the case of GdW$_{10}$, we consider the hamiltonian defined in Eq. 6.1 with $E = 0$. For GdW$_{30}$, a reasonably good fit can only be obtained for $E \neq 0$. The energy ε_m that corresponds to each m level can be obtained by diagonalizing this hamiltonians. The specific heat is then given by the fluctuation-dissipation theorem as follows

$$C_m/R = \frac{1}{T^2}\left(\langle U^2\rangle - \langle U\rangle^2\right) \tag{6.14}$$

where $\langle U\rangle$ are, respectively, the thermally averaged value of the energy and of the squared energy at a given temperature. These averages can be computed by doing

$$\langle U\rangle = \frac{1}{Z}\sum_{m=-J}^{m=J} \varepsilon_m e^{\varepsilon_m/k_\mathrm{B}T} \tag{6.15}$$

$$\langle U^2\rangle = \frac{1}{Z}\sum_{m=-J}^{m=J} \varepsilon_m^2 e^{\varepsilon_m/k_\mathrm{B}T} \tag{6.16}$$

Z being the partition function.

Using Eqs. 6.14, 6.15 and 6.16, we have calculated the magnetic specific heat curves that best describe the experimental results. By doing so, we obtain a value of $B_2^0/k_\mathrm{B} = -0.06$ K for the GdW$_{10}$. This is consistent with the expected uniaxial anisotropy. In the case of GdW$_{30}$, the values that best account for the experimental data are $B_2^0/k_\mathrm{B} = 0.022$ K and $B_2^2/k_\mathrm{B} = 0.013$ K. Again, the sign of these parameters agrees with the easy-plane anisotropy found by S. Cardona-Serra for this family [265].

6.4.4 Electron Paramagnetic Resonance (EPR) spectroscopy

EPR spectroscopy supplies additional information on the electronic structure of our compounds. As it was introduced in chapter 1, measurements are usually performed by sweeping the magnetic field and recording the energy absorbed by the sample at a given frequency. Conventional EPR set-ups operate at fixed frequency values between 1 GHz (within the so-called L-band) and 95 GHz (W-band). The external magnetic fields can be usually varied up to 2 T. These ranges turn out to be ideal for characterizing our samples enabling us to refine the different zero field splitting parameters, estimated before, and also consider the necessity of introducing higher order terms.

Broad band EPR spectroscopy has been performed at the University of Stuttgart in collaboration with Prof. J. Van Slageren and Dr. C. Schlegel. Measurements at different frequencies are possible thanks to a frequency tunable cavity developed during the thesis of Dr. C. Schlegel that we briefly described in chapter 1.

Following this procedure, the EPR spectra of GdW$_{10}$ and GdW$_{30}$ have been measured at 1.7 K and 10 K. At both temperatures the cavity length was varied to obtain different resonant frequencies equivalent to 15, 20, 25, 30 and 35 GHz. The resulting spectra have been analyzed with *Easyspin*, a free MATLAB toolbox designed for the interpretation of EPR data [271]. This software enables the simulation of the EPR spectrum corresponding to a given magnetic field range, resonance frequency (f) and linewidth (lw) and the characteristics of the ion, namely the spin (S), the g factor and the zero field splitting parameters (B_2^0, B_2^2...). Moreover, it enables us to fit the simulated spectrum to the experimental one by varying any of these parameters. Since the values of S and g are known, this software enables us to obtain an accurate estimation of the anisotropy parameters B_2^0, B_2^2...

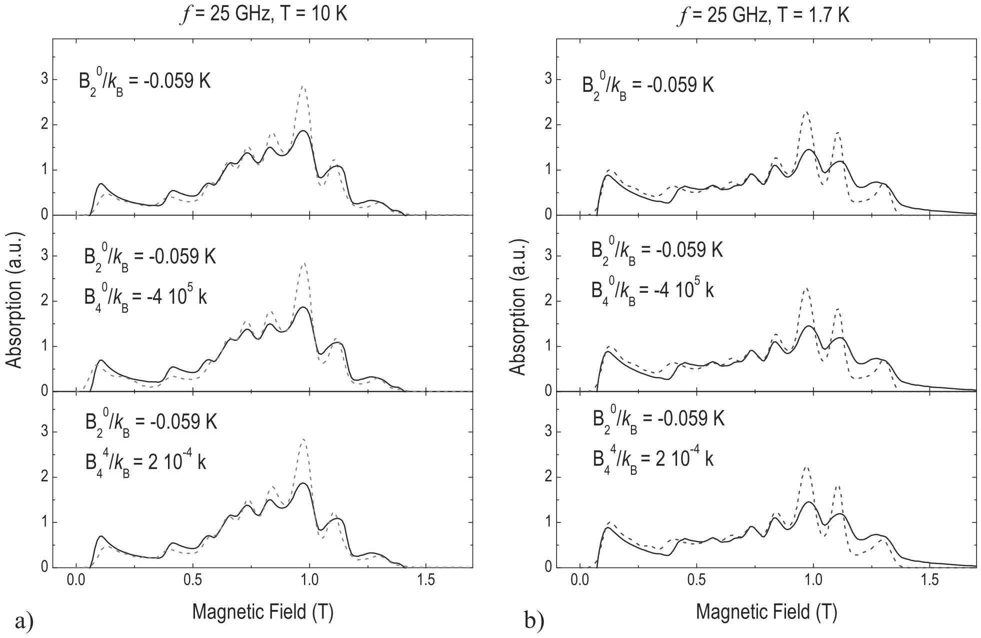

Figure 6.11: EPR spectra of GdW_{10} (solid lines) and the corresponding fitting obtained with *Easyspin* (dotted lines). These spectra have been measured at $f = 25$ GHz and $T = 10$ K (a) and $T = 1.7$ K (b). The addition of different zero field splitting parameters has been explored, the values of which appear in the legend.

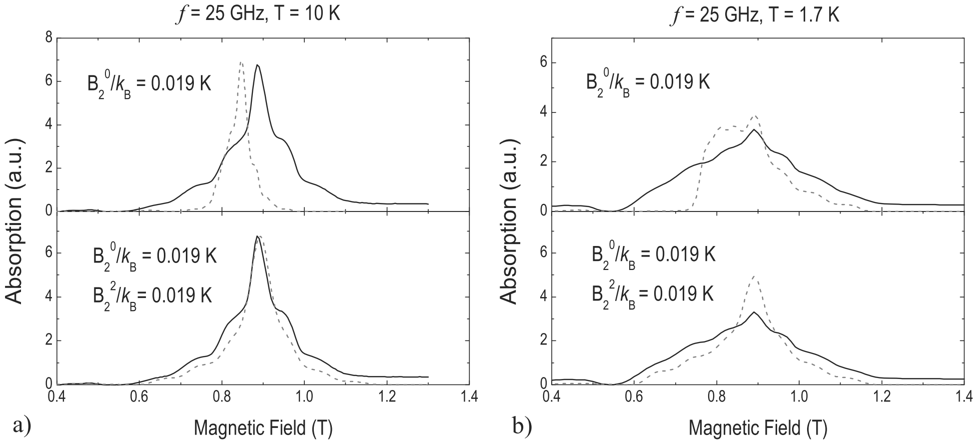

Figure 6.12: EPR spectra of GdW_{30} (solid lines) and the corresponding fits obtained with *Easyspin* (dotted lines) at the same frequency and temperature as in the previous case. As can be seen, the consideration of just the B_2^0 parameter leads to very poor fittings (upper panels). A good agreement is obtained only with the inclusion of a finite B_2^2 (bottom panels).

GdW$_{10}$

Two representative spectra obtained at 1.7 K and 10 K, and at a resonant frequency of 25 GHz are shown in Fig. 6.11. Fixing $S = 7/2$ and $g = 2$ for gadolinium, we have obtained the value of B_2^0 that best fits all the spectra. This gives $B_2^0/k_\mathrm{B} = -0.059$ K, in very good agreement with the value estimated from the specific heat data. Higher order terms can also been considered. For instance, the effect of adding a $B_4^0/k_\mathrm{B} = -4\times10^{-5}$ K can be seen in the middle panels of Fig. 6.11. As it can be seen there, it does not improve the quality of the fit and, for this reason, it will not be considered in the discussion that follows.

GdW$_{30}$

Two representative spectra measured at the same resonant frequency and temperatures as before can be seen in Fig. 6.12. Following the same procedure, the value of B_2^0 was first estimated by fitting all the spectra obtained at different resonant frequencies and temperatures. As it is shown in the upper panels of Fig. 6.12, the consideration of just one parameter results in very poor fittings. For this reason, the next anisotropy term, B_2^2, must be taken into account. We found that $B_2^0/k_\mathrm{B} = 0.019$ K and $B_2^2/k_\mathrm{B} = 0.019$ K provide reasonably good fits of all the spectra. The addition of higher order terms has also been checked but it does not improve the fitting's quality and they will not be considered. Concluding, we found again a very good agreement with the parameters estimated from the analysis of specific heat measurements.

6.4.5 Discussion: tailoring magnetic anisotropy with molecular symmetry

The previous analysis, together with the results obtained from specific heat measurements, provide us a reliable description of the spin hamiltonians of GdW$_{10}$ and GdW$_{30}$. The former consists of just a negative diagonal second order term $B_2^0/k_\mathrm{B} = -0.059$ K. This means that the Gd ion is no longer isotropic but has an easy magnetization axis along the z direction (z being defined in Fig. 6.5a). The origin of this distortion is, without doubt, the electrostatic interaction with the POM molecules that sandwich the ion.

The corresponding classical energy plot can be seen in Fig. 6.3a. However, in order to gain a deeper insight into the spatial distribution of the magnetic moment, we can plot the probability of the spin for pointing along a given direction of the space. This representation has the advantage that it resembles the actual shape of the molecule. The spatial probability plot of GdW$_{10}$ is

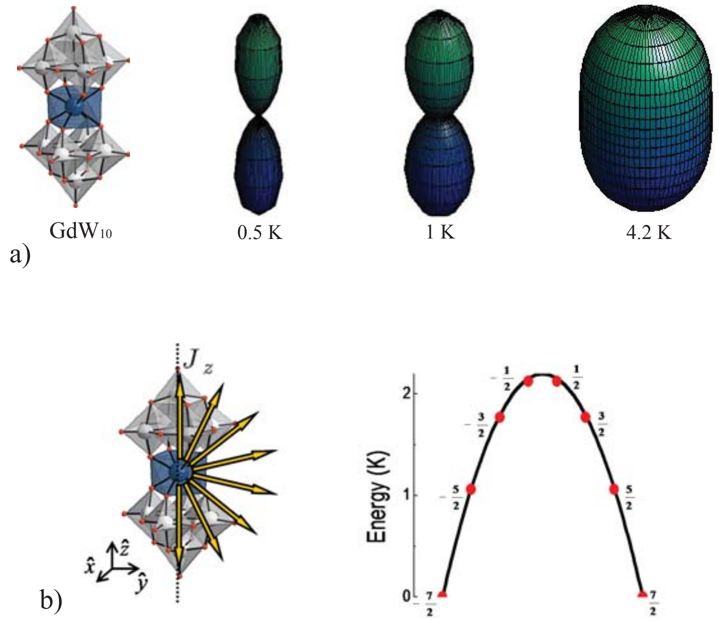

Figure 6.13: a) From left to right we can see an schematic representation of the GdW_{10} molecule, and the population of the distinct spatial J orientations at $T = 0.5$ K, 1 K and 4.2 K. b) Classical potential energy as a function of J_z (line) where the dots give the energies of quantum eigenstates.

depicted in Fig. 6.13.a at different temperatures. As it can be seen there, the spin preferred direction is along the z axis, while the xy plane becomes populated only when the temperature increases. The classical potential energy vs. the spin z-component is depicted in Fig. 6.13b. The system's ground state corresponds to $J_z = \pm 7/2$ and the total height of the anisotropy energy barrier separating these states equals 2.15 K. This is the energy required for the classical thermally activated spin reversal.

On the other hand, the hamiltonian of the GdW_{30} molecule consists of a positive diagonal second order term $B_2^0 = 0.019$ K and a positive transverse second order term $B_2^0 \approx B_2^2$. The corresponding classical potential energy is depicted in Fig. 6.3f. This molecule has a dominant easy-plane magnetic symmetry with a preferred magnetization direction along the y axis. The spatial probability plot at different temperatures is depicted in Fig. 6.14a. As we can see there, the spin remains in the xy plane at low temperatures with a higher probability of pointing along the y axis. However, the anisotropy terms of this molecule are weaker than those of GdW_{10}. This leads to a higher population of the out-of-plane states. In fact, magnetically speaking, the molecule is nearly isotropic at liquid helium temperatures.

In Fig. 6.14b and 6.14c we can see the classical energy vs. the y-component

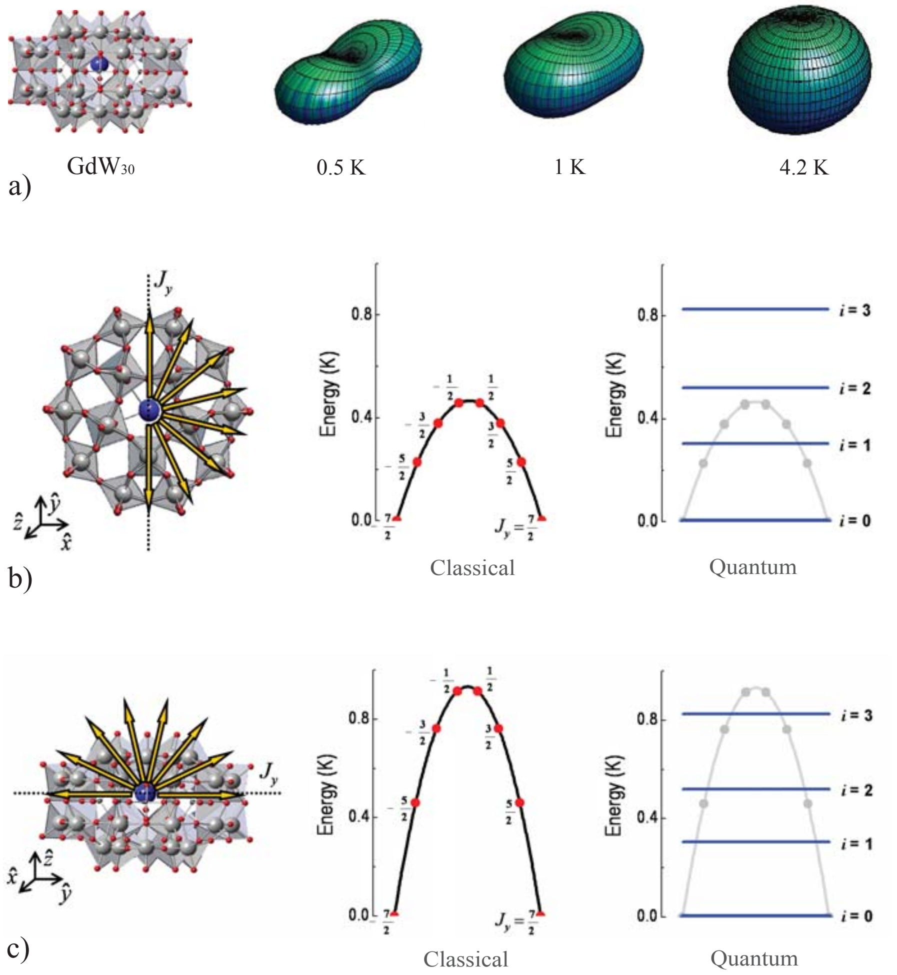

Figure 6.14: a) Schematic representation of GdW_{30}, and the population of the distinct spatial J orientations at $T = 0.5$ K, 1 K and 4.2 K. b) and c) show a plot of the classical potential energy as a function of J_y for the case of in-plane ($J_z = 0$) and out-of-plane ($J_x = 0$) spin inversion, respectively. Both plots are compared in the right part of the figure with the energy levels obtained from the diagonalizitaion of the molecule's spin hamiltonian. As it can be seen, quantum levels are more energetic than those corresponding to the classical spin states with $J_z = 0$ (panel b). On the other hand, quantum levels are less energetic than those corresponding to $J_x = 0$ (panel c). This fact suggests that quantum states are actually superpositions of the three classical projections J_x, J_y and J_z. Spin inversion does not take place in-plane neither out-of-plane but via an admixture of both "paths".

of the magnetic moment corresponding to two different cases: in-plane spin inversion ($J_z = 0$) and out-of-plane spin inversion ($J_x = 0$), respectively. Neither of these classic images correspond however to the energy levels associated with the spin quantum states that are actually combinations of the classic J_y projections. A realistic energy level scheme can only be calculated by diagonalizing the spin-hamiltonian of the molecule. The resulting energy levels are shown in the right part of Fig. 6.14b and Fig. 6.14c.

These levels are associated with symmetric and antisymmetric combinations of J_y. The expectation values of the square of the spin projections along the axes of quantization can be calculated by doing $\langle P^2\rangle_i = \langle \mathcal{H}|P^2|\mathcal{H}\rangle_i$ where $P = J_x$, J_y and J_z, and the subscript denotes the energy level, $i = 0$ for the ground degenerate doublet, $i = 1$ for the first excited degenerate doublet and so on (see Fig. 6.14b or c). For the ground state doublet we obtain $\langle J_x^2\rangle_0 = (1.62)^2$, $\langle J_y^2\rangle_0 = (3.46)^2$ and $\langle J_z^2\rangle_0 = (1.06)^2$. This means that the wavefunctions concentrate in the xy plane and, within it, along the easy axis y. The first and second excited doublets correspond however to $\langle J_x^2\rangle_1 = (2.80)^2$, $\langle J_y^2\rangle_1 = (2.31)^2$ and $\langle J_z^2\rangle_1 = (1.60)^2$ and to $\langle J_x^2\rangle_2 = (2.80)^2$, $\langle J_y^2\rangle_2 = (1.60)^2$ and $\langle J_z^2\rangle_2 = (2.31)^2$, respectively. The corresponding wavefunctions will therefore concentrate again in the xy plane but, in this case, along the x direction. Finally, for the most excited doublet we obtain $\langle J_x^2\rangle_3 = (1.62)^2$, $\langle J_y^2\rangle_3 = (1.06)^2$ and $\langle J_z^2\rangle_3 = (3.46)^2$, which means that the wavefunctions concentrate along the hard axis z. In this way, the actual quantum energy level structure of this molecule lies between the two classical pictures depicted in Fig. 6.14b and 6.14c. Spin inversion does not take place in-plane neither out-of-plane but via an admixture of both ”paths”.

To conclude, let us highlight that the energy level structures of GdW_{30} and GdW_{10} are completely determined by the point group symmetry in which the gadolinium ion lies. The observed symmetries are consistent with what one would expect considering the structural characteristics of these molecules. As we will see in the next section, these differences will determine drastically the dynamic magnetic behavior of both systems.

6.5 Magnetic dynamics at very low temperatures

Associated with the very different underlying magnetic model of these two molecules, we also expect pronounced differences in their magnetic response in the region of low temperatures. Above $4 - 5$ K, both molecules are nearly isotropic and they behave as effective spins equal to 7/2 as it was shown in section 6.4.2. However, as temperature decreases, differences between their dynamical response become apparent as we will show in this section.

6.5.1 Low temperature magnetic response of GdW$_{10}$

The magnetic susceptibility of GdW$_{10}$ was measured down to ~ 22 mK using the μSQUID susceptometer described in chapter 2. For this purpose, a small quantity ($\sim \mu$g) of a powdered sample of GdW$_{10}$ was mixed with Apiezon-N grease and deposited onto the pickup coil of the susceptometer. The cooling down and measurement processes are fully described in Chapters 1 and 2 respectively. The resulting signal is converted to magnetic units (emu/molOe) by scaling it with the data obtained with the MPMS magnetometer in a coincident temperature range.

The temperature dependence of the real susceptibility measured at diverse frequencies was already shown in Fig. 6.8.a. The imaginary part (not shown) exhibits a similar behavior. It will be more convenient now to plot the susceptibility response vs. frequency at different temperatures as can be seen in Fig. 6.15.a. The data closely follow a Cole-Cole law (see Section 3.7.3) enabling us to obtain an accurate estimation of the relaxation time (τ) and the equilibrium susceptibility (χ_T), in a similar way as we did in Section 5.4.5. The relaxation time is plotted vs. $1/T$ in Fig. 6.15.b.

As we anticipated in Section 6.4, the fingerprints of the superparamagnetic blocking of the magnetization are clearly visible below 1 K. As temperature decreases, the susceptibility becomes blocked at successively lower frequencies as typically occurs for a thermally activated process. The energy U involved in this process can be obtained by the linear fit of a $\ln \tau$ vs. $1/T$ plot, according to Arrhenius law (see Eq. 3.6). The result of this fit can be seen in Fig. 6.15.b and gives $U = 2.17 \pm 0.13$ K, in excellent agreement with the theoretical value, i.e. $U(\text{theo}) = 2.15$ K (see section 6.4.5). However, below ~ 100 mK, the relaxation time becomes independent of temperature. As we have seen previously, this behavior is ascribed to a magnetization reversal process solely dominated by pure quantum tunneling.

At even lower temperatures, a new phenomenon shows up. Looking carefully at Fig. 6.8a we can see that the susceptibility peak becomes independent of frequency as the measurement time increases, i.e. as the frequency decreases. Even the equilibrium susceptibility (χ_T) obtained by extrapolating the Cole-Cole fittings of Fig. 6.15a to $f \to 0$ exhibits a peak at $T_{\mathrm{N}} \sim 36$ mK. This time-independent response is due to a magnetic phase transition.

Because of the large separation between the magnetic centers in these materials, intermolecular exchange interactions are negligible and can not be responsible of such behavior. On the other hand, dipolar interactions can be quite important at very low temperatures. The latter can lead to a long-ordered phase of ferro or antiferromagnetic type depending on the crystal

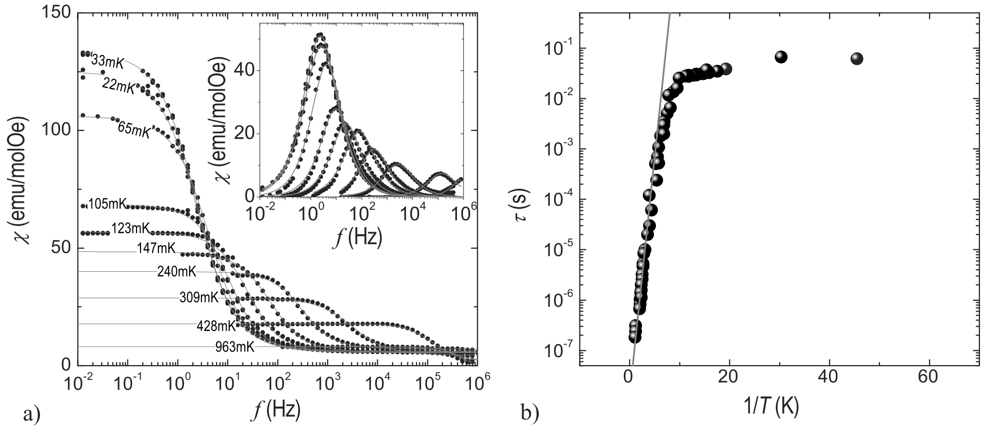

Figure 6.15: a) Real part (scatter) of the susceptibility of GdW$_{10}$ vs. frequency at different temperatures. The inset shows the imaginary part. From a Cole-Cole fit (solid lines) of these curves it is possible to obtain: the equilibrium susceptibility χ_T shown in Fig. 6.8a, the relaxation time shown in the b) panel and the β parameter shown in Fig. 6.18a.

structure [272–274]. As we will argue in the next chapter, antiferromagnetic order is probably occurring in these systems (see section 7.4.1). The important role of dipolar interactions on the tunneling processes will be further analyzed there as well.

The experimental tunnel splitting can be now determined following the model of Prokoféev and Stamp (see Eq. 6.11). The width of the distribution of dipolar energy $\sigma_{\xi_{\mathrm{dip}}}$ can be estimated roughly from the condition $\sigma_{\xi_{\mathrm{dip}}}/k_{\mathrm{B}} \sim T_{\mathrm{N}}$, which gives $\sigma_{\xi_{\mathrm{dip}}}/k_{\mathrm{B}} = 36$ mK. Inserting this value and the temperature independent relaxation time of $\tau = 0.07$ s into Eq. 6.11, we obtain $\Delta/k_{\mathrm{B}} = 4 \times 10^{-6}$ K.

To conclude this section, let us finally mention that the observed phase transition exhibits some features that are typical of first-order phase transitions. This can be seen in the following measurements, shown in the inset of Fig. 6.16. The susceptibility was measured as the temperature decreased at a constant rate. When approaching T_{N}, the cooling process was stopped to maintain the temperature constant for about 10 minutes. During this time, the susceptibility was observed to increase logarithmically with time as shown in Fig. 6.16. After that, we continued to cool down to 22 mK. On the other hand, when the system is slowly heated from the base temperature upwards, the magnetic susceptibility is found to follow a different path. From the latter values, and fitting the susceptibility vs. time to a logarithmic grow law, we find that a time of about 30 minutes should be necessary for the susceptibility to stabilize. This intriguing hysteretic behavior and the observed aging of

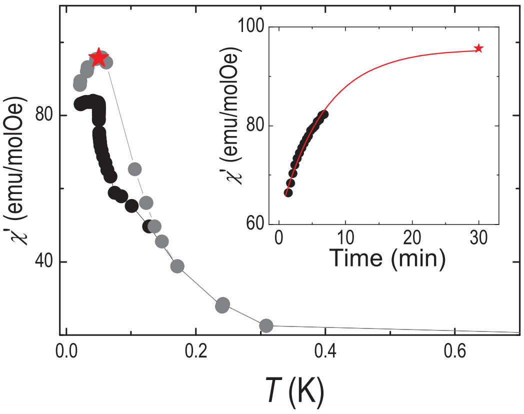

Figure 6.16: Susceptibility measured when cooling the sample and stopping at ∼ 50 mK for ten minutes (black scattered data). During this time the susceptibility grows as depicted in the inset. When the system is slowly heated up from the base temperature an hysteretic response appears (grey scattered data). In the inset we can see that the time evolution of the real part of the susceptibility (scatter) is well described by a logarithmic growth (solid lines). This response is ascribed to a magnetic transition of first order class.

the susceptibility might be due to the energy absorption during the transition while the temperature remains constant, which is characteristic of first-order type transitions.

6.5.2 Low temperature magnetic response of GdW$_{30}$

A powdered sample of GdW$_{30}$ has been measured down to very low temperatures and scaled using the data obtained with the MPMS magnetometer as in the previous case.

The magnetic susceptibility as a function of temperature was shown already in Fig. 6.8.b at different frequencies. Slow relaxation of the magnetization becomes apparent at very low temperatures where a clear dependence with the frequency appears. Fig. 6.17 shows the magnetic susceptibility dependence with frequency where the same behavior can be observed. But, unlike in the case of GdW$_{10}$, thermal equilibrium is maintained down to lower temperatures. This property indicates that the spin reversal of GdW$_{30}$ is less influenced by the crystal field anisotropy as we anticipated in Section 6.4.5.

The origin of the observed slow relaxation is however not a classical thermally assisted relaxation over the energy barrier but spin quantum tunneling. Two facts support our interpretation. First of all, the classical energy barrier created by the anisotropy along the J_x component equals 460 mK. This is therefore the value that one would expect from an Arrhenius fit of the data depicted in Fig. 6.17.b. However, the temperature dependence of τ corresponds to an energy barrier of just 20 mK. Secondly, the dependence of the susceptibility on frequency is characteristic of a quantum relaxation process. Whereas the classical phonon-induced relaxation rate is very similar for all the molecules, as it is determined by the activation energy U, the quantum relaxation rate strongly depends on the local field as we discussed in Section 6.3.1. This phenomenon leads to a temperature-dependent and very wide distribution of relaxation times, that reflects the temperature and spatial dependences of the local field. The latter is not only due to dipolar interactions but also to the hyperfine field originated by the surrounding atoms. Moreover, the hyperfine field can exhibit a wide distribution because of the presence of two isotopes of tungsten and gadolinium. A percentage of $\sim 86\%$ W atoms carry no nuclear spin but the remaining $\sim 14\%$ have $I = 1/2$. In addition, there is about a $\sim 2\%$ of the Gd ions carrying a nuclear spin equal to 1/2.

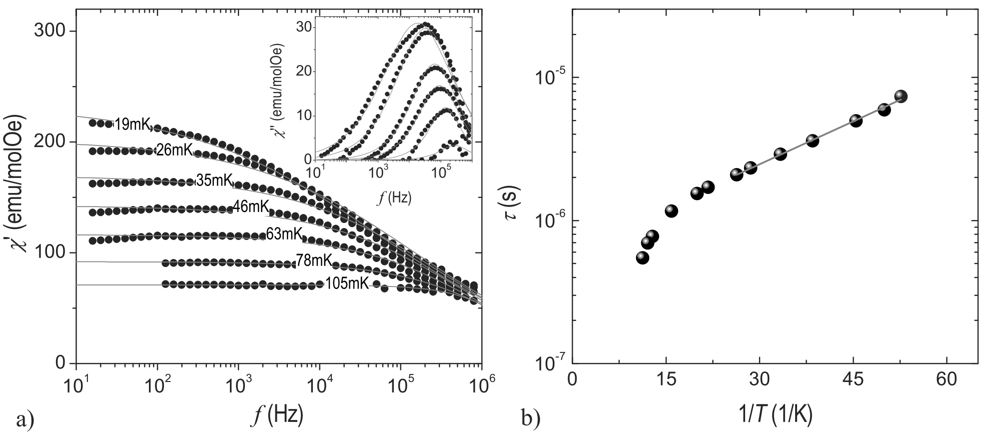

Figure 6.17: a) Real (scatter) and imaginary (scatter data in the inset) of the susceptibility of GdW$_{30}$ vs. frequency at different temperatures and the corresponding Cole-Cole fittings (solid lines). From the latter we obtain again the equilibrium susceptibility presented in Fig. 6.8b, the relaxation time shown in the b) panel and the β parameter shown in Fig. 6.18b.

On the other hand, in these measurements we do not observe the influence of long range order due to dipolar interactions. The strength of the dipolar energy bias must therefore be smaller than 19 mK. The weak strength of the dipolar interactions in this sample can be intuitively understood from the structural characteristics of the molecule. In GdW$_{30}$, the gadolinium ion is much more isolated from the rest of the molecules than in the crystal of GdW$_{10}$.

The dipolar ordering temperature can be approximately estimated considering that of GdW_{10}. The average Gd-Gd distance is ~ 1 nm for the case of GdW_{10} and ~ 2 nm for the case of GdW_{30}. As the dipolar interaction decreases with $1/r^3$, being r the distance between the ions, we can estimate a decrease of one order of magnitude in the value of $\sigma_{\xi_{\mathrm{dip}}}/k_{\mathrm{B}}$ that would therefore be ~ 4 K approximately.

Taking into account the low temperature relaxation time of 7×10^{-6} s and the relationship given by Eq. 6.11, we obtain that the tunneling splitting is $\Delta/k_{\mathrm{B}} \approx 10^{-4}$ K. This is two orders of magnitude larger than that of GdW_{10}.

6.5.3 Calculation of the spin-lattice relaxation rates: comparison with experiments

As we have seen, the magnetic anisotropies and dynamical responses of GdW_{10} and GdW_{30} are completely determined by their molecular symmetry, which in its turn is controlled by the shape of the POM clusters.

In the case of GdW_{10}, the molecular symmetry gives rise to the typical double-well potential characteristic of single molecule magnets. The relaxation towards equilibrium is governed in this case by phonon-absorption and emission processes. The spin exchanges with the lattice vibrations the energy it needs for jumping up or down the anisotropy energy barrier. One phonon of energy $\Delta = E_{m+1} - E_m$ is absorbed at each transition from m to $m+1$ with $m = -S$, $-S+1$, ..., up to the top of the barrier. In the same way, the evolution from the latter state towards the opposite side of the wall implies the successive emission of phonons of energy $\Delta = E_{m+1} - E_m$ with m starting from the top of the barrier down to $m = +S$. The relaxation process can be also assisted by quantum tunneling. In those cases, the spin does not need to climb up the barrier but is able to tunnel between excited energy levels associated with opposite spin states. This is the simplest Spin Lattice Relaxation (SLR) mechanism that involves successive transitions involving the creation or anhilation of just one phonon each time (a more detailed description can be found in the next chater).

Within this model, the relaxation rate is ultimately governed by temperature. This is true even if the spin inversion occurs through quantum tunneling between excited energy states since the latter also requires phonon assistance. Taking into account these considerations, the relaxation rate of the spin can be computed numerically. For this purpose one needs to solve the quantum Pauli master equation for the populations considering a spin-phonon interaction [242]. The latter can be seen as phonon-induced strains and vibrations that lead to small fluctuations in the crystal field. The method followed in this calculation is described in section 7.2.3 in the next chapter.

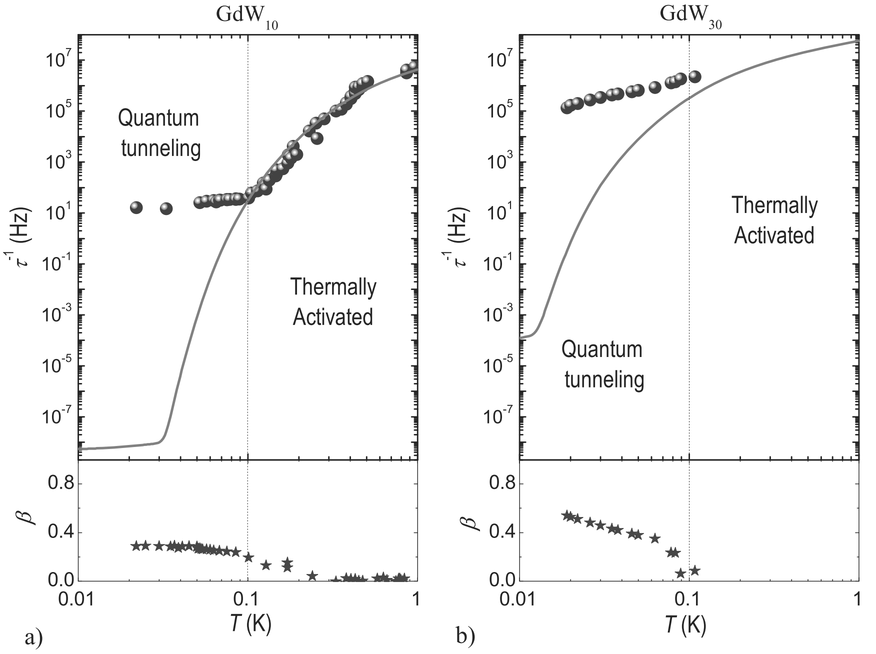

Figure 6.18: The upper panels show the relaxation rate (scatter) of GdW_{10} (a) and GdW_{30} (b) vs. temperature. Solid lines correspond to the theoretical calculation of τ^{-1} that have been performed by solving a quantum master equation for the time-dependent populations of magnetic energy levels obtained using the hamiltonian parameters determined in this section. The bottom panels show the β parameter that accounts for the width of the distribution of relaxation times (see section 3.7.3). As it can be seen, β increases drastically when approaching into the pure quantum tunneling regime in which the probability of spin inversion is much more sensitive to the energy bias distribution.

The result of this numerical computation provides an excellent description of the experimental data above $\sim$ 100 mK as it can be seen in Fig. 6.18a. Below this temperature, τ deviates however drastically from the theoretical predictions. The latter suggests that the relaxation becomes dominated by pure quantum tunneling between the ground states. Since Gd is a Kramers ion, there must be an effective transverse magnetic field able to mix the $m = -7/2$ and $m = +7/2$ states, i.e. an effective transversal dipolar field. As we have seen previously, GdW_{10} undergoes a transition to a magnetically ordered phase driven by dipolar interactions at $T_{\mathrm{N}} = 36$ mK. In the paramagnetic phase (above T_{N}) there is therefore a distribution of dipolar fields along the z and the transversal direction whose width $\sigma_{H_{\mathrm{dip}}}$ can be estimated from $2g\mu_{\mathrm{B}}J\sigma_{H_{\mathrm{dip}}} \sim k_{\mathrm{B}}T_{\mathrm{N}}$, giving $\sigma_{H_{\mathrm{dip}}} \approx 36$ Oe. Its strength is, however, too weak to induce the observed tunneling splitting of $\Delta/k_{\mathrm{B}} \sim 10^{-6}$ K by itself. This can be seen by diagonalizing the hamiltonian

$$\mathcal{H} = B_2^0 \mathbf{O}_2^0 - 2g\mu_\mathrm{B} \left(H_x J_x + H_y J_y + H_z J_z \right)$$

with $B_2^0/k_\mathrm{B} = -0.059$ K and $H_x = H_y = H_z = 36$ Oe. By doing so, we obtain that the energy difference between the ground and first excited levels equals $\Delta/k_\mathrm{B} \sim 10^{-15}$ K.

To account for the relatively large tunneling rate observed experimentally it is therefore necessary to introduce a transverse anisotropy term. As we show in Section 6.5, only diagonal terms are present in the hamiltonian that corresponds to the GdW_{10} point group symmetry (D_{4d}). However, even weak lattice distortions can modify this ideal symmetry allowing the addition of higher order terms. The symmetry reduction from the ideal D_{4d} to a C_4 point group seems to be reasonable in our case and we have therefore decided to include a B_4^4 term (see the hamiltonian defined in Eq. 6.4).

In order to find a quantitative value for B_4^4, we have fitted the EPR data using again *easyspin* software. The experimental spectra admit a B_4^4 parameter as high as $B_4^4/k_\mathrm{B} = 4 \times 10^{-4}$ K as it can be seen in the bottom panels of Fig. 6.11. The addition of this term does not change significantly the classical potential energy neither the spin-lattice relaxation time observed at high temperatures. Now, diagonalizing the hamiltonian

$$\mathcal{H} = B_2^0 \mathbf{O}_2^0 + B_4^4 \mathbf{O}_4^4 - g\mu_\mathrm{B} \left(H_x J_x + H_y J_y + H_z J_z \right)$$

we obtain $\Delta(\mathrm{theo})/k_\mathrm{B} = 0.96 \times 10^{-6}$ K in good agreement with the experimental value, i.e. $\Delta/k_\mathrm{B} = 4 \times 10^{-6}$ K.

Regarding now the GdW_{30} sample, its chemical structure leads to a much faster dynamical response. On the one hand, the energy barrier created by the anisotropy along the J_y component is just 460 mK which provides equilibrium conditions down to lower temperatures than the GdW_{10}. On the other, the large transverse anisotropy parameter in the hamiltonian of GdW_{30} is also the responsible of faster tunneling relaxation rates. Notice that tunneling processes occur between energy levels associated to J_y states.

The relaxation rate of GdW_{30} as a function of temperature is shown in Fig. 6.18b. In this graph, we can also see the theoretical relaxation rate calculated as we did with the GdW_{10}. Unfortunately, our experimental data do not cover the relaxation temperature region dominated by phonon absorption and emission processes. However, a reasonable agreement can be appreciated in the high-T region.

The theoretical values of τ in the region comprised between 100 mK $\leq T \leq$ 400 mK are associated to an effective energy barrier of $U/k_\mathrm{B} \sim 0.52$

K. This value corresponds to the energy of the second excited state of the energy level structure of the molecule (see Fig. 6.14). Our results suggest therefore that spin inversion in this temperature region takes place through the second excited energy levels associated to $\langle J_x^2 \rangle_2 = (2.80)^2$, $\langle J_y^2 \rangle_2 = (1.60)^2$ and $\langle J_z^2 \rangle_2 = (2.31)^2$. This is to say. the spin "rotates" in the xy plane, similar to the classical picture shown in Fig. 6.14b.

We can also estimate the theoretical tunnel splitting of GdW$_{30}$ by diagonalizing the hamiltonian

$$\mathcal{H} = B_2^0 \mathbf{O}_2^0 + B_2^2 \mathbf{O}_2^2 - g\mu_{\mathrm{B}} \left(H_x J_x + H_y J_y + H_z J_z \right)$$

with $B_2^0/k_{\mathrm{B}} = B_2^2/k_{\mathrm{B}} = 0.019$ K and $H_x = H_y = H_z = 4$ Oe. By doing so, we obtain $\Delta(\mathrm{theo})/k_{\mathrm{B}} = 3 \times 10^{-3}$ K which is also in relatively good agreement with the experimental value, i.e. $\Delta/k_{\mathrm{B}} \approx 10^{-4}$ K.

Further evidence for the crossover to a pure quantum relaxation regime can be inferred from the parameter β, which we plot in Figs. 6.18a and b for GdW$_{10}$ and GdW$_{30}$ respectively. This parameter, defined in section 3.7.3, is roughly zero in the temperature region where thermally activated processes dominate, indicating that all molecules relax approximately at the same rate. By contrast, β increases abruptly below $\sim$ 200 mK for GdW$_{10}$ and $\sim$ 60 mK for GdW$_{30}$ reaching relatively high values at very low temperatures. The latter behavior points undoubtedly to a crossover to a quantum mediated spin inversion regime, in which the wide distribution of local fields leads to a very wide distribution of relaxation rates. This holds for both GdW$_{10}$ and GdW$_{30}$.

6.6 Conclusions

We have demonstrated experimentally the enormous influence of the molecular symmetry on the energy level structure and the dynamical magnetic properties of these clusters. Our results show which are the main ingredients to play with in order to design molecules for different applications.

High-density data storage demands the use of systems with high energy barriers that protect the bit state at high temperatures. Lanthanides on the right side of the series would be more appropriated for this purpose since they lead to higher anisotropy terms (see Fig. 6.7).

The compounds presented here could also be used for adiabatic magnetic refrigeration. Both molecules, especially GdW$_{30}$, are quite isotropic and do not undergo any magnetic transition down to very low temperatures. The fulfillment of these conditions make them very interesting and promising candidates for very low temperature cooling applications.

Finally, the physical realization of reliable spin qubits for quantum computing demands other characteristics. The most challenging one is to obtain sufficiently long lived quantum states. As we saw in section 6.2.4, the decoherence time of POM-based clusters is expected to be rather high, compared with other polynuclear candidates, because of the possibility of preparing magnetically diluted and nuclear spin-free crystals.

On the other hand, a very important requirement is that imposed by the iith point in the DiVincenzo's checklist, i.e. the ability to prepare and manipulate the quantum state of the whole system of qubits (see section 6.2.2). Spin-based systems can be initialized in their ground state by cooling down to very low temperatures. The latter usually implies the use of a dilution refrigerator that provides a minimum temperature of ~ 10 mK. For the sake of clarity, let us define δ as the energy difference separating the ground ($|g\rangle$) and excited ($|e\rangle$) state of the spin qubit. The value of δ must be therefore large enough to ensure the thermal depopulation of the excited state at mK temperatures. For instance, 99.99% of the spin qubits would lie at their ground state at $T = 10$ mK for an energy gap equal to $\delta/\hbar = 1.8$ GHz. In this way, values of $\delta/\hbar$ equal to or larger than 1.8 GHz are desirable.

As far as the manipulation of the spin qubit state is concerned, some restrictions are imposed by the state of the art of quantum computing architectures. For instance, manipulation based in conventional EPR setups impose a limitation within an energy range of about $1 \lesssim \delta/\hbar \lesssim 100$ GHz. Other possible implementations, based on the coupling between spin qubit ensembles and superconducting microcircuits, e.g. flux qubits and microstrip resonators, are also limited in frequency. This fact arises from the frequency limitation of the superconducting material itself. When approaching the superconducting gap energy (Δ_{SC}), quasiparticle excitations of electron-hole type arise thereby reducing the number of Cooper pairs. This phenomenon leads to the degradation of the flux qubit performance or the decrease of the microcavity quality factor. This devices are therefore designed in such a way that their resonant frequencies lie well below $\Delta_{\mathrm{SC}}/\hbar$. Aluminium and niobium, the most widely used materials, exhibit typical values of the order of $\Delta_{\mathrm{SC}}/\hbar \sim 10^3$ GHz and $\sim 10^2$ GHz respectively. In addition, superconducting systems based on Josephson junctions (e.g. flux qubits) are also limited by the plasma frequency (ω_p). Typical values are of the order of $\omega_p/2\pi \sim 10^2$ GHz. In this way, the spin qubit's energy level structure must satisfy the condition $\delta/\hbar \ll 10^2$ GHz.

A good qubit candidate should therefore allow transitions between quantum states at energies comprised between $2 \lesssim \delta/\hbar \lesssim 10$ GHz. In this respect, GdW_{30} appears as an ideal candidate (see Fig. 6.19). The two levels corresponding to the ground and first excited state are separated by $\delta/\hbar = 6.35$

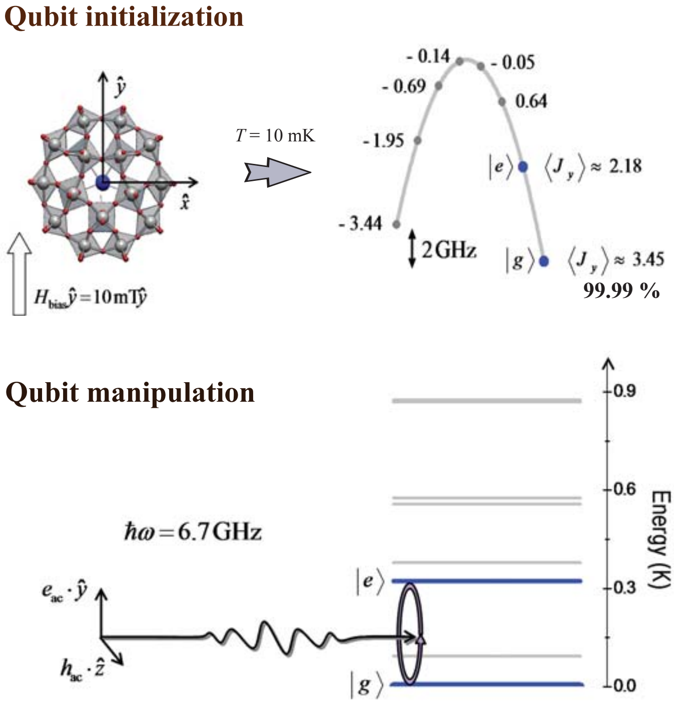

Qubit initialization

Qubit manipulation

Figure 6.19: Performance of a GdW_{30} qubit. A bias magnetic field of $H_{bias} = 10$ mT is applied along the y direction in order to distinguish energy transitions at both sides of the barrier. The energy of the first excited state becomes ~ 2 GHz giving a population of the ground state larger than 99.99% at mK temperatures. Quantum transitions can be driven by electromagnetic microwave radiation provided that the magnetic field component h_{ac} is applied perpendicular to the y axis.

GHz. This transition is however quasi-degenerate with that involving states at the other side of the energy barrier. This problem can be solved very easily by applying a small bias magnetic field (H_{bias}) along the y direction. Applying $H_{\text{bias}} = 10$ mT will be enough to separate the ground and the first excited state by an energy equal to 2 GHz that would enable the spin state initialization. Under the action of this magnetic field, the ground and second excited states become $\langle J_y \rangle \approx 3.45$ and $\langle J_y \rangle \approx 2.18$. We will obtain then a well defined two-level system with $|3.45\rangle \equiv |g\rangle$ and $|2.18\rangle \equiv |e\rangle$ separated by $\delta/\hbar = 6.7$ GHz. These states can be manipulated with electromagnetic microwave radiation produced by any conventional EPR setup, a flux qubit or a superconducting microcavity under the condition that the magnetic component h_{ac} is applied perpendicular to the y axis of the molecule.

On the other hand, the maximum rate at which quantum operations can be performed with our qubit is limited by the so-called Rabi frequency (Ω_{R}). The latter depends on the wave functions describing the ground and excited quantum states, decreasing drastically when the transition between them does not satisfy the corresponding selection rule $\Delta J_y = \pm 1$. Ω_{R} can be estimated as $\Omega_{\mathrm{R}} = g\mu_{\mathrm{B}}\,|\langle e|\mathbf{h}_{\mathrm{ac}}\mathbf{J}|g\rangle|$, where h_{ac} is the magnetic component of the microwave radiation. Using this relation, we obtain $\Omega_{\mathrm{R}}/h_{\mathrm{ac}} = 0.1$ GHz/mT when h_{ac} is applied along the z axis, and $\Omega_{\mathrm{R}}/h_{\mathrm{ac}} = 0.15$ GHz/mT when h_{ac} is applied along the x axis. Transitions between the $|g\rangle$ and $|e\rangle$ states will therefore occur in ~ 1 ns when using electromagnetic radiation of 10 mT.

Superposition states of the type $|\uparrow\rangle - |\downarrow\rangle \equiv |g\rangle$ and $|\uparrow\rangle + |\downarrow\rangle \equiv |e\rangle$ could be also used for our purposes. In this case, these levels are separated by the characteristic tunnel splitting, i.e. $\delta = \Delta$. The latter is usually some orders of magnitude smaller than 2 GHz, as it happens with the clusters studied in this chapter. For instance, the tunnel splitting of GdW_{30} is of the order of $\Delta/\hbar \approx 2$ MHz. The magnitude of Δ can be however increased by applying an external magnetic field. As we have shown in the previous example, a bias magnetic field of 10 mT applied along the y direction would lead to $\Delta = 2$ GHz. However, the use of such bias field entails in turn the localization of the wavefunctions at opposite sides of the barrier. This leads to a decrease of the Rabi frequency down to $\Omega_{\mathrm{R}}/h_{\mathrm{ac}} = 0.005$ GHz/mT. The magnitude of Δ could be also increased while conserving a high probability of transition by applying the bias magnetic field along the x direction. The problem is that much higher magnetic fields are needed for this purpose, which can be inconvenient from an experimental point of view. For instance, $\Delta/\hbar = 2$ GHz and $\Omega_{\mathrm{R}}/h_{\mathrm{ac}} = 0.2$ GHz/mT would result when applying $H_{\mathrm{bias}} = 1.2$ T along the x direction.

The approach presented here could however enable the design of molecules with larger values of Δ. For instance, the hamiltonian corresponding to the LnW_{30} series includes a very high second order transverse term. The latter ”connects” spin states under the condition $\Delta m = \pm 2$. The choice of ions having integer spin like holmium ($J = 8$) or thulium ($J = 6$) would provide higher tunneling probabilities if the ground states are even. This might lead to even higher tunnel splittings that could eventually reach the GHz range in the absence of any external magnetic field.

Let us finally highlight the tremendous enhancement of the relaxation rate of GdW_{10} and GdW_{30} observed at very low temperatures. As we show in Fig. 6.18, the relaxation rate closely follows the theoretical predictions that arise from a phonon-assisted relaxation model down to ~ 100 mK. Below this temperature, spin inversion seems to occur through quantum tunneling between the ground states. The latter interpretation is strongly supported by the excellent agreement that exist between the experimental and theoretical values of Δ. Although phonons play no role in this process, the experimental susceptibility is found to follow Curie's law down to much lower temperatures, i.e. spins are able to ”feel” the temperature of the lattice. How is that possible without the assistance of phonons? In the next chapter we will present some results obtained with a similar molecule (ErW_{10}) that will shed some light on this puzzle.

Chapter 7

Spin-Lattice Relaxation on Molecular Magnets

7.1 Introduction

The fundamental equations of Magnetism, including Curie's law, rely on the ability of magnetic moments to attain *thermal equilibrium* with the solid lattice. In spite of the progress achieved in studying and manipulating individual spins in solids [25–27], the spin-lattice relaxation (SLR) mechanisms are not well understood yet.

Especially interesting is the case of strongly anisotropic spins, e.g. single molecule magnets or rare-earth ions. In those systems, levels corresponding to opposite spins states are separated by the energy barrier created by the anisotropy. As it was suggested by the early theories of SLR, spin relaxation takes place assisted by lattice vibrations. Phonon-emission and absorption processes enable the spin to overcome the energy barrier [240] or to tunnel through excited levels [241–243]. A more intriguing situation arises at sufficiently low temperatures and near to zero field, when thermally activated tunneling processes die out [7, 8, 36]. Under these circumstances, spins can only flip by pure quantum tunneling between the ground states. Concerning SLR, a major difficulty arises then. It stems from the fact that this quantum process modifies the magnetization but conserves the energy of the ensemble of nuclear and electronic spins. Therefore, equilibrium states might well be reached long after the characteristic timescales of quantum tunneling [275, 276] in marked contrast with experimental results [277, 278].

Theoretical descriptions [264, 279, 280] of quantum tunneling in the presence of hyperfine couplings and dipolar spin-spin interactions account well for experiments that measure the time-dependent magnetization [281–284]. As we have seen in the previous chapter, experimental results of the SLR rate of GdW_{10} and GdW_{30} clusters also show an excellent agreement with theoretical predictions for the tunneling rate. Still, in those experiments we have shown that *thermal equilibrium* is reached between the spin system and the crystalline lattice at the same rate. A very efficient mechanism must therefore exist that connects pure tunneling events with phonon-emission or absorption processes. Although some theoretical proposals exist [275], experimental evidences supporting any particular mechanism are still missing.

The central question that we are about to investigate here is the nature of the energy flow between spins and phonons in the absence of thermally activated processes. This question was considered by J. Fernández in ref. [275]. He assumed that detailed balance holds every time a spin flips by tunneling. That is to say, the populations of the different magnetic energy levels are constrained to attain the values given by Boltzmann's law. But, even under these stringent conditions, the predicted SLR rate was found to be much longer than the tunneling rate.

In this chapter we will first present an overview of the classic theories describing the spin-phonon relaxation process. This introduction is also aimed to recognize the different aspects we shall pay attention to. We will then present a complete experimental study of the relaxation rate in ErW_{10} clusters.

This molecule, as GdW_{10}, consists of a single Er ion sandwiched between two polyoxomentalate moieties and behaves as a single-molecule magnet. Thanks to its enormous magnetic anisotropy, ErW_{10} behaves as an effective two-level system, thus it enters a pure quantum regime already above helium temperature. At low temperatures, these clusters relax at sufficiently large relaxation rates enabling us to study their dynamical response down to the vicinity of absolute zero.

The fact that ErW_{10} clusters consist of a single magnetic ion enables us to study also the dependence of the tunneling rate on the strength of dipolar interactions, which results crucial for our purposes. Additionally, we present experimental results showing the effect of external magnetic fields. Since Er has stables isotopes with and without nuclear spin, the influence of hyperfine interactions can be analyzed as well. The direct observation of the tunneling rate under these circumstances provides us the opportunity to a) make a quantitative comparison of the experiments with theories of quantum tunneling and b) conceive a reliable mechanism for the spin lattice relaxation to *thermal equilibrium* assisted by pure quantum tunneling.

7.2 Spin-phonon interaction: an old problem of magnetism

Let us consider a paramagnetic substance immersed in a thermal bath at temperature T_0. This thermal bath can be considered to be infinite, with an infinite heat capacity. All the spins conforming the substance may be regarded as a subsystem having its own temperature (T_s) that does not necessarily need to be the same as the crystal temperature (T_p), given by the thermal motion of the lattice (phonons). Let us suppose that thermal equilibrium exists between the crystalline lattice and the thermal bath, i.e. $T_p = T_0$. Now, the temperature of the spin subsystem will approach that of the lattice at a rate that mainly depends on the energy flow from one to the other. This process, by which spins attain *thermal equilibrium*, receives the name of Spin-Lattice Relaxation (SLR), and the rate is here denoted by τ^{-1}.

In paramagnetic materials, *thermal equilibrium* leads to the well-know $1/T$-dependence found experimentally by P. Curie. It is important to emphasize that the attainment of the equilibrium requires that spin flips fulfill the detailed balance relation, i.e. that they are accompanied by the energy exchange between the spins and the lattice.

7.2.1 The early theories, from P. Curie to R. Orbach

Between 1892 and 1895, Pierre Curie investigated the magnetic response of diverse materials under different conditions of temperature and magnetic field [285]. Measuring, at constant applied magnetic field, the magnetization of oxygen from room temperature up to 450°C he was able to deduce the relation between these quantities (see Fig. 7.1a). In this way, P. Curie enounced the law that was later named after him. The Curie's law establishes that, at weak enough applied magnetic fields (or high enough temperatures), magnetization is inversely proportional to temperature. This simple relation lies at the basis of some technological applications such as magnetic thermometers. Sensing the change in the magnetization of an appropriate paramagnetic material, e.g. rare-earth salts, these thermometers are able to work down to mK temperatures.

Curie's law is a consequence of Boltzmann statistics. In 1905, M. P. Langevin assumed that the spatial distribution of an isotropic magnetic moment at a given temperature, under the action of a magnetic field, could be accounted for by the Boltzmann factor [286, 286]. The equation that relates the magnetization, the temperature and the magnetic field receives therefore the name of Langevin function (see Fig. 7.1b) and has shown to agree very well with experimental data. Moreover, Curie's law can be easily obtained from the Langevin function for the limit of weak magnetic fields or high temperatures ($\mu H \ll k_{\mathrm{B}}T$). But a problem still remained; which is the mechanism that relates the spin system's temperature (T_s) and the temperature of the lattice (T_p)?

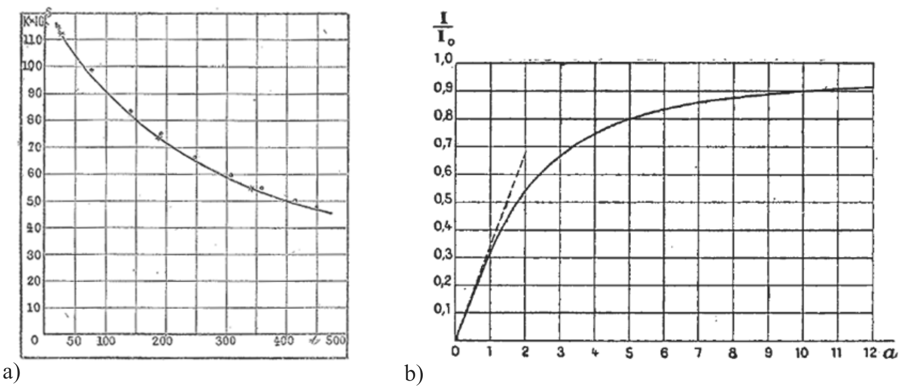

a) b)

Figure 7.1: a) Magnetization of oxygen as a function of temperature fitted to a $1/T$-dependence. Taken from the original paper of P. Curie [285]. b) Langevin function as appeared on the original paper of M. P. Langevin [287].

In 1919, P. Ehrenfest dealt with this question in a short note of the *Leiden Communications Supplement* [288]. He concluded that the thermalization process should take place through energy exchange between the spin ensemble and the lattice vibrations. However, the nature of such interchange would remain unknown until 1936.

The first theoretical explanation was proposed by I. Waller in 1932 [289]. Transitions between the different electronic levels of the spin system separated by an energy difference ΔE, can only be induced by an oscillatory perturbation at the resonant frequency $\omega = \Delta E/\hbar$. I. Waller suggested that the fluctuations of the dipolar interactions under the action of lattice vibrations can lead to the required modulation of the local magnetic field. The magnitude of the spin-lattice relaxation times calculated under these considerations is unfortunately various orders of magnitude larger that the experimental values. A more efficient mechanism was therefore required.

This mechanism was provided by W. Heitler and E. Teller in 1936 [290] and their theory was later elaborated by R. de L. Kronig [291], J. H. Van Vleck [292] and R. Orbach [293]. According to the model, it is not the modulation of the local dipolar magnetic field what induces spin transitions but the modulation of the crystalline electric field (or ligand field). In the same way as a static ligand field splits the electronic energy levels of an ion, a fluctuating ligand field can induce transitions between these levels.

The most comprehensive treatment of the problem is that provided by Van Vleck [292]. It consists of expanding the crystalline electric potential V in powers of the lattice strain ϵ

$$V = V^{(0)} + \epsilon V^{(1)} + \epsilon^2 V^{(2)} + ..., \tag{7.1}$$

Terms going with ϵ will give the dynamic part of the magnetic ion-lattice interaction.

As a first approximation, Van Vleck assumed that $V^{(1)}$, $V^{(2)}$... are of the same order of $V^{(0)}$. This assumption is rather risky since the strain will obviously reduce the local symmetry. On the other hand, it enables to obtain some orders of magnitude of the spin-lattice relaxation time that have proven to agree well with the experimental values.

7.2.2 A brief summary of the theory

The classic theories of spin-lattice relaxation were developed considering three types of relaxation processes towards thermal equilibrium, namely the direct, Orbach and Raman processes. These mechanisms are schematically represented in Fig. 7.2 and summarized in the following.

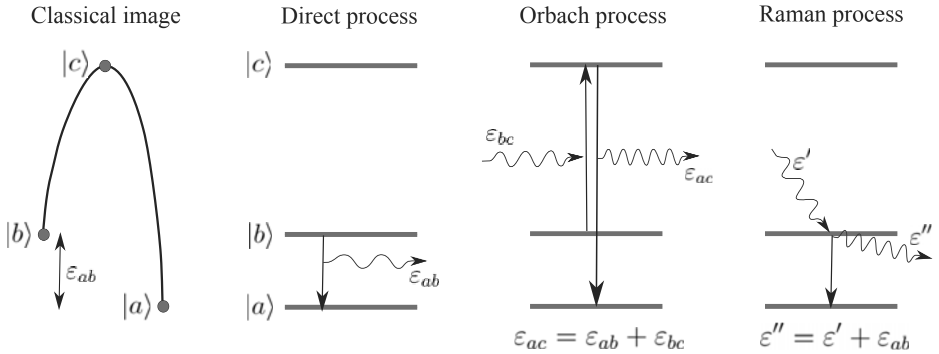

Figure 7.2: Schematic representation of three possible relaxation mechanisms in a three-level system ($S = 1$): Direct, Orbach and Raman process

The direct process implies the spin relaxation from an excited state $|b\rangle$ to the ground state $|a\rangle$ accompanied by the emission of one phonon of energy $\hbar\omega = \varepsilon_{ab}$. Notice that the direct transition from $|b\rangle$ to $|a\rangle$ can be forbidden in the classical image (e.g. in the case of $S > 1/2$) but, in quantum mechanics, there is some probability for such transition to occur. The relaxation rate in those cases will be weighted by the overlap between the wave functions corresponding to the $|b\rangle$ and $|a\rangle$ energy levels. In this way, quantum tunneling between states of different energy can occur assisted by lattice vibrations. The latter process must not be confused with pure, i.e. not assisted by phonons, quantum tunneling between ground quantum states, in which the energy of the spin subsystem is conserved.

The relaxation rate corresponding to the direct process contributes noticeably to τ^{-1} only at low temperatures since it is proportional to the number of phonons of low energy. According to the theory [291–293], it depends linearly on temperature ($\tau_{\mathrm{D}}^{-1} \propto T_0$) in the region where $\varepsilon_{ab} \ll k_{\mathrm{B}}T_0 \ll \varepsilon_{ac}$. The theory also predicts that this contribution increases under the action of an external magnetic field as $\tau_{\mathrm{D}}^{-1} \propto H^4$ for Kramers doublets, and $\tau_{\mathrm{D}}^{-1} \propto H^2$ for non-Kramers doublets.

The relaxation from $|b\rangle$ to $|a\rangle$ can also occur in a two-stage process. In this case, the spin flips to a third intermediated excited state $|c\rangle$ absorbing a phonon of energy $\hbar\omega = \varepsilon_{bc}$. Then, there may be a spin transition to the ground state $|a\rangle$ accompanied with the creation of a phonon of energy $\hbar\omega = \varepsilon_{ac}$. These process is usually referred to as Orbach process [293]. The relaxation rate depends exponentially on temperature, as $\tau_{\mathrm{O}}^{-1} \propto e^{\varepsilon_{bc}/k_{\mathrm{B}}T_0}$.

Finally, the energy can be transferred to the lattice through inelastic scattering with phonons. This process, named Raman process due to its analogy with the Raman effect in optics, involves the simultaneous absorption of a phonon of energy $\hbar\omega = \varepsilon$', and the emission of another of energy $\hbar\omega = \varepsilon$"$= \varepsilon$'$+\varepsilon_{ab}$. The probability of the Raman process may be comparable to that of the Orbach process or even dominate at high temperatures. It depends strongly on temperature as $\tau_{\mathrm{R}}^{-1} \propto T_0^9$ for Kramers and as $\tau_{\mathrm{R}}^{-1} \propto T_0^7$ for non-Kramers doublets. It depends weakly on H as $\tau_{\mathrm{R}}^{-1} = \tau_0^{-1}(b+pCH^2)/(b+CH^2)$, where τ_0^{-1} is the relaxation rate for zero field, b is the specific heat constant ($C_m = b/T^2$), C is the Curie constant $\chi = C/T$, and p is a constant factor that depends on the material.

To summarize, the total relaxation rate of the spin system results from the addition of these three contributions $\tau^{-1} = \tau_{\mathrm{D}}^{-1} + \tau_{\mathrm{O}}^{-1} + \tau_{\mathrm{R}}^{-1}$, where the subscripts refer to the direct, Orbach and Raman processes, respectively. In this way, for a Kramers doublet we have [294]

$$\tau^{-1} \approx R_{\mathrm{D}}\varepsilon_{ab}^5 \coth\left(\frac{\varepsilon_{ab}}{2k_{\mathrm{B}}T_0}\right) + R_{\mathrm{O}}\varepsilon_{bc}^3 \exp\left(-\frac{\varepsilon_{bc}}{k_{\mathrm{B}}T_0}\right) + R_{\mathrm{R}}T_0^9 \tag{7.2}$$

where R_{D}, R_{O} and R_{R} are parameters in an obvious notation.

On the other hand, the predictions regarding the dependence of the relaxation rate with the magnetic field can be summarized as follows. τ^{-1} depends weakly on H at high temperatures, increasing or decreasing with it depending on the material. However, at low temperatures, where only the direct processes are important, a pronounced H^4-dependence should be observed in Kramers doublets.

7.2.3 Extension to multilevel systems: the Pauli master equation

As we have said, the SLR rate can be estimated by expanding the crystalline electric potential V in powers of the lattice strain ϵ [292]. This problem becomes however very difficult when dealing with atoms or molecules having a multilevel energy structure ($S > 1$). In those cases, it will be more useful to compute the SLR rate numerically. For this purpose we have made use of a C code written by E. Burzurí based on the following [295].

The populations (P_k) of the different spin energy-levels of a given spin system evolve in time towards the values corresponding to thermal equilibrium. The long time evolution of these populations can be calculated using the Pauli master equation [242]

$$\frac{dP_k}{dt} = \sum_{k' \neq k} W_{k \leftarrow k'} P_{k'} - P_k \sum_{k' \neq k} W_{k' \leftarrow k} = \sum_{k'} W_{kk'} P_{k'} \tag{7.3}$$

where $W_{k \leftarrow k'}$ are the the transition probabilities from state k' to k induced by phonons. These elements can be ordered in a matrix $\widehat{W}$ and therefore Eq. 7.3 can be rewritten as

$$\frac{d\overrightarrow{P}}{dt} = \widehat{W}\overrightarrow{P} \tag{7.4}$$

The eigenvectors and eigenvalues of $\widehat{W}$ fulfill the relation

$$\widehat{W} P_\lambda = \lambda P_\lambda \tag{7.5}$$

The values of λ give therefore the SLR rates that we are looking for. Let us see now how to calculate the elements of the $\widehat{W}$ matrix.

The non-diagonal elements ($W_{k \leftarrow k'}$) give the probability of a transition between any two energy-levels k and k'. These elements can be computed by using Fermi's golden rule [296]

$$W_{k \leftarrow k'} = q \left| E_k - E_{k'} \right|^3 \left| \left\langle k' \left| \widetilde{V}_{sp-ph} \right| k \right\rangle \right|^2 f(T) \tag{7.6}$$

An appropriate spin - phonon interaction $\widetilde{V}_{sp-ph}$ could be expressed as small fluctuations in the crystal field

$$\left| \left\langle k' \left| \widetilde{V}_{sp-ph} \right| k \right\rangle \right|^2 = \left| \left\langle k' \left| (S_x S_z + S_z S_x) \right| k \right\rangle \right|^2 + \left| \left\langle k' \left| (S_y S_z + S_z S_y) \right| k \right\rangle \right|^2 \tag{7.7}$$

This expression reflects the effect of the lattice strain and rotations on the anisotropy [241, 297, 298].

The action of temperature is introduced via the function $f(T)$ defined as

$$f(T) = \frac{1}{1 - \exp\left(-\frac{E_{k'} - E_k}{k_B T}\right)} \tag{7.8}$$

when the initial state is more energetic than the final state ($E_{k'} < E_k$). On the other hand,

$$f(T) = \frac{\exp\left(-\frac{E_{k'} - E_k}{k_B T}\right)}{1 - \exp\left(-\frac{E_{k'} - E_k}{k_B T}\right)} \tag{7.9}$$

when the final state is more energetic than the initial. In this way we make sure that the internal energy of the phonon bath is conserved. This is known as detailed balance relation.

The parameter q in Eq. 7.6 sets the magnitude of the spin-phonon relaxation. This constant approximately depends on the anisotropy and the elastic properties of the lattice as [298]

$$q = \frac{3(B_2^0)^2}{2\pi \rho_m c_s^5 \hbar^4} \tag{7.10}$$

where B_2^0 is the simplest uniaxial crystal field parameter, ρ_m is the mass density and c_s is the average speed of sound in the medium.

On the other hand, the diagonal terms (W_{kk}) of the $\widehat{W}$ matrix are defined as the reciprocal average lifetime of a level k. These values can be calculated by adding the probabilities to leave every k level

$$W_{kk} = -\sum_{k' \neq k} W_{k' \leftarrow k} \tag{7.11}$$

where $W_{k' \leftarrow k}$ are those values calculated by using Eq. 7.6.

The eigenvalues of the matrix $\widehat{W}$ provide the relaxation rates. The lowest non-zero eigenvalue corresponds to the relaxation rate that is usually measured at not too high frequencies ($f < 1$ MHz). It typically corresponds to the mutual equilibration of the populations of the two lowest lying energy levels. The higher values are associated with fast relaxation modes.

7.2.4 A theory that works... always?

The success of this theory was unquestionable. In the 60's several authors reported measurements performed on rare-earth salts showing an excellent agreement with these theoretical predictions. For instance, R. H. Ruby, H. Benoit

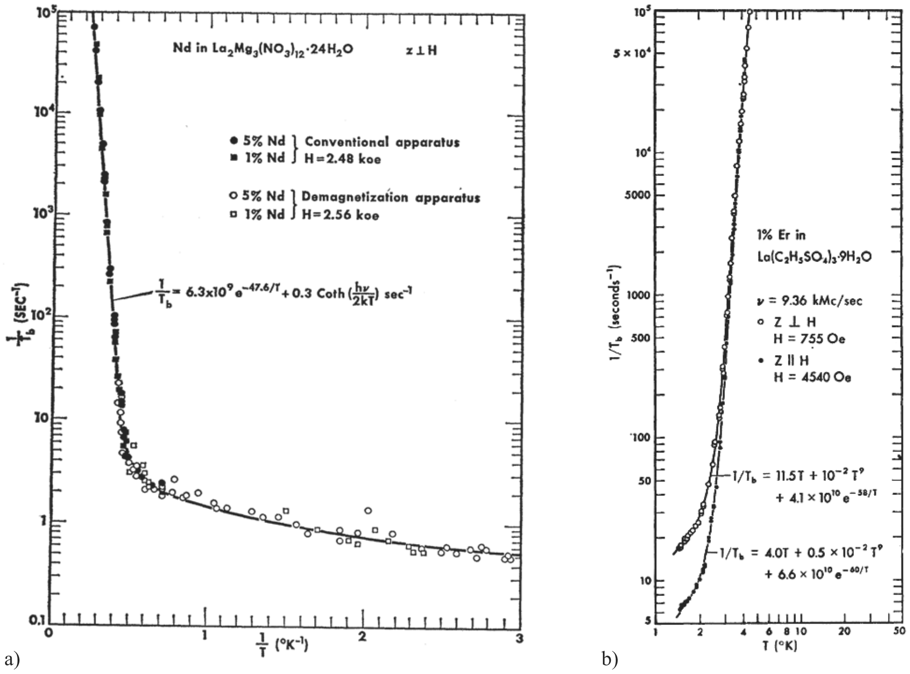

Figure 7.3: a) Relaxation rate for Nd^{3+} in $La_2Mg_3(NO_3)_{12} \cdot 24H_2O$ with H perpendicular to the easy magnetization axis. The overall data are well accounted for by an Orbach process plus a direct process (after [299]) b) Relaxation rate for Er^{3+} in ethyl sulfate showing the influence of the direct, Orbach and Raman processes (after [300]).

and C. D. Jeffries showed that the relaxation rate for Nd^{3+} in $La_2Mg_3(NO_3)_{12} \cdot 24H_2O$ could be accurately fitted by Eq. 7.2 with $R_R = 0$ (Fig. 7.3a). Another example is that given by G. H. Larson and C. D. Jeffries on the relaxation rate for Er^{3+} in ethyl sulfate that shows the influence of the direct, Orbach and Raman processes. As it can be seen in Fig. 7.3b, the experimental data closely follow the relation given by Eq. 7.2.

But, as far as the dependence with the magnetic field is concerned, the theory developed by R. de L. Kronig, J. H. Van Vleck and R. Orbach faced serious problems. Experimental measurements of the relaxation time at $T \sim 1$ K performed by W. J. de Haas and F. K. du Pré on iron ammonium alum showed that τ increases proportionally to the applied magnetic field [41] (see Fig. 7.4a). G. Weber studied the relaxation time on Nd, Gd, Dy and Er chlorides down to $T \sim 1$ K. Although the dependence of τ with T could be reasonably well explained by the theory, it failed completely for the dependence with H at low temperatures [301] (see Fig. 7.4b). Quoting J. H. Van Vleck [292] *"At helium temperatures, where the direct rather than Raman processes are important, the predicted dependence on field strength is entirely wrong. [...] the relaxation time should decrease with field strength, in marked contradiction*

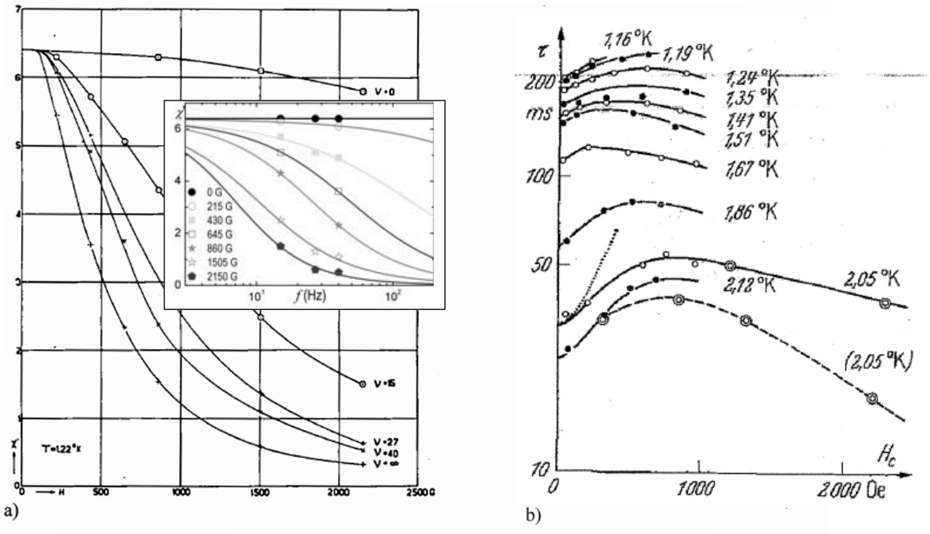

Figure 7.4: a) Differential magnetic susceptibility of iron ammonium alum measured at 1.22 K at different frequencies and as a function of the external magnetic field (After [41]). For the sake of clarity, we have plotted these data in the inset as a function of frequency and fitted to a Cole-Cole law. b) Relaxation time of $ErCl_3 \cdot 6H_2O$ vs. magnetic field (after [301]). Both measurements show that, at least at low temperatures, the SLR rate decreases with the applied magnetic field, in marked contrast with the theoretical predictions.

with the experimental data."

To finish this section let us highlight that, as it can be seen in Fig. 7.4b, the relaxation time of Er chloride measured by G. Weber decreases with H, as predicted by the theory, above 10^3 Oe. On the other hand, all the measurements referred to previously, in which an excellent agreement with the theory was evident (e.g. those in Fig. 7.3), were performed under the action of magnetic fields of the order of 10^3 Oe or even larger. It seemed that, at least at low temperatures, the agreement between the experimental and theoretical dependence of τ on T and H was only reached when applying relatively high magnetic fields.

7.2.5 ErW$_{10}$: an ideal system of study

More recently, a few experiments have revived these old problems. Specific heat studies [277, 278] indicate that Mn_4 and Fe_8 single-molecule magnets attain thermal equilibrium at rates that are many orders of magnitude faster than those predicted by the classic SLR theories. NMR experiments on Mn_{12} clusters [302] show that the nuclear spin and bath temperatures remain the same down to the neighborhood of absolute zero. It has been shown in these experiments that relaxation to thermal equilibrium is dominated by direct tunneling transitions within the ground state doublets. Since this quantum phenomenon conserves the energy of the spin subsystem, no direct link with phonons exists. Therefore, it could be expected that thermal equilibrium would be reached long after the characteristic timescales of quantum tunneling [275], in marked contrast with these experimental results.

In order to elucidate the nature of the SLR mechanism and its relationship with quantum tunneling, direct measurements of the SLR rates as a function of temperature, magnetic field, concentration of spins, etc are clearly desirable. Studying the SLR of molecular nanomagnets at very low temperatures and under weak magnetic fields is, however, a demanding experimental task because tunneling timescales are of the order of days even for clusters made of a few atoms. In order to overcome this difficulty, simpler molecules need to be studied. In this work, we concentrate on the study of $[\mathrm{Er(W_5O_{18})_2}]^{9-}$, hereafter referred to as $\mathrm{ErW_{10}}$. This molecule belongs to the family of polioxometalate-based SMM presented in the previous chapter providing therefore all the advantages exhibited by these systems. We can for instance study the influence of dipolar interactions by preparing magnetically diluted crystals. Since Er has stable isotopes with and without nuclear spin, it is also possible to study the influence of hyperfine couplings on the relaxation processes.

$\mathrm{ErW_{10}}$ clusters exhibit a strong uniaxial anisotropy as we will show. For this reason, these clusters behave as ideal two-level systems at relatively high temperatures providing direct access to the pure quantum limit. Moreover, the relaxation rate of $\mathrm{ErW_{10}}$ fits ideally within the frequency capabilities of our experimental setup, e.g. $\tau \simeq 2$ kHz (at $T = 4.2$ K).

7.3 Magnetic properties of $\mathbf{ErW_{10}}$

In this section we present first some of the main characteristics of erbium in its trivalent cationic state. When this ion is encapsulated between two $[\mathrm{W_5O_{18}}]^{6-}$ moieties, it behaves as a single molecule magnet at low temperatures [16]. The anisotropy parameters that describe the spin hamiltonian of $\mathrm{ErW_{10}}$ have been previously estimated by S. Cardona-Serra *et al* using the magnetic susceptibility of powdered samples measured at high temperatures [265]. In this section we show a series of measurements that enable us to refine these parameters, namely specific heat and single crystal susceptibility.

The magnetic susceptibility of $\mathrm{ErW_{10}}$ single crystals was measured, above 1.8 K, using a commercial MPMS magnetometer that enables rotating the sample in situ as described in chapter 1. Experiments on diluted compounds and the isotopically enriched sample were performed on powdered specimens. Specific heat measurements were performed on powdered specimens using a PPMS platform from Quantum Design (see chapter 1).

Experiments below 1.8 K (presented in section 7.4) were performed using one of our first-generation μSQUID susceptometers. The sample was an $800 \times 400 \times 200\ \mu\mathrm{m}^3$ ErW_{10} single crystal, whose anisotropy axis was oriented approximately 42 degrees with respect to the ac magnetic field. The chemical synthesis of all the samples has been carried out by S. Cardona-Serra [265].

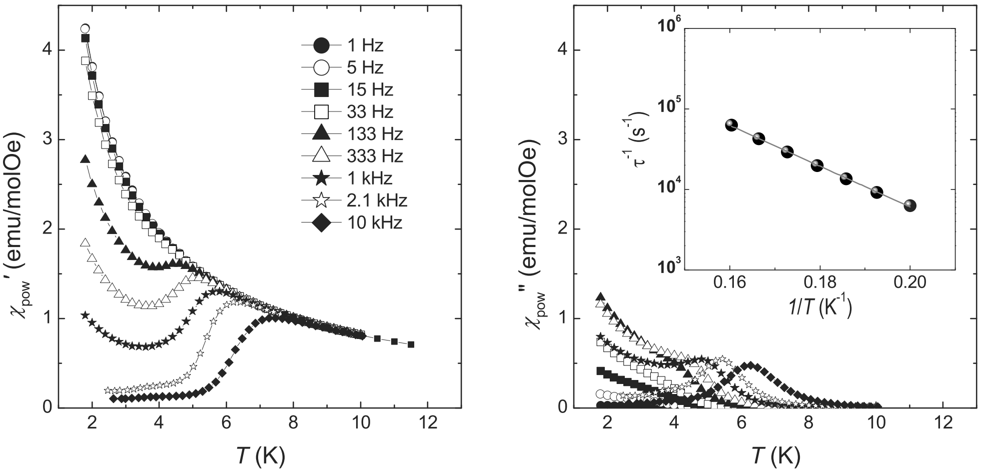

Figure 7.5: Real (left) and imaginary (right) parts of the ac susceptibility of ErW_{10} measured at different frequencies on a powdered sample. The temperature dependent peaks of the imaginary part indicate the magnetic blocking and enable the determination of the SLR rate. The inset shows values of τ^{-1} as a function of $1/T$ fitted to an Arrhenius law giving an activation energy of $U/k_{\mathrm{B}} = 63(1)$ K. Measurements at 2.1 kHz and 10 kHz were performed by S. Cardona-Serra and co-workers in a Quantum Design PPMS platform.

7.3.1 Er^{3+} as a free ion

Erbium is the 12th element in the series of lanthanides. It is commonly used for its optical properties. For instance Er^{3+} ions are used as staining agents due to its characteristic pink color. Crystals doped with these cations are also used as optical amplification media in laser applications. Approximately 77% of natural Er carries no nuclear spin. The remaining 23% corresponds to one stable isotope, $^{167}\mathrm{Er}$, having a nuclear spin $I = 7/2$.

Its electronic configuration is [Xe], $4\mathrm{f}^{12}$, $6\mathrm{s}^2$. In its trivalent state, this turns to [Xe], $4\mathrm{f}^{11}$ that, according to Hund's rules, leads to a total spin mo-

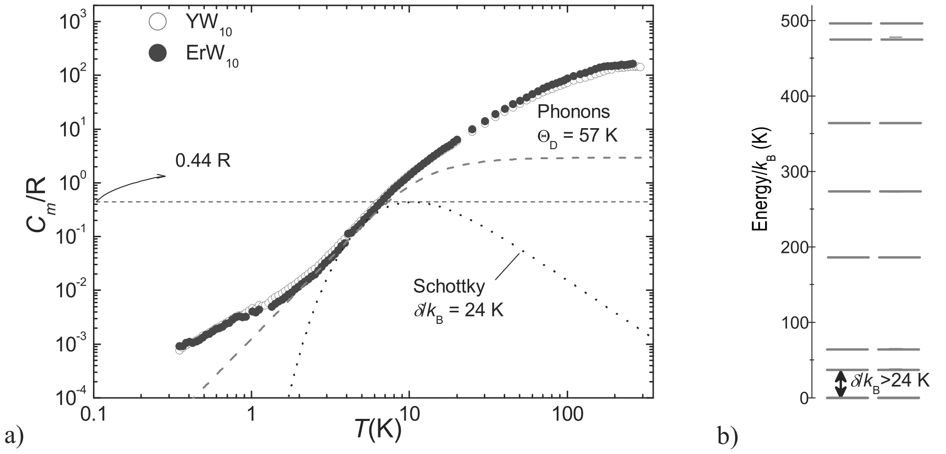

Figure 7.6: a) Specific heat of ErW$_{10}$ and its non-magnetic counterpart YW$_{10}$. The dotted line corresponds to a Schottky anomaly with $\Delta = 17$ cm^{-1}. The fact that no peak of this type is observed below $\sim$ 10 K, indicates that this is the minimum value for the energy difference between the ground and the first excited levels. The energy level structure calculated from the high temperature susceptibility data can be seen in b).

mentum $S = 3/2$ and orbital momentum $L = 6$. Its corresponding electronic orbital configuration can be seen in Fig. 6.6b. The ground state configuration corresponds to $^4\mathrm{I}_{15/2}$ where $J = 15/2$ is the total angular momentum. The g factor of Erbium has been tabulated by Stevens [262] and equals $g = 6/5$.

7.3.2 Single molecule magnet character of ErW$_{10}$

ErW$_{10}$ clusters exhibit the typical features associated with the single molecule magnet behavior. As we can see in Fig. 7.5, the slow relaxation of the magnetic moment becomes apparent below $\sim$ 5 K signaling the "freezing" of the spins by the anisotropy barriers. This blocking is however not complete and not even observable at all for $f < 10$ Hz. This behavior indicates that the thermally activated spin reversal is gradually replaced, below 4 K, by a temperature-independent relaxation mechanism. The nature of the latter mechanism will be investigated in this chapter.

7.3.3 Specific heat

Specific heat data measured under zero magnetic field are shown in Fig. 7.6. They are compared with data measured, under identical conditions, on a non-magnetic derivative containing yttrium (YW$_{10}$). We observe that the two set of data overlap, within the experimental uncertainties, over the whole temperature range. This is a clear indication that the specific heat is fully dominated by contributions that are equally present in the two compounds. The upward trend observed below 2 K of both specific heats is a background produced probaly by the sample holder.

In the temperature range between 2 K and 8 K, the specific heat is approximately proportional to T^3, in agreement with the Debye model for the specific heat of acoustic phonons. The fit gives a Debye temperature $\Theta_{\mathrm{D}} = 57$ K. From the latter we can obtain the speed of sound in ErW_{10} crystals. In a first approximation, the value of c_s can be obtained as

$$c_s = \frac{k_B \Theta_D}{\hbar} \left(\frac{6\pi^2 N}{V} \right)^{-\frac{1}{3}} \tag{7.12}$$

where N is the number of molecules per unit cell with volume V. Inserting in Eq. 7.12 with $N = 2$, $V = 3260.8$ Å^3 and $\Theta_{\mathrm{D}} = 57$ K we obtain $c_{\mathrm{s}} = 2.3 \times 10^5$ cm/s.

Concerning the electronic levels of the Er ions, we can estimate from these data a lower bound for the energy difference between the ground state and the first excited doublet. For two doublets separated an energy δ, the Schottky shows a peak at $T_{max} = 0.42\delta/k_{\mathrm{B}}$, where the maximum value of the specific heat is given by $C_{m,max} = 0.44R$. As no such contribution is observed below 10 K, the gap δ should not be smaller than 17 cm^{-1} ($\delta/k_{\mathrm{B}} = 24.4$ K). An illustrative example of this magnetic contribution is provided by the dotted line in Fig. 7.6

7.3.4 Single crystal experimental susceptibility

In this section we present a study of the magnetic susceptibility of ErW_{10} performed on a single crystal as a function of Ψ, this is, the angle formed by the applied ac magnetic field (h_{ac}) and the direction perpendicular to the crystal plane (see inset in Fig. 7.7a and 7.8). The latter will enable us to determine the longitudinal (χ_z') and transverse ($\chi_\perp$') components of the susceptibility that will provide very useful information about the crystal anisotropy.

Measurements of χ' vs. Ψ performed at $T = 8$ K are shown in Fig. 7.7a. As it can be seen there, susceptibility is maximum for $\Psi_z \approx 26°$. The value of χ' at this point coincides approximately with the value of $3\chi'_{T,\mathrm{pow}}$ obtained at $T = 8$ K, where $\chi'_{T,\mathrm{pow}}$ is the low frequency limit of the real part of the ac susceptibility measured on a powdered specimen (see Fig. 6.1). This fact suggests that the easy magnetization axis of ErW_{10} forms $\Psi_z \approx 26°$ with the direction perpendicular to the crystal plane (see inset of Fig. 7.7a). The susceptibility measured for $\Psi_z \approx 26°$ will therefore correspond to χ_z'. On the

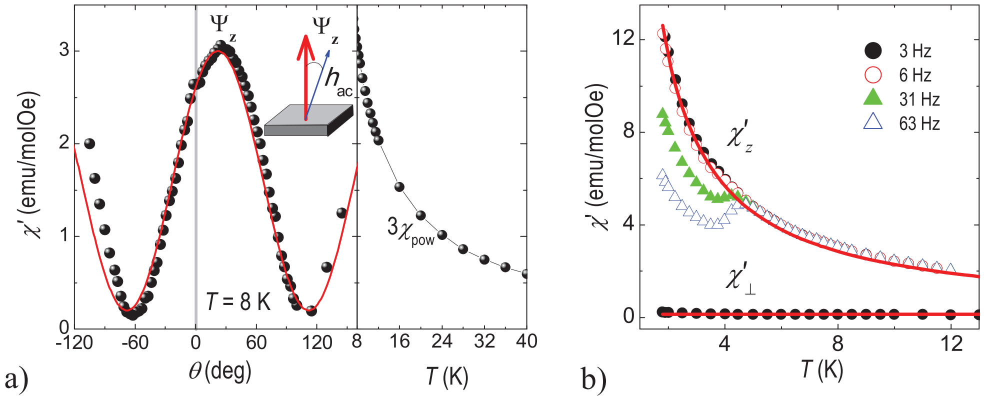

Figure 7.7: a) On the left part we can see the real part of the susceptibility vs. Ψ measured at $T = 8$ K. On the right part, the susceptibility measured on a powdered sample is plotted multiplied by 3. b) Longitudinal and transverse real parts of the susceptibility vs. temperature. These values are obtained measuring at $\Psi_z = 26°$ and $\Psi_\perp = 26° + 90°$, respectively. Lines represent the equilibrium susceptibilities ($\chi_{z,T}$ and $\chi_{\perp,T}$) calculated from the energy-level structure shown in the next section.

other hand, the susceptibility measured under the condition $\Psi_\perp \approx 26° + 90°$ corresponds to $\chi_\perp$'.

Figure 7.7b shows the longitudinal and transverse real part of the susceptibility measured as described above. The very large ratio between χ_z' and $\chi_\perp$' confirms the strong uniaxial character of the magnetic anisotropy [260].

The previous data will also serve to determine the longitudinal and transverse real part of the susceptibility measured with the μSQUID susceptometer. As we saw in chapter 2, the SQUID output voltage is proportional to the susceptibility of the sample measured along the direction defined by the ac excitation magnetic field created by the primary coils. This can be expressed as $\chi'_\Psi = FV_0$, where V_0 is the in-phase component of the output voltage and F is the calibration factor. In order to obtain the absolute value of χ_z' and $\chi_\perp$' we need therefore to determine first the values of F and Ψ_z, i.e. the angle formed by the ac excitation magnetic field ($h_{\rm ac}$) and the easy axis of magnetization of the crystal z.

This problem can be solved as follows. Figure 7.8 shows a measurement of V_0 as a function of frequency performed at $T = 4.2$ K. The high frequency limit ($V_{0,s}$) is related to the transverse susceptibility as

$$\chi'_\perp \sin^2(\Psi_z) = FV_{0,s} \tag{7.13}$$

On the other hand, the low frequency limit ($V_{0,T}$) corresponds to

$$\chi'_z \cos^2(\Psi_z) = FV_{0,T} - FV_{0,s} \tag{7.14}$$

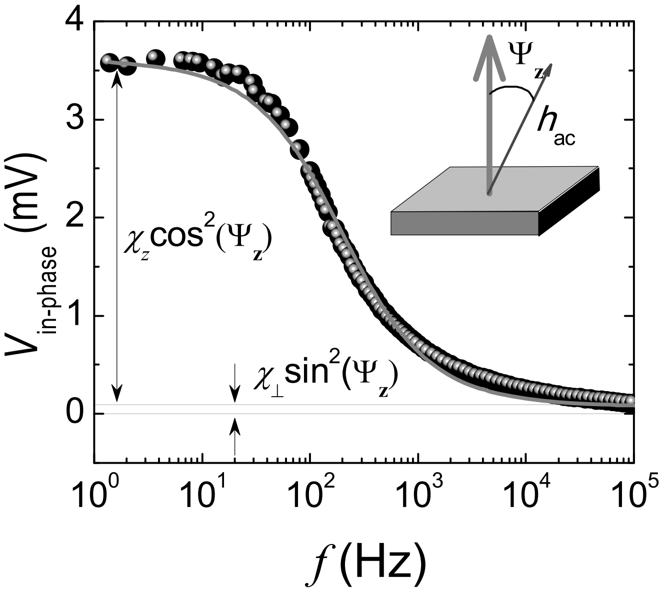

Figure 7.8: In-phase output voltage ($\propto$ χ') as a function of frequency. The low and high frequency limit enable us to determine both Ψ_z, the angle formed by the excitation ac magnetic field and z, and F, the calibration factor.

Inserting in these equations the experimental values of $\chi'_z = 5.96$ emu/molOe and $\chi'_\perp = 0.147$ emu/molOe, obtained at $T = 4.2$ K, and $V_{0,s} = 0.07$ mV and $V_{0,T} = 3.62$ mV, we obtain $\Psi_z \approx 42°$ and $F = 0.93$ emu(mol Oe mV)$^{-1}$.

Let us finally compare the experimental values of Ψ_z with the crystalline structure of the system determined by S. Cardona-Serra and co-workers [265]. ErW$_{10}$ crystallizes in a triclinic body-centered structure with $Z = 2$ molecules per unit cell (see Fig. 7.9). We assume that the easy magnetization axis corresponds to the line connecting both POM molecules that surround the lanthanide. Under these circumstances, the expected value of Ψ_z is approximately $\Psi_z \sim 30°$ in quite good agreement with the experimental values that we found for the single crystal measured with the MPMS magnetometer ($\Psi_z \approx 26°$) and that measured with our μSQUID susceptometer ($\Psi_z \approx 42°$). Small deviations can be accounted for by the possible tilt of the crystalline plane with respect to the holder plane. This fact is not surprising since both single crystals we have used were deposited over an Apiezon-N layer.

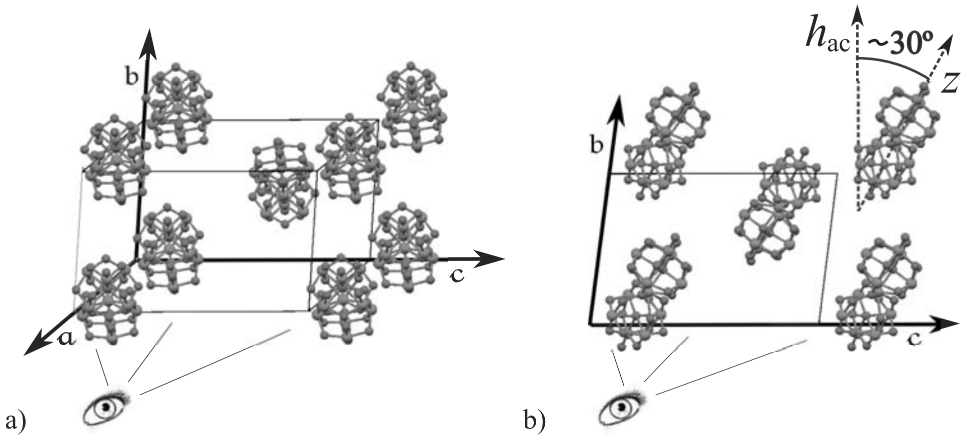

Figure 7.9: Crystalline structure of ErW$_{10}$ as determined by S. Cardona-Serra and co-workers [265]. a) shows a view in perspective while b) shows the backdrop projection.

7.3.5 Magnetic energy level scheme of ErW$_{10}$: a model two level system

The molecular structure of ErW$_{10}$ is equivalent to that of GdW$_{10}$. It consists of an isolated Er^{3+} ion sandwiched between two polyoxometalate moieties with a D_{4d} local symmetry. Under these circumstances, the spin hamiltonian can be written as

$$\mathcal{H} = A_2^0\langle r^2\rangle\theta_2\mathbf{O}_2^0 + A_4^0\langle r^4\rangle\theta_4\mathbf{O}_4^0 + A_6^0\langle r^6\rangle\theta_6\mathbf{O}_6^0 + g\mu_{\rm B}\mathbf{J}\cdot\mathbf{H} \tag{7.15}$$

where the coefficients θ_2, θ_4 and θ_6 are the constants tabulated by Stevens [262]. The anisotropy parameters $B_2^0 = A_2^0\langle r^2\rangle\theta_2$, $B_4^0 = A_4^0\langle r^4\rangle\theta_4$ and $B_6^0 = A_6^0\langle r^6\rangle\theta_6$ have been determined by S. Cardona-Serra and co-workers [265] using the approach described in section 6.5. That is, by the simultaneous fit of the high temperature susceptibility data for the whole family of LnW$_{10}$ compounds. These values can be refined by fitting the theoretical equilibrium susceptibility calculated from the energy-level structure that arises from 7.15 to the single crystal experimental susceptibility data shown in Fig. 7.7b.

The energy ε_m that corresponds to each m level can be obtained by diagonalizing the hamiltonian of Eq. 7.15. The equilibrium susceptibility along any direction defined by $\hat{n}$ is then given by

$$\chi_{\hat{n},T} = \frac{g^2\mu_{\rm B}^2}{k_{\rm B}T}\left[\langle(\hat{n}\cdot\mathbf{J})^2\rangle - \langle\hat{n}\cdot\mathbf{J}\rangle^2\right] + \chi_{\rm vv} \tag{7.16}$$

where $\langle\hat{n}\cdot\mathbf{J}\rangle$ and $\langle(\hat{n}\cdot\mathbf{J})^2\rangle$ are, respectively, the thermally averaged value of the spin and squared spin component along the direction defined by $\hat{n}$ at a

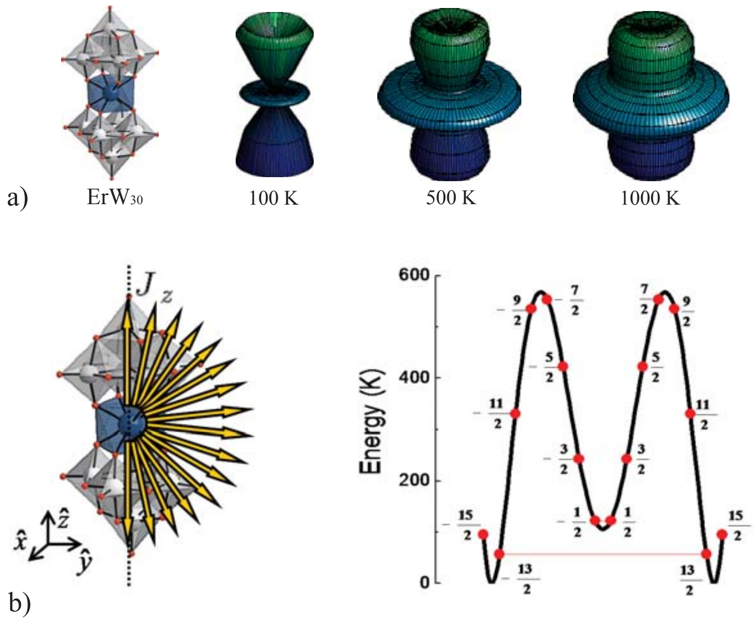

Figure 7.10: a) From left to right we can see an schematic representation of the ErW$_{10}$ molecule, and the population of the distinct spatial J orientations at $T = 100$ K, 500 K and 1000 K. b) Classical potential energy as a function of J_z. The high anisotropy barrier of this molecule accounts for the large anisotropy shown in a).

given temperature. These averages can be computed as follows

$$\langle \hat{n} \cdot \mathbf{J} \rangle = \frac{1}{Z} \sum_{m=-J}^{m=J} \hat{n} \cdot \mathbf{J} e^{\varepsilon_m / k_\mathrm{B} T} \tag{7.17}$$

$$\langle (\hat{n} \cdot \mathbf{J})^2 \rangle = \frac{1}{Z} \sum_{m=-J}^{m=J} (\hat{n} \cdot \mathbf{J})^2 e^{\varepsilon_m / k_\mathrm{B} T} \tag{7.18}$$

Z being the partition function. The last term in Eq. 7.16 is the Van Vleck susceptibility that can be calculated by doing

$$\chi_\mathrm{vv} = \frac{g\mu_\mathrm{B}}{Z} \sum_{m=-J}^{m=J} \frac{\partial \langle m | \hat{n} \cdot \mathbf{J} | m \rangle}{\partial H} e^{\varepsilon_m / k_\mathrm{B} T} \tag{7.19}$$

The longitudinal and transverse susceptibilities can be computed in this way for $\hat{n} \cdot \mathbf{J} = J_z$ and $\hat{n} \cdot \mathbf{J} = J_x$, respectively. Following this method, we have calculated the susceptibility curves that best describe the experimental results. By doing so we obtain $B_2^0/k_\mathrm{B} = -1.35$ K, $B_4^0/k_\mathrm{B} = -1.07 \times 10^{-2}$ K, and $B_6^0/k_\mathrm{B} = 1.07 \times 10^{-4}$ K. The theoretical calculations of $\chi_{z,T}$ and $\chi_{\perp,T}$ obtained using these parameters are shown in Fig. 7.7b.

The classical potential energy ensuing from Eq. 7.15 for these parameters is very similar to that depicted in Fig. 6.3c in the previous chapter. However, it might be more illustrative to plot the probability of the spin for pointing along a given direction of the space as we did with GdW$_{10}$ and GdW$_{30}$. These plots, obtained at $T = 100$, 500, and 1000 K, can be seen in Fig. 7.10a. The fact that the spin is still constrained along certain spatial directions at very high temperatures attests the strong uniaxial character of the magnetic anisotropy.

The classical energy levels corresponding to the different projections of the spin along the easy magnetization axis (J_z) are shown in Fig. 7.10b. Electronic states of the type $\pm J_z$ are degenerate at zero field. Below 4 K, the population of excited states above the ground state $J_z = \pm 13/2$ doublet becomes smaller than 1 in 10^4. This cluster represents therefore a model two-level system.

7.4 Mechanisms for the attainment of *thermal equilibrium* in ErW$_{10}$

In this section, we describe a detailed experimental study of the spin-lattice relaxation in ErW$_{10}$. For this purpose, we shall first show that *thermal equilibrium* is attained down to very low temperatures. We will then study the spin-lattice relaxation processes for varying temperatures. At "high" temperatures ($T \gtrsim 4$ K), the SLR rate closely follows the classic theoretical predictions. By contrast, in the low temperature region ($T \lesssim 4$ K) an enormous disagreement between theory and experiment is found.

7.4.1 Spin-lattice relaxation to *thermal equilibrium*

As it can be seen in Fig. 7.11, the low-frequency limit of χ' (measured at $f = 3$ Hz) follows Curie-Weiss' law above 100 mK, $\chi' = C(T - \theta)$ with $\theta = -88$ mK. χ' attains a maximum at 81 mK, which marks the onset of long-range magnetic order driven by dipolar interactions. The fulfilment of Curie-Weiss' law shows undoubtedly that, at least above 100 mK, the linear-response experiments measure SLR to *thermal equilibrium*, and not the spin-spin relaxation within the "spin-bath".

In section 7.3.4 we have obtained the experimental values of the susceptibility measured along the direction perpendicular to the crystal plane, i.e. along the direction defined by the ac excitation magnetic field created by the primary coils of the μSQUID susceptometer. These data can be used to distinguish between the possible types of magnetic order attained at $T_{\mathrm{N}} = 81$

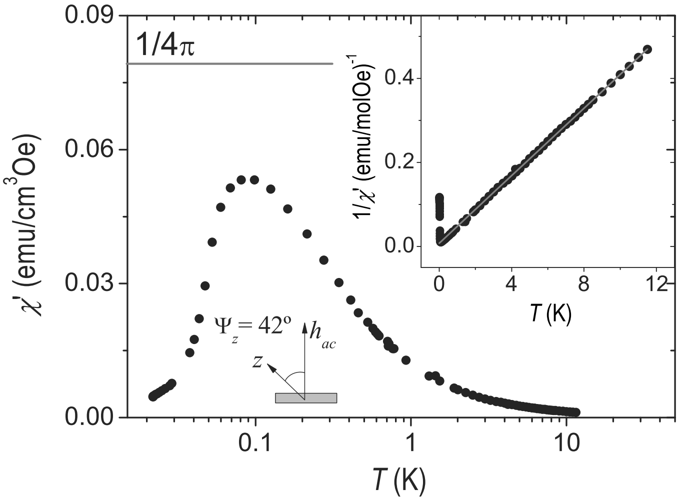

Figure 7.11: Low frequency limit (f = 3 Hz) of the real ac susceptibility measured with the ac excitation magnetic field forming an angle of $\Psi = 42°$. At $T \approx 0.08$ K, χ_z' drops due to the onset of long-range magnetic order. The linear dependence of $1/\chi$' on T (inset) illustrates the excellent agreement with Curie-Weiss' law.

mK. If the order is ferromagnetic, the maximum value of the volume susceptibility approaches the ferromagnetic limit $1/N$, where N is the demagnetizing factor. On the other hand, the experimental maximum value of χ' remain well below $1/N$ if the order is antiferromagnetic. The demagnetizing factor of a flat single crystal in c.g.s. units equals $N = 4\pi$. Under these circumstances, the ferromagnetic limit is given by $1/N \gtrsim 0.079$ emu/cm^{3}Oe.

At $T_{\mathrm{N}} = 81$ mK, we find χ' ≈ 0.053 emu/cm^{3}Oe. This experimental value is approximately 30% lower than the ferromagnetic limit suggesting that the order is antiferromagnetic, in agreement with the negative sign of θ.

7.4.2 Spin-lattice relaxation mechanisms in ErW$_{10}$

To determine, at each temperature, the spin-lattice relaxation rate τ^{-1} we fit the frequency-dependent in-phase χ' and out-of-phase χ'' susceptibility data using a Cole-Cole function [106]. Figure 7.12 shows some examples. The values of τ^{-1} that we obtain from these fits are plotted in Fig. 7.14 as a function of temperature.

7.4.2.1 Relaxation above ~ 4 K

We first discuss the SLR rates measured for temperatures above ~ 4 K. In this region, relaxation appears to be thermally activated, as τ^{-1} strongly depends

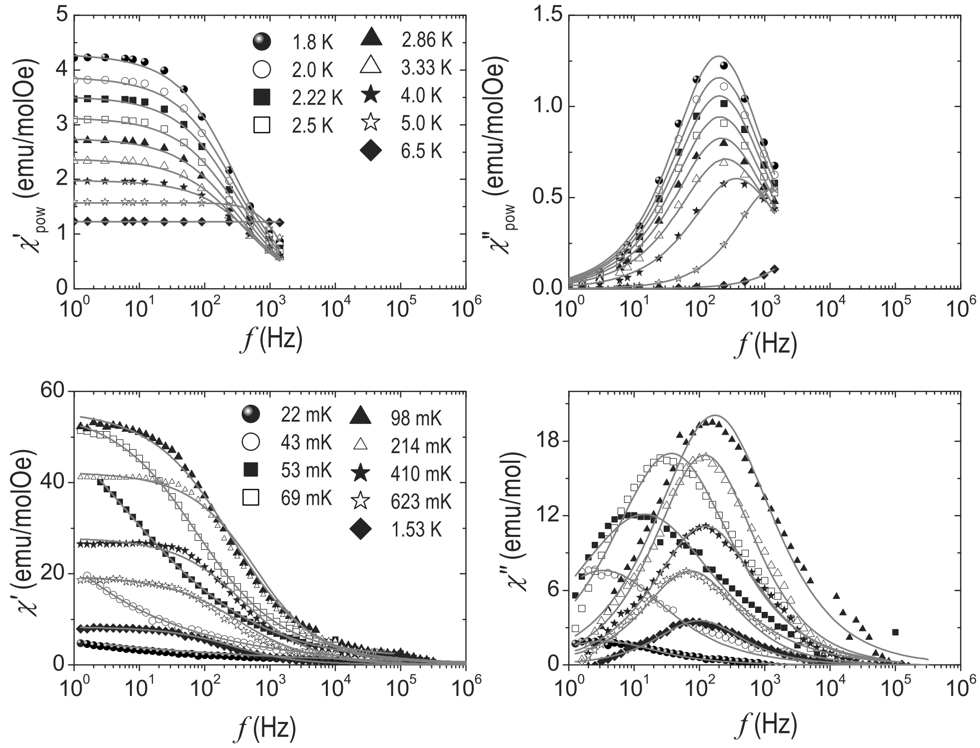

Figure 7.12: Real (left panels) and imaginary (right panels) parts of the ac susceptibility. Values above $T = 1.8$ K (upper panels) have been obtained from the ac susceptibility measurements performed on a powdered sample using the MPMS magnetometer. Those below $T = 1.8$ K (lower panels) correspond to measurements performed on a single crystal using the μSQUID susceptometer. Under these circumstances, the ac excitation magnetic field forms an angle of $\Psi_z = 42°$ with the crystal plane. The experimental data have been fitted to Cole-Cole's laws (lines) that enable an accurate determination of τ^{-1} and β.

on T. From the Arrhenius fit of τ^{-1} vs. $1/T$, we obtain an activation energy of $U/k_B = 63(1)$ K (see the inset in Fig. 7.5b). The theoretical SLR rate can be computed numerically as we describe in section 7.2.3 using the spin-hamiltonian parameters of ErW_{10}.

The result of this computation does not account however for the large relaxation rates measured experimentally. As it may be remembered by the reader, the energy barrier created by anisotropy is considerably high in this molecule (the energy of the most excited levels is ≈ 496 K). This means that spin relaxation occurs through low-lying energy levels, assisted by quantum tunneling. Direct phonon induced transitions are forbidden since Erbium is a Kramers ion. As we saw in section 6.3.1, transversal magnetic fields of dipolar origin can "break" Kramers degeneracy enhancing the tunnel rate. Still, dipo-

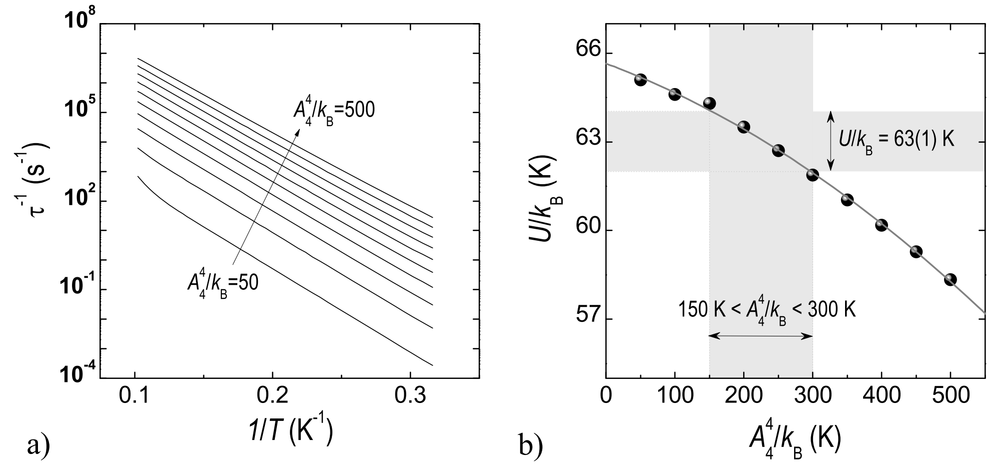

Figure 7.13: a) Theoretical values of τ^{-1} obtained using different values for the A_4^4 parameter. These values correspond to $A_4^4/k_\mathrm{B} = i50$, where $i = 1, 2, ..., 10$ increasing as indicated by the arrow. b) Theoretical values for the activation energy corresponding to the different values of A_4^4.

lar fields in ErW$_{10}$ are not strong enough to lead to the SLR rates observed experimentally. For these reasons, we need to consider now the inclusion of a non-diagonal term in the spin-hamiltonian, e.g. the B_4^4.

Figure 7.13a shows the theoretical SLR rates obtained by solving a quantum master equation for the time-dependent populations of magnetic energy levels above $\sim$ 4 K. In these calculations, we have used the value of the speed of sound obtained experimentally in section 7.3.3. In this way, the q parameter defined in section 7.2.3 can be calculated inserting in Eq. 7.10 the values of $D/k_\mathrm{B} = 3B_2^0/k_\mathrm{B} = -1.35$ K, $\rho = 3.411$ g/cm^3 and $c_\mathrm{s} = 2.3 \times 10^5$ cm/s

Fitting these curves to an Arrhenius law we obtain the values of the theoretical activation energy as a function of the A_4^4 parameter ($B_4^4 = A_4^4\langle r^4\rangle\theta_4$, see section 6.3). From these data (see Fig. 7.13b) we conclude that $A_4^4/k_\mathrm{B} = 225(75)$ K is required to account for the experimental value of U/k_B.

To refine these estimations we have used the SLR rates measured on another molecule belonging to the family LnW$_{10}$, namely HoW$_{10}$. The diagonal terms of the spin hamiltonian of HoW$_{10}$ were determined by S. Cardona-Serra using the method described in section 6.5, i.e. from the high-T susceptibility data. Now, we assume that the non-diagonal coefficients, e.g. A_4^4, can be also expressed as a linear function of the number of f electrons [266]. By a simultaneous fit of the experimental values of τ^{-1} measured on ErW$_{10}$ and HoW$_{10}$ (see Fig. 2.26 in chapter 2) we obtain $A_4^4/k_\mathrm{B} = 250$ K that gives $B_4^4/k_\mathrm{B} = -1.11 \times 10^{-2}$ K.

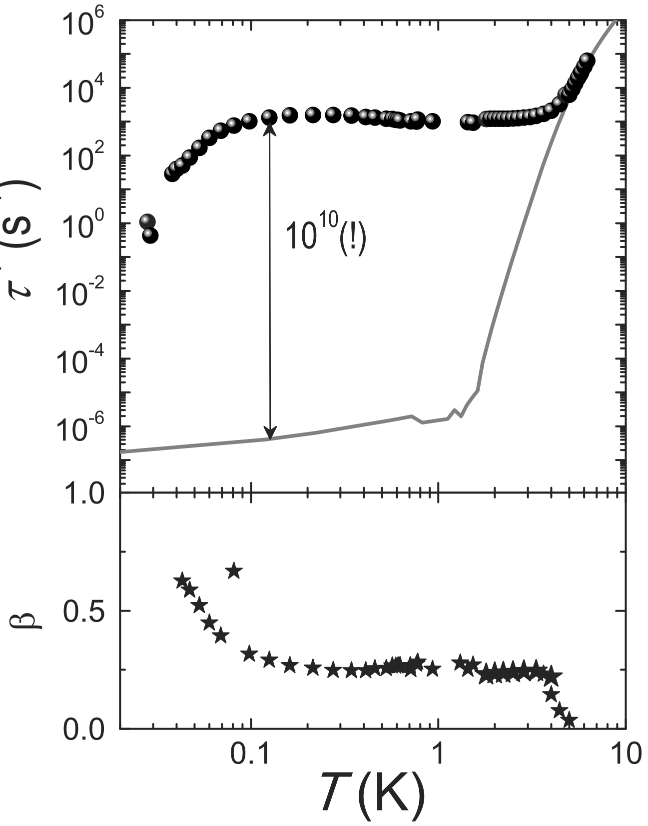

Figure 7.14: The top panel shows the SLR rate measured as a function of temperature (scatter) and the theoretical prediction that arises from the classical phonon-induced relaxation theories (line). The bottom panel shows the values of the β parameter. β increases abruptly at $T \sim 4$ K coinciding with the deviation of τ^{-1} from the theoretical predictions. This fact points undoubtedly to the entrance in a region dominated by pure quantum tunneling between the ground states.

The addition of this term does not change noticeably the energy-level structure shown in Fig. 7.10. From these considerations, we can conclude that the simplest spin-hamiltonian that accounts well for the susceptibility response at high temperatures, the specific heat, the equilibrium susceptibility and the relaxation rate of ErW_{10} above ~ 4 K can be written as follows

$$\mathcal{H}_{ErW_{10}} = B_2^0\mathbf{O}_2^0 + B_4^0\mathbf{O}_4^0 + B_4^4\mathbf{O}_4^4 + B_6^0\mathbf{O}_6^0 + g\mu_{\mathrm{B}}\mathbf{J}\cdot\mathbf{H} \tag{7.20}$$

Considering the energy level structure that arises from this hamiltonian, the experimental SLR rate above ~ 4 K can be very accurately accounted for by the classic theories of spin-phonon interaction presented in section 7.2.2.

7.4.2.2 Relaxation below ~ 4 K

Below ~ 4 K, the observed relaxation is, by contrast, no longer compatible with this theory. To begin with, the experimental values of τ^{-1} remain approximately constant as the temperature decreases. The latter is in marked contrast with the behavior expected form a classical phonon-induced relaxation process at very low temperatures, dominated by the direct process ($\tau_{\mathrm{D}}^{-1} \propto T_0$). Furthermore, the relaxation rate follows a weak increasing tendency as the Néel temperature is approached. On the other hand, a strong quantitative disagreement is found as well: the rate measured on ErW_{10} becomes ten(!) orders of magnitude faster than the rate of direct phonon-induced transitions.

This behavior suggests a transition to a pure quantum regime below ~ 4 K. This interpretation is strongly supported by the abrupt dependence of the β parameter on temperature (see bottom panel on Fig. 7.14). As we have shown in section 3.7.3, this parameter is associated to the width of the distribution of relaxation rates. Thermally activated (Orbach) relaxation processes are usually characterized by well-defined value of τ ($\beta \to 0$). On the other hand, the resonant character of pure tunneling leads to a wide variety of relaxation rates as a consequence of the distribution of dipolar or hyperfine fields ($\beta \to 1$). It seems therefore reasonable to ascribe the abrupt increase of β below ~ 4 K to the beginning of a pure quantum regime. Notice that this behavior was also observed in GdW_{10} and GdW_{30} (see section 6.5.3).

Another intriguing phenomenon is the abrupt drop of τ^{-1} near $T_{\mathrm{N}} = 81$ mK, that is, the temperature at which the system undergoes a transition to an antiferromagnetically ordered phase. The unconventional character of the SLR mechanism will be further analyzed in the following sections.

7.5 SLR in the quantum regime of ErW_{10}: an experimental study

From the arguments presented in section 7.4.1 we can conclude that spins are able to attain thermal equilibrium at least down to $T_{\mathrm{N}} = 81$ mK. This means that spins are able to "feel" the temperature of the lattice. On the other hand, as it has been discussed on the previous section, thermally activated processes die out below ~ 4 K and pure quantum tunneling between the ground state doublet seems to dominate. A conflict appears now since the latter phenomenon does not require any energy interchange with the lattice vibrations and, therefore, should not reflect the temperature of the phonon bath. We shall therefore demonstrate first that the observed spin-lattice relaxation processes below ~ 4 K occur via pure quantum tunneling processes indeed. For this purpose we analyze the tunneling rate dependence on ambient parameters, such as temperature and magnetic field, as well as on the concentration of spins and isotopic concentration.

Although it has been already recalled in the previous chapter, it might be useful to rewrite here the expression obtained by N. V. Prokof'ev and P. C. E. Stamp [264]. This equation describes the average spin tunneling rate τ_{T}^{-1} in the presence of hyperfine couplings and dipolar spin-spin interactions.

$$\tau_{\mathrm{T}}^{-1} \approx \frac{\Delta^2}{\hbar} P(\xi_{\mathrm{dip}} = 0) \tag{7.21}$$

where Δ is the tunnel splitting, i.e. the energy difference separating two levels that are degenerate in classical physics, and $P(\xi_{\mathrm{dip}})$ is the distribution of energy bias of dipolar origin.

For the sake of clarity, in this section we will use the following notation. τ_{T}^{-1} refers to the tunneling rate expected from the Prokof'ev-Stamp model. On the other hand, we reserve the label τ^{-1} for the SLR rate measured experimentally.

7.5.1 Quantitative comparison of τ^{-1} and τ_T^{-1}

Above the Néel temperature, spin-spin interactions give rise to distributions $P(H_{\mathrm{dip,z}})$ and $P(H_{\mathrm{dip},\perp})$ of, respectively, longitudinal and transverse dipolar fields. The width $\sigma_{H_{\mathrm{dip}}}$ can be estimated roughly from the condition $2g\mu_{\mathrm{B}}J\sigma_{H_{\mathrm{dip}}} \sim k_{\mathrm{B}}T_{\mathrm{N}}$, which gives $\sigma_{H_{\mathrm{dip}}} \simeq 70$ Oe. Dipolar fields split the ground state doublet by the amount $\Delta E = (\Delta^2 + \xi_{\mathrm{dip}}^2)^{1/2}$, where Δ is the quantum tunnel splitting given by $\Delta \equiv g_\perp \mu_{\mathrm{B}} H_{\mathrm{dip},\perp}$ and ξ_{dip} is the dipolar energy bias given by $\xi_{\mathrm{dip}} \equiv g_z \mu_{\mathrm{B}} H_{\mathrm{dip,z}}$. In these expressions, g_z and $g_\perp$ are the longitudinal and transverse effective gyromagnetic ratios, respectively.

At zero field, only the small fraction of clusters fulfilling the "tunnel window" condition $-\Delta/2 \leq \xi_{\mathrm{dip}} \leq \Delta/2$ can reverse its magnetic moment at any given time. The net tunneling rate τ_{T}^{-1} is then approximately described by the Prokof'ev and Stamp model [264] and can be calculated using the relation given by Eq. 7.21. For this purpose, we need to calculate the theoretical value of Δ. This can be done by diagonalizing the hamiltionian of Eq. 7.20 for $H_{\mathrm{dip},\perp} = \sigma_{H_{\mathrm{dip}}}$. The result of this calculation gives $\Delta/k_{\mathrm{B}} \approx 1.6 \times 10^{-5}$ K (see Fig. 7.20a). On the other hand, $P(\xi_{\mathrm{dip}} = 0) = \sqrt{2\pi}\sigma_{\xi_{\mathrm{dip}}}$ if we assume a gaussian distribution of the dipolar energy bias. The value of $\sigma_{\xi_{\mathrm{dip}}}$ can be estimated from the Neél temperature $\sigma_{\xi_{\mathrm{dip}}}/k_{\mathrm{B}} \approx 0.08$ K. Inserting these values in Eq. 7.21 we obtain $\tau_{\mathrm{T}}^{-1} \sim 2 \times 10^2$ s^{-1}.

This value is independent of T and, more importantly, ten orders of magnitude larger than the rate of direct phonon-induced transitions, in fair agree-

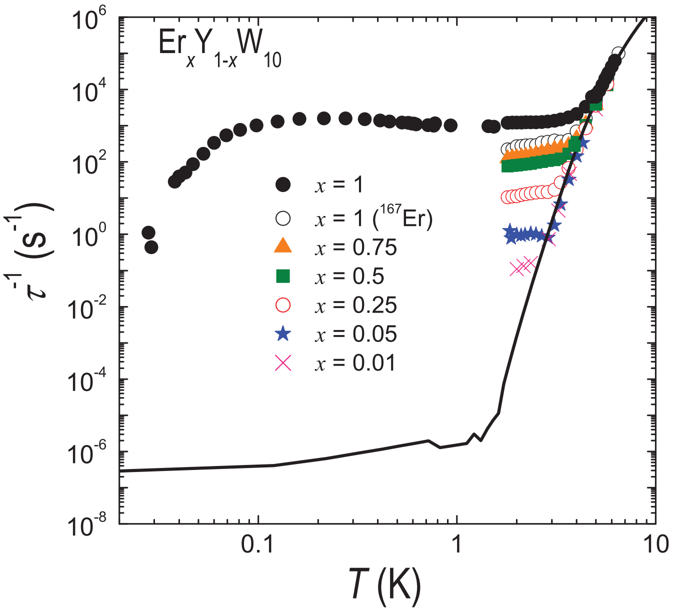

Figure 7.15: SLR rate of the undiluted sample compared with that of $^{167}\mathrm{ErW}_{10}$ and diluted samples. The line corresponds to the SLR rate calculated from the classical phonon-induced relaxation theories using the hamiltonian of Eq. 7.20. As it can be seen, the classical theoretical predictions are progressively recovered as the concentration decreases.

ment with the experimental value $\tau^{-1} \simeq 1.2 \times 10^3$ s^{-1}. The observed SLR relaxation agrees therefore well with predictions for the direct tunneling rate τ_{T}^{-1} thereby suggesting that a direct link exists between these two phenomena.

7.5.2 The effect of dipolar interactions: $\mathbf{Er}_x\mathbf{Y}_{x-1}\mathbf{W}_{10}$

We have investigated the effect of dipolar interactions on the relaxation rate below $\sim$ 4 K. For this purpose, magnetically diluted samples containing yttrium have been prepared leading to the formula $\mathrm{Er}_x\mathrm{Y}_{x-1}\mathrm{W}_{10}$. The ratio between magnetic (Er) and non-magnetic (Y) molecules has been varied from $x = 0.75$, to 0.01. The relaxation rate of these samples has been determined experimentally by fitting the real and imaginary components of the susceptibility to a Cole-Cole law, in the same way as we did with the pure crystal ($x = 1$). The values of τ that we obtain are shown in Fig. 7.15 for all the concentrations studied. As we can see there, the theoretical values for the SLR rate expected from the classical theory of phonon-induced transitions are slowly approached as the magnetic concentration decreases.

Diluting the spins reduces $\sigma_{H_{\mathrm{dip}}}$, which affects both Δ (through $H_{\mathrm{dip},\perp}$)

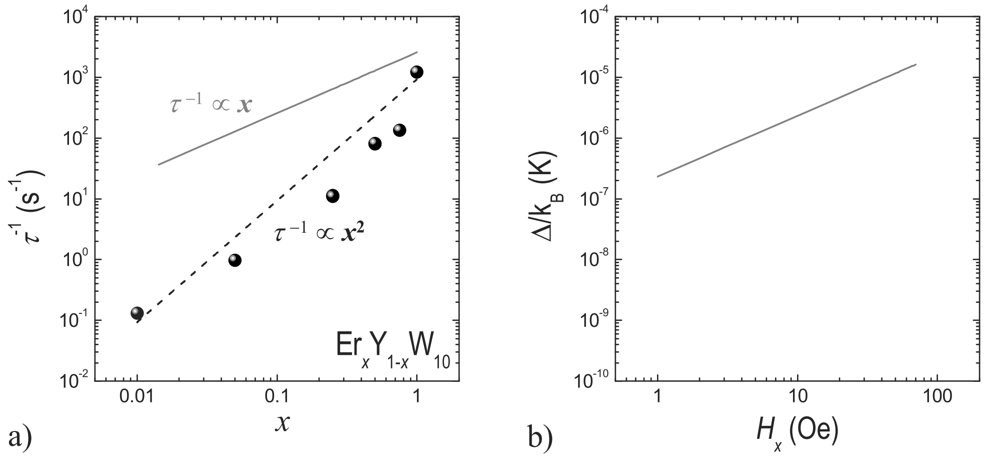

Figure 7.16: a) Experimental SLR rate as a function of the concentration of Er (scatter). The dotted line is a quadratic fit to the experimental data whereas the red line describes the dependence $\tau_T^{-1} \propto x$ oreducted bt the Prokof'ev-Stamp theory of tunneling. b) Dependence of the quantum tunnel splitting Δ on the transverse magnetic field. As it can be seen, Δ depends linearly on the transversal magnetic field. Values of Δ have been computed considering the full spin hamiltonian of the molecule (see Eq. 7.20).

and $\sigma_{\xi_{\text{dip}}}$ (through $H_{\text{dip,z}}$). According to the Prokof'ev and Stamp model (see Eq. 7.21), τ_T^{-1} depends linearly on $\sigma^2_{H_{\text{dip}}}$ (since $\Delta \propto H_{\text{dip},\perp}$, see Fig. 7.16b) and inversely on $\sigma_{\xi_{\text{dip}}}$. Taking, as a first approximation, $\sigma_{H_{\text{dip}}} \propto x$ leads to an *increase* of $\tau_T^{-1} \propto x$, in qualitative agreement with the concentration dependence of τ^{-1} shown in Fig. 7.15. The experimental values of τ^{-1} at $T = 2$ K and zero applied field are shown in Fig. 7.16a as a function of the concentration. As it can be seen there, we find however a dependence of the type $\tau^{-1} \propto x^2$. This deviation will be reexamined in section 7.7.

These arguments can also explain qualitatively the slowing down observed near T_N. In the antiferromagnetic phase, the distribution $P(\xi_{\text{dip}})$ becomes narrower. In fact, as T_N is approached, this distribution evolves form a gaussian centered at $\xi_{\text{dip}} = 0$ towards a delta function centered at $\xi_{\text{dip}} \sim k_B T_N$ [272]. A curious competition arises then: the onset of magnetic order, turns tunneling, as well as relaxation towards the ordered state, progressively slower.

From this discussion we can conclude that the dependence of the SLR rate on the spin concentration can also be reasonably well accounted for by the predictions of the direct tunneling rate. The reduction of dipolar interactions leads, as we have seen, to an effective blocking of the tunneling probability because Er is a Kramers ion. In this way, the classical theory of R. de L. Kronig, J. H. Van Vleck and R. Orbach is progressively recovered as the concentration

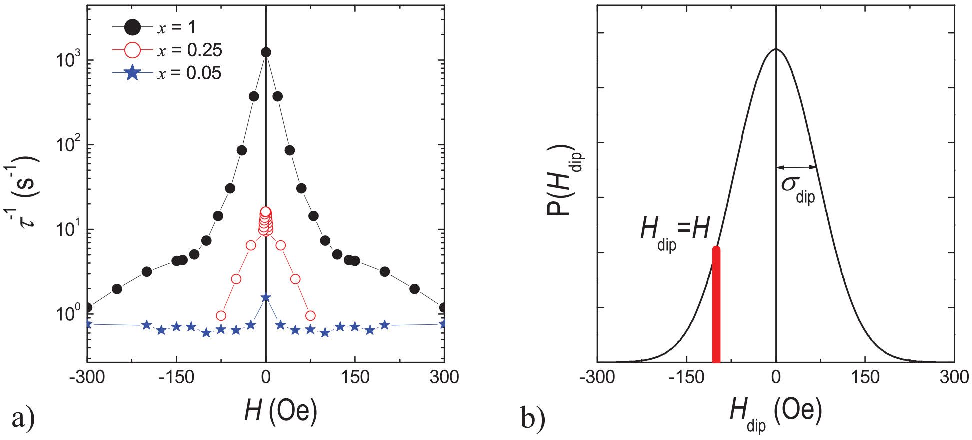

Figure 7.17: a) Dependence on the applied magnetic field of the SLR rate of three samples with different Er concentrations. The experimental results show the strong resonant character of the relaxation mechanisms pointing to pure quantum tunneling. b) Distribution of dipolar magnetic fields in a pure crystal of ErW$_{10}$. The distribution width $\sigma_{\mathrm{dip}} \simeq 70$ Oe has been obtained from the condition $2g\mu_{\mathrm{B}}J\sigma_{\mathrm{dip}} \sim k_{\mathrm{B}}T_{\mathrm{N}}$. The red line indicates the displacement of the "tunneling window" under the action of a bias field H_z.

decreases, i.e. as pure tunneling processes become blocked.

7.5.3 The effect of an external magnetic field

Some additional information on the nature of the SLR process can be extracted by studying the dependence of τ^{-1} on external magnetic fields. Indeed, phonon-induced tunneling is a non-resonant process, i.e. its probability is not maximum at zero field, whereas the opposite applies to the pure tunneling process between the two ground states. In the latter case, the external bias H_z blocks tunneling by energetically detuning spin-up and spin-down states, giving quantum tunneling a strongly resonant character.

The dependence of τ^{-1} on H has been studied for the undiluted and diluted samples described above. Three examples are shown in Fig. 7.17a for $x = 1$, $x = 0.25$ and $x = 0.05$. These data show that τ^{-1} is strongly reduced (notice the logarithmic scale) by the application of relatively weak magnetic fields.

This phenomenon can be also understood on basis of the theory of quantum tunneling. The tunneling rate is maximum at zero field, when the spin satisfies the "tunnel window" condition $-\Delta/2 \leq \xi_{\mathrm{dip}} \leq \Delta/2$. Spins are driven out of this window by the effect of an external field H_z that increases the bias $\xi_{\mathrm{dip}} = \pm\xi_{\mathrm{Zeeman}}$. This effect is schematically illustrated in Fig. 7.17b. Under these circumstances, the tunneling rate should decrease as the modulus of H_z

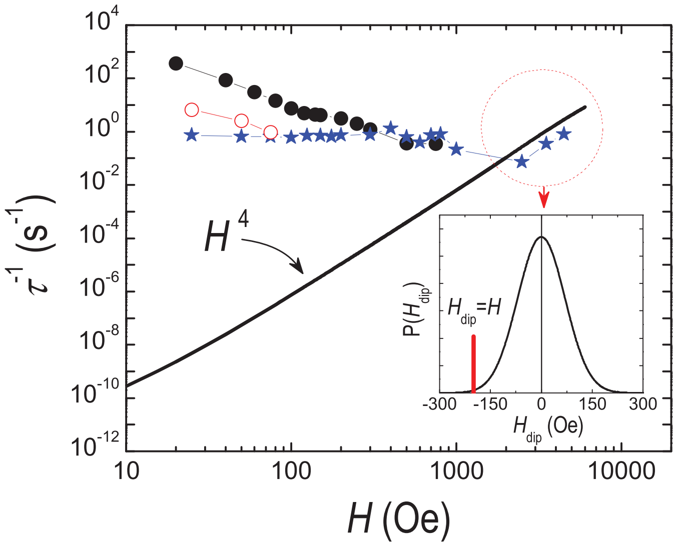

Figure 7.18: Dependence of τ^{-1} (scatter) on the external magnetic field up to 5×10^3 Oe. The dependence predicted by the classical theories (line) is approached as the strength of the external magnetic field is increased. This is accounted for by the progressive blocking of the tunneling rate under the action of a bias field. This fact is illustrated in the inset. At strong enough bias fields, the ”tunneling window” is completely driven out of the accessible energy spectrum provided by dipolar interactions.

increases reflecting the shape of the distribution of dipolar fields as predicted by Eq. 7.21 [281]. This is exactly what we observe experimentally, although the distribution function describing the dipolar fields in the crystal resembles more a Lorentzian function than a gaussian (see Fig. 7.17a). We can therefore conclude that the experimental dependence of τ^{-1} on H agrees also very well with the predictions for the direct tunneling rate.

We have also investigated the effect of stronger magnetic fields ($H \sim 10^3$ Oe) on τ^{-1}. As it can be seen in Fig. 7.18, τ^{-1} slowly approaches the H^4-dependence predicted by the theory of R. de L. Kronig, J. H. Van Vleck and R. Orbach as the field is increased. The same effect that we have shown in the previous section occurs. That is, the classical theory is progressively recovered as pure tunneling processes between the ground state doublet become blocked.

7.5.4 The effect of hyperfine interactions: SLR of ^{167}ErW$_{10}$

The last ingredient we have investigated experimentally is the effect of hyperfine interactions. We have repeated the same experiments on a sample, ^{167}ErW$_{10}$, enriched with a 95.3 % of the ^{167}Er isotope ($I = 7/2$).

The χ'' vs. frequency curves measured on the enriched sample are broader

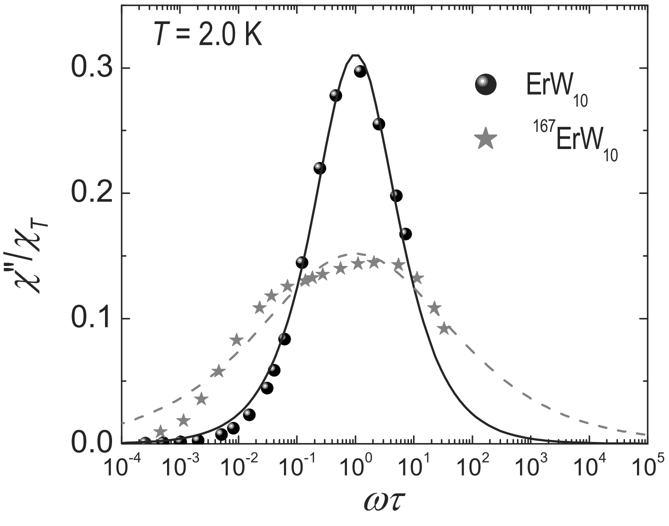

Figure 7.19: Reduced imaginary ac susceptibility χ''/χ_T vs. the reduced frequency $\omega\tau$ corresponding to ErW_{10} ($I = 0$) and $^{167}\mathrm{ErW}_{10}$ ($I = 7/2$). Lines correspond to least-square Cole-Cole fits which give $\tau^{-1} = 1.2 \times 10^3$ s^{-1} and $\beta = 0.23$ for ErW_{10} and $\tau^{-1} = 2.7 \times 10^2$ s^{-1} and $\beta = 0.623$ for $^{167}\mathrm{ErW}_{10}$. The broadening of the enriched sample evidences the broadening of the width of the distribution function of τ^{-1}.

than those measured on the standard sample. This fact is illustrated in Fig. 7.19 which compares experiments performed on both. The broadening reveals the co-existence of multiple SLR processes, associated with the splitting of the ground state electronic doublet into an electronuclear multiplet (see Fig. 7.20b). More apparently shown in Fig. 7.15, the (average) zero-field τ^{-1} of $^{167}\mathrm{ErW}_{10}$ is about 4.5 times smaller than the rate measured for ErW_{10} under the same conditions. The drastic slowing-down of SLR by hyperfine interactions contrasts sharply with the enhancement predicted for spin-phonon processes [291–293]. The enhancement of direct phonon-induced relaxation rates by hyperfine interactions was observed for instance, in ESR experiments performed on $\mathrm{Er}_x\mathrm{Y}_{1-x}(\mathrm{C}_2\mathrm{H}_5\mathrm{SO}_4)3 \cdot 9\ \mathrm{H}_2\mathrm{O}$ by G. H. Larson and C. D. Jeffries [303].

These measurements also serve us to confirm that the fast SLR of the non-enriched sample cannot be originated by cross-relaxation with ^{167}Er spins. This phenomenon, first described by N. Bloembergen *et al* [304], consists of the increase in the SLR rate of one spin species when it is in contact with another spin species with a larger SRL rate and similar energy splitting. Since the relaxation rate of ^{167}Er spins is smaller, the enhanced relaxation rate of ions with $I = 0$ must be attributed to pure quantum tunneling processes.

The isotopic effect can, in fact, be easily reconciled with the idea of SLR via pure quantum tunneling. On the one hand, the hyperfine splitting detunes

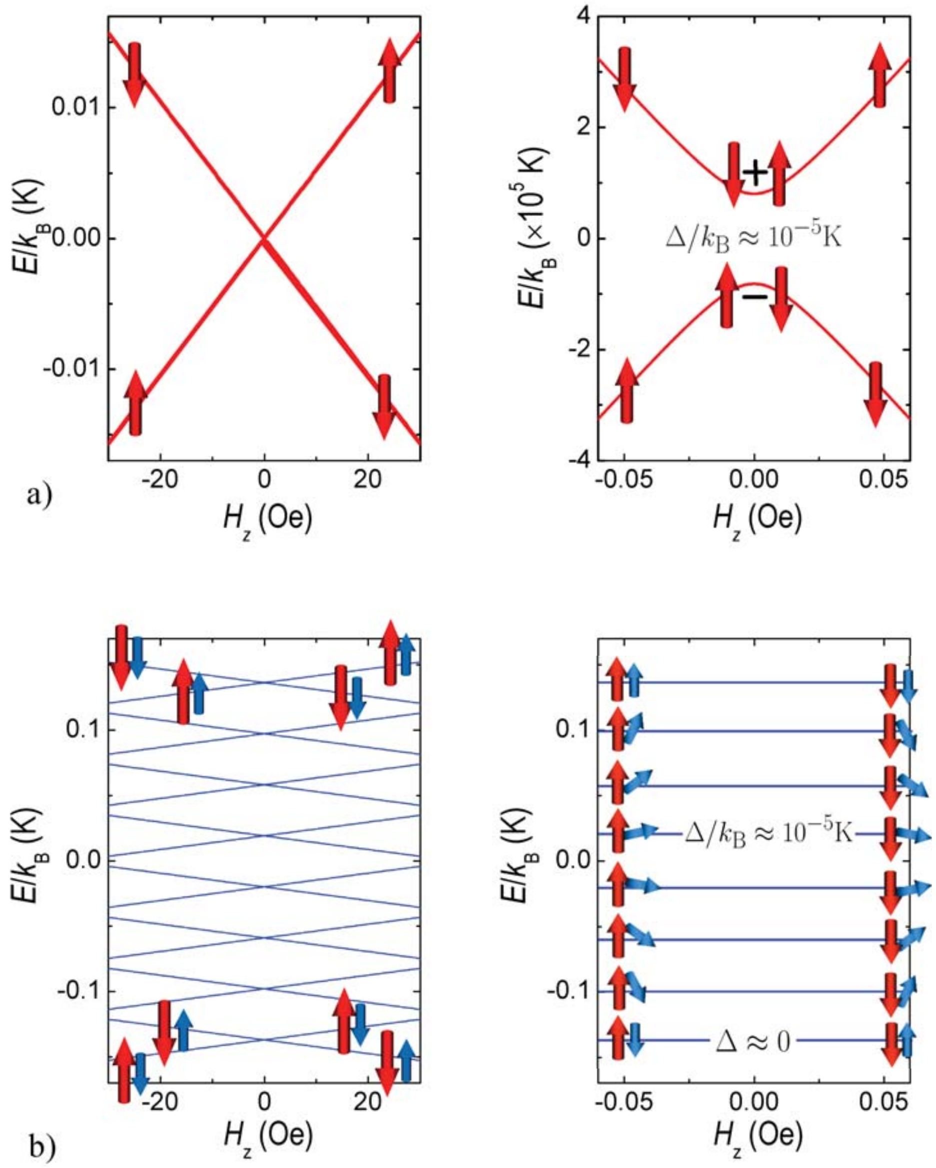

Figure 7.20: a) Energy of the ground state doublet of ErW$_{10}$ as a function of the bias field H_z. The panel on the right shows an amplification that enables to distinguish the avoided-crossing between the symmetric and antisymmetric wavefunctions. b) The ground sate splits into 8 doublets when the hyperfine interaction with the nuclear spin of ^{167}ErW$_{10}$ is introduced. The tunnel splitting of the low-lying and higher levels is $\Delta \sim 0$. However, it increases considerably between intermediate levels. Big red arrows and small blue arrows represent the electronic- and nuclear-spin orientations, respectively.

energetically states related by the flip of the electronic spin (see Fig. 7.20b). For the lowest lying states, the effect is then equal to that of a bias magnetic field. On the other, the tunnel splitting associated with the simultaneous reversal of the electronic and nuclear spins becomes $\Delta \sim 0$. Still, relaxation can take place through intermediate nuclear states, with ($\Delta \gtrsim 0$), that can be thermally populated ($\Delta E_{\rm hyp}/k_{\rm B} = 0.314$ K). Indeed, the tunneling window is quite high between these levels reaching values of $\Delta/k_{\rm B} \approx 10^{-5}$. Notice that this effect is quite similar to that observed in the CoO nanoparticles synthesized in ferritin that we studied in chapters 4 and 5. In the present case the electronic spin plays the role of the CoO nanoparticles magnetic moment, and the nuclear spin is equivalent to the ”environmental” spins.

The enhancement of Δ becomes however hindered by the increase of the bias field. The effect of hyperfine interactions is similar to that produced by an external magnetic field $\xi_{\rm dip} = \pm\xi_{\rm hyp}$. The latter can be estimated as $\xi_{\rm hyp} = 2A\mathbf{JI}$, where A is the hyperfine coupling constant that, for the case of erbium equals $A/k_{\rm B} = -6 \times 10^{-3}$ K. This value leads to $\xi_{\rm hyp}/k_{\rm B} = 0.314$ K, enough to reduce the tunneling probability as observed experimentally. From these considerations we can also conclude that the SLR rate of the ^{167}Er isotope can be also very well accounted for by the predictions for the direct tunneling rate.

7.6 Can quantum tunneling assist the spins to attain thermal equilibrium?

As we have shown experimentally, relaxation to *thermal equilibrium* is assisted at low temperatures by pure tunneling processes between the spin ground state doublet, a mechanism that should not in principle provide any contact between spins and phonons. This section will be devoted to give a tentative explanation to this puzzle. We propose a mechanism able of connecting spin flips produced by pure tunneling with the phonon bath.

This mechanism is schematized in Fig. 7.21. At very low temperatures, when the direct processes become enormously slow ($\tau_D^{-1} \to 10^{-7}$ s^{-1}), the spin bath chooses a more efficient mechanism towards *thermal equilibrium.* Tunneling events, that are considerably faster ($\tau_T^{-1} \approx 10^3$ s^{-1}), enable the spin bath to ”visit” different configurations. These configurations are energetically equivalent but some of them might be especially well coupled to the phonon bath. In this way, the collective emission of a single phonon by many spins could provide a very efficient relaxation path, in timescales probably shorter than 1 ms.

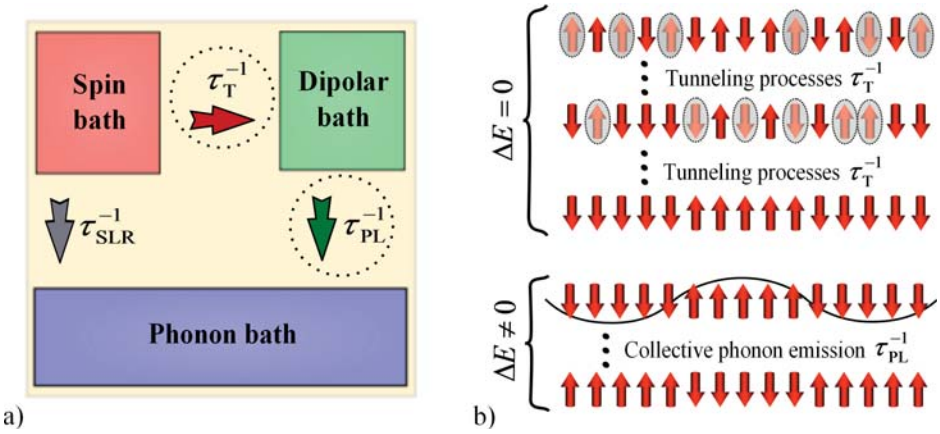

Figure 7.21: a) Scheme showing the spin-lattice relaxation via quantum tunneling. At low temperatures, the direct process becomes enormously slow $\tau_D^{-1} \approx 10^{-7}$ s^{-1}. On the other hand, tunneling events enable the spin to "visit" energetically equal configurations at a rate given by $\tau_T^{-1} \approx 10^3$ s^{-1}. Energy can be then delivered to the phonon bath through the collective emission of one phonon at the phonon-laser rate $\tau_{\mathrm{PL,max}}^{-1} \approx 10^4$ s^{-1}. b) Cartoon image of the relaxation mechanism. Spins that undergo tunneling processes are highlighted within a circle. The resulting configurations have the same energy but are not equivalent. There might be some of them characterized by a wave vector q close to that of a phonon that is subsequently emitted.

Our interpretation is strongly supported by three experimental observations. In the first place, the strong dependence of τ^{-1} on the spin concentration (x). From simple considerations based on the Prokof'ev-Stamp model, we have argued that the SLR rate must be proportional to x. However, experimentally we have found that $\tau^{-1} \propto x^2$. In view of this fact, we speculate that dipolar interactions are not just playing the role of effective fields but mediating the energy transfer between the spins and the lattice. Because of their mutual dipolar couplings, spins behave no longer as individual entities but as a collective system, that we refer to as the "dipolar bath". Our experiments suggest that the dipolar bath relaxes to the lattice much more efficiently than individual spins.

This possibility had been considered by the early theories of SLR [291–293, 305] and recently associated with the "phonon superradiance" and "phonon laser" phenomena by E. M. Chudnovsky and D. A. Garanin [276]. The maximum phonon-laser rate is given by

$$\tau_{\mathrm{PL,max}}^{-1} = J \left(\frac{\Delta E}{8\hbar M c_{\mathrm{s}}^2} \right)^{1/2} \tag{7.22}$$

where c_{s} is the speed of sound and $M = \rho V$, with ρ the density and V the unit cell volume. Inserting in this equation $c_{\mathrm{s}} = 2.3 \times 10^5$ cm/s, $\rho = 3.411$

g/cm^3 and $V = 3260.8$ Å^3 we find $\tau_{\mathrm{PL,max}}^{-1} \simeq 10^4$ s^{-1}, one order of magnitude larger than the experimental tunneling rate in ErW$_{10}$. Within this picture, the overall relaxation process becomes bottle-necked in the step connecting the spin and the dipolar bath. In this way, the experimental relaxation rate corresponds to the tunneling rate and is strongly dependent on the strength of the dipolar interactions, as observed experimentally.

The third argument supporting our interpretation is the following. Changes in temperature modify the width of the dipolar bias distribution, an effect that should become specially important when the spin system develops long-range magnetic order near $T_{\mathrm{N}} = 80$ mK. As we observe experimentally, τ^{-1} drops abruptly at this point, indeed. Within our simple picture, this might be understood rather easily since the distribution in energies of the dipolar bath approaches a delta function for all spins. Interactions become then equivalent to a external bias field and are therefore unable to mediate the energy transfer to the lattice.

7.7 Conclusions

In this chapter we have faced one of the most striking problems of magnetism, i.e. the thermalization of strongly anisotropic paramagnetic spins at very low temperatures. We have experimentally shown that spins are able to ”feel” the temperature of the lattice at rates that are enormously higher than the classic predictions for spin-phonon interaction at very low temperatures. We have also shown the important role played by dipolar interactions and quantum tunneling in such process.

In view of this fact, we have proposed a mechanism whereby *thermal equilibrium* conditions can be achieved via pure quantum events. This mechanism is consistent with recent theories of ”phonon-laser” effects, based on the analogy between excited electronic states in magnetic ions and excited atoms in laser physics. In the same way as atoms interact between them leading to the collective emission of photons, a coupled system of magnetic spins can also lead to the collective emission of phonons. Our experimental results strongly suggest that dipolar interactions are responsible for the collective behavior of the spin system, therefore referred to as the ”dipolar bath”. Within this frame, quantum tunneling plays a major role. It mediates the transition between dipolar configurations, some of which are able of relax by emitting a single phonon.

The strong resonant character of quantum tunneling, makes this mechanism quite sensitive to external stimulus. Our results show that spins can be effectively disconnected from the lattice by properly diluting them or by applying magnetic fields of moderate amplitude. Our work shows therefore an easy way of stabilizing off-equilibrium conditions, as required for the realization of quantum operations.

It is also worth mentioning that fluctuations of electronic spins determine also the thermal noise of materials hosting electron spins as impurities. The mechanism described here might therefore play a role in diverse phenomena such as the spin-lattice relaxation of nuclear spins [302] or the low-frequency noise of superconducting devices [306].

General conclusions

- **Circuit edit of superconducting microcircuits**. Our ability of fabricating superconducting micro and nanowires has been demonstrated. The resulting circuits are fully operative at liquid helium temperatures providing a most-useful technique for fixing errors in device designs, repairing damaged circuits, or modifying existing ones (chapter 2).

- **Low-T ultrasensitive broad band μSQUID susceptometer**. The previous technique has been applied to transform commercial μSQUID sensors into genuine μSQUID susceptometers. These devices provide i) the high sensitivity ($\sim 300\ \mu_{\mathrm{B}}/Hz^{1/2}$) inherent to μSQUID technologies, ii) an extremely broad bandwidth of operation (1 mHz $\leq f \leq$ 1 MHz) supplied by commercial readout electronics and iii) the possibility of working down to the close vicinity of the absolute zero ($T \sim 13$ mK) provided by the use of a dilution refrigerator (chapters 1 and 2).

- **The magnetic response of real systems of nanoparticles**. A straightforward method has been derived to determine the magnetic moment distribution of samples of magnetic nanoparticles. This method, based on a combined analysis of the magnetization and susceptibility data, has been successfully applied to the study of ferritin-based maghemite nanoparticles of different sizes (chapters 3 and 4)

- **Biology leaves its mark on ferritin-based nanomagnets**. The magnetic properties of ferritin-based nanocrystals of maghemite have been studied revealing an enhanced degree of disorder. The latter leads to an enhancement of the magnetic anisotropy that determines the stability of the nanoparticle's magnetic memory. These properties seem to be a consequence of the special mechanisms of crystal growth inside the protein (chapter 4).

- **Antiferromagnetism lays bare**. The magnetic properties of ferritin-based antiferromagnetic nanoparticles has been studied down to very low temperatures. These studies reveal the existence of a thermoinduced magnetic moment. The spin excitations involved in the rising of the latter differ however drastically from those expected using the classical theory of spin waves in bulk antiferromagnets. In addition, we have been able for the first time to observe experimentally the magnetic response that arises solely from the existence of uncompensated spins in the particle's surface and core (chapter 4 and 5).

- **Ferritin-based nanomagnets suiting superconducting μsensors**. The tiny magnetic signal produced by a submonolayer arrangement of just 10^7 ferritin-based nanoparticles was successfully measured. This demanding goal was achieved by maximizing the coupling between the samples and the sensor's pickup coils by means of dip pen nanolithography. Our experiments showed that ferritin-based nanoparticles arranged on surfaces retain their single-molecule magnet character (chapter 5).

- **Molecular design of spin-based qubits**. We have presented a magnetic study of a novel family of single molecule magnets consisting of individual lanthanide ions encapsulated within different polyoxometalate architectures. The enormous influence of the polyoxometalate ligands on the molecule's spin hamiltonian and, therefore on its dynamical behavior, has been demonstrated. Our results show how the magnetic properties of these clusters can be tailored, opening new avenues in the design of molecules for different applications (chapter 6).

- **A solid candidate for quantum computing**. We have proposed the use of one of these molecules, the GdW_{30}, as an excellent candidate for quantum computing. Its decoherence time could be rather large providing the preparation of nuclear spin-free and magnetically diluted systems. Under the application of a bias magnetic field of ~ 10 mT, quantum operations driven by electromagnetic radiation of 6.7 GHz could be performed in ~ 1 ns according to our estimations (chapter 6).

- **Quantum-mediated spin-phonon interaction**. We have investigated the intriguing mechanisms of spin-lattice relaxation in ErW_{30} clusters at very low temperatures. Our studies reveal the existence of an hitherto unknown mechanism which is up to nine orders of magnitude faster than spin-phonon mediated processes. Pure quantum tunneling processes between the ground states, though conserving energy, are able to mediate an effective spin-phonon interaction as we have shown. Based on our experimental results, we have proposed a mechanism whereby this effective interaction can take place (chapter 7).

Bibliography

[1] R. Sessoli, D. Gatteschi, A. Caneschi and M. A. Novak, Magnetic bistability in a metal-ion cluster, Nature 365 (1993) 141.

[2] A. O. Caldeira, A. J. Leggett, Influence of dissipation on quantum tunneling in macroscopic systems, Phys. Rev. Lett. 46 (4) (1981) 211–214.

[3] E. M. Chudnovsky, L. Gunther, Quantum Tunneling of Magnetization in Small Ferromagnetic Particles, Phys. Rev. Lett. 60 (8) (1988) 661–664.

[4] D. D. Awschalom, J. F. Smyth, G. Grinstein, D. P. DiVincenzo, D. Loss, Macroscopic quantum tunneling in magnetic proteins, Phys. Rev. Lett. 68 (20) (1992) 3092–3095.

[5] B. B. L. Gunther (Ed.), Quantum Tunneling of Magnetization, Vol. 301 of NATO Science Series E, 1995.

[6] F. Luis, E. del Barco, J. M. Hernández, E. Remiro, J. Bartolomé, J. Tejada, Resonant spin tunneling in small antiferromagnetic particles, Phys. Rev. B 59 (18) (1999) 11837–11846.

[7] J. M. Hernández, X. X. Zhang, F. Luis, J. Bartolomé, J. Tejada, R. Ziolo, Field tuning of thermally activated magnetic quantum tunnelling in Mn_{12}-Ac molecules, Europhys. Lett. 35 (4) (1996) 301.

[8] J. R. Friedman, M. P. Sarachik, J. Tejada, R. Ziolo, Macroscopic measurement of resonant magnetization tunneling in high-spin molecules, Phys. Rev. Lett. 76 (20) (1996) 3830–3833.

[9] J. M. Hernandez, X. X. Zhang, F. Luis, J. Tejada, J. R. Friedman, M. P. Sarachik, R. Ziolo, Evidence for resonant tunneling of magnetization in mn_{12}sacetate complex, Phys. Rev. B 55 (9) (1997) 5858–5865.

[10] F. Luis, F. L. Mettes, J. Tejada, D. Gatteschi, L. J. de Jongh, Observation of quantum coherence in mesoscopic molecular magnets, Phys. Rev. Lett. 85 (20) (2000) 4377–4380.

[11] E. del Barco, N. Vernier, J. M. Hernandez, J. Tejada, E. M. Chudnovsky, E. Molins, G. Bellessa, Quantum coherence in Fe_8 molecular nanomagnets, Europhys. Lett. 47 (6) (1999) 722.

[12] W. H. Zurek, Decoherence and the transition from quantum to classical, Physics Today 44 (10) (1991) 36–44.

[13] A. J. Leggett, Testing the limits of quantum mechanics: motivation, state of play, prospects, J. Phys.: Cond. Mat. 14 (15) (2002) R415.

[14] M. N. Leuenberger, D. Loss, Quantum computing in molecular magnets, Nature 410 (2001) 789–793.

[15] C. I. L. Nielsen M. A., Quantum Computation and Quantum Information, Cambridge Univ. Press., 2002.

[16] M. A. AlDamen, S. Cardona-Serra, J. M. Clemente-Juan, E. Coronado, A. G.-A. no, C. Martí-Gastaldo, F. Luis, O. Montero, Mononuclear Lanthanide Single Molecule Magnets Based on the Polyoxometalates $[Ln(W_5O_{18})_2]^{9-}$ and $[Ln(\beta_2\text{-}SiW_{11}O_{39})_2]^{13-}$ (Ln^{III}) Tb, Dy, Ho, Er, Tm, and Yb), Inorg. Chem. 48 (2009) 3467–3479.

[17] V. Bouchiat, Detection of magnetic moments using a nano-squid: limits of resolution and sensitivity in near-field squid magnetometry, Supercond. Sci. Technol. 22 (2009) 064002.

[18] J.-P. Cleuziou, W. Wernsdorfer, V. Bouchiat, T. Ondarçuhu and M. Monthioux, Carbon nanotube superconducting quantum interference device, Nature Nanotechnol. 1 (2006) 53 – 59.

[19] M. Jamet, W. Wernsdorfer, C. Thirion, D. Mailly, V. Dupuis, P. Mélinon, and A. Pérez, Magnetic anisotropy of individual cobalt clusters, Phys. Rev. Lett. 86 (2001) 4676.

[20] Lam, S. K. H., Yang, W., Wiogo, H. T. R., Foley C. P., Attachment of magnetic molecules on a nanoSQUID, Nanotechnology 19 (2008) 285303.

[21] Drung D, Aßmann C, Beyer J, Kirste A, Peters M, Ruede F and Schurig Th, Highly sensitive and easy-to-use SQUID sensors, IEEE Trans. Appl. Supercond. 17 (2) (2007) 699.

[22] Magnicon gmbh.
URL `http://www.magnicon.com/`

[23] E. Bellido, R. de Miguel, J. Sesé, D. Ruíz-Molina, A. Lostao, and D. Maspoch, Nanoscale positioning of inorganic nanoparticles using biological ferritin arrays fabricated by dip-pen nanolithography, SCANNING 31 (2010) 35–41.

[24] R. D. Piner, J. Zhu, F. Xu, S. Hong, and C. A. Mirkin, Dip-pen nanolithography, Science 283 (1999) 661–663.

[25] S. Ghosh, R. Parthasarathy, T. F. Rosenbaum, G. Aeppli, Coherent Spin Oscillations in a Disordered Magnet, Science 296 (5576) (2002) 2195–2198.

[26] S. Bertaina, S. Gambarelli, A. Tkachuk, I. N. Kurkin, B. Malkin, A. Stepanov and B. Barbara, Rare-earth solid-state qubits, Nature Nanotechnol. 2 (2007) 39.

[27] Bertaina, S. Gambarelli, S. Mitra, T. Tsukerblat, B. Muller, A. Barbara, B., Quantum oscillations in a molecular magnet, Nature 453 (2008) 203.

[28] Quantum design.
URL `http://www.qdusa.com/`

[29] Servicios de apoyo a la investigación de la Universidad de Zaragoza. Servicio de instrumentación científica.
URL `http://wzar.unizar.es/invest/sai/ins_ele/ins_ele.html`

[30] R. Bachmann, F. J. DiSalvo Jr., T. H. Geballe, R. L. Greene, R. E. Howard, C. N. King, H. C. Kirsch, K. N. Lee, R. E. Schwall, H.U. Thomas, R. B. Zubeck, Heat Capacity Measurements on Small Samples at Low Temperatures, Rev. Sci. Instrum. 43 (1972) 205.

[31] F. Pobell, Matter and Methods at Low Temperatures, 2nd Edition, Springer, UK, 1996.

[32] D. Kramer, DOE begins rationing helium-3, Physics Today 63 (2010) 22.

[33] C. Schlegel, Quantum coherence in molecular magnets, Ph.D. thesis, University of Stuttgart (2009).

[34] M. D. C. Schlegel, J. van Slageren, Broadband electron spin resonance at 4-40 ghz and magnetic fields up to 10 t, Rev. Sci. Instrum. 81 (2010) 093901.

[35] P. H. I. Utke, J. Melngailis, Gas-assisted focused electron beam and ion beam processing and fabrication, J. Vac. Sci. Technol. 26 (4) (2008) 1197.

[36] L. Thomas, F. Lionti, R. Ballou, D. Gatteschi, R. Sessoli and B. Barbara, Macroscopic quantum tunnelling of magnetization in a single crystal of nanomagnets, Nature 383 (1996) 145.

[37] A. Timco, S. Carretta, F. Troiani, F. Tuna, R. J. Pritchard, E. J. L. McInnes, A. Ghirri, A. Candini, P. Santini, G. Amoretti, M. Affronte, and R. E. P. Winpenny, Engineering the coupling between molecular spin qubits by coordination chemistry, Nature Nanotechnol. 4 (2009) 173.

[38] J. Tejada, E. M. Chudnovsky, E. del Barco, J. M. Hernandez, T. P. Spiller, Magnetic qubits as hardware for quantum computers, Nanotechnology 12 (2) (2001) 181.

[39] C. P. Foley, H. Hilgenkamp, Why nanoSQUIDs are important: an introduction to the focus issue, Supercond. Sci. Technol. 22 (6) (2009) 064001.

[40] S. Boyd, V. Kotsubo, R. Cantor, A. Theodorou, J. Hall, Miniature Thin-Film SQUID Susceptometer for Magnetic Microcalorimetry and Thermometry, IEEE Trans. Appl. Supercon. 19 (3) (2009) 697 –701.

[41] W. de Haas, F. du Pré, Paramagnetic relaxation in iron ammonium alum at low temperatures, Physica 5 (6) (1938) 501–506.

[42] E. S. Sadki, S. Ooi, K. Hirata, Focused-ion-beam-induced deposition of superconducting nanowires, Applied Physics Letters 85 (25) (2004) 6206–6208.

[43] Guillamón I, Suderow H, Vieira S, Fernández-Pacheco A, Sesé J, Córdoba R, De Teresa J M and Ibarra M R , Nanoscale superconducting properties of amorphous W-based deposits grown with a focused-ion-beam, New J. Phys. 10 (9) (2008) 093005.

[44] Guillamón I, Suderow H, Fernández-Pacheco A, Sesé J, Córdoba R, De Teresa J M, Ibarra M R and Vieira S, Direct observation of melting in a 2D superconducting vortex lattice, Nature Phys. 5 (9) (2009) 651.

[45] F. London, Superfluids, Wiley, New York, 1950.

[46] J. Bardeen, L. N. Cooper, J. R. Schrieffer, Theory of superconductivity, Phys. Rev. 108 (5) (1957) 1175–1204.

[47] B. D. Josephson, Possible new effects in superconductive tunnelling, Phys. Lett. 1 (7) (1962) 251 – 253.

[48] P. W. Anderson, J. M. Rowell, Probable Observation of the Josephson Superconducting Tunneling Effect, Phys. Rev. Lett. 10 (6) (1963) 230.

[49] K. K. Likharev, Superconducting weak links, Rev. Mod. Phys. 51 (1) (1979) 101–159.

[50] R. C. Jaklevic, J. Lambe, A. H. Silver, J. E. Mercereau, Quantum interference effects in josephson tunneling, Phys. Rev. Lett. 12 (7) (1964) 159–160.

[51] A. I. B. John Clarke (Ed.), The SQUID Handbook: Fundamentals and Technology of SQUIDs and SQUID Systems, Volume I, Wiley.

[52] D. Drung, R. Cantor, M. Peters, H. J. Scheer, and H. Koch, Low-noise high-speed dc superconducting quantum interference device magnetometer with simplified feedback electronics, Appl. Phys. Lett. 57 (1990) 406.

[53] V. Foglietti, M. Giannini, G. Petrocco, A double DC-SQUID device for flux locked loop operation, IEEE Trans. Mag. 27 (2) (1991) 2989 –2992.

[54] Y. Maslennikov, A. Baljaev, O. Snigirev, O. Kaplunenko, R. Mezzena, A double dc SQUID based magnetometer, IEEE Trans. Appl. Supercon. 5 (2) (1995) 3241 – 3243.

[55] R. Welty, J. Martinis, A series array of DC SQUIDs, IEEE Trans. Mag. 27 (2) (1991) 2924 –2926.

[56] R. Welty, J. Martinis, Two-stage integrated SQUID amplifier with series array output, IEEE Trans. Appl. Supercon. 3 (1) (1993) 2605 –2608.

[57] D. Drung, C. Hinnrichs, H.-J. Barthelmess, Low-noise ultra-high-speed dc squid readout electronics, Supercond. Sci. Technol. 19 (5) (2006) S235.

[58] A. I. B. John Clarke (Ed.), The SQUID Handbook: Applications of SQUIDs and SQUID Systems, Volume II, Wiley.

[59] A. Shnirman, G. Schön, Z. Hermon, Quantum manipulations of small josephson junctions, Phys. Rev. Lett. 79 (12) (1997) 2371–2374.

[60] D. V. Averin, Adiabatic quantum computation with cooper pairs, Sol. St. Commun. 105 (10) (1998) 659 – 664.

[61] L.B. Ioffe, V.B. Geshkenbein, M.V. Feigelman, A.L. Fauchére, G. Blatter, Quiet sds josephson junctions for quantum computing, Nature 398 (1999) 679.

[62] A. S. Y. Makhlin, G. Schön, Josephson junction qubits with controlled couplings, Nature 386 (1999) 305.

[63] J.E. Mooij, T.P. Orlando, L. Levitov, L. Tian, C.H van der Wal, S. Lloyd, Josephson persistent current qubit, Science 285 (1999) 1036.

[64] J. T. Y. Nakamura, Y.A. Pashkin, Coherent control of macroscopic quantum states in a single cooper pair box, Nature 398 (1999) 786.

[65] M. B. Ketchen, T. Kopley, H. Ling, Miniature SQUID susceptometer, Appl. Phys. Lett. 44 (10) (1984) 1008–1010.

[66] D. D. Awschalom, J. R. Rozen, M. B. Ketchen, W. J. Gallagher, A. W. Kleinsasser, R. L. Sandstrom, B. Bumble, Low-noise modular microsusceptometer using nearly quantum limited dc SQUIDs, Appl. Phys. Lett. 53 (21) (1988) 2108–2110.

[67] D. D. Awschalom, J. Warnock, Picosecond magnetic spectroscopy with integrated DC SQUIDs, IEEE Trans. on Mag. 5 (2) (1989) 1186.

[68] W. Wernsdorfer, K. Hasselbach, D. Mailly, B. Barbara, A. Benoit, L. Thomas, G. Suran, Dc-squid magnetization measurements of single magnetic particles, J. Magn. Magn. Mat. 145 (1-2) (1995) 33 – 39.

[69] S. K. H. Lam, D. L. Tilbrook, Development of a niobium nanosuperconducting quantum interference device for the detection of small spin populations, Appl. Phys. Lett. 82 (7) (2003) 1078 –1080.

[70] H. K. N, Introduction to Focused Ion Beams, New York: Springer, 2005.

[71] FEI.
URL `http://www.fei.com/`

[72] Fujita J, Ishida M, Ichihashi T, Ochiai Y, Kaito T and Matsui S, Growth of three-dimensional nano-structures using fib-cvd and its mechanical properties, Nucl. Instrum. Methods Phys. Res. 206 (2003) 472.

[73] De Teresa J M, Fernández-Pacheco A, Córdoba R, Sesé J, Ibarra M R, Guillamón I, Suderow H and Vieira S, Transport properties of superconducting amorphous W-based nanowires fabricated by focused-ion-beaminduced-deposition for applications in nanotechnology, Mater. Res. Soc. Symp. Proc. 1180.

[74] Spoddig D, Schindler K, Rodiger P, Barzola-Quiquia J, Fritsch K, Mulders H and Esquinazi P, Transport properties and growth parameters of pdc and wc nanowires prepared in a dual-beam microscope, Nanotechnology 18 (49) (2007) 495202.

[75] Tripathi S. K., Shukla N. and Kulkarni W. N., Exploring a new strategy for nanofabrication: deposition by scattered ga ions using fib, Nanotechnology 20 (7) (2009) 075304.

[76] C. D. Tesche, J. Clarke, dc squid: Noise and optimization, J. Loe. Temp. Phys. 29 (3-4) (1977) 301–331.

[77] J. J. P. Bruines, V. J. Waal and J. E. Mooij, Comment on: ”dc squid: Noise and optimization” by tesche and clarke, J. Low. Temp. Phys. 46 (3-4) (1982) 383–386.

[78] F. C. Wellstood, C. Urbina, J. Clarke, Hot-electron limitation to the sensitivity of the dc superconducting quantum interference device, Appl. Phys. Lett 54 (25) (1989) 2599–2601.

[79] S. Sendelbach, D. Hover, A. Kittel, M. Mück, J. M. Martinis, R. McDermott, Magnetism in squids at millikelvin temperatures, Phys. Rev. Lett. 100 (22) (2008) 227006.

[80] M. Ketchen, D. Awschalom, W. Gallagher, A. Kleinsasser, R. Sandstrom, J. Rozen, B. Bumble, Design, fabrication, and performance of integrated miniature SQUID susceptometers, IEEE Trans. Mag. 25 (2) (1989) 1212 –1215.

[81] M. E. Huber, N. C. Koshnick, H. Bluhm, L. J. Archuleta, T. Azua, P. G. Bjornsson, B. W. Gardner, S. T. Halloran, E. A. Lucero, K. A. Moler, Gradiometric micro-SQUID susceptometer for scanning measurements of mesoscopic samples, Rev. Sci. Instrum. 79 (5) (2008) 053704.

[82] C. Granata, E. Esposito, A. Vettoliere, L. Petti, M. Russo, An integrated superconductive magnetic nanosensor for high-sensitivity nanoscale applications, Nanotechnology 19 (27) (2008) 275501.

[83] K. Takeda, K. Awaga, T. Inabe, A. Yamaguchi, H. Ishimoto, T. Tomita, H. Mitamura, T. Goto, N. Môri, H. Nojiri, Magnetic anisotropy, tunneling effects, high-frequency EPR, and molecular structure of fast-relaxation species of Mn_{12} , Phys. Rev. B 65 (9) (2002) 094424.

[84] R. Feynman, There’s plenty of room at the bottom (1960).
URL `http://www.zyvex.com/nanotech/feynman.html`

[85] L. Néel, Influence des fluctioations thermiques surl’aimantation de grains ferromagnétiques très fins, C. R. Hebd. Seances Acad. Sci. 228 (1949) 664.

[86] W. F. Brown, Thermal fluctuations of a single-domain particle, Phys. Rev. 130 (5) (1963) 1677–1686.

[87] S. Mørup, D. E. Madsen, C. Frandsen, C. R. H. Bahl, M. F. Hansen, Experimental and theoretical studies of nanoparticles of antiferromagnetic materials, J. Phys.: Condens. Matter 19 (21) (2007) 213202.

[88] Kodama, R. H., Magnetic nanoparticles, J. Mag. Mag. Mater. 200 (1999) 359–372.

[89] Q. A. Pankhurst, J. Connolly, S. K. Jones, J. Dobson, Applications of magnetic nanoparticles in biomedicine, J. Phys. D: Appl. Phys. 36 (13) (2003) R167.

[90] J.-G. Zhu, New heights for hard disk drives, Materials Today 6 (7-8) (2003) 22 – 31.

[91] V. Skumryev, S. Stoyanov, Y. Zhang, G. Hadjipanayis, D. Givord and J. Nogués, Beating the superparamagnetic limit with exchange bias, Nature 423 (2003) 850–853.

[92] I. I. Yaacob, A. C. Nunes, A. Bose, Magnetic nanoparticles produced in spontaneous cationic-anionic vesicles: Room temperature synthesis and characterization, J. Colloid and Interf. Sci. 171 (1) (1995) 73–84.

[93] C. Estournés, T. Lutz, J. Happich, T. Quaranta, P. Wissler, J. L. Guille, Nickel nanoparticles in silica gel: Preparation and magnetic properties, J. Magn. Magn. Mater. 173 (1-2) (1997) 83 – 92.

[94] R. D. Zysler, C. A. Ramos, E. D. Biasi, H. Romero, A. Ortega, D. Fiorani, Effects of magnetic interactions in $(Fe_{0.26}Ni_{0.74})_{50}B_{50}$ magnetic nanoparticles, J. Magn. Magn. Mater. 221 (1-2) (2000) 37 – 44.

[95] Luis, F. and Torres, J. M. and García, L. M. and Bartolomé, J. and Stankiewicz, J. and Petroff, F. and Fettar, F. and Maurice, J.-L. and Vaurés, A. , Enhancement of the magnetic anisotropy of nanometer-sized co clusters: Influence of the surface and of interparticle interactions, Phys. Rev. B 65 (9) (2002) 094409.

[96] T. Kinoshita, S. Seino, K. Okitsu, T. Nakayama, T. Nakagawa, T. A. Yamamoto, Magnetic evaluation of nanostructure of gold-iron composite particles synthesized by a reverse micelle method, J. Alloy. Comp. 359 (1-2) (2003) 46 – 50.

[97] S. Kilcoyone and R. Cywinsky, Ferritin: a model superparamagnet, J. Magn. Magn. Mater. 140 (1995) 1466.

[98] S. A. Makhlouf, F. T. Parker, and A. E. Berkowitz, Magnetic hysteresis anomalies in ferritin, Phys. Rev. B 55 (1997) R14717.

[99] J. G. E. Harris, J. E. Grimaldi, D. D. Awschalom, A. Chiolero, D. Loss, Excess spin and the dynamics of antiferromagnetic ferritin, Phys. Rev. B 60 (5) (1999) 3453–3456.

[100] M. S. Seehra, V. S. Babu, A. Manivannan, J. W. Lynn, Neutron scattering and magnetic studies of ferrihydrite nanoparticles, Phys. Rev. B 61 (5) (2000) 3513–3518.

[101] N. J. O. Silva, V. S. Amaral, L. D. Carlos, V. de Zea Bermudez, Ferrihydrite antiferromagnetic nanoparticles in a sol-gel derived organic-inorganic matrix, J. Magn. Magn. Mater. 272-276 (Part 2) (2004) 1549.

[102] S. Mörup, C. Frandsen, Thermoinduced magnetization in nanoparticles of antiferromagnetic materials, Phys. Rev. Lett. 92 (21) (2004) 217201.

[103] J. L. García Palacios, L. B. Gong, and F. Luis, Equilibrium susceptibilities of superparamagnets: longitudinal and transverse, quantum and classical, J. Phys.: Condens. Matter 29 (2009) 456006.

[104] F. Luis, J. Bartolomé, J. Tejada, E. Martínez, Ac susceptibility study of the magnetic relaxation phenomena in CrO_2 digital compact cassette magnetic tapes, J. Magn. Magn. Mater. 157-158 (1996) 266 – 267, european Magnetic Materials and Applications Conference.

[105] F. Luis, E. del Barco, J. M. Hernández, E. Remiro, J. Bartolomé, J. Tejada, Resonant spin tunneling in small antiferromagnetic particles, Phys. Rev. B 59 (18) (1999) 11837–11846.

[106] K. S. Cole, R. H. Cole, Dispersion and absorption in dielectrics i. alternating current characteristics, J. Chem. Phys. 9 (1941) 341.

[107] N. Bontemps, J. Rajchenbach, R. V. Chamberlin, R. Orbach, Dynamic scaling in the $Eu_{0.4}Sr_{0.6}S$ spin-glass, Phys. Rev. B 30 (11) (1984) 6514.

[108] J. T. Richardson, W. O. Milligan, Magnetic properties of colloidal nickelous oxide, Phys. Rev. 102 (5) (1956) 1289–1294.

[109] J. Cohen, K. M. Creer, R. Pauthenet, and K. Srivastava, J. Phys. Soc. Jpn. Suppl. B-1 17 (1962) 685.

[110] J. T. Richardson, D. I. Yiagas, C. Turk, K. Forster, and M. V. Twigg, Origin of superparamagnetism in nickel oxide, J. Appl. Phys. 70 (1991) 6977.

[111] S. A. Makhlouf, F. T. Parker, F. E. Spada, and A. E. Berkowitz, Magnetic anomalies in NiO nanoparticles, J. Appl. Phys. 81 (1997) 5561.

[112] R. H. Kodama, S. A. Makhlouf, A. E. Berkowitz, Finite Size Effects in Antiferromagnetic NiO Nanoparticles, Phys. Rev. Lett. 79 (7) (1997) 1393–1396.

[113] A. Punnoose, H. Magnone, M. S. Seehra, J. Bonevich, Bulk to nanoscale magnetism and exchange bias in CuO nanoparticles, Phys. Rev. B 64 (17) (2001) 174420.

[114] L. Néel, Superparamagnétisme des grains trés fins antiferromagnétiques, C. R. 252 (1961) 4075.

[115] L. Néel, Superposition de l'antiferromagnétisme et du superparamagnétisme dans un grain trés fin, C. R. 253 (1961) 9.

[116] L. Néel, Sur le calcul de la susceptibilité additionelle superantiferromagnétique des grais fins et sa variation thermique, C. R. 253 (1961) 1286.

[117] B. Barbara and E. M. Chudnovsky, Macroscopic quantum tunneling in antiferromagnets, Phys. Rev. A 145 (1990) 205.

[118] D. H. Martin, Magnetism in solids, M.I.T. Press, Cambridge, 1967.

[119] L. Néel, Ann. de Physique 3 (1948) 137.

[120] N. J. O. Silva, V. S. Amaral, L. D. Carlos, Relevance of magnetic moment distribution and scaling law methods to study the magnetic behavior of antiferromagnetic nanoparticles: Application to ferritin, Phys. Rev. B 71 (18) (2005) 184408.

[121] D. E. Madsen, S. Mørup, and M. F. Hansen, On the interpretation of magnetization data for antiferromagnetic nanoparticles, J. Magn. Magn. Mater. 305 (2006) 95.

[122] J. A. Sawanson, Physical versus logical coupling in memory systems, IBM J. Res. Dev. 4 (1960) 305.

[123] B. Barbara, W. Wernsdorfer, L. C. Sampaio, J. G. Park, C. Paulsen, M. A. Novak, R. Ferré, D. Mailly, R. Sessoli, and A. Caneschi, Mesoscopic quantum tunneling of the magnetization, J. Magn. Magn. Mater. 140-144 (1995) 1825–1828.

[124] M. M. Ibrahim, S. Darwish, M. S. Seehra, Nonlinear temperature variation of magnetic viscosity in nanoscale FeOOH particles, Phys. Rev. B 51 (5) (1995) 2955–2959.

[125] H. Yamazaki, G. Tatara, K. Katsumata, K. lshibashi, and Y. Aoyagi, Magnetic relaxation in Ni wires, J. Magn. Magn. Mater. 156 (1996) 135.

[126] M. J. O'Shea and P. Perera, Influence of nanostructure on magnetic properties of strong anisotropy systems, J. Magn. Magn. Mater. 156 (1996) 141.

[127] X. X. Zhang, J. M. Hernandez, J. Tejada, R. F. Ziolo, Magnetic properties, relaxation, and quantum tunneling in $CoFe_2O_4$ nanopatticles embedded in potassium silicate, Phys. Rev. B 54 (1996) 4101–4106.

[128] F. C. Meldrum, V. J. Wade, D. L. Nimmo, B. R. Heywood and S. Mann, Synthesis of inorganic nanophase materials in supramolecular protein cages, Nature 349 (1991) 684–687.

[129] Uchida M, Flenniken ML, Allen M, Willits DA, Crowley BE, Brumfield S, Willis AF, Jackiw L, Jutila M, Young MJ, Douglas T., Targeting of cancer cells with ferrimagnetic ferritin cage nanoparticles, J. Am. Chem. Soc. 128 (2006) 6626–6633.

[130] A. Soriano-Portillo, M. Clemente-León, C. J. Gómez-García, E. Coronado, N. Gálvez, E. Colacio, and J. M. Domínguez-Vera, On ferritin heterogeneity. further evidence for heteropolymer, Synthetic Metals 148 (2005) 7–10.

[131] O. Kasyutich, D. Tatchev, A. Hoell, F. Ogrin, C. Deewhurst, and W. Schwarzacher, Small angle X ray and neutron scattering study of disordered and three dimensional ordered magnetic protein arrays, J. Appl. Phys. 105 (2009) 07B528.

[132] O. Kasyutich, R. D. Desautels, B. W. Southern, J. van Lierop, Novel Aspects of Magnetic Interactions in a Macroscopic 3D Nanoparticle-Based Crystal, Phys. Rev. Lett. 104 (12) (2010) 127205.

[133] F. C. Meldrum, B. R. Heywood and S. Mann, Magnetoferritin: in vitro synthesis of a novel magnetic protein, Science 257 (1992) 522–523.

[134] S. Gider, D. D. Awschalom, T. Douglas, S. Mann, and M. Chaparala, Classical and quantum magnetic phenomena in natural and artificial ferritin proteins, Science 268 (1995) 77–803.

[135] K. K. W. Wong, T. Douglas, S. Gider, D. D. Awschalom, and S. Mann, Biomimetic synthesis and characterization of magnetic proteins (magnetoferritin), Chem. Mat 10 (1998) 279–285.

[136] Berkowitz A E, Schuele W J and Flanders P J, Influence of Crystallite Size on Magnetic Properties of Acicular-Fe_2O_3 Particles, J. Appl. Phys. 39 (1968) 1261–1263.

[137] J. M. D. Coey, Noncollinear spin arrangement in ultrafine ferrimagnetic crystallites, Phys. Rev. Lett. 27 (17) (1971) 1140–1142.

[138] M. P. Morales, S. Veintemillas, M. I. Montero, C. J. Serna, A. Roig, Ll. Casas, B. Martínez, and F. Sandiumenge, Surface and Internal Spin Canting in γ-Fe_2O_3 Nanoparticles, Chem. Mater. 11 (1999) 3058–3064.

[139] Millán A, Urtizberea A, Silva N J O, Palacio F, Amaral V S, Snoeck E and Serin V, Surface effects in maghemite nanoparticles, J. Mag. Mag. Mater. 312 (2007) L5–L9.

[140] A. E. Berkowitz, J. A. Lahut, I. S. Jacobs, L. M. Levinson, D. W. Forester, Spin pinning at ferrite-organic interfaces, Phys. Rev. Lett. 34 (10) (1975) 594–597.

[141] F. Bødker, S. Mørup, S. Linderoth, Surface effects in metallic iron nanoparticles, Phys. Rev. Lett. 72 (2) (1994) 282–285.

[142] R. H. Kodama, A. E. Berkowitz, E. J. McNiff, Jr., S. Foner, Surface Spin Disorder in $NiFe_2O_4$ Nanoparticles, Phys. Rev. Lett. 77 (2) (1996) 394–397.

[143] B. Martínez, X. Obradors, L. Balcells, A. Rouanet, C. Monty, Low Temperature Surface Spin-Glass Transition in γ- Fe_2O_3 Nanoparticles, Phys. Rev. Lett. 80 (1) (1998) 181–184.

[144] K. Gilmore, Y. U. Idzerda, M. T. Klem, M. Allen, T. Douglas and M. Young, Surface contribution to the anisotropy energy of spherical magnetite particles, J. Appl. Phys. 97 (2005) 10B301.

[145] H. Li, M.T Klem, K. B. Sebby, D.J. Singel, M. Young, T. Douglas, YU. Idzerda, Determination of anisotropy constants of protein encapsulated iron oxide nanoparticles by electron magnetic resonance, J. Magn. Magn. Mat. 321 (2009) 175–180.

[146] R. H. Kodama, A. E. Berkowitz, Atomic-scale magnetic modeling of oxide nanoparticles, Phys. Rev. B 59 (9) (1999) 6321–6336.

[147] O. Iglesias, A. Labarta, Finite-size and surface effects in maghemite nanoparticles: Monte carlo simulations, Phys. Rev. B 63 (18) (2001) 184416.

[148] J. L. García Palacios, On the statics and dynamics of magnetoanisotropic nanoparticles, Adv. Chem. Phys. 112 (2000) 1–210.

[149] A. Urtizberea, F. Luis, A. Millán, E. Natividad, F. Palacio, E. Kampert, U. Zeitler, Thermoinduced magnetic moment in akaganèite nanoparticles, accepted for Phys. Rev. B (2011).

[150] V. Laufberger, Sur la cristallisation de la ferritine, Bull. Soc. Chim. Biol. 19 (1937) 1575–1582.

[151] Granick S., Ferritin I. Physical and chemical properties of horse spleen ferritin, J. Biol. Chem. 146 (1942) 451–461.

[152] Granick S., and Michaelis L., Ferritin II. Apoferritin of horse spleen, J. Biol. Chem. 147 (1943) 91–97.

[153] Michaelis L., Coryell C. D., and Granick S., Ferritin III. The magnetic properties of ferritin and some other colloidal ferric compounds, J. Biol. Chem. 148 (1943) 463–480.

[154] Granick S., Ferritin IV. Occurrence and immunological properties of ferritin, J. Biol. Chem. 149 (1943) 157–167.

[155] Fankuchen I., Ferritin V. X-ray diffraction data on ferritin and apoferritin, J. Biol. Chem. 150 (1943) 57–59.

[156] Hahn P. F., Granick S., Bale W. F., and Michaelis L., Ferritin VI. Conversion of inorganic and hemoglobin iron into ferritin iron in the animal body. Storage function of ferritin iron as shown by radioactive and magnetic measurements, J. Biol. Chem. 150 (1943) 407–412.

[157] Granick S., and Hahn P. F. , Ferritin VIII. Speed of uptake of iron by the liver and its conversion to ferritin iron, J. Biol. Chem. 155 (1943) 661–669.

[158] Granick S., Ferritin IX. Increase of the protein apoferritin in the gastrointestinal mucosa as a direct response to iron feeding. The function of ferritin in the regulation of iron absorption, J. Biol. Chem. 164 (1946) 737–746.

[159] Lawson D.M., Artymiuk P.J., Yewdall S.J., Smith J.M., Livingstone J.C., Treffry A., Luzzago A., Levi S., Arosio P., Cesareni G., et al., Synthesis of inorganic nanophase materials in supramolecular protein cages solving the structure of human h ferritin by genetically engineering intermolecular crystal contacts, Nature 349 (1991) 541–544.

[160] T. Douglas and V. T. Stark, Nanophase cobalt oxyhydroxide mineral synthesized within the protein cage of ferritin, Inorg. Chem. 39 (2000) 1828–1830.

[161] R. Tsukamoto, K. Iwahori, M. Muraoka, I. Yamashita, Synthesis of co_3o_4 nanoparticles using the cage-shaped protein apoferritin, Bull. Chem. Soc. Jpn. 78(11) (2005) 2075–2081.

[162] M. T. Klem, J. Mosolf, M. Young and T. Douglas, Photochemical mineralization of europium, titanium, and iron oxyhydroxide nanoparticles in the ferritin protein cage, Inorg. Chem. 48 (2008) 9041.

[163] N. Gálvez, P. Sánchez and J.M. Domínguez-Vera, Preparation of Cu and CuFe Prussian Blue derivative nanoparticles using the apoferritin cavity as nanoreactor, J. Mat. Chem 15 (2005) 2492.

[164] T. Ueno, M. Suzuki, T. Goto, T. Matsumoto, K. Nagayama, Y. Watanabe, Size-Selective Olefin Hydrogenation by a Pd Nanocluster Provided in an Apo-Ferritin Cage, Ang. Chem.-Int. Ed. 43 (2004) 2527–2530.

[165] N. Gálvez, P. Sánchez, J. M. Domínguez- Vera, A. Soriano-Portillo, M. Clemente-León and E. Coronado, Apoferritin encapsulated Ni and Co superparamagnetic nanoparticles, J. Mat. Chem. 16 (2006) 2757.

[166] R. M. Kramer, C. Li, D. C. Carter, M. O. Stone, and R. R. Naik, Engineered protein cages for nanomaterial synthesis, J. Am. Chem. Soc. 126 (2004) 13282–13286.

[167] B. Warne, O. I. Kasyutich, E. L. Mayes, J. A. L. Wiggins, and K. K. W. Wong, Self Assembled Nanoparticulate Co : Pt for Data Storage Applications, IEEE Trans. Magn. 36 (2000) 3009–3011.

[168] M. Okuda, K. Iwahori, I. Yamashita, H. Yoshimura, Fabrication of In_2O_3 Indium Oxide Semiconductor Nano-particles using Apoferritin, Biotech. Bioeng. 84 (2003) 187.

[169] M. Allen, D. Willits, J. Mosolf, M. Young, T. Douglas, Protein cage constrained synthesis of ferrimagnetic iron oxide nanoparticles, Adv. Mat. 14 (2002) 1562–1565.

[170] M. Allen, D. Willits, M. Young, T. Douglas, Constrained synthesis of cobalt oxide nanomaterials in the 12-subunit protein cage from *Listeria innocua*, Inorg. Chem 42 (2003) 6300–6305.

[171] T. Douglas and M. Young, Host-guest encapsulation of materials by assembled virus protein cages, Nature 393 (1998) 152–155.

[172] Douglas T, Strable E, Willits D, Aitouchen A, Libera M, Young M, Protein engineering of a viral cage for constrained nano-materials synthesis, Adv. Mat. 14 (2002) 415–418.

[173] M. L. Flenniken, D. A. Willits, S. Brumfield, M. J. Young, and T. Douglas, The small heat shock protein cage from *Methanococcus jannaschii* is a versatile nanoscale platform for genetic and chemical modification, Nano Letters 13 (2003) 1573–1676.

[174] E. L. Mayes and S. Mann, Nanobiotechnology, VCH, Weinheim, 2004.

[175] Liepold L, Anderson S, Willits D, Oltrogge L, Frank JA, Douglas T, Young M., Viral capsids as mri contrast agents., Magn. Reson. Med. 58 (2007) 871–879.

[176] Zhen Y., Xiaoyong W., Huajia D., Junfeng Z., Hongyan L., Hongzhe S. and Zijian G., Encapsulation of platinum anticancer drugs by apoferritin, Chem. Commun. (2007) 3453–3455.

[177] C. R. Kaiser, M. L. Flenniken, E. Gillitzer, A. L Harmsen, A. G. Harmsen, M. A. Jutila, T. Douglas, and M. J. Young, Biodistribution studies of protein cage nanoparticles demonstrate broad tissue distribution and rapid clearance in vivo, Int. J. Nanomedicine 2(4) (2007) 715–733.

[178] R. de Miguel, Ph.D. thesis, Instituto de Nanociencia de Aragón (INA), University of Zaragoza (2011).

[179] National High Magnetic Field Laboratory, Florida State University - Los Alamos National Laboratory - University of Florida, Museum of electricity and magnetism, `http://www.magnet.fsu.edu/`.

[180] R. J. Hill, J. R. Craig, G. V. Gibbs, Systematics of the spinel structure type, Phys. Chem. Miner. 4 (1979) 317–339.

[181] G. A. Clegg, J. E. Fitton, P. M. Harrison, A. Treffry, Ferritin: molecular structure and iron-storage mechanisms., Prog. Biophys. Molec. Biol. 36 (1980) 53–86.

[182] M. J. Martínez-Pérez, R. de Miguel, C. Carbonera, M. Martínez-Júlvez, A. Lostao, C. Piquer, C. Gómez-Moreno, J. Bartolomé, F. Luis, Size-dependent magnetic properties of magnetoferritin, Nanotechnology 21 (2010) 465707.

[183] A. Cabot, A. P. Alivisatos, V. F. Puntes, L. Balcells, O. Iglesias, A. Labarta, Magnetic domains and surface effects in hollow maghemite nanoparticles, Phys. Rev. B 79 (9) (2009) 094419.

[184] F. Luis, F. Bartolomé, F . Petroff, J. Bartolomé, L. M. García, C. Deranlot, H. Jaffrès, M. J. Martínez, P. Bencok, F. Wilhelm, A. Rogalev and N. B. Brookes, Tuning the magnetic anisotropy of Co nanoparticles by metal capping, Europhys. Lett. 76 (1) (2006) 142.

[185] N. C. Tombs and H. P. Rooksby, Structure of monoxides of some transition elements at low temperatures, Nature 165 (1950) 442–443.

[186] M. M. Foëx, Sur un type de transformation commun aux protoxydes de manganèse, cobalt, fer et nickel, C. R. Acad. Sc. 227 (1948) 193–196.

[187] H. la Blanchetais, Contribution a l'étude de l'antiferromagnètisme. Étude thermomagnètique des protoxydes de cobalt et de nickel, Le Journal de Physique et Le Radium 12 (1951) 765–771.

[188] C. G. Shull, W. A. Strauser, E. O. Wollan, Neutron diffraction by paramagnetic and antiferromagnetic substances, Phys. Rev. 83 (2) (1951) 333–345.

[189] W. L. Roth, Magnetic Structures of MnO, FeO, CoO, and NiO, Phys. Rev. 110 (6) (1958) 1333–1341.

[190] N. Elliott, Magnetic Behavior of the System CoO-MgO at Elevated Temperatures, J. Chem. Phys 22 (1954) 1924.

[191] P. S. Silinsky, M. S. Seehra, Principal magnetic susceptibilities and uniaxial stress experiments in coo, Phys. Rev. B 24 (1) (1981) 419–423.

[192] J. Kanamori, Theory of the Magnetic Properties of Ferrous and Cobaltous Oxides, I, Prog. Theoret. Phys. 17 (2) (1957) 177–196.

[193] J. R. Singer, Magnetic Susceptibility of NiO and CoO Single Crystals, Phys. Rev. 104 (4) (1956) 929–932.

[194] K. Inagawa, K. Kamigaki, and S. Miura, Spin Flopping in CoO Crystal in the Pulsed Intense Magnetic Field, J. Phys. Soc. Jpn 31 (1971) 1276.

[195] M. Hassel and H.-J. Freund, High Resolution XPS Study of a Thin CoO(111) Film Grown on Co(0001), Surf. Sci. Spectra 4 (1996) 273.

[196] S. A. Chambers, R. F. C. Farrow, S. Maat, M. F. Toney, L. Folks, J. G. Catalano, T. P. Trainor, G. E. Brown, Molecular beam epitaxial growth and properties of $CoFe_2O_4$ on MgO (001), J. Magn. Magn. Mater. 426 (2002) 124–139.

[197] M. J. Martínez-Péreza, E. Bellido, R. de Miguel, J. Sesé, A. Lostao, C. Gómez-Moreno, D. Drung, T. Schurig, D. Ruiz-Molina and F. Luis, Optimum integration of ferritin-based nanomagnets into superconducting microsensors., submitted (2011).

[198] S. N. Klausen, P.-A. Lindgård, K. Lefmann, F. Bødker, and S. Mørup, Temperature Dependence of the Magnetization of Disc Shaped NiO Nanoparticles, Phys. Stat. Sol. 189 (2002) 1039–1042.

[199] A. Punnoose, H. Magnone, M. S. Seehra, J. Bonevich, Bulk to nanoscale magnetism and exchange bias in cuo nanoparticles, Phys. Rev. B 64 (17) (2001) 174420.

[200] P. V. Hendriksen, S. Linderoth, P.-A. Lindgård, Finite-size modifications of the magnetic properties of clusters, Phys. Rev. B 48 (10) (1993) 7259.

[201] J. M. Wesselinowa, I. Apostolova, Size and anisotropy effects on static and dynamic properties of ferromagnetic nanoparticles, J. Phys. Condens. Mat. 19 (21) (2007) 216208.

[202] M. Feygneson, X. Teng, S. E. Inderhees, Y. Yiu, W. Du, W. Han, J. Wen, Z. Xu, A. A. Podlesnyak, J. L. Niedziela, M. Hagen, Y. Qiu, C. M. Brown, L. Zhang, M. C. Aronson, Low energy magnetic excitations in Co Core/CoO shell nanoparticles, Phys. Rev. B.

[203] F. Luis, F. L. Mettes, J. Tejada, D. Gatteschi, L. J. de Jongh, Observation of quantum coherence in mesoscopic molecular magnets, Phys. Rev. Lett. 85 (20) (2000) 4377–4380.

[204] D. Sellmyer, R. Skomski, Advanced Magnetic Nanostructures, 1st Edition, Springer, New York, 2005.

[205] M. Mannini, P. Sainctavit, R. Sessoli, C. Cartier dit Moulin, F. Pineider, M. A. Arrio, A. Cornia, and D. Gatteschi, XAS and XMCD Investigation of Mn_{12} Monolayers on Gold, Chem. Eur. J. 14 (2008) 7530.

[206] M. Mannini, F. Pineider, P. Sainctavit, C. Danieli, E. Otero, C. Sciancalepore, A. M. Talarico, M. A. Arrio, A. Cornia, D. Gatteschi, and R. Sessoli, Magnetic memory of a single-molecule quantum magnet wired to a gold surface, Nature Mat. 8 (2009) 194.

[207] C. Iacovita, M. V. Rastei, B. W. Heinrich, T. Brumme, J. Kortus, L. Limot, J. P. Bucher, Visualizing the spin of individual cobalt-phthalocyanine molecules, Phys. Rev. Lett. 101 (11) (2008) 116602.

[208] S. Krause, G. Herzog, T. Stapelfeldt, L. Berbil-Bautista, M. Bode, E. Y. Vedmedenko, R. Wiesendanger, Magnetization Reversal of Nanoscale Islands: How Size and Shape Affect the Arrhenius Prefactor, Phys. Rev. Lett. 103 (12) (2009) 127202.

[209] V. F. Puntes, P. Gorostiza, D. M. Ruguete, N. G. Bastus, and A. P. Alivisatos, Collective behaviour in two-dimensional cobalt nanoparticle assemblies observed by magnetic force microscopy, Nature Mat. 3 (2004) 236.

[210] Y. Li, P. Xiong, S. von Molnár, S. Wirth, Y. Ohno, and H. Ohno, Hall magnetometry on a single iron nanoparticle, Appl. Phys. Lett. 80 (2002) 4644.

[211] W. Wernsdorfer, K. Hasselbach, D. Mailly, B. Barbara, A. Benoit, L. Thomas, and G. Swan, DC-SQUID magnetization measurements of single magnetic particles, J. Magn. Magn. Mater. 145 (1995) 33.

[212] C. Haginoya, S. Heike, M. Ishibashi, K. Nakamura, and T. Yoshimura, Magnetic nanoparticle array with perpendicular crystal magnetic anisotropy, J. Appl. Phys. 85 (1999) 8327.

[213] J. I. Martiín, J. Nogués, K. Liu, J. L. Vicent, and I. K. Schuller, Ordered magnetic nanostructures: fabrication and properties, J. Magn. Magn. Mater. 256 (2003) 449.

[214] A. D. Kent, T. M. Shaw, S. Molnár, and D. D. Awschalom, Growth of high aspect ratio nanometer-scale magnets with chemical vapor deposition and scanning tunneling microscopy, Science 262 (1993) 1249.

[215] C. I. Pakes, D. P. George, S. Ramelow, A. Cimmino, D. N. Jamieson, and S. Prawer, Manipulation of single magnetic protein particles using atomic force microscopy, J. Magn. Magn. Mater. 272–276 (2004) e1231.

[216] P. Rabl, D. DeMille, J. M. Doyle, M. D. Lukin, R. J. Schoelkopf, P. Zoller, Hybrid quantum processors: Molecular ensembles as quantum memory for solid state circuits, Phys. Rev. Lett. 97 (3) (2006) 033003.

[217] A. Imamoğlu, Cavity QED Based on Collective Magnetic Dipole Coupling: Spin Ensembles as Hybrid Two-Level Systems, Phys. Rev. Lett. 102 (8) (2009) 083602.

[218] E. Bellido, R. de Miguel, D. Ruíz-Molina, A. Lostao, and D. Maspoch, Controlling the number of proteins with dip-pen nanolithography, Adv. Mater. 21 (2010) 352.

[219] A. C. Ewing, The Fountain Pen: A Collector's Companion, Running Press, Philadelphia, 1997.

[220] S. Hong, J. Zhu, and C. A. Mirkin, Multiple ink nanolithography: Toward a multiple-pen nano-plotter, Science 286 (1999) 523–525.

[221] S. Hong and C. A. Mirkin, A nanoplotter with both parallel and serial writing capabilities, Science 288 (2000) 1808–1811.

[222] K.-B. Lee, S.-J. Park, C. A. Mirkin, J. C. Smith, M. Mrksich, Protein nanoarrays generated by dip-pen nanolithography, Science 295 (2002) 1702 – 1705.

[223] S. W. Lee, B.-K. Oh, R. G. Sanedrin, K. Salaita, T. Fujigaya, C. A. Mirkin, Biologically active protein nanoarrays generated using parallel dip-pen nanolithography, Adv. Mat. 18 (2006) 1133 – 1136.

[224] L. M. Demers, D. S. Ginger, S.-J. Park, Z. Li, S.-W. Chung, C. A. Mirkin, Direct patterning of modifed oligonucleotides on metals and insulators by dip-pen nanolithography, Science 296 (2002) 1836–1838.

[225] A. Ivanisevic and C. A. Mirkin, Dip-pen nanolithography on semiconductor surfaces, J. Am. Chem. Soc. 123 (2001) 7887–7889.

[226] Y. Li, B. W. Maynor, and J. Liu, Electrochemical AFM Dip-Pen Nanolithography, J. Am. Chem. Soc. 123 (2001) 2105–2106.

[227] E. Bellido, Ph.D. thesis, Centro de Investigación en Nanociencia y Nanotecnología. Universidad Autónoma de Barcelona (2011).

[228] J. Sesé, F. Lera, A. Camón, C. Rillo, Calculation of effective inductances of superconducting devices. application to the cryogenic current comparator, IEEE Trans. Appl. Supercon. 9 (1999) 58–62.

[229] W. H. Zurek, Decoherence, einselection, and the quantum origins of the classical, Rev. Mod. Phys. 75 (2003) 715–765.

[230] Kubo, Y. and Ong, F. R. and Bertet, P. and Vion, D. and Jacques, V. and Zheng, D. and Dréau, A. and Roch, J.-F. and Auffeves, A. and Jelezko, F. and Wrachtrup, J. and Barthe, M. F. and Bergonzo, P. and Esteve, D. , Strong Coupling of a Spin Ensemble to a Superconducting Resonator, Phys. Rev. Lett. 105 (14) (2010) 140502.

[231] D. I. Schuster, A. P. Sears, E. Ginossar, L. DiCarlo, L. Frunzio, J. J. L. Morton, H. Wu, G. A. D. Briggs, B. B. Buckley, D. D. Awschalom, R. J. Schoelkopf, High-cooperativity coupling of electron-spin ensembles to superconducting cavities, Phys. Rev. Lett. 105 (14) (2010) 140501.

[232] C. Sangregorio, T. Ohm, C. Paulsen, R. Sessoli, D. Gatteschi, Quantum tunneling of the magnetization in an iron cluster nanomagnet, Phys. Rev. Lett. 78 (24) (1997) 4645–4648.

[233] D. Loss, D. P. DiVincenzo, G. Grinstein, Suppression of tunneling by interference in half-integer-spin particles, Phys. Rev. Lett. 69 (22) (1992) 3232–3235.

[234] J. von Delft, C. L. Henley, Destructive quantum interference in spin tunneling problems, Phys. Rev. Lett. 69 (22) (1992) 3236–3239.

[235] R. Sessoli, H. L. Tsai, A. R. Schake, S. Wang, J. B. Vincent, K. Folting, D. Gatteschi, G. Christou, D. N. Hendrickson, High-spin molecules: $[Mn_{12}O_{12}(O_2CR)_{16}(H_2O)_4]$, J. Am. Chem. Soc. 115 (5) (1993) 1804.

[236] N. Domingo, B. E. Williamson, J. Gómez-Segura, P. Gerbier, D. Ruiz-Molina, D. B. Amabilino, J. Veciana, J. Tejada, Magnetism of isolated Mn_{12} single-molecule magnets detected by magnetic circular dichroism: Observation of spin tunneling with a magneto-optical technique, Phys. Rev. B 69 (5) (2004) 052405.

[237] F. El Hallak, J. van Slageren, J. Gómez-Segura, D. Ruiz-Molina, M. Dressel, High-frequency ESR and frequency domain magnetic resonance spectroscopic studies of single molecule magnets in frozen solution, Phys. Rev. B 75 (10) (2007) 104403.

[238] C. Carbonera, F. Luis, J. Campo, J. Sánchez-Marcos, A. Camón, J. Chaboy, D. Ruiz-Molina, I. Imaz, J. van Slageren, S. Dengler, M. González, Effect of crystalline disorder on quantum tunneling in the single-molecule magnet Mn_{12} benzoate, Phys. Rev. B 81 (1) (2010) 014427.

[239] F. Palacio, P. Oliete, U. Schubert, I. Mijatovic, N. Husing, H. Peterlik, Magnetic behaviour of a hybrid polymer obtained from ethyl acrylate and the magnetic cluster $Mn_{12}O_{12}(\text{acrylate})_{16}$, J. Mater.Chem. 14 (2004) 1873–1878.

[240] J. Villain, F. Hartman-Boutron, R. Sessoli, A. Rettori, Magnetic relaxation in big magnetic molecules, Europhys. Lett. 27 (2) (1994) 159.

[241] D. A. Garanin, E. M. Chudnovsky, Thermally activated resonant magnetization tunneling in molecular magnets: Mn_{12}-Ac and others, Phys. Rev. B 56 (17) (1997) 11102–11118.

[242] F. Luis, J. Bartolomé, J. F. Fernández, Resonant magnetic quantum tunneling through thermally activated states, Phys. Rev. B 57 (1) (1998) 505–513.

[243] A. Fort, A. Rettori, J. Villain, D. Gatteschi, R. Sessoli, Mixed Quantum-Thermal Relaxation in Mn_{12} Acetate Molecules, Phys. Rev. Lett. 80 (3) (1998) 612–615.

[244] M. Affronte, Molecular nanomagnets for information technologies, J. Mater. Chem. 19 (2009) 1731–1737.

[245] M. Evangelisti, A. Candini, A. Ghirri, M. Affronte, E. K. Brechin, and E. J. L. McInnes, Spin-enhanced magnetocaloric effect in molecular nanomagnets, Appl. Phys. Lett. 87 (2005) 072504.

[246] V. K. Pecharsky, K. A. G. Jr., Magnetocaloric effect and magnetic refrigeration, J. Magn. Magn. Mater. 200 (1-3) (1999) 44 – 56.

[247] D. D. P, Topics in quantum computers: Mesoscopic Electron Transport, NATO ASI Series, 1997.

[248] T. D. Ladd, F. Jelezko, R. Laflamme, Y. Nakamura, C. Monroe, and J. L. O'Brien, Quantum computing in molecular magnets, Nature 464 (2010) 45–53.

[249] J. V. Dante Gatteschi, Roberta Sessoli, Molecular Nanomagnets, Oxford University Press, 2006.

[250] J. Gómez-Segura, J. Veciana, D. Ruíz-Molina, Advances on the nanostructuration of magnetic molecules on surfaces: the case of single-molecule magnets, Chem. Com. (Camb) 36 (2007) 3699.

[251] T. Lis, Preparation, structure, and magnetic properties of a dodecanuclear mixed-valence manganese carboxylate, Acta Cryst. B 36 (9) (1980) 2042–2046.

[252] A. Caneschi, D. Gatteschi, R. Sessoli, A. L. Barra, L. C. Brunel, M. Guillot, Alternating current susceptibility, high field magnetization, and millimeter band EPR evidence for a ground $S = 10$ state in $[Mn_{12}O_{12}(Ch_3COO)_{16}(H_2O)_4] \cdot 2CH_3COOH \cdot 4H_2O$, J. Am. Chem. Soc. 113 (15) (1991) 5873–5874.

[253] K. J. I. Weighardt, K. Pohl, G. Huttner, Hydrolysis Products of the Monomeric Amine Complex $(C_6H_{15}N_3)FeCl_3$: The Structure of the Octameric Iron(III) Cation of $\{[(C_6H_{15}N_3)_6Fe_84(\mu_3\text{-}O)_2(\mu_2\text{-}OH)_{12}]Br_7(H_2O)\}$ $Br_7(H_2O)$, Angew. Chem. Int. Ed. Engl. 23 (1) (1984) 1521–3773.

[254] A.-L. Barra, P. Debrunner, D. Gatteschi, C. E. Schulz, R. Sessoli, Superparamagnetic-like behavior in an octanuclear iron cluster, Europhys. Lett. 35 (2) (1996) 133.

[255] Larsen, F. K. McInnes, E. J. L. Mkami, H. E. Overgaard, J. Piligkos, S. Rajaraman, G. Rentschler, E. Smith, A. A. Smith, G. M. Boote, V. Jennings, M. Timco, G. A. and Winpenny, R. E. P. TI, Synthesis and Characterization of Heterometallic Cr_7M Wheels, Angew. Chem. Int. Ed. Engl. 42 (1) (2003) 101–105.

[256] F. Meier, D. Loss, Thermodynamics and spin-tunneling dynamics in ferric wheels with excess spin, Phys. Rev. B 64 (22) (2001) 224411.

[257] A. Ardavan, O. Rival, J. J. L. Morton, S. J. Blundell, A. M. Tyryshkin, G. A. Timco, R. E. P. Winpenny, Will spin-relaxation times in molecular magnets permit quantum information processing?, Phys. Rev. Lett. 98 (5) (2007) 057201.

[258] A. Müller, J. A. Döring, A novel heterocluster with D3-symmetry containing twenty-one core atoms: $[\mathrm{As}_6^{\mathrm{III}}\mathrm{V}_1^{\mathrm{IV}}5\mathrm{O}_{42}(\mathrm{H}_2\mathrm{O})]^{6-}$., Angew. Chem. Int. Ed. Engl. 27 (1988) 1721.

[259] N. Ishikawa, M. Sugita, T. Ishikawa, S.-y. Koshihara, Y. Kaizu, Lanthanide double-decker complexes functioning as magnets at the single-molecular level, J. Am. Chem. Soc. 125 (29) (2003) 8694–8695.

[260] M. A. AlDamen, J. M. Clemente-Juan, E. Coronado, C. Martí-Gastaldo, A. Gaita-Ariño, Mononuclear lanthanide single-molecule magnets based on polyoxometalates, J. Am. Chem. Soc. 130 (28) (2008) 8874–8875.

[261] P. C. E. Stamp, A. Gaita-Arino, Spin-based quantum computers made by chemistry: hows and whys, J. Mater. Chem. 19 (2009) 1718–1730.

[262] K. W. H. Stevens, Matrix elements and operator equivalents connected with the magnetic properties of rare earth ions, Proceedings of the Physical Society. Section A 65 (3) (1952) 209.

[263] B. Bleaney, K. W. H. Stevens, Paramagnetic resonance, Rep. Progr. Phys. 16 (1) (1953) 108.

[264] N. V. Prokof'ev, P. C. E. Stamp, Low-temperature quantum relaxation in a system of magnetic nanomolecules, Phys. Rev. Lett. 80 (26) (1998) 5794–5797.

[265] S. Cardona-Serra, Ph.D. thesis, Instituto de Ciencia Molecular (ICMoL), University of Valencia (2011).

[266] N. Ishikawa, Simultaneous determination of ligand-field parameters of isostructural lanthanide complexes by multidimensional optimization, J. Phys. Chem. A 107 (30) (2003) 5831–5835.

[267] N. Ishikawa, M. Sugita, T. Okubo, N. Tanaka, T. Iino, Y. Kaizu, Determination of ligand-field parameters and f-electronic structures of double-decker bis(phthalocyaninato)lanthanide complexes, Inorganic Chemistry 42 (7) (2003) 2440–2446.

[268] W. Low, D. Shaltiel, Paramagnetic-resonance spectrum of gadolinium in single crystals of thorium oxide, J. Phys. Chem. Sol. 6 (4) (1958) 315–323.

[269] B. Bleaney, H. E. D. Scovil, R. S. Trenam, The paramagnetic resonance spectra of gadolinium and neodymium ethyl sulphates, Proc. Phys. Soc. A 223 (1152) (1954) pp. 15–29.

[270] S. Geschwind, J. P. Remeika, Paramagnetic Resonance of Gd^{3+} in Al_2O_3, Phys. Rev. 122 (3) (1961) 757–761.

[271] A. S. Stefan Stoll, Easyspin, a comprehensive software package for spectral simulation and analysis in epr, J. Magn. Reson. 178 (1) (2006) 42–55.

[272] J. M. Luttinger, L. Tisza, Theory of dipole interaction in crystals, Phys. Rep. 70 (1946) 954.

[273] J. F. Fernández, J. J. Alonso, Ordering of dipolar ising crystals, Phys. Rev. B 62 (2000) 53–56.

[274] J. F. Fernández, J. J. Alonso, Erratum: Ordering of dipolar ising crystals, Phys. Rev. B 65 (2002) 189901(E).

[275] J. F. Fernández, Dipolar ordering of molecular magnets, Phys. Rev. B 66 (6) (2002) 064423.

[276] E. M. Chudnovsky, D. A. Garanin, Phonon superradiance and phonon laser effect in nanomagnets, Phys. Rev. Lett. 93 (25) (2004) 257205.

[277] M. Evangelisti, F. Luis, F. L. Mettes, N. Aliaga, G. Aromí, J. J. Alonso, G. Christou, L. J. de Jongh, Magnetic long-range order induced by quantum relaxation in single-molecule magnets, Phys. Rev. Lett. 93 (11) (2004) 117202.

[278] M. Evangelisti, F. Luis, F. L. Mettes, R. Sessoli, L. J. de Jongh, Giant Isotope Effect in the Incoherent Tunneling Specific Heat of the Molecular Nanomagnet Fe_8, Phys. Rev. Lett. 95 (22) (2005) 227206.

[279] N. V. Prokof'ev, P. C. E. Stamp, Theory of the spin bath, Rep. Progr. Phys. 63 (4) (2000) 669.

[280] J. F. Fernández, J. J. Alonso, Magnetization process of single molecule magnets at low temperatures, Phys. Rev. Lett. 91 (4) (2003) 047202.

[281] W. Wernsdorfer, T. Ohm, C. Sangregorio, R. Sessoli, D. Mailly, C. Paulsen, Observation of the distribution of molecular spin states by resonant quantum tunneling of the magnetization, Phys. Rev. Lett. 82 (19) (1999) 3903–3906.

[282] W. Wernsdorfer, A. Caneschi, R. Sessoli, D. Gatteschi, A. Cornia, V. Villar, C. Paulsen, Effects of Nuclear Spins on the Quantum Relaxation of the Magnetization for the Molecular Nanomagnet Fe_8, Phys. Rev. Lett. 84 (13) (2000) 2965–2968.

[283] R. Giraud, W. Wernsdorfer, A. M. Tkachuk, D. Mailly, B. Barbara, Nuclear Spin Driven Quantum Relaxation in $LiY_{0.998}Ho_{0.002}F_4$, Phys. Rev. Lett. 87 (5) (2001) 057203.

[284] M. S. N. Ishikawa, W. Wernsdorfer, Quantum Tunneling of Magnetization in Lanthanide Single-Molecule Magnets: Bis(phthalocyaninato)terbium and Bis(phthalocyaninato)dysprosium Anions, Ang. Chem. Int. Ed. 44 (2005) 2931.

[285] P. Curie, Sur les propriétés magnétiques de l'oxygàne à diverses températures, C. R. Acad. Sci. 115 (1892) 1292–1295.

[286] M. P. Langevin, Sur la théorie du magnétisme, P. J. de Physique 4 (1905) 678.

[287] M. P. Langevin, Magnétisme et théorie des électrons, Annales de Chimie et Physique 5 (1905) 70.

[288] P. Ehrenfest, Note on the paramagnetism of solids, Leiden Commun. Suppl. 44b (157-168) (1919) 55–60.

[289] I. Waller, Über die Magnetisierung von paramagnetischen Kristallen in Wechselfeldern, Z. Phys. A-Hadron Nucl. 79 (5-6) (1932) 370–388.

[290] W. Heitler, E. Teller, Time effects in the magnetic cooling method. i, P. Roy. Soc. Lond. A Mat. 155 (886) (1936) 629–639.

[291] R. d. L. Kronig, On the mechanism of paramagnetic relaxation, Physica 6 (1939) 33.

[292] J. H. Van Vleck, Paramagnetic relaxation times for titanium and chrome alum, Phys. Rev. 57 (1940) 426.

[293] R. Orbach, Spin-lattice relaxation in rare-earth salts, P. Roy. Soc. Lond. A Mat. A264 (1961) 458.

[294] A. Abragam, B. Bleaney, Electron parmagnetic resonance of Transition Ions, Dover publications, INC., 1970.

[295] E. Burzurí, Ph.D. thesis, Instituto de Ciencia de Materiales de Aragón, CSIC-Universidad de Zaragoza (2011).

[296] C. Cohen-Tannoudji, B. Diu, F. Laloe, Quantum Mechanics, Wiley, New York, 1977.

[297] K. W. H. Stevens, The theory of paramagnetic relaxation, Rep. Progr. Phys. 30 (1) (1967) 189.

[298] M. N. Leuenberger, D. Loss, Spin relaxation in Mn_{12}-acetate, Europhys. Lett. 46 (5) (1999) 692.

[299] R. H. Ruby, H. Benoit, C. D. Jeffries, Paramagnetic Resonance below 1 K: Spin-Lattice Relaxation of Ce^{3+} and Nd^{3+} in Lanthanum Magnesium Nitrate, Phys. Rev. 127 (1) (1962) 51–56.

[300] G. H. Larson, C. D. Jeffries, Spin-Lattice Relaxation in Some Rare-Earth Salts I. Temperature Dependence, Phys. Rev. 141 (1) (1966) 461–478.

[301] G. Weber, Paramagnetische Spin-Gitterrelaxation der wasserhaltigen Chloride von Nd, Gd, Dy und Er im Temperaturbereich von 1.1 bis 4.2 K, Z. Phys. A-Hadron Nucl. 171 (2) (1962) 335–348.

[302] A. Morello, O. N. Bakharev, H. B. Brom, R. Sessoli, L. J. de Jongh, Nuclear spin dynamics in the quantum regime of a single-molecule magnet, Phys. Rev. Lett. 93 (19) (2004) 197202.

[303] G. H. Larson, C. D. Jeffries, Spin-Lattice Relaxation in Some Rare-Earth Salts II. Angular Dependence, Hyperfine Effects, and Cross Relaxation, Phys. Rev. 145 (1) (1966) 311–324.

[304] N. Bloembergen, S. Shapiro, P. S. Pershan, J. O. Artman, Cross-relaxation in spin systems, Phys. Rev. 114 (2) (1959) 445–459.

[305] H. N. V. Temperley, Time effects in the magnetic cooling method, Proc. Camb. Phil. Soc. 35 (1939) 256.

[306] D. D. P. Koch, R. H., J. Clarke, Model for $1/f$ flux noise in squids and qubits, Phys. Rev. Lett. 98 (2007) 267003.

List of Publications

1. M. J. Martínez-Pérez, J. Sesé, S. Cardona-Serra, C. Schlegel, J. van Slageren, J. M. Clemente-Juan, E. Coronado and F. Luis, Molecular design of spin-based qubits. In preparation.

2. M. J. Martínez-Pérez, J. L. García-Palacios and F. Luis. Analytical expressions for the magnetic susceptibility of a non-homogenes system of magnetic nanoparticles. In preparation.

3. M. J. Martínez-Pérez, R. de Miguel, J. Sesé, E. Burzurí, A. Lostao and F. Luis. Low temperature study of cobalt oxide nanoparticles: antiferromagnetism lays bare. In preparation.

4. A. Repollés, M. J. Martínez-Pérez, D. Aguilà, O. Roubeau, D. Zueco, M. Evangelisti, A. Camón, J. Sesé, L. A. Barrios, G. Aromí, and F. Luis. Molecular Prototypes for Spin-Based CNOT and SWAP Quantum Gates. Phys. Rev. Lett. **107** (2011) 117203.

5. M. J. Martínez-Pérez, E. Bellido, R. de Miguel, C. Gómez-Moreno, J. Sesé, A. Lostao, D. Drung, T. Schurig D. Ruíz-Molina and F. Luis. Ac magnetic susceptibility of a molecular magnet submonolayer directly patterned onto a micro superconducting quantum interference device. Appl. Phys. Lett. **99** (2011) 032504.

6. M. J. Martínez-Pérez, J. Sesê, F. Luis, R. Córdoba, D. Drung, T. Schurig, E. Bellido, R. de Miguel, C. Gómez-Moreno, A. Lostao, and D. Ruíz-Molina. Ultrasensitive broad band SQUID microsusceptometer for magnetic measurements at very low temperatures. IEEE Trans. Appl. Supercond. **21** (2011) 345.

7. M. J. Martínez-Pérez, R. de Miguel, Ch. Carbonera, M. Martínez-Júlvez, A. Gracía-Lostao, C. Piquer, C. Gómez-Moreno, J. Bartolomé and F. Luis. Size-dependent magnetic properties of magnetoferritin. Nanotechnol. **21** (2010) 465707.

8. F. Luis, E. Coronado, M. J. Martínez-Pérez, S. Cardona-Serra, O. Montero, C. Martí-Gastaldo, J. M. Clemente-Juan, J. Sesé, D. Drung, and T. Schurig. Spin-lattice relaxation via quantum tunneling in an Er^{3+}-polyoxometalate molecular magnet. Phys. Rev. B **82** (2010) R 060403.

9. M. J. Martínez-Pérez, J. Sesé, F. Luis, D. Drung and T. Schurig. Highly sensitive superconducting quantum interference device microsusceptometers inside the mixing chamber of a dilution refrigerator Rev. Sci. Instrum. **81** (2010) 016108.

10. M. J. Martínez-Pérez, J. Sesé, R. Córdoba, F. Luis, D. Drung and T. Schurig. Circuit edit of superconducting microcircuits. Supercond. Sci. Technol. **22** (2009) 125020.

11. F. Bartolomé, F. Petroff, J. Bartolomé, L. M. García, C. Deranlot, H. Jaffrès, M. J. Martínez-Pérez, P. Bencok, F. Wilhelm, A. Rogalev, and N. B. Brookes. Tuning the magnetic anisotropy of Co nanoparticles by metal capping. Europhys. Lett. **76** (2006) 142.

12. F. Luis, J. Bartolomé, F. Bartolomé, M. J. Martínez-Pérez, L. M. García, F. Petroff, C. Deranlot, F. Wilhelm, and A. Rogalev. Enhancement of the magnetic anisotropy of Co clusters by Au capping. J. Appl. Phys **99** (2005) 8.

Agradecimientos

En primer lugar me gustaría dar las gracias a mis dos directores de tesis. Gracias a los dos por haber estado disponibles en todo momento y sobre todo por haber confiado en mi. A Fernando gracias por todas las cosas que me has enseñado, por tu ilusión, por tus millones de ideas, por preocuparte por mi y por animarme para seguir. A Javier gracias por tu paciencia, por explicar tan bien, por todas las horas frente al ordenador, por llevarme a Broadway y por tu sentido del humor.

Muchas gracias a todas las personas con las que he tenido la oportunidad de trabajar, Agustín Camón, Ana Repollés, Carlos Trullén, Chiara Carbonera, Cristina Piquer, David Zueco, Emma Lythgoe, Enrique Burzurí, Fernando Palacio, Javier Campo, Juan Bartolomé, Juan José Morales, Marco Evangelisti, Marisa Bonilla, Mark Jenkins, Olivier Roubeau, Oscar Montero, Pablo Alonso y Román López-Ruiz. Gracias a todos por haberme dedicado vuestro tiempo. En especial, gracias a Nico, David y Marco, por vuestras bromas y porque hacéis que este trabajo sea algo mucho más divertido. Gracias también a Jesus Chaboy por haber compartido tu despacho conmigo.

Al grupo del Instituto de Ciencia Molecular de la Universidad de Valencia, Eugenio Coronado, Carlos Martí-Gastaldo, Modesto Clemente y Salva Cardona-Serra. Gracias por la síntesis y caracterización de muestras de imanes moleculares además de vuestra enorme disponibilidad.

Al grupo del Centre d'investigació en Nanociència i Nanotecnologia de Barcelona, Dani Ruiz-Molina y Elena Bellido, por todo el esfuerzo que habéis dedicado a los experimentos de DPN, por vuestra compañía y sobre todo por vuestra amistad.

Al grupo del Instituto de Nanociencia de Aragón, Anabel Lostao y Rocío de Miguel y a Marta Martínez-Júlvez del departamento de bioquímica de la Universidad de Zaragoza, por la síntesis y caracterización de muestras de ferritina, por vuestro apoyo en general y por vuestra simpatía. También a Rosa Córdoba del INA, gracias por tu tiempo y amabilidad.

I would like to thank Joris van Slageren, Christoph Schlegel and Lapo Bogani from the University of Stuttgart for the nice collaboration and for your support in EPR measurements. From the University of Nottingham I would like to thank Fabrizio Moro and Francesco Piga for your help, friendship and the good moments we spent there.

From the Physikalisch-Technische Bundesanstalt in Berlin I would like to thank Thomas Schurig, Dietmar Drung, Joern Beyer, Cornelia Aßmann, Marianne Fleischer, Margret Peters and Frank Ruede, for your help, collaboration

and fruitful discussions.

Al servicio de medidas físicas, Ainhoa Urtizberea, Ana Arauzo y Enrique Guerrero. Muy en especial al servicio de criogenia, Conrado Rillo, Fernando Gómez, Marta Castrillo y Leticia Tocado. Muchísimas gracias también al servicio de instrumentación, Ángel López, Ángel Lara y Pedro Téllez, sobre todo a Pedro por bajar al laboratorio siempre que lo he necesitado.

Muchísimas gracias a toda mi familia. A mis padres, gracias por quererme tanto y por haberme enseñado a ser feliz. A Concha, Mari y Bels por cuidarme y protegerme siempre. Muchísimas gracias de vuestra hermanita pequeña. Gracias también a todos mis cuñados y cuñadas porque, junto a vosotros, las comidas familiares son mucho más divertidas.

A mis amiguitas de Huesca, Ale, Andrea, Cris, Elenon, Pilar, Salas. Gracias por haberme hecho reir tantísimo y sobre todo, gracias de corazón por haber sido siempre mi via de escape. Victor, gracias a ti también porque siempre consigues "quitarle hierro al asunto". Muy en especial a Salius porque nunca me has juzgado, porque me conoces mejor que yo misma y porque contigo nada me da miedo. Gracias por ser mi "genio del mal".

A mis becarios de la uni, Clarobla, Enrique, Jesús, Juancho, Kike, María, Raquel, Sara, Sol, Vera. Ojalá tenga la oportunidad de volver a trabajar junto a gente como vosotros. Gracias por escucharme durante muchos cafés, comidas, cenas, cervezas... A Enrique gracias porque me encanta estar a tu lado. A Sol por nuestras vidas paralelas y porque contigo nunca me he sentido extraña. Gracias también a todos los demás becarios y postdocs del departamento, mis compis de despacho Ana y Ainhoa, Alexey, Alberto, Cris, Diego, Jorge S., Keisuke, Nuno, Roberto B., Saeid, Teo y muchos más... por los capazos y por alguna que otra fiesta.

A mis amig-osos del santa, Ana, Andriu, Bels, Berti, Cris, Luci, Migu, Mor, Raquel, Silvi. Si me dais a elegir, elijo volver a entrar al primero y pasar otros cinco años junto a vosotros. A mis oscenses, Andriu y Mig, gracias por haberme dejado ser el catalizador y por todas las risas que nos echamos. Gracias en general a todas las personas que vivieron esos años a mi lado. Chema, Glez, Mac, Rous y todos los demás... En particular, muchísimas gracias a Magallón por seguir estando a mi lado después de todo.

Danke an meine lieben Freunde aus Berlin, Arthur, Daniel und Renchen. Berlin halte ich ganz fest in meinem Herzen, die wunderschönste Stadt der Welt, aber nur weil ihr dort seid. Danke für jede unvergessliche Reise, danke für eure endlose Liebe. Arthur, bei dir bedanke ich mich besonders, weil du mein Leben total verändert hast... auch wenn wir uns eigentlich schon kennengelernt hatten. Du weisst, wir verlieren uns nie.

ISBN 978-84-15274-82-7

9 788415 274827

1542

Prensas Universitarias
Universidad Zaragoza